Active/Passive Optimization of Helicopter Rotor Blades for Improved Vibration, Noise, and Performance Characteristics

by

Bryan Glaz

A dissertation submitted in partial fulfillment
of the requirements for the degree of
Doctor of Philosophy
(Aerospace Engineering)
in The University of Michigan
2008

Doctoral Committee:

Professor Peretz P. Friedmann, Chair
Professor Panos Y. Papalambros
Professor Wei Shyy
Professor Anthony M. Waas

Acknowledgements

I wish to thank all who made this work possible. The guidance and constant drive for excellence of my advisor Professor Friedmann has been the driving force behind this work. I have no doubt that working with him has made me the best researcher and communicator that I can be. I also wish to thank my co-author on all of the papers associated with this thesis, Dr. Li Liu. His expertise and willingness to help were critical to the completion of this thesis. It would be impossible for me to overstate how grateful I am to him. I wish to thank Professor Raphael Haftka and Dr. Tushar Goel for the enlightening collaboration I had the opportunity to participate in. In addition, I would like to thank Professor Haftka for his guidance in selecting a graduate school. He played a significant role in my decision to attend the University of Michigan, which I consider to be the best decision I have ever made. It has truly been a privilege to work with these individuals, without whom the quality of this thesis would have suffered immeasurably. The work of Drs. Kuo-An Yuan, Thomas Millott, Tim Myrtle, Marino de Terlizzi, Richard Cribbs, Gilles Depailler, and Dan Patt are gratefully acknowledged for establishing the foundation on which this research was built. I am grateful to Professor Panos Papalambros and Dr. Subroto Gunawan for providing one of the kriging algorithms used in this study. In addition, I am grateful to my thesis committee members for the time and effort they spent.

I am also grateful to my friends from the University of Michigan, Professor Jack McNamara, Dr. Rafael Palacios, Abhijit Gogulapati, Satish Chimakurthi, Matt Leach, Hsengji

Huang, Pete Gustafson, Wooseok Ji, Smith Thepvongs, Jesse Thomas, and Sonca Nguyen for the enlightening, and sometimes comical, discussions. Also, my thanks to the staff at the University of Michigan, Brock Palen, Denise Phelps, and Margaret Fillion, for their help.

Finally, partial support from the NASA Graduate Student Research Program with Dr. W. Warmbrodt as grant monitor, the Center for Rotorcraft Innovation under WBS 2007-B-01-01.2-A17, the Vertical Lift Research Center of Excellence (VLRCOE) sponsored by the NRTC with Dr. M. Rutkowski as grant monitor, and the Rackham School of Graduate Studies for their support in the form of the Rackham Engineering Award are also hereby acknowledged.

Table of Contents

List of Figures

Figure

List of Tables

Table

List of Appendices

Appendix

List of Symbols

a	Lift curve slope
a_j, r_j, E_j	Empirical coefficient associated with the dynamic stall model
A	Blade cross sectional area
b	Blade semi-chord
c	Speed of sound
c_b	Blade chord
c_{cs}	Control surface chord
c_{wu}	Scalar parameter used to enforce saturation limits on the flap deflection
$[C]$	Damping matrix
C_{d0}	Blade profile drag coefficient
C_{ij}	Material elastic moduli
C_L, C_M, C_{Hm}	Sectional lift, moment and hinge moment coefficients for RFA
$C_{Pi}, i = 1, \cdots, n$	Pressure coefficient at the i^{th} panel chordwise
C_T	Thrust coefficient
C_W	Helicopter weight coefficient
$\mathbf{C_0}, \mathbf{C_1}, \mathbf{C}_n, \mathbf{D}, \mathbf{E}, \mathbf{R}$	Coefficient matrices from the RFA aerodynamic model
$\mathbf{C}_{Oj}$, $\mathbf{C}_{Ij}$, $\mathbf{C}_{NWij}$	Influence coefficients used in the free wake calculation
d_1, d_2	User defined parameters used in weighted average surrogate construction
D	Drag
D_0	Generalized flap deflection
D_1	Generalized flap angular velocity
D_f	Parasitic drag of the fuselage
$\mathbf{D}$	Vector of design variables
D_A	Sectional profile drag
D_S	Separated flow sectional drag
$\mathbf{D}(\psi, \phi)$	Wake distortion

e_1	Blade root offset from center of rotation
$\hat{e}_x, \hat{e}_y, \hat{e}_z$	Orthonormal triad of element coordinate system
$\hat{e}_x, \hat{e}_\eta, \hat{e}_\zeta$	Orthonormal triad of undeformed curvilinear coordinate system
$\hat{e}'_x, \hat{e}'_\eta, \hat{e}'_\zeta$	Orthonormal triad of deformed curvilinear coordinate system
$\mathbf{E}_x, \mathbf{E}_\eta, \mathbf{E}_\zeta$	Basis vectors of deformed elastic axis
E_i	Global error metric corresponding to the $i^{th} surrogate$
E_{avg}	Average of the global error metrics for all surrogates
EIF	Expected improvement function
$f = 0$	Function that describes the moving surface generating sound
f_{ij}	Strain tensor in curvilinear coordinates
$f(\mathbf{x})$	Assumed polynomials which account for the 'global' behavior in kriging
$\mathbf{f_x}$	Vector of basis functions associated with assumed polynomials in kriging
$\mathbf{F}$	Matrix of basis functions associated with assumed polynomials in kriging
$\mathbf{f}$	Generalized load vector
$\mathbf{f}^p$	Generalized pressure vector
$\mathbf{f_b}(\cdot)$	Blade motion equations
$\mathbf{f_t}(\cdot)$	Trim equations
$\mathbf{F}$	Load vector in equations of motion
F_T	Vertical force
$\mathbf{F_H}$	Instantaneous hub shear
F_{HX}, F_{HY}, F_{HZ}	Components of hub shear
F_{4X}, F_{4Y}, F_{4Z}	4/rev hub shears, non-dimensionalized by $m_0\Omega^2R^2$
$\hat{F}_{4X}, \hat{F}_{4Y}, \hat{F}_{4Z}$	Surrogates for the non-dimensional 4/rev hub shears
$\mathbf{F_{N_bcH}}, \mathbf{F_{N_bsH}}$	cos and sin components of N_b/rev vibratory loads of hub shears
$\mathbf{F_{Rk}}$	Resultant blade root forces for the k^{th} blade
g	Green's function
$\mathrm{g}(\mathbf{D})$	Constraints
$\mathbf{g}_x, \mathbf{g}_\eta, \mathbf{g}_\zeta$	Basis vectors of undeformed beam
$\mathbf{G}_x, \mathbf{G}_\eta, \mathbf{G}_\zeta$	Basis vectors of deformed beam
$\mathbf{g_a}(\cdot)$	Aerodynamic (RFA) state equations
$\mathbf{g_{aR}}(\cdot)$	Reduced form of the aerodynamic (RFA) state equations
$\mathbf{g_{dR}}(\cdot)$	Reduced form of the aerodynamic (ONERA) state equations
$\mathbf{G}$	Laplace transform of $\mathbf{f}$

$GMSE_i$	Generalized mean square error corresponding to the i^{th} surrogate
h	Plunge displacement at 1/4-chord, expressed in semi-chords
$\mathbf{h}_e$	Offset of beam element in-board node from blade root
H	Horizontal force
H_m	Sectional hinge moment
$\mathbf{h}$	Generalized motion vector = $[W_0, W_1, D_0, D_1]$
$\mathbf{H}$	Laplace transform of the generalized motion vector
$N_{H06}, \ldots, N_{H17}$	Noise levels of the 6^{th} - 17^{th} harmonics of blade passage frequency
i	$= \sqrt{-1}$
$\hat{\mathbf{i}}_b, \hat{\mathbf{j}}_b, \hat{\mathbf{k}}_b$	Orthonormal triad of preconed, pitched, blade-fixed coordinate system
$\hat{\mathbf{i}}_{nr}, \hat{\mathbf{j}}_{nr}, \hat{\mathbf{k}}_{nr}$	Orthonormal triad of nonrotating, hub-fixed coordinate system
$\hat{\mathbf{i}}_r, \hat{\mathbf{j}}_r, \hat{\mathbf{k}}_r$	Orthonormal triad of rotating, hub-fixed coordinate system
I_P	Mass polar moment of inertia of the rotor
J_1, J_2	Objectives functions which are combined in the weighted sum approach
$J_{ACF}(\mathbf{z}_k, \mathbf{u}_k)$	Quadratic-form of the ACF objective function
$J_{_V}, J_{_N}, J_{_P}$	Vibration, noise, and rotor power passive optimization objective functions
J_{sum}	Weighted sum objective function
$\hat{J}_{_V}$	Surrogate vibration objective function
$J_{_{DS}}, J_{_{BVI}}$	Vibration objective functions for dynamic stall and BVI regimes
k	Reduced frequency = $\omega_\alpha b/U$
$[K]$	Stiffness matrix
K	Kernel for Possio integral equation
K_{NW}	Number of azimuthal steps retained for modeling the near wake
l_e	Length of beam element
l_i	Components of local force intensity that acts on the fluid, $l_i = P_{ij} n_j$
l_r	Local force intensity on fluid in radiation direction $l_r = l_i r_i$
$\dot{l_r}$	$= \dot{l}_i r_i$
L	Sectional lift
L_A, L_S	Attached flow and separated flow sectional lift
L_b	Blade length
L_{cs}	Control surface length

m_{cs}	Mass of control surface per unit length
M	Local mach number
M	Sectional moment
$[M]$	Mass matrix
M_A, M_{A_S}	Sectional moment with respect to the aerodynamic center for the attached and separated flow regimes
M_b	Mass of one blade
M^{pt}	Rotor pitching moment about the hub center
M_r	Mach number in the radiation direction
M^{rl}	Rotor rolling moment about the hub center
M^{yw}	Rotor yawing moment about the hub center
$\mathbf{M_H}$	Instantaneous hub moment
M_{HX}, M_{HY}, M_{HZ}	Components of hub moment
$\mathbf{M_{N_bcH}}, \mathbf{M_{N_bsH}}$	$\cos$ and $\sin$ components of N_b/rev vibratory loads of hub moments
M_{4X}, M_{4Y}, M_{4Z}	4/rev hub moments, non-dimensionalized by $m_0\Omega^2R^3$
$\hat{M}_{4X}, \hat{M}_{4Y}, \hat{M}_{4Z}$	Surrogates for the non-dimensional 4/rev hub moments
$\mathbf{M_{Rk}}$	Resultant blade root moments for the k^{th} blade
n_L	Number of aerodynamic lag terms in the RFA approach
N_b	Number of rotor blades
N_c	Number of behavior constraints
N_{dv}	Number of design variables
N_{sp}	Number of sample points
N_{sm}	Number of surrogate models
N_{RBF}	Number of radial basis functions associated with RBNN's
N_{Hi}	i^{th} BVI noise harmonic
N_{OF}	Total number of objective functions
N_p	Number of available processors
p	Air pressure
p_0	Empirical quantities used in Petot's dynamic stall model
p'	Acoustic pressure $p - p_0$
$\bar{p}$	Nondimensional air pressure
P_0	Reference pressure
$\mathbf{P}$	Distributed force vector along elastic axis
$P(x,t)$	Surface pressure distribution
$\mathbf{p_A}$	Distributed aerodynamic loads
$\mathbf{p_I}$	Distributed inertial loads

p_k, ϑ_k	Fitting parameters in kriging corresponding to the k^{th} design variable
$p(\mathbf{x})$	Surrogate function considered in GSA
$\mathbf{q}$	Vector of finite element nodal degrees of freedom
$\mathbf{q}_0$	Nonlinear equilibrium position in hover
q_∞	Dynamic Pressure
$\mathbf{q_t}$	Vector of trim variables
$\mathbf{q_A}$	Distributed aerodynamic moments
$\mathbf{q_I}$	Induced velocity
$\mathbf{Q}$	Distributed moment vector along elastic axis
$\mathbf{Q}$	RFA transfer matrix
$\mathbf{Q}$	Active control weighting matrix on quantities to be reduced
Q_t	Tail rotor torque
$\mathbf{r_b}$	Position of the wake blade when it generates the wake element
$\mathbf{r_w}$	Position of a wake element
$\mathbf{r_{EA}}$	Position vector for a point on the elastic axis
$\mathbf{r}$	Position vector of undeformed beam
R	Blade radius
R_{LM}, R_D	Reverse flow factors for lift(moment) and drag, respectively
$\mathbf{R}$	Position vector of deformed beam
$\mathbf{R}_0$	Position vector of deformed elastic axis
$\mathbf{R_t}$	Vector of trim residuals
r	Distance between observer and source $\lvert\mathbf{x}-\mathbf{y}\rvert$
r_i	Components of vector $\hat{r}$
$\hat{r}$	Unit vector in radiation direction $(\mathbf{x}-\mathbf{y})/r$
$\mathbf{R}_{\mathrm{krg}}$	Spatial correlation matrix used in kriging
$R_{\mathrm{krg}}(\cdot)$	Spatial correlation function in kriging
$\mathbf{r}_{\mathrm{krg}}(\mathbf{x})$	Spatial correlation vector in kriging
$\mathbf{R}_{\mathrm{RBF}}$	Spatial correlation matrix in RBF interpolation
$R_{\mathrm{RBF}}(\cdot)$	Spatial correlation function in RBF interpolation
$\mathbf{r}_{\mathrm{RBF}}(\mathbf{x})$	Spatial correlation vector in RBF interpolation
$R_{\mathrm{RBNN}}(\cdot)$	Radial basis functions used in RBNN's
$\bar{s}$	Nondimensional Laplace variable $\bar{s} = \frac{s_L b}{U}$
$s(\mathbf{x})$	Predicted error in the kriging surrogate objective function
S_i^{total}	Total sensitivity index due to the i^{th} design variable
$S_{i\ldots k}$	Partial sensitivity index due to the interactions among the $i^{th}\ldots k^{th}$ design variables
t	Observer time

$\bar{t}$	Nondimensional time, reduced time
T	Kinetic energy
$[T_{rn}], [T_{br}], [T_{eb}],$ $[T_{ce}], [T_{dc}], [T_{de}]$	Transformation matrices between coordinate systems
T_t	Tail rotor thrust
T_{ij}	Lighthill stress tensor $T_{ij} = \rho v_i v_j + P_{ij} - a_\infty \rho' \delta_{ij}$
$T_{_{NL}}$	Threshold noise level (dB)
$\mathbf{T}$	Transfer matrix
$\mathbf{T}$	Sensitivity matrix relating control input to plant output
u, v, w	Displacements of a point on the blade's elastic axis due to blade deformation
U	Strain energy
$U, U(t)$	Air velocity relative to the blade section
$\mathbf{U}$	Total air velocity vector
U_P,U_T	Perpendicular and tangential components of freestream velocity experienced by the blade
v_n	Surface normal velocity
v_i, v_j	Components of fluid velocity in directions x_i and x_j
$\mathbf{v}$	Velocity vector
$V(p)$	Total variance in the function $p(\mathbf{x})$
$\mathbf{V_A}$	Airflow velocity due to forward flight, blade rotation and induced inflow
$\mathbf{V_{EA}}$	Velocity of a point on the elastic axis of the blade due to blade dynamics
V_i^{total}	Partial variance due to the interactions among the $i^{th} \ldots k^{th}$ design variables
w	Weight used in the weighted expected improvement function
$\bar{w}$	Nondimensional velocity
$w_{\text{poly}}, w_{\text{krg}}, w_{\text{RBNN}}$	Weight coefficients corresponding to each surrogate
$W_{_H}$	Helicopter weight
W	Weight of the objective function
W_e	Work of nonconservative loads
$W(x,t)$	Normal velocity distribution
W_0	Angle of attack generalized coordinate
W_1	Pitch rate generalized coordinate
$\mathbf{W}_{\text{u}}$	Weighting matrix on control input
$\mathbf{W}_\alpha$	Active control weight setting
x	Streamwise coordinate
x, η, ζ	Curvilinear coordinates

x_1, x_2, x_3	Indicial notations for x, η, ζ
x_{cs}	Distance from the hub to the center of the control surface
x_{rev}	Reverse flow boundary
X_t	Horizontal offset of tail rotor center from hub
X_A	Offset between the aerodynamic center and the elastic axis
X_H	Offset between the hinge point and the elastic axis
X_{Ib}	Offset of the blade cross-sectional center of mass from the elastic axis
X_{Ic}	Offset of the control surface cross-sectional center of mass from the hinge point
X_{IIb}	Offset of the blade cross-sectional center of area from the elastic axis
X_{IIc}	Offset of the control surface cross-sectional center of area from the hinge point
X_{FA},Z_{FA}	Longitudinal and vertical offsets between rotor hub and helicopter aerodynamic center (see Fig. 6.1)
X_{FC},Z_{FC}	Longitudinal and vertical offsets between rotor hub and helicopter center of gravity (see Fig. 6.1)
$\mathbf{x}_a$	Aerodynamic state vector
$\mathbf{X}_a$	Laplace transform of the aerodynamic state vector
$\mathbf{x}^{(i)}$	i^{th} sample point
y_1, y_2, y_3	Local Cartesian coordinates
$\mathbf{y}$	Vector of generalized coordinates in modal space
$\mathbf{y}$	Source position vector
Y	Lateral force
$y(\mathbf{x})$	Unknown function to be approximated
$y^{(i)}$	output response at $\mathbf{x}^{(i)}$
$\mathbf{y}$	Vector of observed function outputs
$\hat{y}(\mathbf{x})$	Approximation of $y(\mathbf{x})$
$\bar{y}$	Factor used to normalize errors
$\mathbf{z}_k$	Vector of quantities to be reduced by active control
Z_t	Vertical offset of tail rotor center from hub
$Z(\mathbf{x})$	Realization of a stochastic process in kriging
α	Amplitude of warping
α	Angle of attack of the airfoil
α_A	Blade local angle of attack
α_{cr}	Critical angle of attack of the airfoil (ONERA)
α_r	Control algorithm relaxation factor
α_R	Rotor shaft angle of attack

β_p	Blade precone angle
$\beta(x)$	Pretwist angle distribution along the blade
$\boldsymbol{\beta}$	Vector of coefficients used in kriging
$\hat{\boldsymbol{\beta}}$	Generalized least squares estimate of $\boldsymbol{\beta}$
$\beta_0, \beta_i, \beta_{ij}$	Fitting coefficients in polynomial regression
$\gamma_{\eta\zeta}, \gamma_{x\zeta}, \gamma_{x\eta}$	Shear strain components
$\bar{\gamma}_{x\eta}, \bar{\gamma}_{x\zeta}$	Transverse shears at elastic axis
δ	Dirac delta function
δ_f	Flap deflection angle
$\delta_{\max}$	Maximum flap deflection
δ_{ij}	Kronecker delta
$\delta\mathbf{u}$	Virtual displacement vector of elastic axis
$\delta\boldsymbol{\Theta}$	Virtual rotation vector of elastic axis
$\Delta C_L, \Delta C_M, \Delta C_D$	Empirical quantities used in Petot's dynamic stall model
$\Delta\tau$	Dynamic stall nondimensional delay
ϵ_{pr}	Approximation error in polynomial regression
ε	Absolute percent error of surrogate predictions
$\varepsilon_{xx}, \varepsilon_{\eta\eta}, \varepsilon_{\zeta\zeta}$	Normal strain components
$\bar{\varepsilon}_{xx}$	Axial strain at elastic axis
$\lambda_x, \lambda_y, \lambda_z$	Induced velocity components
λ_k	Hover stability eigenvalue for the k^{th} mode
ϕ	Elastic twist about the elastic axis
ϕ_w	Wake age
ϕ_R	Lateral roll angle
ϕ_{den}	Normal density function
Φ_{dist}	Normal distribution function
ρ	Air density, also mass density of beam
ρ_{filler}	Material density for non-structural filler mass
ρ_{struct}	Material density for the structural member of the blade
γ	Lock number
γ_i	Rational approximant poles
γ_n	Poles for RFA
γ_s	Strength of shed vorticity
γ_t	Strength of trailed vorticity
Γ_{j2}	States associated with dynamic stall
$\Gamma(r)$	Circulation distribution
Γ_I, Γ_O	Inboard and outboard circulation peaks, in dual wake model
η, ζ	Curvilinear coordinates

η_c, ζ_c	Coordinates in the flap attached coordinate system
μ	Advance ratio $= V_\infty \cos\alpha / \Omega R$
$\kappa_\eta, \kappa_\zeta$	Curvatures of the deformed beam
$[\kappa]$	Transformation matrix between $(\hat{e}'_x, \hat{e}'_\eta, \hat{e}'_\zeta)$ and its derivatives
$[\kappa_0]$	Transformation matrix between $(\hat{e}_x, \hat{e}_\eta, \hat{e}_\zeta)$ and its derivatives
χ_1, χ_2	Components of the expected improvement function
ψ	Azimuth angle
Ψ	Out-of-plane warping shape function
σ	Rotor solidity
$\sigma_{xx}, \sigma_{\eta\eta}, \sigma_{\zeta\zeta}$	Normal stress components
$\sigma_{\eta\zeta}, \sigma_{x\zeta}, \sigma_{x\eta}$	Shear stress components
$\sigma_{allowable}$	Allowable blade stress
$\sigma_{_Y}$	Yield stress
σ^2_{var}	Variance of the Gaussian process $Z(\mathbf{x})$
$\hat{\sigma}^2_{var}$	Generalized least squares estimate of σ^2_{var}
τ	Nondimensional time
τ	Source time
τ	Twist of deformed beam
τ_0	Initial twist of the beam $(= \beta_{,x}\,)$
τ_{RBF}	Fitting parameter in RBF interpolation
τ_{RBNN}	Parameter which control radius of influence for each neuron in RBNN's
$\theta_{\mathrm{coll}}, \theta_{1s}, \theta_{1c}$	Collective and cyclic pitch components
θ_{0t}	Tail rotor collective pitch
θ_{FP}	Flight path angle, positive for descending flight (see Fig. 6.1)
θ_{pc}	Pilot pitch input $\theta_0 + \theta_{1c}\cos\psi + \theta_{1s}\sin\psi$
θ_{pt}	Linear built-in pretwist distribution
θ_0	Built-in pretwist angle at the root
$\theta_{_1}, \theta_{_2}$	Pretwist angle design variables at the 50% and 100% blade stations
θ_G	Geometric pitch angle, $\theta_{pc} + \theta_{tw}$
ω_k, ζ_k	Imaginary and real parts of λ_k, respectively
Ω	Rotor angular velocity
$\omega_{F1},\ \omega_{L1},\ \omega_{T1}$	Fundamental rotating flap, lead-lag and torsional frequencies, /rev
ω_L, ω_U	Lower and upper bounds for frequency constraints, /rev
∇^2	Laplacian in two dimensions

$\dot{()}$	$d()/dt$

Acronyms

ACF	Actively controlled flap (see Fig. 1.2)
BVI	Blade-vortex interaction
EGO	Efficient global optimization
EIF	Expected improvement function
GSA	Global sensitivity analysis
HHC	Higher harmonic control
MSE	Mean squared error
NLABS	Nonlinear Active Beam Solver
OLH	Optimal Latin hypercube
RFA	Rational function approximation
RBF	Radial basis function
RBNN	Radial basis neural network
SBO	Surrogate based optimization
SPL	Sound pressure level
WEIF	Weighted expected improvement function
VABS	Variational Asymptotic Beam Sectional Analysis

Chapter I

Introduction and Literature Review

Due to their unique capacity for low speed maneuverability and vertical takeoff, helicopters fulfill a variety of military and civil missions which are beyond the capabilities of fixed wing aircraft. However, high vibration and noise levels limit the helicopter's community acceptance and mission effectiveness. While many sources, including the main rotor, tail rotor, engine, and gearbox, contribute to the overall vibration levels and noise generation, the dominant source of vibration and noise is the main rotor. Since the state of rotorcraft technology is relatively mature, design improvements are achieved through "evolution, not revolution [146]", of current configurations. Therefore, improved main rotor blade designs are critical to the development of advanced rotorcraft.

Vibratory loads transferred from the main rotor to the fuselage, at harmonics that are predominantly N_b/rev, have been a critical concern from the earliest days of rotorcraft development [54, 97, 127]. In addition to passenger comfort, reliability and fatigue life of components are adversely affected by vibration. Although significant levels of vibration reduction have been achieved over the past 50 years, modern helicopters still do not meet the ultimate goal of a "jet smooth" ride. Depending on the flight regime, different phenomena will be responsible for significant vibratory loads on the blades. At low advance ratios,

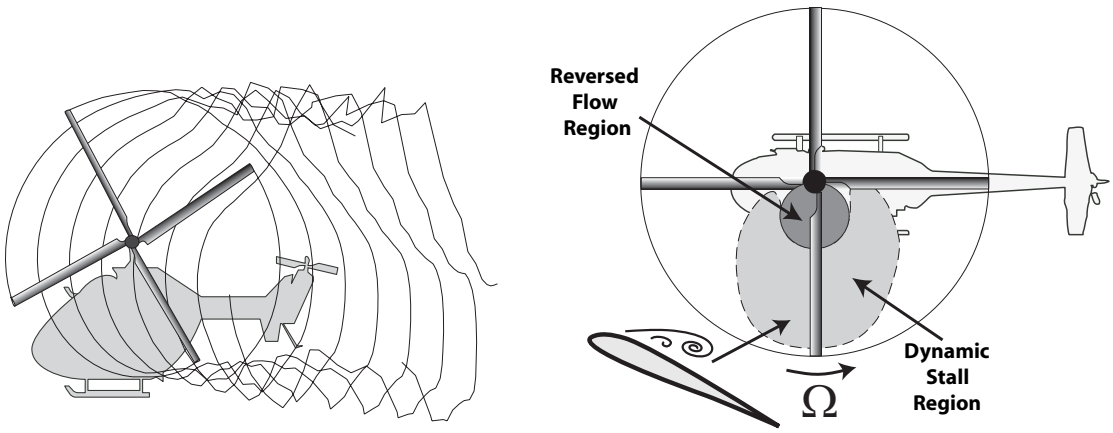

(a) BVI **(b) Dynamic stall**

Figure 1.1: Illustrations of BVI and dynamic stall

i.e. low speed forward flight, and descending flight, relatively high vibration levels are produced by blade-vortex interaction (BVI) effects which occur when the rotating blades encounter the tip vortices shed by the preceding blades, as illustrated in Fig. 1.1(a). At high advance ratios, the dominant source of vibratory loads is dynamic stall, which is characterized by flow separation on the retreating side of the rotor plane as shown in Fig. 1.1(b). Therefore, effective design aimed at vibration reduction needs to address vibration characteristics throughout the entire flight envelope. Furthermore, significant increases in operational costs due to active and/or passive vibration reduction approaches would prevent implementation in production helicopters. Therefore, vibration reduction approaches must not increase the power consumption associated with the main rotor. This is important at higher advance ratios since the helicopter is likely to spend most of its mission profile in cruising flight.

The physical sources and characteristics of rotor noise vary with flight speed, maneuver, and descent condition. At high speed level forward flight, compressibility and transonic

effects at the tip produce high-speed impulsive (HSI) noise, which is beyond the scope of this study. The focus of this study is on high noise levels associated with helicopters in low speed approach flight conditions, which significantly limit the community acceptance of civilian rotorcraft, and may affect the likelihood of detection during military missions. In order to meet FAA flyover noise level requirements as well as military specifications, a substantial body of research has been aimed at modeling and reduction of low speed noise due to BVI effects [172]. Furthermore, since high vibration and noise levels at low advance ratios are due to the same sources, reduction of BVI induced vibration and noise must be treated simultaneously in order to eliminate potential penalties associated with seeking improvement in only one of these effects.

Precise modeling of the blade's aeroelastic response is critical for accurate vibration and acoustic predictions. The aeroelastic response of helicopter rotor blades in forward flight is characterized by the interaction of the rotor blade with the unsteady aerodynamic environment, and is inherently multidisciplinary [43]. Therefore, comprehensive rotorcraft analysis codes are necessary for vibratory hubload and noise level predictions. However, due to the complex rotary wing aerodynamic environment, such analysis codes are computationally expensive, which has limited their use for design optimization applications. Reviews of the current state of rotorcraft analysis codes and requirements for the next generation can be found in Refs. 25, 40, and 79.

Substantial effort has been devoted toward improved rotor blade vibration, noise, and performance characteristics. A review of the relevant studies is provided in order to provide perspective on the contributions made in this research. Sections 1.1 – 1.3 pertain

to studies devoted to individual treatment of vibration reduction, BVI noise reduction, or performance enhancement when considered as single objectives. Multi-objective investigations are documented in Section 1.4. A review of techniques designed for optimization of expensive objective functions, and the limited number of applications of such methods to rotor blade design, is provided in Section 1.5. Finally, the objectives and contributions of this dissertation are presented in Sections 1.6 and 1.7 respectively.

1.1 Review of Vibration Reduction Literature

The focus of this thesis is on vibratory hubloads associated with the main rotor. Thus, other sources of vibration, such as the engine and gearbox, are not considered.

1.1.1 Passive Vibration Reduction

The earliest and most widely implemented approach to vibration reduction involves the use of passive and semi-passive devices such as cabin suppressors and isolators. However, these devices have significant weight penalties and are tuned for particular operating conditions and payloads [97, 127]. Furthermore, such devices do not decrease vibration at the source, i.e. the main rotor, as opposed to the use of structural optimization to modify the mass, stiffness, and geometric properties of the rotor blade. Therefore, structural optimization is the passive approach upon which this thesis is focused. In this approach, the vibration reduction problem is formulated as a mathematical optimization problem subject to appropriate constraints. The objective function consists of a suitable combination of the N_b/rev hub shears and moments which are computed by an aeroelastic response code;

constraints are specified on blade stability margins, frequency, blade geometry, autorotational properties, and blade stresses. The design variables can be dimensions of the blade cross-section, mass and stiffness distributions along the span, or geometrical parameters. Survey papers on structural optimization of helicopter rotor blades have been written by Friedmann, Celi, and Ganguli [13, 39, 49]; therefore only the key representative studies are discussed below.

Friedmann and Shanthakumaran [45] were the first to consider minimization of vibration with aeroelastic stability constraints. The objective function consisted of the peak-to-peak 4/rev vertical hub shear or rolling moment at an advance ratio $\mu = 0.30$, and behavior constraints were placed on the blade frequencies and aeroelastic stability margins in hover. In order to overcome the significant computational cost associated with objective function evaluations, a local search of the design space was conducted in the vicinity of a single design point by optimizing Taylor series approximations of the objective function. Vibration reduction of $15 - 40\%$ was achieved for an isotropic soft-in-plane configuration. The results demonstrated that non-structural masses are most effective for vibration reduction when distributed over the outboard 1/3 of the blade. Furthermore, while the blade was optimized at $\mu = 0.30$ only, it was shown that the optimum design corresponded to reduced vibration at other advance ratios. Based on the results from this study, most of the subsequent vibration reduction studies only considered optimization at $\mu = 0.30$.

Lim and Chopra [93, 94] employed the local search algorithm CONMIN [155], which is based on the method of feasible directions. As an alternative to numerically calculating gradients required by CONMIN, Lim and Chopra utilized analytical sensitivity relations in

which derivatives of the vibration objective function and stability constraints were written in terms of the design variables. Using this approach, $20 - 50\%$ vibration reduction was obtained, and an 80% reduction in computer time compared to optimization with finite difference methods was reported. However, this approach breaks down when using modern free-wake and unsteady aerodynamic models because it becomes extremely complicated to obtain analytical, or semi-analytical sensitivity relations [13]. Other contributions from Refs. 93 and 94 include the use of a coupled trim/aeroelastic response analysis, and the introduction of a vibration objective function in which the three hub shears and three hub moments are combined.

Yuan and Friedmann [174,175] studied optimization of composite rotor blades with advanced geometry tips. The aeroelastic response analysis was based on a relatively simple quasi-steady, incompressible aerodynamic model with a uniform inflow assumption. Similar to Ref. 45, a local search of the design space was conducted using local Taylor series approximations of the objective function and the DOT optimization package [128]. The authors concluded that proper combination of composite ply angles and tip sweep/anhedral can be used to reduce vibrations while improving aeroelastic stability characteristics.

The representative studies discussed above were based on relatively simple aerodynamic models. Modern rotary wing aeroelastic analyses model unsteady aerodynamics, dynamic stall, and distortion of the wake geometry due to self-induced velocities. Ganguli and Chopra [50, 51] examined the effects of using low fidelity aerodynamics in vibration reduction studies. In Refs. 50 and 51, composite rotor blades were optimized at $\mu = 0.30$ using a quasi-steady aerodynamic model with a linear inflow assumption. Using the opti-

mum design, a higher fidelity aeroelastic analysis, which included a free-wake model [136] and an unsteady aerodynamic model with dynamic stall effects [92], was conducted. Although the low fidelity analysis underpredicted the vibration levels, the resulting optimum design produced similar levels of vibration reduction compared to the analysis based on free-wake and unsteady aerodynamic models for $0.15 \leq \mu \leq 0.40$. However, the blade was not optimized using the high fidelity aeroelastic analysis. Thus, there was no comparison between the original optimum design and that which would have been obtained with the more accurate aerodynamic model.

While the studies described above were purely computational, optimized blade designs have been experimentally validated in Refs. 26, 164, and 169. Although the analysis codes employed in the studies did not always accurately predict the experimentally measured loads, the optimum designs corresponded to reduced vibrations in wind tunnels. These studies indicate that numerical optimization based on analysis codes is an effective approach to rotor blade design.

It is important to note that none of the previous studies compared optimum designs corresponding to different advance ratios. While the results from Refs. 45, 50, and 51 demonstrate that optimizing at one advance ratio can lead to vibration reduction at other advance ratios, selection of the *best* design for vibration reduction over the entire flight envelope was not addressed.

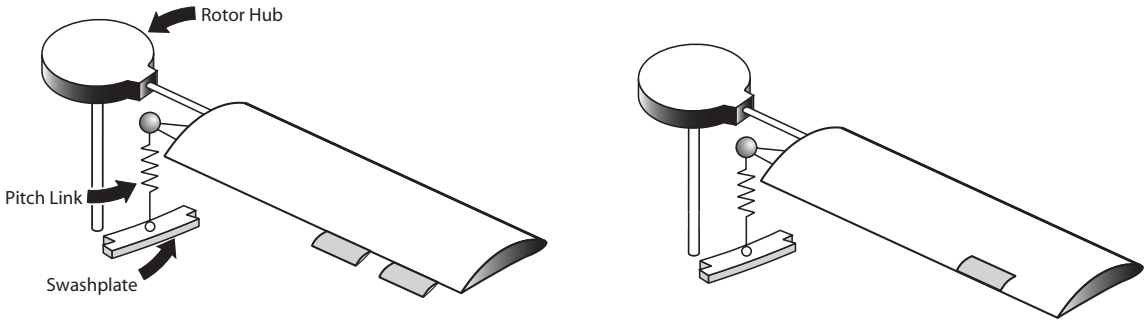

(a) Dual servo flap configuration **(b) Single plain flap configuration**

Figure 1.2: Helicopter rotor blades with partial span trailing edge flaps

1.1.2 Active Control of Vibration

Similar to the passive approach based on structural optimization, active vibration reduction using onboard devices has been extensively investigated. A comparison of the principal active control approaches is provided in Ref. 44, and more recent reviews of the applications of such techniques can be found in Refs. 20, 95 and 116. Among the various techniques, partial span actively controlled flaps (ACF's), which are depicted in Fig. 1.2, have emerged as an attractive means of active control due their low power requirement compared to blade root actuation approaches [44]. Therefore, active control is implemented with ACF's in this study. This approach is usually denoted as individual blade control (IBC) because control inputs are introduced in the rotating system and different control inputs can be provided to each blade.

Deflecting the ACF effects vibratory loads due to induced time dependent elastic twist, which results in a redistribution of the unsteady aerodynamic loading. Millott and Friedmann [103] conducted the first computational study which demonstrated that active control with ACF's was an effective means of vibration reduction. A modified version of quasi-

steady Theodorsen's theory was used to model the aerodynamic loads for the blade/flap combination, and the control algorithm was based on higher harmonic control (HHC) [76]. Using a servo-flap configuration, active control resulted in $80 - 90\%$ reduction of the vibratory loads at $\mu = 0.30$. Although the level of vibration reduction was comparable to IBC implemented through blade-root actuation, the ACF system required almost an order of magnitude less power.

Myrtle and Friedmann [108, 109] extended the work in Ref. 103 to include a two-dimensional, compressible, unsteady aerodynamic model based on a rational function approximation (RFA) approach. The results indicated that the ACF remained an effective means of vibration control when including the effects of compressibility and unsteadiness, even though larger flap deflections are required. A free-wake model was subsequently included in the analysis in order to accurately model BVI induced vibration at low advance ratios [28]. Over 80% vibration reduction under BVI conditions was reported in Ref. 28.

Since dynamic stall is the dominant source of vibration at higher speeds, active control of vibration due to dynamic stall was investigated by Depailler and Friedmann [30–32]. For the separated flow regime, unsteady aerodynamic loads were calculated using the ONERA dynamic stall model [121]. The aerodynamic states associated with the RFA attached flow and the ONERA separated flow models were combined to produce the time-domain, state space aerodynamic model. Furthermore, a simple linear drag model which accounts for the increase in drag due to flap deflection was implemented [31].

In addition to computational studies, the effectiveness of active vibration reduction using ACF's has been experimentally validated [27, 33, 47, 87, 102, 150–152]. Although an

active vibration control system based on ACF's has yet to be implemented on a production rotor, the numerous computational and experimental studies have demonstrated the effectiveness of the approach for vibration reduction under BVI and dynamic stall conditions.

Based on the computational and experimental results demonstrating that structural optimization and active control with ACF's are effective means of vibration reduction, it is clear that optimum rotor design should take advantage of the benefits associated with active and passive approaches. Zhang, Smith, and Wang [177, 178] were the first to demonstrate the value of an active/passive approach to vibration reduction based on structural optimization and ACF's. In Refs. 177 and 178, the optimization algorithm was based on the method of feasible directions [128], which is a local search method. Aerodynamic loads on the blade were calculated with quasi-steady blade element theory using the UMARC comprehensive rotorcraft analysis code [6]. The effects of dynamic stall were not modeled. Calculation of the unsteady loading due to arbitrary motion of the trailing edge flap was based on the indicial concept [63], and the non-uniform inflow distribution was determined by a free-wake analysis [5]. The blade was modeled as a beam undergoing small strains and moderate deflections using the finite element method. The results showed that the active/passive method can produce much lower vibration levels compared to utilization of only one approach at $\mu = 0.15$ and $\mu = 0.30$. Furthermore, it was demonstrated that optimizing the blade/flap combination simultaneously can lead to superior levels of vibration reduction compared to the sequential approach of adding ACF's to structurally optimized designs. The effects on noise levels and the required rotor power were not considered. Thus, the simultaneous blade/flap optimization approach employed in Refs. 177 and 178 was not formulated for

multi-objective design applications.

1.2 Review of BVI Noise Reduction Approaches

The physical mechanisms of noise generated by the main rotor are well documented [135], and significant advances in acoustic modeling have been made over the past 40 years [11]. At low speeds, and especially during descent, high frequency pressure fluctuations induced by BVI result in a distinct impulsive sound [172]. Blade-vortex interaction noise is particularly troublesome because: (1) it is very intense during descending flight, which is characteristic of a helicopter approaching for landing over a populated area, (2) BVI noise tends to propagate out of the plane of rotation, which makes it more audible to observers on the ground, and (3) the impulsive nature produces sound harmonics which are particularly annoying to the human ear.

1.2.1 Passive Reduction of BVI Noise

Passive methods of noise reduction have focused on modification of the geometric characteristics of the blade, such as planform shape and tip sweep/anhedral. Yu [172] documented various computational and wind tunnel studies in which taper and sweep of the blade tip were shown to produce $3-6$ dB of noise reduction. Although modification of the blade's planform geometry has been established as an effective means for BVI noise reduction, structural optimization of the blade's mass and stiffness distribution for noise reduction was never examined in previous studies.

1.2.2 Active Control of BVI Noise

Trailing edge flap deflections can modify the aerodynamic loading on the blade, which in turn effects parameters known to have an affect on BVI noise, such as tip vortex strength and blade-vortex miss distance. As in the case of vibration reduction, the ACF's have also been shown to be effective for BVI noise reduction in a variety of computational and experimental studies [172, 173]. Using primarily open-loop control inputs, typical levels of BVI noise reduction of $4 - 7$ dB have been reported in wind tunnel tests [27, 157]. In addition to computational studies based on approximate aerodynamic models [4, 16, 119], a study of the effects of ACF's on BVI noise using a high fidelity CFD aerodynamic model was presented in Ref. 3. Based on various open-loop control inputs, up to 5.6 dB noise reduction was reported, and it was shown that the lowest peak sound pressure levels corresponded to the largest blade-vortex miss distances. It is worth noting that the significance of the blade-vortex miss distance has been noted in studies based on approximate aerodynamic models, such as Refs. 116 and 120.

1.3 Review of Performance Enhancement Studies

For the purposes of this study, helicopter performance is characterized by the required power to drive the main rotor, which is a function of drag. Modification of the blade design can lead to power reduction due to the effects on induced drag and profile drag.

1.3.1 Passive Approaches to Performance Enhancement

Walsh [158] studied structural optimization of the blade's spanwise variation of chord and pretwist for power reduction in hover, with a constraint on the drag in forward flight. In Ref. 158, CAMRAD [74] was used to calculate the required rotor power in forward flight. The aerodynamic model for both hover and forward flight was based on experimental two-dimensional airfoil data. The forward flight analysis was conducted with both a uniform inflow model and a prescribed wake, and the CONMIN local optimization code was used to search the design space. When optimizing at hover, $5-7\%$ power reduction was reported. Although the blade was optimized for hover, the power required by the optimum designs at $\mu = 0.30$ was $8-11\%$ lower than the reference blade. It was concluded that wake models should be included in the analysis since optimization with and without a wake model resulted in different blade designs.

He and Peters [64] considered structural optimization of the spanwise chord and pretwist distribution for performance enhancement at hover, with a constraint on the blade stresses. Power required by the main rotor was calculated from combined blade element and momentum theory with Prandtl's 2-D tip loss factor [75]. The optimum design corresponded to 4% power reduction. Furthermore, the results indicated that the stress constraint was active for this problem. It should be noted that interactions between the airloads and structure were not modeled in this study.

1.3.2 Active Control for Performance Enhancement

As in the cases of vibration and noise reduction, active control of the aerodynamic environment has shown potential for performance enhancement. Performance enhancement of $4 - 7\%$ has been reported in previous studies which utilized blade root actuation approaches, i.e. higher harmonic control (HHC) and conventional individual blade control (IBC) [18, 19, 71, 138, 153]. Use of the ACF for performance enhancement was investigated in Ref. 150, but the results were inconclusive. A preliminary computational study of performance enhancement under BVI conditions was conducted by Patt, Liu, and Friedmann [118]. At $\mu = 0.15$, it was found that power reduction could be achieved with trailing edge flaps for a modified model of an MBB BO-105 rotor in which the fundamental torsion frequency was under 2.5/rev.

1.4 Literature Review of Multi-Objective Studies

Since structural design of the blade and active control of the aerodynamic environment affect vibration, noise, and performance characteristics, active and/or passive approaches must account for the effects of improving one objective on the other. Furthermore, in order to design a blade which corresponds to the best trade-offs between the various objectives, multi-objective function optimization approaches are required. However, while the rotor blade design problem is inherently multi-objective in nature, there have only been a limited number of studies that treat it as such.

1.4.1 Simultaneous BVI Noise and Vibration Reduction

Patt, Liu, and Friedmann [95, 116, 119, 120] established that ACF's could be used to simultaneously reduce noise and vibration under BVI conditions. In Ref. 119, the effect of active vibration control on noise was investigated using a computational aeroelastic/aeroacoustic model which was validated against experimental data from Ref. 147. Results were generated for a rotor resembling a full-scale MBB BO-105 rotor operating at $\mu = 0.15$ and a 6° descent angle. The controller was based on the HHC algorithm, with enhancements for stability and robustness [117]. The results indicated that by enforcing limits on the maximum flap deflections, or *saturation limits*, the noise increase associated with vibration control was relatively small compared to the penalties associated with conventional HHC and IBC observed in wind tunnel tests.

In a follow up study to Ref. 119, the effects of noise control on vibration, and the effectiveness of control for simultaneous noise and vibration reduction was investigated in Ref. 120. It was observed that vibration levels can increase when controlling for noise with saturation limits, although the vibration penalty was not considered to be significant. By employing a control algorithm formulated for simultaneous improvement, up to 5 dB noise reduction on the advancing side of the rotor plane and about 40% vibration reduction was achieved.

1.4.2 Simultaneous Vibration and Power Reduction

In Ref. 159, the study in Ref. 158 was extended to consider simultaneous reduction of rotor power in hover and forward flight, as well as the vertical hub shear in level forward

flight. The objective function consisted of a weighted sum of these quantities in which the weights were selected in an ad hoc fashion, and the cross-sectional stiffnesses were included in addition to the design variables used in Ref. 158. For one set of weights selected by the authors, the rotor power was reduced by 6.5% in hover, and $4.1 - 6.7\%$ in forward flight. In addition, the vertical hub shear was reduced by 14%. Although the selected weights resulted in a design corresponding to simultaneous vibration reduction and performance enhancement, no attempt was made to find the best trade-off, or Pareto optimal, designs. In Ref. 160, cross-sectional dimensions were added as design variables in a "lower-level" optimization problem in which the goal was to recover the optimum set of cross-sectional stiffnesses. The lower-level problem was subject to a stress constraint.

The potential for simultaneous vibration and power reduction with ACF's in a servo-flap configuration was investigated in Ref. 96. The analysis included the ONERA dynamic stall model [121] and a linear increase in drag with respect to flap deflection [31]. Compared to a baseline rotor resembling an MBB BO-105, performance was enhanced by 1.73% at $\mu = 0.35$ using a single flap. However, the vibratory loads were increased by over 100% when controlling for power reduction. When controlling for simultaneous reduction at various thrust coefficients, $0.40 - 1.82\%$ power reduction and $47 - 68\%$ vibration reduction was achieved. The results from this computational study indicate that not only can active control with ACF's reduce vibration without incurring a penalty in power consumption, but simultaneous vibration reduction and performance enhancement can be achieved.

1.4.3 Simultaneous Noise and Power Reduction

Zhao and Xu [179] experimentally investigated the performance and noise characteristics of an advanced geometry blade with a curved and swept tip known as the CLOR (China Laboratory of Rotorcraft) tip. A computational analysis based on Navier-Stokes, compressible potential flow, and free-wake models was used to design the CLOR tip. Experimental tests in hover demonstrated that the CLOR blade required less torque to maintain a constant rotational speed of 1000 RPM compared to a rectangular planform blade. Furthermore, the CLOR blade corresponded to $1.9 - 2.7$ dB less noise at two observer locations below the rotor. It is worth noting that the CLOR blade was only compared to blades with "conventional" tip shapes. So it is not clear how the CLOR blade compares with rotors resembling production models, or with other advanced geometry low noise designs.

1.5 Review of Surrogate Based Optimization (SBO) Literature

The aeroelastic response simulations needed for vibratory load, acoustic, and power calculations are computationally expensive due to the complex rotary-wing aerodynamic environment, which means that numerous evaluations of the objective functions are costly. Therefore, direct combination of the objective functions generated by an aeroelastic response simulation with traditional optimization algorithms is not computationally tractable. Moreover, traditional optimization search algorithms can converge to local optima, which are known to occur for this class of problems.

To overcome these obstacles, approximation concepts have been used. A widely used

approach in rotor blade optimization studies for approximating the objective function and constraints is to use Taylor series expansions about local design points [134]. The derivatives needed for the Taylor series are calculated using finite difference formulas, or analytical sensitivity derivatives. These approximations of the objective function and constraints are used to replace the actual problem with an approximate one that is used in conjunction with an optimizer to obtain an optimal design. Representative examples of the application of this method to the rotor blade optimization problem are provided in Sections 1.1 and 1.3. The disadvantages of this method are that it utilizes a local approximation in the vicinity of a design point and a local search procedure. Even when augmenting such methods with move limits or a trust region strategy [2, 168], convergence is only guaranteed to a local optima.

An alternative to local search methods is to use computationally efficient global approximation, or surrogate, concepts; i.e. methods which try to capture the behavior of a function over the entire design space. While local Taylor series approximations can also be classified as surrogates, for the purposes of this study surrogates will refer to global approximations. The advantages of surrogate-based optimization (SBO) with global approximations are threefold: fewer "true" function evaluations (thus fewer expensive aeroelastic simulations), the formulation is conducive to parallel computing, and the approach facilitates a more global search of the design space.

Since techniques for constructing the surrogates have been thoroughly reviewed in several recent papers [17,123,140,142,161], a review of the numerous approximation methods is not presented in this thesis. Details pertaining to the various approximation methods em-

ployed in this study are presented in Section 7.3. A review of the various frameworks for using surrogates to locate optimum designs is presented in this section so that the methods employed in this study can be placed in context relative to the modern approaches developed by optimization researchers, and those which have been used for rotor blade design applications. Single objective function approaches are reviewed in Sections 1.5.1 – 1.5.3, and multi-objective function optimization frameworks are discussed in Section 1.5.4. The studies representing the current state of SBO techniques which have been applied to rotor blade design are described in Section 1.5.5.

1.5.1 One-shot Approaches

One-shot approaches refer to methods in which the surrogate objective function is optimized directly, and the computationally expensive objective function is evaluated at the predicted optimum to obtain the "actual" characteristics of the design. The predicted design is accepted as the actual optimum and the surrogate is not updated with information from the expensive function evaluation regardless of differences between the predicted and actual responses. One-shot approaches enable the use of global optimization algorithms which require numerous evaluations of the objective function, such as genetic algorithms or simulated annealing, since the prediction time associated with surrogates is negligible compared to the cost of evaluating the expensive analysis code.

Simpson et al. [141] examined the performance of 2nd order polynomial response surfaces [107] and kriging surrogates [131] for optimum nozzle design of an aerospike rocket engine. The nozzle was characterized by 3 design variables and the surrogates were con-

structed from 25 fitting points generated by an orthogonal array [111]. For both the polynomial and kriging surrogates, the predicted responses at the optimum designs were less than 5% different from the actual values. These results demonstrated that the surrogates were accurate representations of the objective functions at the optimum designs. The authors concluded that both approximation methods were equally suited for design optimization.

In another illustrative example of one-shot optimization, Palmer and Realff [114, 115] considered minimization of an ammonia synthesis plant's operating costs. The operating cost consisted of the summation of 8 underlying responses and was a function of 6 design variables. Latin hypercube sampling [100] was used to generate 16 fitting points and two methods were considered for creating kriging and 2nd order polynomial approximations of the objective function: (1) the overall response was directly approximated, and (2) the 8 underlying responses were approximated, which were then summed to form the surrogate objective function. The kriging models led to superior designs compared to the polynomial response surfaces when fitting the underlying responses. However, the opposite trend was observed when directly approximating the objective function. Furthermore, in contrast to the study described in Ref. 141, the surrogates were not accurate at their predicted optima.

Zerpa et al. [176] applied SBO to the design of an alkaline-surfactant-polymer (ASP) flooding process for maximum oil production. In addition to 2nd order polynomials and kriging, a radial basis function (RBF) surrogate [110] was considered. Furthermore, combining the individual surrogates using a weighted sum approach was an important contribution of Ref. 176. The weights associated with each surrogate were based on a pointwise estimate of the prediction variance associated with each model; i.e. surrogates with lower

variance were assigned more weight. The ASP was characterized by 4 design variables and the surrogates were constructed from 66 and 88 point Latin hypercubes. Optimum designs associated with the 3 individual surrogates and the weighted average model were located by the DIRECT [80] global optimization algorithm. The kriging surrogate led to the best design when using the 66 point data set. However, rather than assume that kriging will result in the best design when using the 88 fitting points, all of the surrogates were optimized for the larger data set. The results showed that the polynomial response surface based on 88 fitting points led to the best design instead of kriging. For this problem, assuming that kriging is the best approximation method based on the results with 66 fitting points would have led to an inferior design when considering 88 fitting points. However, applying a multiple surrogate approach protected against this. Furthermore, the weighted average models led to designs which were almost as good as the best designs obtained with the individual approximation methods. In Ref. 60, the weighted average surrogate approach was extended to include a global error metric for determining the weights.

1.5.2 Updating Approaches

One-shot optimization of a surrogate objective function may lead to poor designs if the approximate objective function is not accurate everywhere in the designs space. To protect against this, an updating approach proceeds as follows:

1. Potential optima are obtained by optimizing the surrogate objective function.

2. The high fidelity simulation is evaluated at the predicted optima in order to obtain the actual value of the objective function.

3. The additional sample data is added to the original fitting data and the surrogate is recalibrated.

4. The process is repeated until a stopping condition is reached.

In an updating approach, the likelihood of being led to a poor design is decreased as the number of iterations is increased. Note that the one-shot approach does not involve steps 3 and 4. Some recent implementations of updating approaches are described next.

In the approach developed by Wang, Shan, and Wang [162], a global RBF is constructed from all available fitting points in the current iteration. Next, a mode-pursuing sampling (MPS) algorithm [46] identifies additional fitting points in the vicinity of the RBF's predicted optimum, or mode. A local 2nd order polynomial response surface is then constructed in the vicinity of the mode and used to determine whether the global optimum is within the sub-region. The MPS method successfully located the global optimum corresponding to various analytical test functions and design problems ranging from $2 - 16$ design variables. However, the performance of the algorithm was not compared to other SBO approaches.

Won and Ray [167] proposed a genetic algorithm based framework for SBO. The algorithm is initialized with randomly selected design points, which are used to construct RBF or kriging surrogates. The elite designs from the data set are selected for mating, and the fitness measure, i.e. the objective function, is evaluated using the surrogates at each child design. The child designs which the surrogate predicts to be elite are selected for evaluation by the expensive analysis code, and a new set of "actual" elites is generated. If the stopping condition is not reached, the surrogates are recalibrated with the additional fitting data, a

new generation of children are obtained, and the process is repeated. The framework was tested on problems with $4-10$ design variables and the results demonstrated that superior designs were obtained compared to a non-surrogate based optimization approach.

Regis and Shoemaker [125] described various improvements over existing updating approaches based on RBF's. The methods were designed to improve the convergence to the global optimum when multiple local optima exist. Sixteen computationally inexpensive test functions with $2-10$ design variables were used to demonstrate the effectiveness of the new strategies. The results indicated that the improved RBF frameworks outperformed existing methods for some of the test problems, while maintaining performance for the others. The proposed optimization algorithms were not tested on a computationally expensive design problem.

In some design applications, various levels of fidelity are available in the analysis codes. For instance, low fidelity models can be used for the initial conceptual design, and models which incorporate the full physics are used for the final analyses. Gano et al. [52, 53] developed a surrogate framework in which the bulk of the optimizer's objective function calls are to the relatively inexpensive low fidelity model. In order to guarantee convergence to the optimum design corresponding to the computationally expensive high fidelity model, a correction factor is used to convert the low fidelity analysis outputs to the values predicted by the high fidelity analysis. The correction factor is evaluated at number of design points throughout the designs space, and based on the fitting data, a kriging approximation of the factor is generated. Using the approach proposed in Refs. 52 and 53, convergence can only be guaranteed to a local optima since the variable fidelity approach is executed within a

trust-region framework.

1.5.3 Updating Approaches Based on Explicit Measures of Uncertainty

Updating the surrogate represents the conventional method of accounting for uncertainty in the surrogate's predictions since the optimum design is iterated upon rather than accepting the first potential optimum returned by the one-shot approach as the "true" optimum. However, if the optimum lies in a region of the design space in which the surrogate is inaccurate, then a significant number of iterations may be required to locate it since conventional updating approaches only sample designs which the surrogate predicts to be optimal, regardless of the error in the predictions.

As a more efficient alternative to conventional updating approaches, Jones, Schonlau, and Welch [82] introduced the Efficient Global Optimization (EGO) algorithm, which includes an explicit measure of the uncertainty in the surrogate's predictions as part of the criteria for selecting additional sample points. The uncertainty measure and a term representing probability of improvement over the current best design are combined to form the *expected improvement function* (EIF). The design space is sampled at points corresponding to the highest expected improvement. Therefore, the EGO algorithm facilitates a balanced search of the design space by sampling in regions where the surrogate predicts improved designs to be located *and* in regions where there is much uncertainty in the surrogate's predictions. By accounting for prediction uncertainty, EGO does not require numerous iterations to locate optima which the surrogate cannot accurately predict. It should be noted that EGO was originally formulated for deterministic computer models, which is the appli-

cation considered in this research; however, the algorithm has been adapted for computer models with random errors [70].

Several improvements to the original EGO algorithm were proposed in Refs. 132 and 133, including approaches for handling nonlinear constraints and the use of various sample criteria. A generalized expected improvement function was suggested for controlling the balance between searching in regions of high uncertainty and in regions corresponding to predicted improvement. The user can dictate the emphasis of the search with EGO by selecting a single integer parameter in the generalized expected improvement function. However, there is no clear method of selecting the parameter. In Refs. 132 and 133, different sampling criteria were tested on various test problems and multiple metrics were used to evaluate their effectiveness. A single sampling criteria did not distinguish itself as the best in terms of all metrics. It was concluded in Ref. 132 that nonlinear constraints could be treated effectively by enforcing the constraints when maximizing the sampling criteria.

Sóbester, Leary, and Keane [143] proposed a parallel updating version of the EGO algorithm in which multiple designs are selected for sampling during each iteration, as opposed to only selecting the design with the highest expected improvement. The authors proposed that a number of local optima of the expected improvement function should be identified during each iteration of EGO. The EGO algorithm is then updated with fitting data corresponding to a number of local optima equal to the number of available processors. In Ref. 143, the parallel updating approach and non-surrogate based optimization methods – i.e. no approximations of the objective function combined with genetic algorithms or gra-

dient based search methods – were used to find the optima of closed form five-dimensional test functions. The test functions were not computationally expensive to evaluate, and were only used to test the SBO method. Not only did the parallel updating algorithm converge to the optima in less time, but the optima were superior to those obtained from conventional optimization algorithms which did not utilize surrogate objective functions.

In addition to the parallel updating scheme, Sóbester, Leary, and Keane [144] introduced the weighted expected improvement function (WEIF), which utilizes a user defined parameter to control the balance between searching in regions of high uncertainty and in regions corresponding to predicted improvement. As opposed to the generalized expected improvement function [133], the relative impact of different values of the weight parameter on the expected improvement function is easy for the user to understand. The results in Ref. 144 demonstrated that the weight settings which led to the optimum in the fewest objective function evaluations differed for various test problems. For most of the test problems considered in Ref. 144, the WEIF outperformed other optimization algorithms, including EGO based on the conventional EIF.

An algorithm which sequentially improves the global accuracy of a surrogate was proposed in Ref. 36. A measure of uncertainty, or "irregularity," is used to identify regions in the design space where additional sampling is likely to produce the greatest gains in model accuracy. The algorithm places more points in regions where the actual function is likely to exhibit irregular, i.e. multi-modal, behavior since less points are needed to capture the behavior in regions where the function is not changing rapidly. The algorithm is only designed to increase the global accuracy of the surrogate, and thus does not account for any

measures of improvement over the current best design.

It is worth noting that an important limitation of the EIF is that the uncertainty measure is based on a single approximation method, and EGO may perform poorly if the uncertainty measure is a poor representation of the error in the surrogate's predictions [81]. As an alternative, it is possible to generate a measure of prediction uncertainty which is based on multiple surrogates, and thus less susceptible to potentially deceptive error measures derived from a single approximation method. The multiple surrogate approach employed in Ref. 176 was extended by Goel et al. [60] to include a measure of prediction uncertainty. The variance associated with the predictions from the multiple surrogates was proposed as an uncertainty measure - i.e. the uncertainty is directly proportional to the amount of disagreement in the surrogates' predictions. However, combining the multiple surrogate based uncertainty measure with a predicted improvement metric into an "expected improvement-like" function has not been studied and is beyond the scope of this thesis.

1.5.4 Multi-Objective Frameworks

The SBO approaches described in Sections 1.5.1 – 1.5.3 have been formulated for single-objective function optimization. However, design of aerospace vehicles is driven by multiple objectives, and effective approaches must locate the designs corresponding to the best trade-offs between the objectives, or the *Pareto* optimal designs. Therefore, the future acceptance of SBO as a viable means of aerospace design optimization depends on the applicability of such approaches to multi-objective function optimization problems.

The most commonly used approach to multi-objective function optimization is to com-

bine the objectives using a weighted sum approach. Since the multi-objective function problem is converted into a single objective function problem, the variety of methods which have been formulated for single objective optimization can be employed. The weighted sum approach was applied to the design of a high speed civil transport vehicle by Koch et al. [86] In Ref. 86, 2nd order polynomial response surfaces were used to replace the objective functions, and various trade-off designs were identified as a result of different weighting schemes. In addition to the surrogate based multi-objective function optimization framework, another important contribution of Ref. 86 was to examine the effects of large numbers of design variables. To overcome issues associated with size, Koch et al. presented approaches for eliminating relatively unimportant design variables

Knowles [84] proposed a multi-objective function optimization approach based on EGO and the weighted sum approach. At each iteration of ParEGO (Pareto/EGO), the weights corresponding to each objective function were randomly selected to produce a single objective function. The ParEGO algorithm then proceeded in a manner similar to the conventional EGO algorithm. Therefore, the goal of ParEGO is to gradually locate all Pareto optima, i.e. the entire Pareto front, by applying EGO to different weighted sum objective functions for each iteration.

The major limitation of a weighted sum approach is that an evenly distributed set of weights may not lead to a uniform distribution of designs on the Pareto front [24, 84]. To overcome this limitation, surrogates have been used to facilitate direct identification of the entire Pareto front. Since surrogate prediction times are usually negligible, approximate objective functions can be evaluated over a set of designs which are densely spaced

throughout the entire design space, and the Pareto optima can be filtered from the predictions. In one such study, Wilson et al. [166] considered 2nd order polynomial and kriging surrogates for Pareto front exploration. The approximate Pareto fronts compared well with the actual Pareto fronts for the relatively simple set of test problems considered in Ref. 166. However, the results also demonstrated that the approximate Pareto front may be a poor representation of the actual Pareto front if the surrogates are not sufficiently accurate.

Goel et al. [61] demonstrated the benefits of generating surrogate Pareto fronts by approximating a set of Pareto points in the objective function space. The approximated Pareto front can be used to aid the designer in visualization of the competing objectives and to asses trade-offs. In Ref. 61, polynomial response surfaces were used to approximate the Pareto front and a method was proposed to determine the boundaries of the region within which the surrogate Pareto front is valid. The approach was applied to a rocket injector design problem, and led to an increased understanding of the interactions between the objective functions.

Keane [83] extended the EGO algorithm for multi-objective optimization by employing a modified version of the expected improvement function in which "improvement" is achieved if a design is predicted to augment or dominate the designs in the current Pareto set. The statistical metrics derived by Keane provided more diversely populated Pareto fronts than a genetic algorithm based updating scheme known as NSGA-II [29] for the problems considered. While the approach in Ref. 83 represents a statistically consistent manner of extending the single objective EIF for application to multiple objectives, the formulation was not compared to other methods of using the EIF for Pareto front explo-

ration. Therefore, it is not clear if Keane's formulation would outperform other EIF based methods, such as ParEGO [84] or the approach described in Section 7.4 of this thesis.

Messac and Mullur [101] proposed a Pareto front exploration scheme based on a sequence of RBF surrogates. The framework is initialized by identifying the optimum corresponding to one of the objective functions, which is referred to as an anchor point. A locally accurate RBF surrogate is constructed within the vicinity of the anchor point and used to find the next design on the Pareto front. Another locally accurate RBF is constructed about the new Pareto point, and the process repeats. Therefore, the Pareto front is gradually identified by conducting a sequence of local searches in the vicinity of known Pareto points. However, if the next Pareto point is not located in the vicinity of a current Pareto design, then numerous local searches in sub-optimal regions may be required before the correct region of the design space is located. Therefore, the sequential local search approach described in Ref. 101 may not be as effective as global search algorithms, such as EIF-based methods, for locating designs on the Pareto front which are much different than a current set of Pareto points.

1.5.5 Helicopter Applications

Although global optimization of helicopter rotor blades is an application which requires SBO techniques, there has only been a limited amount of study on the benefits of such approaches for optimum rotor blade design. Furthermore, the SBO methods which have been considered in the helicopter literature typically lag behind the approaches described in Sections 1.5.1 – 1.5.4, which have been developed by the optimization and statistics

communities. The studies which characterize the state of SBO of helicopter rotor blades are described below.

Ganguli [48] used a 2nd order polynomial global approximation of the vibration objective function and obtained 30% vibration reduction using a one-shot approach at $\mu = 0.30$. The 2nd order polynomial was found to be accurate only in the vicinity of the baseline design. Murugan and Ganguli [105] extended the work described in Ref. 48 to include an unsteady aerodynamic model, and to enhance lag mode damping. The optimum vibration design corresponded to 18% vibration reduction, while optimization for stability enhancement led to a 125% increase in the lag mode damping and a 59% increase in vibration levels. However, designs corresponding to simultaneous vibration reduction and stability enhancement were obtained by constraining the level of vibration increase. For future work, the authors noted the importance of including a free-wake model in the analysis and treating the problem in a multi-objective manner.

Lee and Hajela [90] employed a decomposition approach to optimization for vibration reduction. In Ref. 90, the blade was characterized by 42 design variables. In order to conduct a global search of the design space with genetic algorithms, the overall problem was decomposed into more tractable sub-problems which were functions of design variable subsets. The genetic algorithm is able to operate on each sub-problem in a reasonable amount of time since each sub-problem is a function of a smaller set of design variables. Neural network surrogates were used to maintain sub-problem coupling since the constraints associated with each sub-problem are not independent of the design variables assigned to the other sub-problems. The neural network predictions of the objective

function and constraints exhibited maximum errors of less than 10%, and thus were able to accurately maintain sub-problem connectivity. The decomposition approach outperformed an all-in-one approach in which the full 42 design variable problem was optimized with a genetic algorithm.

In Ref. 7, surrogate based methods were applied to minimization of helicopter vibration, using 31 design variables to characterize the rotor blade. The cross-sectional design variables were mass, center of gravity offset from the elastic axis, and the blade stiffnesses. The analysis code Tech01 [139] was used to generate hub shears and moments, and the stochastic process based method known as kriging interpolation was used to approximate the objective function. The results showed that kriging could be used to find reduced vibration designs in an efficient manner. However, it is important to note that the principal focus of Booker et al. was on the effectiveness of the SBO framework, and therefore accurate modeling of the aerodynamic environment of a rotor blade during flight was not considered to be important. Consequently, accurate free-wake models were sacrificed for a computationally less expensive prescribed wake model. Furthermore, no constraints were placed on the aeroelastic stability of the blade. Thus, the model of the helicopter vibratory loads was not sufficiently reliable to produce a realistic blade design.

A multi-objective optimization approach to blade design for reduced noise and power consumption was studied in Ref. 21. Six design variables were used to characterize the tip sweep and anhedral as well as the spanwise chord and pretwist distributions. The four objective functions consisted of a noise and power objective for hover and $\mu = 0.28$. Constraints on the blade design were not included in the analysis. The objective functions were

replaced with 2nd order polynomial response surfaces which were evaluated over 4 million random designs. The Pareto optima were filtered from the 4 million surrogate predictions, and one Pareto design was selected for further analysis. The selected design corresponded to 5.6% power reduction and a 0.2 dB decrease in the noise objective function at hover; 3.9% and 1.1 dB power and noise reduction respectively was observed for the forward flight objective functions. Although optimum designs corresponded to simultaneous noise and power reduction, the vibratory loads were significantly higher than the baseline.

1.5.6 Global Sensitivity Analysis

In addition to replacing computationally expensive objective functions in optimization, the surrogates can also be used to replace expensive *global sensitivity analysis* (GSA) [145] function evaluations. Global sensitivity analysis is used to rank the design variables in terms of influence on the objective function over the entire design space, as opposed to partial derivatives which estimate the local sensitivity of a function in the vicinity of a design point. The GSA based on Ref. 145 has been used in various applications [69, 123, 154], however identification of the most important design variables using surrogates and GSA has not been considered in previous helicopter vibration studies.

1.6 Objectives of this Dissertation

Based on the literature review, it is clear that a comprehensive examination of active/passive rotor blade optimization, subject to multiple objectives, has not been investigated. Furthermore, the effectiveness of multi-objective SBO techniques for engineering

design applications characterized by a large number of design variables and computationally expensive function evaluations has received limited attention. Therefore, the overall objectives of this dissertation are to (1) develop active/passive rotor blade optimization approaches based on SBO and ACF's, and to (2) apply the approaches to previously unexamined multi-objective function optimization problems involving vibration, noise, and performance characteristics. The specific objectives of this research are to:

1. Examine the applicability of several global approximation methods to the rotor blade vibration reduction problem in forward flight by considering a flight regime subject to significant BVI effects.

2. Illustrate the advantages of utilizing a multiple surrogate approach, including a weighted average model, by applying such methods to the helicopter vibration reduction problem.

3. Perform surrogate based GSA to identify the most significant design variables for helicopter vibration reduction using structural optimization.

4. Demonstrate the superiority of EGO to optimization approaches which do not explicitly account for prediction uncertainty, when employed for vibration reduction at low advance ratios, where BVI induced vibrations dominate, as well as high advance ratios where dynamic stall induced vibrations are critical.

5. Examine optimal blade designs for vibration reduction at these two regimes of the flight envelope in order to determine whether these impose conflicting requirements on the blade design.

6. Develop multi-objective function optimization techniques based on EGO in order to identify Pareto optimal designs which can be used for selection of the "best" design for vibration reduction over the entire flight envelope.

7. Demonstrate the effectiveness of EGO for structural optimization of the rotor blade to minimize BVI induced noise and identify the designs corresponding to the best trade-offs between BVI noise and vibration characteristics.

8. Demonstrate the effectiveness of an active/passive approach based on ACF's and SBO for vibration and noise reduction, as well as simultaneous noise and vibration reduction.

9. Identify the designs corresponding to the best trade-offs between vibration and performance characteristics at high advance ratios in which dynamic stall effects are significant.

10. Examine the benefits of augmenting structurally optimized designs with ACF's and controlling for power and vibration reduction.

11. Develop a combined active/passive optimization approach in which the blade/flap combination is optimized simultaneously for the best trade-offs between vibration and power reduction.

1.7 Key Contributions Made in this Dissertation

Accomplishing the stated objective will make substantial contributions toward improving advanced blade design methodologies, and toward an increased understanding of the effectiveness of SBO techniques for engineering design applications. The following contributions are unique to this study:

1. A hover stability analysis which accounts for the aerodynamic states associated with the RFA aerodynamic model was developed.

2. The performance of various approximation techniques for modeling helicopter vibrations and leading to improved blade designs was thoroughly investigated.

3. This study represents the first application of the EGO algorithm for rotor blade design optimization, as well as the first application of a modified EGO algorithm based on the WEIF which is suitable for multi-objective function optimization.

4. Structural optimization of the blade's mass and stiffness distribution for noise reduction was considered.

5. The blade optimization problem was formulated in a multi-objective manner in order to locate the designs corresponding to the best trade-offs between (a) vibration reduction throughout the entire flight envelope, (b) noise and vibration reduction at low advance ratios, and (c) vibration reduction and performance enhancement at high advance ratios.

6. A combined approach, in which the blade/flap combination is optimized simultaneously, was developed for active/passive multi-objective optimization.

Chapter II

Model Description and Coordinate Systems

The basic assumptions, coordinate systems, and coordinate transformations which form the basis of the aeroelastic response model are similar to those presented in Refs. 95 and 174, and are included here for the purpose of completeness and convenience. Thorough validation studies of the aeroelastic analysis components can be found in Refs. 28, 30, 95, 108, 116 and 174.

2.1 Modeling Assumptions

The basic assumptions used to develop the aeroelastic analysis for the blade are as follows:

2.1.1 Structural and Kinematic Assumptions

1. The rotor blade is cantilevered at the hub, with a root offset e_1 from the axis of rotation (see Fig. 2.1).

2. The blade has a precone angle β_p (see Fig. 2.2) and a built-in pretwist distribution τ_0 about the reference axis of the blade.

3. The blade has no sweep, droop or torque offset.

4. The blade is modeled by beam type finite elements along the reference axis of the blade.

5. The blade cross section can have arbitrary shape with distinct shear center, aerodynamic center, tension center and center of mass.

6. The blade feathering axis coincides with the reference axis of the blade.

7. The effects of transverse shear deformations and out-of-plane warping are included.

8. The blade undergoes moderate deflections, which implies small strains and moderate rotations.

9. The blade has completely coupled flap, lead-lag, torsional, and axial dynamics.

10. The mass and stiffness properties of the blade, and its chord and pretwist, are allowed to vary along the span of the blade.

11. Although the blade model can account for generally anisotropic materials, only isotropic cross-sections are treated in this study.

12. The leading edge of the actively controlled flap (ACF) is attached to the trailing edge of the blade with a series of hinges located at a number of discrete points, constraining the flap to rotate only in the plane of the blade cross section.

13. The ACF cross section is assumed to be symmetric with respect to its major principal axes.

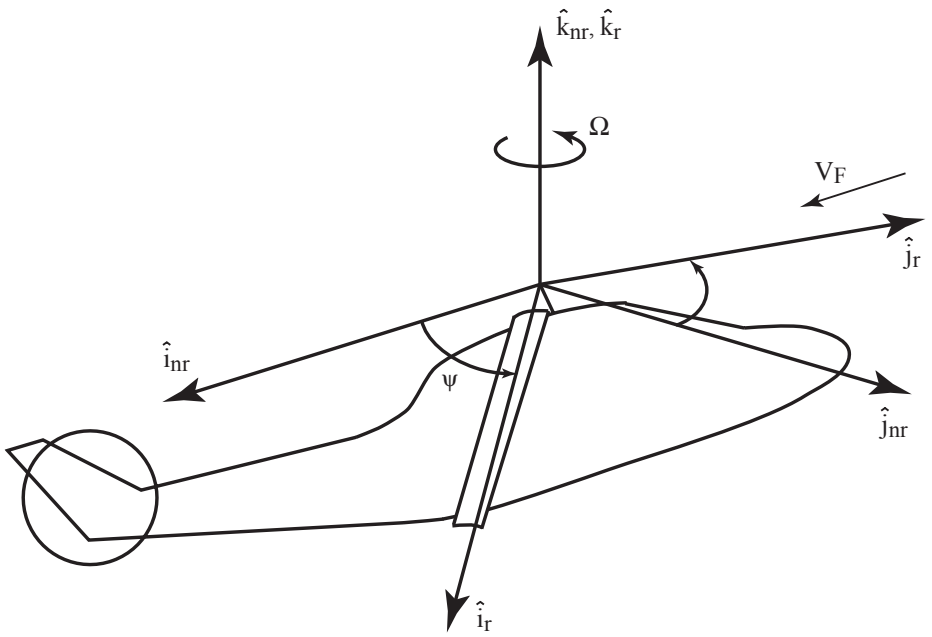

Figure 2.1: Nonrotating and rotating hub-fixed coordinate systems

14. The ACF is assumed to be inextensible.

15. The ACF is assumed to have the same pretwist distribution as the blade.

16. The structural effects of the ACF are neglected.

2.1.2 Aerodynamic Modeling Assumptions

1. The distributed aerodynamic loads in the attached flows regime are modeled using the rational function approximation (RFA) approach, which accounts for compressibility, unsteady free stream effects, and the presence of trailing-edge flaps.

2. The separated flow aerodynamic loads are calculated by the ONERA dynamic stall model, which does not include the effects of flap deflection. Therefore, separated flow loads are not modeled for blade sections with flaps.

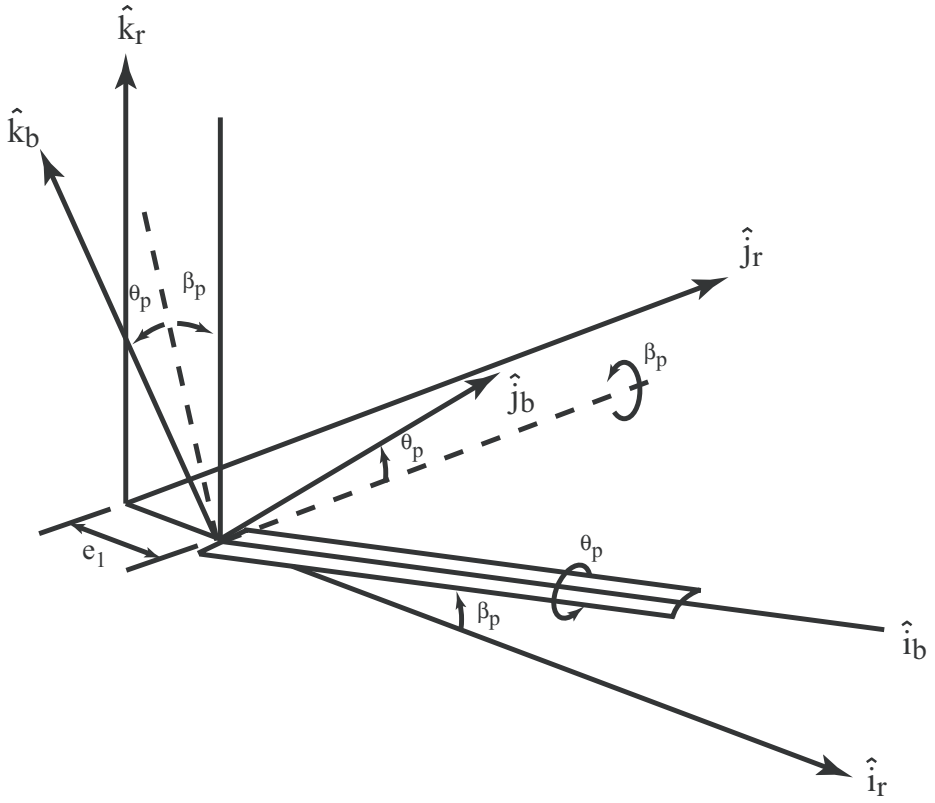

Figure 2.2: Preconed, pitched, blade-fixed coordinate system

3. The induced inflow is nonuniform and is obtained by a free wake analysis included in the aeroelastic model.

4. Reverse flow effects are included by setting the lift and moment equal to zero and by changing the sign of the drag force inside the reverse flow region (see Fig. 4.7).

5. The rotor shaft is assumed to be rigid and the speed of rotation Ω of the rotor is constant.

6. The helicopter is in trimmed, steady, level or descending flight. Either propulsive or wind tunnel trim can be implemented.

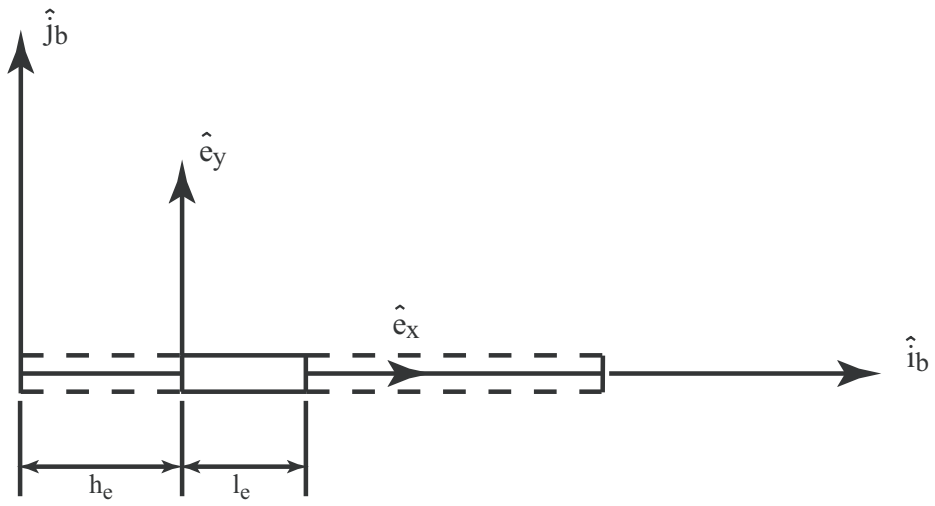

Figure 2.3: Undeformed element coordinate system

2.2 Coordinate Systems

Several coordinate systems are required to fully describe the geometry and deformation of the blade. Each coordinate system is symbolically represented by a set of orthonormal triad. The first three systems, namely, the nonrotating, hub-fixed system $(\hat{\mathbf{i}}_{nr}, \hat{\mathbf{j}}_{nr}, \hat{\mathbf{k}}_{nr})$, the rotating, hub-fixed system $(\hat{\mathbf{i}}_r, \hat{\mathbf{j}}_r, \hat{\mathbf{k}}_r)$, and the preconed, pitched, blade-fixed system $(\hat{\mathbf{i}}_b, \hat{\mathbf{j}}_b, \hat{\mathbf{k}}_b)$, respectively, are used to position and orient the blade relative to the hub through rigid-body motions, as shown in Figs. 2.1 and 2.2. The next two systems, $(\hat{e}_x, \hat{e}_y, \hat{e}_z)$ and $(\hat{e}_x, \hat{e}_\eta, \hat{e}_\zeta)$, respectively, are used to position and orient each beam finite element relative to the $(\hat{\mathbf{i}}_b, \hat{\mathbf{j}}_b, \hat{\mathbf{k}}_b)$ system in the undeformed configuration of the blade, as shown in Figs. 2.3 and 2.4. Another system, $(\hat{e}'_x, \hat{e}'_\eta, \hat{e}'_\zeta)$, is used to represent the orientation of the local blade geometry after deformation. A flap attached system $(\hat{e}_{x\,cs}, \hat{e}_{\eta\,cs}, \hat{e}_{\zeta\,cs})$ is used to position and orient the control surface. These coordinate systems are similar to those used in Ref. [103].

Nonrotating, Hub-fixed Coordinate System

The $(\hat{\mathbf{i}}_{nr}, \hat{\mathbf{j}}_{nr}, \hat{\mathbf{k}}_{nr})$ system, shown in Fig.2.1, is an inertial reference frame and has its origin at the hub center. The vector $\hat{\mathbf{i}}_{nr}$ points toward the helicopter tail; $\hat{\mathbf{j}}_{nr}$ points to starboard; and $\hat{\mathbf{k}}_{nr}$ coincides with the rotation vector of the rotor. $\hat{\mathbf{i}}_{nr}$ and $\hat{\mathbf{j}}_{nr}$ are in the plane of rotation. Hub shears and moments are defined in this coordinate system.

Rotating, Hub-fixed Coordinate System

The $(\hat{\mathbf{i}}_r, \hat{\mathbf{j}}_r, \hat{\mathbf{k}}_r)$ system, shown in Fig. 2.1, also has its origin at the hub center but rotates with a constant angular velocity $\Omega\hat{\mathbf{k}}_r$. The vector it coincides with the azimuth position of the blade, while $\hat{\mathbf{k}}_r$ is coincident with the vector $\hat{\mathbf{k}}_{nr}$; $\hat{\mathbf{i}}_r$ and $\hat{\mathbf{j}}_r$ are also in the plane of rotation of the rotor.

Preconed, Pitched, Blade-fixed Coordinate System

The $(\hat{\mathbf{i}}_b, \hat{\mathbf{j}}_b, \hat{\mathbf{k}}_b)$ system, shown in Fig. 2.2, rotates with the blade and has its origin at the blade root, offset from the hub center by $e_1\hat{\mathbf{i}}_r$. The vector $\hat{\mathbf{i}}_b$ coincides with the pitch axis, which is also the undeformed reference axis of the straight portion of the blade. The $(\hat{\mathbf{i}}_b, \hat{\mathbf{j}}_b, \hat{\mathbf{k}}_b)$ system is oriented by rotating the $(\hat{\mathbf{i}}_r, \hat{\mathbf{j}}_r, \hat{\mathbf{k}}_r)$ system about $-\hat{\mathbf{j}}_r$ axis by the precone angle β_p, and subsequently introducing a second rotation about the rotated $\hat{\mathbf{i}}_r$ axis by the geometric pitch angle θ_p. In the finite element model of the blade, the $(\hat{\mathbf{i}}_b, \hat{\mathbf{j}}_b, \hat{\mathbf{k}}_b)$ system is the global coordinate system.

Undeformed Element Coordinate System

The $(\hat{e}_x, \hat{e}_y, \hat{e}_z)$ system, shown in Fig. 2.3, has its origin at the inboard node of the finite element. The vector $\hat{e}_x$ is aligned with the beam reference axis; while the vectors $\hat{e}_y$ and $\hat{e}_z$ are defined in the cross section of the beam. For the straight portion of the blade, the $(\hat{e}_x, \hat{e}_y, \hat{e}_z)$ system has the same orientation as the $(\hat{\mathbf{i}}_b, \hat{\mathbf{j}}_b, \hat{\mathbf{k}}_b)$ system. For the swept tip element, the $(\hat{e}_x, \hat{e}_y, \hat{e}_z)$ system is oriented by rotating the $(\hat{\mathbf{i}}_b, \hat{\mathbf{j}}_b, \hat{\mathbf{k}}_b)$ system about $-\hat{\mathbf{k}}_b$ by the sweep angle Λ_s and then about $-\hat{\mathbf{j}}_b$ by the anhedral angle Λ_a. The $(\hat{e}_x, \hat{e}_y, \hat{e}_z)$ system is also the local coordinate system for the blade finite element model. The displacement components and the applied loads of the beam finite element are defined in this coordinate system.

Undeformed Curvilinear Coordinate System

In the $(\hat{e}_x, \hat{e}_\eta, \hat{e}_\zeta)$ system, the vectors $\hat{e}_\eta$ and $\hat{e}_\zeta$ are defined parallel to the modulus weighted principal axes of the cross section; and the pretwist angle $\beta(x)$ is defined as the change in the orientation of $\hat{e}_\eta, \hat{e}_\zeta$ with respect to $\hat{e}_y, \hat{e}_z$, respectively, at any location along the beam element, as shown in Fig. 2.4. The strain components, the material properties, and the cross section warping function are all derived in this coordinate system.

Deformed Curvilinear Coordinate System

The $(\hat{e}'_x, \hat{e}'_\eta, \hat{e}'_\zeta)$ system represents the orientation of the local blade geometry after deformation. The orientation of the $(\hat{e}'_x, \hat{e}'_\eta, \hat{e}'_\zeta)$ system is obtained by rotating the $(\hat{e}_x, \hat{e}_\eta, \hat{e}_\zeta)$ system through three Euler angles in the order of $\theta_z eta$,θ_η and θ_x about $\hat{e}_\zeta$, rotated $\hat{e}_\eta$ and

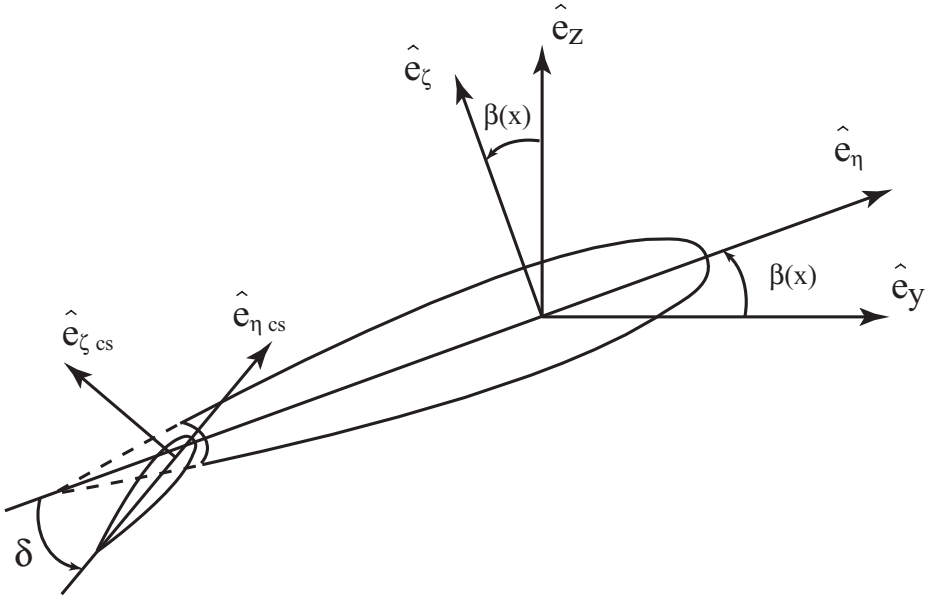

Figure 2.4: Undeformed curvilinear coordinate system

rotated $\hat{e}_x$, respectively. The vector $\hat{e}'_x$ is chosen to be tangent to the local deformed reference axis.

Preconed, Blade-fixed Coordinate System

The $(\hat{\mathbf{i}}_p, \hat{\mathbf{j}}_p, \hat{\mathbf{k}}_p)$ system is identical to the preconed, pitched, blade-fixed system $(\hat{\mathbf{i}}_b, \hat{\mathbf{j}}_b, \hat{\mathbf{k}}_b)$ when the pitch angle θ_p is equal to zero. The $(\hat{\mathbf{i}}_p, \hat{\mathbf{j}}_p, \hat{\mathbf{k}}_p)$ system is oriented by rotating the $(\hat{\mathbf{i}}_b, \hat{\mathbf{j}}_b, \hat{\mathbf{k}}_b)$ about $-\hat{\mathbf{i}}_b$ by the pitch angle θ_p, thereby canceling the pitch rotation inherent in the definition of the $(\hat{\mathbf{i}}_b, \hat{\mathbf{j}}_b, \hat{\mathbf{k}}_b)$ system. Blade response and blade root loads are expressed in this coordinate system because they can be more conveniently compared to similar results available in the literature.

Flap Attached Coordinate System

The $(\hat{e}_{x\,cs}, \hat{e}_{\eta\,cs}, \hat{e}_{\zeta\,cs})$ system has its origin at the hinge point of the control flap, located a distance X_H behind the blade reference axis. The $(\hat{e}_{x\,cs}, \hat{e}_{\eta\,cs}, \hat{e}_{\zeta\,cs})$ system rotates with control flap deflection δ such that the vector $\hat{e}_{x\,cs}$ remain parallel to $\hat{e}'_x$, and the vectors $\hat{e}_{\eta\,cs}$ and $\hat{e}_{\zeta\,cs}$ remain aligned with the principal axes of the control surface cross-section (Fig. 2.4)

2.3 Coordinate Transformations

The coordinate transformations between the various coordinate systems described above are presented in this section.

Rotating to Nonrotating Transformation

$$\left\{ \begin{array}{c} \hat{\mathbf{i}}_r \\ \hat{\mathbf{j}}_r \\ \hat{\mathbf{k}}_r \end{array} \right\} = [T_{rn}] \left\{ \begin{array}{c} \hat{\mathbf{i}}_{nr} \\ \hat{\mathbf{j}}_{nr} \\ \hat{\mathbf{k}}_{nr} \end{array} \right\} \tag{2.1}$$

the transformation matrix $[T_{rn}]$ is given by

$$[T_{rn}] = \left[\begin{array}{ccc} \cos\psi & \sin\psi & 0 \\ -\sin\psi & \cos\psi & 0 \\ 0 & 0 & 1 \end{array} \right] \tag{2.2}$$

Blade-fixed to Hub-fixed Transformation

$$\begin{Bmatrix} \hat{\mathbf{i}}_b \\ \hat{\mathbf{j}}_b \\ \hat{\mathbf{k}}_b \end{Bmatrix} = [T_{br}] \begin{Bmatrix} \hat{\mathbf{i}}_r \\ \hat{\mathbf{j}}_r \\ \hat{\mathbf{k}}_r \end{Bmatrix} \tag{2.3}$$

the transformation matrix $[T_{br}]$ is given by

$$[T_{br}] = \begin{bmatrix} 1 & 0 & 0 \\ 0 & \cos\theta_p & \sin\theta_p \\ 0 & -\sin\theta_p & \cos\theta_p \end{bmatrix} \begin{bmatrix} \cos\beta_p & 0 & \sin\beta_p \\ 0 & 1 & 0 \\ -\sin\beta_p & 0 & \cos\beta_p \end{bmatrix} \tag{2.4}$$

Element to Blade Transformation

$$\begin{Bmatrix} \hat{e}_x \\ \hat{e}_y \\ \hat{e}_z \end{Bmatrix} = [T_{eb}] \begin{Bmatrix} \hat{\mathbf{i}}_b \\ \hat{\mathbf{j}}_b \\ \hat{\mathbf{k}}_b \end{Bmatrix} \tag{2.5}$$

where

$$[T_{eb}] = \begin{bmatrix} 1 & 0 & 0 \\ 0 & 1 & 0 \\ 0 & 0 & 1 \end{bmatrix} \tag{2.6}$$

for a straight blade. The transformation for a swept tip can be found in Ref. 174

Undeformed Curvilinear to Undeformed Element Transformation

$$\begin{Bmatrix} \hat{e}_x \\ \hat{e}_\eta \\ \hat{e}_\zeta \end{Bmatrix} = [T_{ce}] \begin{Bmatrix} \hat{e}_x \\ \hat{e}_y \\ \hat{e}_z \end{Bmatrix} \tag{2.7}$$

the transformation matrix $[T_{ce}]$ is given by

$$[T_{ce}] = \begin{bmatrix} 1 & 0 & 0 \\ 0 & \cos\beta & \sin\beta \\ 0 & -\sin\beta & \cos\beta \end{bmatrix} \tag{2.8}$$

Differentiating Eq. (2.7) with respect to x gives

$$\begin{Bmatrix} \hat{e}_{x,x} \\ \hat{e}_{\eta,x} \\ \hat{e}_{\zeta,x} \end{Bmatrix} = \begin{Bmatrix} 0 \\ \tau_0 \hat{e}_\zeta \\ -\tau_0 \hat{e}_\eta \end{Bmatrix} \tag{2.9}$$

where

$$\tau_0 = \beta_{,x} \tag{2.10}$$

Deformed to Undeformed Curvilinear Transformation

$$\begin{Bmatrix} \hat{e}'_x \\ \hat{e}'_\eta \\ \hat{e}'_\zeta \end{Bmatrix} = [T_{dc}] \begin{Bmatrix} \hat{e}_x \\ \hat{e}_\eta \\ \hat{e}_\zeta \end{Bmatrix} \tag{2.11}$$

the transformation matrix $[T_{dc}]$ is given by

$$[T_{dc}] = \begin{bmatrix} 1 & 0 & 0 \\ 0 & \cos\theta_x & \sin\theta_x \\ 0 & -\sin\theta_x & \cos\theta_x \end{bmatrix} \begin{bmatrix} \cos\theta_\eta & 0 & \sin\theta_\eta \\ 0 & 1 & 0 \\ -\sin\theta_\eta & 0 & \cos\theta_\eta \end{bmatrix} \begin{bmatrix} \cos\theta_\zeta & \sin\theta_\zeta & 0 \\ -\sin\theta_\zeta & \cos\theta_\zeta & 0 \\ 0 & 1 & 0 \end{bmatrix} \tag{2.12}$$

Deformed Curvilinear to Undeformed Element Transformation

$$\begin{Bmatrix} \hat{e}'_x \\ \hat{e}'_\eta \\ \hat{e}'_\zeta \end{Bmatrix} = [T_{de}] \begin{Bmatrix} \hat{e}_x \\ \hat{e}_y \\ \hat{e}_z \end{Bmatrix} \tag{2.13}$$

the transformation matrix $[T_{de}]$ is given in terms of the displacement variables u, v, w and ϕ

$$[T_{de}] = [T_{dc}][T_{ce}] = \begin{bmatrix} 1 & v_{,x} & w_{,x} \\ -v_{,x}c\beta\phi - w_{,x}s\beta\phi & c\beta\phi & s\beta\phi \\ v_{,x}s\beta\phi - w_{,x}c\beta\phi & -s\beta\phi + \tau'_c c\beta & c\beta\phi + \tau'_c s\beta \end{bmatrix} \tag{2.14}$$

where

$$\tau'_c = (v_{,x}\sin\beta - w_{,x}\cos\beta)(v_{,x}\cos\beta + w_{,x}\sin\beta)$$

and the notations $c\beta\phi$, $s\beta\phi$, $c\beta$ and $s\beta$ used in Eq. (2.14) are defined as

$$c\beta\phi \equiv \cos(\beta+\phi), \quad c\beta \equiv \cos\beta, \quad s\beta\phi \equiv \sin(\beta+\phi), \quad s\beta \equiv \sin\beta$$

Preconed, Blade-fixed to Preconed, Pitched, Blade-fixed Transformation

$$\begin{Bmatrix} \hat{\mathbf{i}}_p \\ \hat{\mathbf{j}}_p \\ \hat{\mathbf{k}}_p \end{Bmatrix} = [T_{pb}] \begin{Bmatrix} \hat{\mathbf{i}}_b \\ \hat{\mathbf{j}}_b \\ \hat{\mathbf{k}}_b \end{Bmatrix} \tag{2.15}$$

the transformation matrix $[T_{pb}]$ is given by

$$[T_{pb}] = \begin{bmatrix} 1 & 0 & 0 \\ 0 & \cos\theta_p & -\sin\theta_p \\ 0 & \sin\theta_p & \cos\theta_p \end{bmatrix} \tag{2.16}$$

Deformed Curvilinear to Flap Attached Transformation

$$\begin{Bmatrix} \hat{e}_{x\,cs} \\ \hat{e}_{\eta\,cs} \\ \hat{e}_{\zeta\,cs} \end{Bmatrix} = [T_{fd}] \begin{Bmatrix} \hat{e}'_x \\ \hat{e}'_\eta \\ \hat{e}'_\zeta \end{Bmatrix} \tag{2.17}$$

the transformation matrix $[T_{fd}]$ is given by

$$[T_{fd}] = \begin{bmatrix} 1 & 0 & 0 \\ 0 & \cos\delta & -\sin\delta \\ 0 & \sin\delta & \cos\delta \end{bmatrix} \tag{2.18}$$

Chapter III

Structural Dynamic Model

The structural dynamic model is based on an analysis developed by Yuan and Friedmann [174, 175] which is capable of modeling composite blades with transverse shear deformations, cross-sectional warping, and swept tips. This study is limited to the behavior of straight isotropic blades with spanwise varying properties. The finite element model was modified by de Terlizzi and Friedmann [28] to include the effects of trailing edge flaps.

In the structural dynamic analysis, the rotor blade is modeled as an elastic rotating beam with constant angular velocity Ω. Precone, control pitch setting, pretwist, and root offset are included in the model. The blade is discretized by a series of straight beam finite elements along the reference axis of the blade. Nonlinear strain-displacement relations are derived assuming a moderate deflection theory (small strains and finite rotations), and the equations of motion are formulated using a finite element discretization of Hamilton's principle. The moderate deflection simplification is justified since helicopter rotor blades are designed from low stress and long-cycle fatigue considerations, while large displacements imply larger strains and thus higher stresses and increased fatigue. Therefore, it is unlikely that a

well designed rotor blade will be subject to large displacements.

3.1 Beam Kinematics

The nonlinear kinematics of deformation is based on the mechanics of curved rods [163, 165]. The strain components are first derived in a curvilinear coordinate system so that the effects of pretwist is properly accounted for. These strain components are then transformed to a local Cartesian coordinate system which the stress-strain relations are assumed to be defined in. The kinematical assumptions used in the derivation are:

1. The deformations of the cross section in its own plane are neglected; i.e. no in-plane warping;

2. The strain components are small compared to unity and no assumption is made regarding the relative magnitude between the axial and shear strains;

3. Higher order warping terms are neglected.

The position vector of a point $\mathbf{P}\,(x, \eta, \zeta)$ on the undeformed beam is written as

$$\mathbf{r}(x, \eta, \zeta) = e_1\hat{\mathbf{i}}_r + h_e\hat{\mathbf{i}}_b + x\hat{e}_x + \eta\hat{e}_\eta + \zeta\hat{e}_\zeta \ . \tag{3.1}$$

The corresponding undeformed base vectors at point $\mathbf{P}$ are defined by

$$\mathbf{g}_x = \mathbf{r}_{,x} = \hat{e}_x - \zeta\tau_0\hat{e}_\eta + \eta\tau_0\hat{e}_\zeta \tag{3.2a}$$

$$\mathbf{g}_\eta = \mathbf{r}_{,\eta} = \hat{e}_\eta \tag{3.2b}$$

$$\mathbf{g}_\zeta = \mathbf{r}_{,\zeta} = \hat{e}_\zeta \tag{3.2c}$$

where the derivatives of the orthonormal triad $(\hat{e}_x, \hat{e}_\eta, \hat{e}_\zeta)$ are related to the initial twist, τ_0, of the undeformed beam by

$$\begin{Bmatrix} \hat{e}_{x,x} \\ \hat{e}_{\eta,x} \\ \hat{e}_{\zeta,x} \end{Bmatrix} = \begin{bmatrix} 0 & 0 & 0 \\ 0 & 0 & \tau_0 \\ 0 & -\tau_0 & 0 \end{bmatrix} \begin{Bmatrix} \hat{e}_x \\ \hat{e}_\eta \\ \hat{e}_\zeta \end{Bmatrix} \tag{3.3}$$

and

$$\tau_0 = \beta_{,x} \tag{3.4}$$

Since the in-plane deformations of the beam cross-section are neglected, the position vector of the point $\mathbf{P}$ in the deformed configuration can be written as

$$\mathbf{R}(x, \eta, \zeta) = \mathbf{R}_0(x) + \eta\mathbf{E}_\eta + \zeta\mathbf{E}_\zeta + \alpha(x)\mathbf{\Psi}(\eta, \zeta)\hat{e}'_x \tag{3.5}$$

where

$$\mathbf{R}_0(x) = \mathbf{R}(x, 0, 0) \tag{3.6}$$

is the corresponding position vector of a point on the deformed reference axis; and

$$\mathbf{E}_i(x) = \mathbf{R}_{,i}(x,0,0), \qquad i = x, \eta, \zeta \tag{3.7}$$

are the basis vectors of a point on the deformed reference axis. In Eq. 3.5, the first three terms represent translations and rotations of the cross-section, and the last term is the out-of-plane cross-sectional warping. The unknown warping amplitude is given by $\alpha(x)$ and $\mathbf{\Psi}(\eta, \zeta)$ is the out-of-plane warping shape function, with

$$\mathbf{\Psi}(0,0) = \mathbf{\Psi}_{,\eta}(0,0) = \mathbf{\Psi}_{,\zeta}(0,0) = 0 \tag{3.8}$$

The warping shape functions are based on the St. Venant solution of a tip-loaded prismatic beam [88] and thus are known for a given cross-section.

With the assumption that in-plane deformations of the beam cross-section are neglected, the deformed reference axis basis vectors are expressed as [165]

$$\mathbf{E}_x = (1 + \bar{\varepsilon}_{xx})\hat{e}'_x \tag{3.9a}$$

$$\mathbf{E}_\eta = \bar{\gamma}_{x\eta}\hat{e}'_x + \hat{e}'_\eta \tag{3.9b}$$

$$\mathbf{E}_\zeta = \bar{\gamma}_{x\zeta}\hat{e}'_x + \hat{e}'_\zeta \tag{3.9c}$$

where $\bar{\varepsilon}_{xx}, \bar{\gamma}_{x\eta}$ and $\bar{\gamma}_{x\zeta}$ can be shown to be the axial and the transverse shear strains, respectively, at the reference axis. Equations 3.9a – c imply that cross sections, which are normal to the reference axis before deformation (e. g. $\hat{e}'_\eta - \hat{e}'_\zeta$ plane), will no longer be normal to

the reference axis after deformation (e. g. $\mathbf{E}_\eta - \mathbf{E}_\zeta$ plane) due to the presence of transverse shear strains. The deformed basis vectors at point $\mathbf{P}$ are defined as

$$\mathbf{G}_x = \mathbf{R}_{,x}, \quad \mathbf{G}_\eta = \mathbf{R}_{,\eta}, \quad \mathbf{G}_\zeta = \mathbf{R}_{,\zeta} \tag{3.10}$$

where the derivatives of the orthonormal triad $(\hat{e}'_x, \hat{e}'_\eta, \hat{e}'_\zeta)$ are related to the curvatures, $\kappa_\eta, \kappa_\zeta$, and twist, τ, of the deformed beam by

$$\begin{Bmatrix} \hat{e}'_{x,x} \\ \hat{e}'_{\eta,x} \\ \hat{e}'_{\zeta,x} \end{Bmatrix} = \begin{bmatrix} 0 & \kappa_\eta & \kappa_\zeta \\ -\kappa_\eta & 0 & \tau \\ -\kappa_\zeta & -\tau & 0 \end{bmatrix} \begin{Bmatrix} \hat{e}'_x \\ \hat{e}'_\eta \\ \hat{e}'_\zeta \end{Bmatrix} \tag{3.11}$$

3.2 Strain Components and Strain-Displacement Relations

In general, the set of coordinates (x, η, ζ) are non-orthogonal curvilinear coordinates since the basis vector $\mathbf{g}_x$, expressed in Eq. 3.2a is neither a unit vector nor orthogonal to $\mathbf{g}_\eta$ and $\mathbf{g}_\zeta$ for an arbitrary point on the beam with nonzero initial twist τ_0. In the description that follows, the notations (x_1, x_2, x_3) will be used in place of (x, η, ζ) whenever convenient.

The components of the strain tensor in the curvilinear coordinates are defined by [163]

$$f_{ij} = \frac{1}{2}(\mathbf{G}_i \cdot \mathbf{G}_j - \mathbf{g}_i \cdot \mathbf{g}_j), \quad i, j = x, \eta, \zeta \tag{3.12}$$

One can define a system of local Cartesian coordinates (y_1, y_2, y_3) at point $\mathbf{P}$ with its unit vectors parallel to the orthonormal triad $(\hat{e}_x, \hat{e}_\eta, \hat{e}_\zeta)$ of the cross section. The stress-strain

relations of the beam are assumed to be given in the local Cartesian coordinate system. The transformation relation between the curvilinear coordinates (x_1, x_2, x_3) and the local Cartesian coordinates (y_1, y_x, y_3) is given in matrix form by

$$\left[\frac{\partial x_i}{\partial y_j}\right] = [\mathbf{g}_k \cdot \mathbf{g}_i]^{-1}[\mathbf{g}_k \cdot \hat{e}_j] = \begin{bmatrix} 1 & 0 & 0 \\ \zeta\tau_0 & 1 & 0 \\ -\eta\tau_0 & 0 & 1 \end{bmatrix} \tag{3.13}$$

The strain tensor defined in the local Cartesian coordinates, ε_{ij}, is obtained from the transformation

$$\varepsilon_{ij} = \sum_{k=1}^{3}\sum_{l=1}^{3} \frac{\partial \mathrm{x_k}}{\partial y_i}\frac{\partial \mathrm{x_l}}{\partial y_j} f_{kl} \tag{3.14}$$

Combining Eqs. 3.2, 3.5, and 3.9 – 3.14, the strain components in the local Cartesian coordinates become

$$\begin{aligned}
\varepsilon_{xx} &= \bar{\varepsilon}_{xx} - \eta\kappa_\eta - \zeta\kappa_\zeta + \alpha_{,x}\mathbf{\Psi} + \alpha\tau_0(\zeta\mathbf{\Psi}_{,\eta} - \eta\mathbf{\Psi}_{,\zeta}) && \text{(3.15a)} \\
&\quad + \frac{1}{2}(\eta^2 + \zeta^2)(\tau - \tau_0)^2 + \eta(\bar{\gamma}_{x\eta,x} - \tau_0\bar{\gamma}_{x\zeta}) + \zeta(\bar{\gamma}_{x\zeta,x} + \tau_0\bar{\gamma}_{x\eta}) \\
\gamma_{x\eta} &= \bar{\gamma}_{x\eta} + \alpha\mathbf{\Psi}_{,\eta} - \zeta(\tau - \tau_0) && \text{(3.15b)} \\
\gamma_{x\zeta} &= \bar{\gamma}_{x\zeta} + \alpha\mathbf{\Psi}_{,\zeta} + \eta(\tau - \tau_0) && \text{(3.15c)} \\
\varepsilon_{\eta\eta} &\simeq \varepsilon_{\zeta\zeta} \simeq \gamma_{\eta\zeta} \simeq 0 && \text{(3.15d)}
\end{aligned}$$

where

$$\gamma_{x\eta} \equiv 2\varepsilon_{x\eta}, \quad \gamma_{x\zeta} \equiv 2\varepsilon_{x\zeta}, \quad \gamma_{\eta\zeta} \equiv 2\varepsilon_{\eta\zeta}$$

The strain components in Eqs. 3.15a – c are valid for small strains and large deflections and are expressed in terms of seven unknown functions of the axial coordinate x : $\bar{\varepsilon}_{xx}$, $\bar{\gamma}_{x\eta}$, $\bar{\gamma}_{x\zeta}$, κ_η, κ_ζ, τ and α. The first three are the axial and transverse shear strains, respectively, at the reference axis; the next three are curvatures and twist, respectively, of the deformed beam; α is the amplitude of warping.

In developing an aeroelastic model, it is desirable to express the strain components in terms of the displacement components – u, v, w – of the reference axis and the elastic twist ϕ so that the structural model can be more conveniently combined with the inertial and aerodynamic models. After applying an ordering scheme [174] which is consistent with a moderate deflection theory (small strains and moderate rotations), the strain components can be expressed in terms of u, v, w and ϕ as follows:

$$\begin{aligned}
\varepsilon_{xx} &= u_{,x} + \frac{1}{2}(v_{,x})^2 + \frac{1}{2}(w_{,x}^2) - v_{,xx}[\eta\cos(\beta+\phi) - \zeta\sin(\beta+\phi)] \qquad (3.16a)\\
&\quad -w_{,xx}[\eta\sin(\beta+\phi) + \zeta\cos(\beta+\phi)] + \frac{1}{2}(\eta^2+\zeta^2)(\phi_{,x})^2\\
&\quad +\alpha_{,x}\mathbf{\Psi} + \alpha\tau_0(\zeta\mathbf{\Psi}_{,\eta} - \eta\mathbf{\Psi}_{,\zeta}) + \eta(\bar{\gamma}_{x\eta,x} - \tau_0\bar{\gamma}_{x\zeta}) + \zeta(\bar{\gamma}_{x\zeta,x} + \tau_0\bar{\gamma}_{x\eta})\\
\gamma_{x\eta} &= \bar{\gamma}_{x\eta} + \alpha\mathbf{\Psi}_{,\eta} - \zeta(\phi_{,x} + \phi_0) \qquad (3.16b)\\
\gamma_{x\zeta} &= \bar{\gamma}_{x\zeta} + \alpha\mathbf{\Psi}_{,\zeta} + \eta(\phi_{,x} + \phi_0) \qquad (3.16c)
\end{aligned}$$

The seven unknown functions of the axial coordinate, x, in the strain-displacement relations, Eqs. 3.16a – c, become: u, v, w, ϕ, α, $\bar{\gamma}_{x\eta}$ and $\bar{\gamma}_{x\zeta}$. The strain components in Eqs. 3.16a – c are valid for moderate deflection analysis, which is suitable for accurately modeling blade displacements up to $10 - -15\%$ of the blade's radius.

3.3 Constitutive Relations

The constitutive relations are defined based on the assumptions that the material properties are linear elastic and generally orthotropic (anisotropic behavior) and that the in-plane stress components within the cross section are set to zero ($\sigma_{\eta\eta} = \sigma_{\zeta\zeta} = \sigma_{\eta\zeta} = 0$). The anisotropic stress-strain relations for a linearly elastic body are written as

$$\begin{bmatrix} \sigma_{xx} \\ \sigma_{\eta\eta} \\ \sigma_{\zeta\zeta} \\ \sigma_{\eta\zeta} \\ \sigma_{x\zeta} \\ \sigma_{x\eta} \end{bmatrix} = \begin{bmatrix} C_{11} & C_{12} & C_{13} & C_{14} & C_{15} & C_{16} \\ C_{12} & C_{22} & C_{23} & C_{24} & C_{25} & C_{26} \\ C_{13} & C_{23} & C_{33} & C_{34} & C_{35} & C_{36} \\ C_{14} & C_{24} & C_{34} & C_{44} & C_{45} & C_{46} \\ C_{15} & C_{25} & C_{35} & C_{45} & C_{55} & C_{56} \\ C_{16} & C_{26} & C_{36} & C_{46} & C_{56} & C_{66} \end{bmatrix} \begin{bmatrix} \varepsilon_{xx} \\ \varepsilon_{\eta\eta} \\ \varepsilon_{\zeta\zeta} \\ \gamma_{\eta\zeta} \\ \gamma_{x\zeta} \\ \gamma_{x\eta} \end{bmatrix} \tag{3.17}$$

Setting in-plane stresses equal to zero and applying back substitution, the constitutive relations are

$$\begin{Bmatrix} \sigma_{xx} \\ \sigma_{x\zeta} \\ \sigma_{x\eta} \end{Bmatrix} = \begin{bmatrix} Q_{11} & Q_{15} & Q_{16} \\ Q_{15} & Q_{55} & Q_{56} \\ Q_{16} & Q_{56} & Q_{66} \end{bmatrix} \begin{Bmatrix} \varepsilon_{xx} \\ \gamma_{x\zeta} \\ \gamma_{x\eta} \end{Bmatrix} \tag{3.18}$$

where

$$[Q] = [C_{bb}] - [C_{bs}][C_{ss}]^{-1}[C_{sb}]$$

$$[C_{bb}] = \begin{bmatrix} C_{11} & C_{15} & C_{16} \\ C_{15} & C_{55} & C_{56} \\ C_{16} & C_{56} & C_{66} \end{bmatrix}$$

$$[C_{ss}] = \begin{bmatrix} C_{22} & C_{23} & C_{24} \\ C_{23} & C_{33} & C_{34} \\ C_{24} & C_{34} & C_{44} \end{bmatrix}$$

$$[C_{bs}] = [C_{sb}]^T = \begin{bmatrix} C_{12} & C_{13} & C_{14} \\ C_{25} & C_{35} & C_{45} \\ C_{26} & C_{36} & C_{46} \end{bmatrix}$$

3.4 Equations of Motion

The nonlinear equations of motion and the corresponding finite element matrices are derived for each beam element using Hamilton's principle

$$\int_{t_1}^{t_2} (\delta U - \delta T - \delta W_e) dt = 0 \tag{3.19}$$

where δU, δT and δW_e represent the strain energy variation, kinetic energy variation, and virtual work of external loads, respectively.

3.4.1 Strain Energy

The variation of the strain energy for each beam element is

$$\delta U = \int_0^{l_e} \int\int_A \begin{Bmatrix} \delta\varepsilon_{xx} \\ \delta\gamma_{x\zeta} \\ \delta\gamma_{x\eta} \end{Bmatrix}^T \begin{bmatrix} Q_{11} & Q_{15} & Q_{16} \\ Q_{15} & Q_{55} & Q_{56} \\ Q_{16} & Q_{56} & Q_{66} \end{bmatrix} \begin{Bmatrix} \varepsilon_{xx} \\ \gamma_{x\zeta} \\ \gamma_{x\eta} \end{Bmatrix} d\eta d\zeta dx \tag{3.20}$$

Integrating Eq. 3.20 over the cross section yields three sets of modulus weighted section constants, which are presented in Ref. 174. These section constants can be calculated by a separate linear, two-dimensional analysis which is decoupled from the nonlinear, one-dimensional global analysis for the beam. The cross sectional analysis as developed in Ref. 88, 89 is based upon the solution of Saint Venant's flexure and torsion problems. It uses the principle of minimum potential energy and two-dimensional finite element analysis to solve for the displacement and stress distribution in an anisotropic composite blade cross section. This two-dimensional cross sectional analysis has undergone modifications to account for differences in kinematic assumptions, resulting in a set of cross-sectional constants that are provided in Ref. 174.

It should be noted that the analysis described in Ref. 88 is subject to limitations which are overcome by the VABS composite cross-section analysis code [15]. The compatibility between VABS and the beam model described in Ref. 174, as well as the advantages of using VABS are demonstrated in the Appendix A.

3.4.2 Kinetic Energy

The variation of the kinetic energy for each beam element is

$$\delta T = \int_0^{l_e} \int\int_A \rho \mathbf{V} \cdot \delta \mathbf{V} \, d\eta d\zeta dx \tag{3.21}$$

where the velocity vector, $\mathbf{V}$, is obtained by

$$\mathbf{V} = \dot{\mathbf{R}} + \Omega \hat{\mathbf{k}}_r \times \mathbf{R} \tag{3.22}$$

with the position vector, $\mathbf{R}$, of a point $\mathbf{P}$ on the deformed beam written in the form

$$\mathbf{R} = e_1\hat{\mathbf{i}}_r + h_e\hat{\mathbf{i}}_b + (x+u)\hat{e}_x + v\hat{e}_y + w\hat{e}_z + \eta\mathbf{E}_\eta + \zeta\mathbf{E}_\zeta + \alpha\mathbf{\Psi}\hat{e}'_x \tag{3.23}$$

All the terms in the expressions of the velocity vector, $\mathbf{V}$, in Eq. 3.22 were transformed to the $(\hat{e}_x, \hat{e}_y, \hat{e}_z)$ system before carrying out the algebraic manipulations. Integrating Eq. 3.21 over the cross section yields mass weighted section constants about the shear center, which are also presented in Ref. 174.

3.4.3 External Work Contributions

The effects of the nonconservative distributed loads are included using the principle of virtual work. The virtual work done on each beam element is

$$\delta W_e = \int_0^{l_e} (\mathbf{P}\cdot\delta\mathbf{u} + \mathbf{Q}\cdot\delta\mathbf{\Theta})dx \tag{3.24}$$

where $\mathbf{P}$ and $\mathbf{Q}$ are the distributed force and moment vectors, respectively, along the elastic axis; $\delta\mathbf{u}$ and $\delta\mathbf{\Theta}$ are the virtual displacement and virtual rotation vectors, respectively, of a point on the deformed elastic axis. In the aeroelastic analysis, components of $\mathbf{P}$ and $\mathbf{Q}$ are replaced by the corresponding components of aerodynamic forces and moments.

3.5 Modifications Due to the Presence of Flaps

The modifications to the structural model due to the flaps have been implemented by De Terlizzi and Friedmann [28]. The control surface is modeled as partial span trailing edge flaps located on the outboard section of the blade.

It is assumed that the flap does not change the blade structural model. The influence of the flap dynamics is taken into account through the flap inertial loads, which are formulated as an additional external work contribution in Eq. 3.24. The detailed expressions are given in Ref. 28. The aerodynamic model of this study is capable of modeling the aerodynamic loads of a flapped airfoil, which will be treated in Chap. IV.

3.6 Finite Element Discretization

The spatial discretization of the blade equations of motion is achieved by using the finite element method. The straight portion of the blade is divided into a number of beam elements, while the swept tip is modeled as a single beam element. The discretized form of Hamilton's principle as given in Eq. 3.19 is written as

$$\int_{t_1}^{t_2} \sum_{i=1}^{n} (\delta U_i - \delta T_i - \delta W_{ei}) dt = 0 \tag{3.25}$$

Hermite interpolation polynomials are used to discretize the space dependence of the generalized coordinates: cubic polynomials for v and w; quadratic polynomials for ϕ, u, α, $\bar{\gamma}_{x\eta}$ and $\bar{\gamma}_{x\zeta}$. The seven unknown generalized coordinates of the beam finite element can be

expressed in the following form

$$\begin{bmatrix} v \\ w \\ \phi \\ u \\ \alpha \\ \bar{\gamma}_{x\eta} \\ \bar{\gamma}_{x\zeta} \end{bmatrix} = \begin{bmatrix} \{\Phi_v\}^T & 0 & 0 & 0 & 0 & 0 & 0 \\ 0 & \{\Phi_w\}^T & 0 & 0 & 0 & 0 & 0 \\ 0 & 0 & \{\Phi_\phi\}^T & 0 & 0 & 0 & 0 \\ 0 & 0 & 0 & \{\Phi_u\}^T & 0 & 0 & 0 \\ 0 & 0 & 0 & 0 & \{\Phi_\alpha\}^T & 0 & 0 \\ 0 & 0 & 0 & 0 & 0 & \{\Phi_\eta\}^T & 0 \\ 0 & 0 & 0 & 0 & 0 & 0 & \{\Phi_\zeta\}^T \end{bmatrix} \begin{bmatrix} \{V\} \\ \{W\} \\ \{\phi\} \\ \{U\} \\ \{\alpha\} \\ \{\Gamma_\eta\} \\ \{\Gamma_\zeta\} \end{bmatrix} \tag{3.26}$$

where $\{\Phi_v\}$,$\{\Phi_w\}$,$\{\Phi_\phi\}$,$\{\Phi_u\}$,$\{\Phi_\alpha\}$,$\{\Phi_\eta\}$,$\{\Phi_\zeta\}$ are the Hermite interpolation polynomials, and $\{V\}, \{W\}, \{\phi\}, \{U\}, \{\alpha\}, \{\Gamma_\eta\}$, $\{\Gamma_\zeta\}$ are time dependent nodal parameters for v, w, ϕ, u, α, $\bar{\gamma}_{x\eta}$ and $\bar{\gamma}_{x\zeta}$, respectively. Each beam element consists of two end nodes and one internal node at its mid-point, resulting in a total of 23 nodal degrees of freedom, as shown in Fig. 3.1. The quadratic polynomial has the capability of modeling a linear variation of strains along the element length, thus being compatible with the cubic polynomial for transverse deflections v and w. These polynomials also satisfy all inter-element compatibility requirements associated with the variational principle in this formulation.

3.6.1 Element Matrices Associated with the Strain Energy Variation

Using the interpolation of the generalized coordinates with nodal parameters given by Eq. 3.26, the variation of the strain energy in Eq. 3.20 can be expressed in the following form

$$\delta U = \delta \mathbf{q}^T([\mathrm{K}^{\mathrm{L}}] + [\mathrm{K}^{\mathrm{NL}}(\mathbf{q})])\mathbf{q} \tag{3.27}$$

where

$$\mathbf{q} = [\{V\}^T, \{W\}^T, \{\phi\}^T, \{U\}^T, \{\alpha\}^T, \{\Gamma_\eta\}^T, \{\Gamma_\zeta\}^T]^T$$

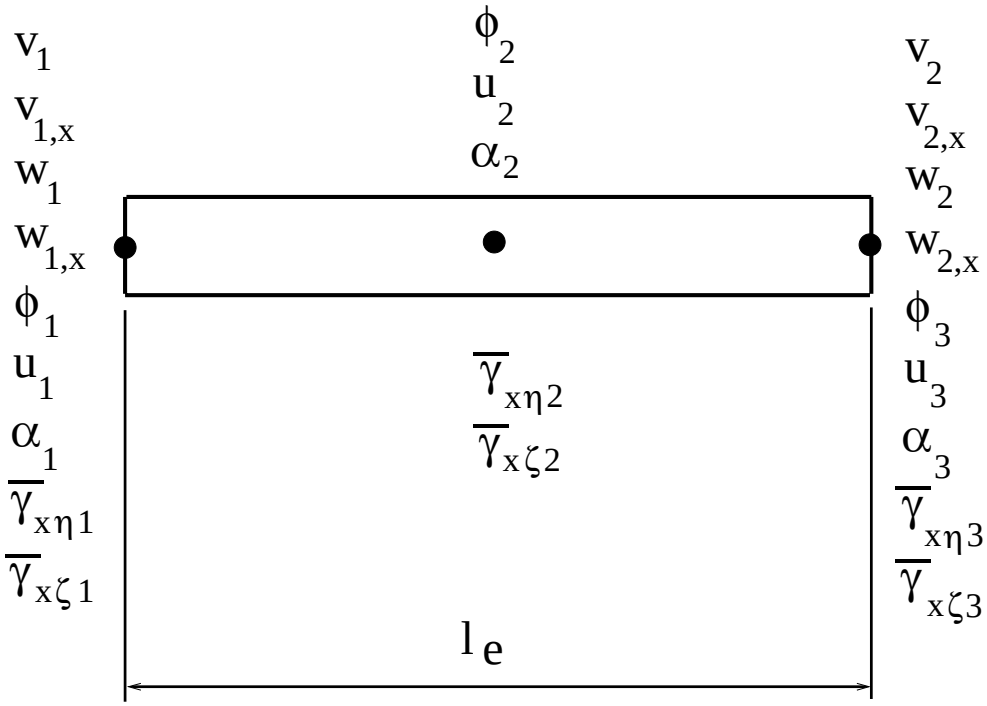

Figure 3.1: Finite element nodal degrees of freedom

and $[\mathrm{K}^{\mathrm{L}}]$ and $[\mathrm{K}^{\mathrm{NL}}]$ are the linear stiffness matrix(symmetric) and nonlinear stiffness matrix, respectively. Detailed expressions for the stiffness matrices are presented in Ref. 174.

3.6.2 Element Matrices Associated with the Kinetic Energy Variation

The variation of the kinetic energy in Eq. 3.21 can be expressed in the following form, utilizing Eq. 3.26

$$\delta T = \delta \mathbf{q}^T([\mathrm{M}]\ddot{\mathbf{q}} + [\mathrm{M}^{\mathrm{C}}]\dot{\mathbf{q}} + [\mathrm{K}^{\mathrm{CF}}]\mathbf{q} + \{\mathrm{F}^{\mathrm{CF}}\}) \tag{3.28}$$

where $[\mathrm{M}]$ is the mass matrix(symmetric), $[\mathrm{M}^{\mathrm{C}}]$ is a Coriolis damping matrix(anti-symmetric), $[\mathrm{K}^{\mathrm{CF}}]$ is a centrifugal stiffening matrix(symmetric when $\mathbf{\Omega}$ is constant, and $\{\mathrm{F}^{\mathrm{CF}}\}$ is a cen-

trifugal force vector. Detailed expressions for these matrices are presented in Ref. 174.

3.6.3 Element Matrices Associated with the Virtual Work of External Loads

The virtual work of external loads in Eq. 3.24 has the form

$$\delta W_e = -\delta \mathbf{q}^T([\mathrm{K^I}]\mathbf{q} + \{\mathrm{F^I}\}) \tag{3.29}$$

where $[\mathrm{K^I}]$ is a stiffness type matrix associated with applied distributed moments, and $\{\mathrm{F^I}\}$ is an applied force vector. Detailed expressions for these matrices are presented in Ref. 174.

3.6.4 Summary of the Beam Finite Element Equations of Motion

The finite element equations of motion for a single beam element are obtained by substituting Eqs. 3.27 – 3.29 into the discretized form of Hamilton's principle, Eq. 3.25

$$[\mathrm{M_i}]\ddot{\mathbf{q}} + [\mathrm{C_i}]\dot{\mathbf{q}} + [\mathrm{K_i}]\mathbf{q} + \mathbf{F_i} = \mathbf{0} \tag{3.30}$$

where

$$\begin{aligned}
[\mathrm{M_i}] &= [\mathrm{M}]_i \\
[\mathrm{C_i}] &= [\mathrm{M^C}]_i \\
[\mathrm{K_i}] &= [\mathrm{K^L}]_i + [\mathrm{K^{CF}}]_i + [\mathrm{K^I}]_i + [\mathrm{K^{NL}}(\mathbf{q})]_i \\
\mathbf{F_i} &= \{\mathrm{F^{CF}}\}_i + \{\mathrm{F^I}\}_i
\end{aligned}$$

The global mass, damping, stiffness matrices and force vector can then be assembled using standard finite element assembly procedure, using the boundary conditions of the cantilevered blade.

Chapter IV

Aerodynamic Model

The *attached flow* blade section aerodynamics are calculated using a rational function approach (RFA) developed by Myrtle and Friedmann [108, 109]. The RFA approach is a two-dimensional unsteady time-domain theory that accounts for compressibility as well as variations in the oncoming flow velocity. For the *separated flow* regime, unsteady aerodynamic loads are calculated using the ONERA dynamic stall model described in Ref. 121. The aerodynamic states associated with RFA attached flow and ONERA separated flow are combined to produce the time-domain, state space aerodynamic model. Furthermore, a simple linear drag model which accounts for increase in drag due to flap deflection is implemented [31]. The two-dimensional aerodynamic model is linked to an enhanced free-wake model which provides a non-uniform inflow distribution at closely spaced azimuthal steps [77, 78, 119, 136].

4.1 RFA Model of the Attached Flow Loads

In the RFA approach, approximate frequency domain transfer functions between the airloads and the generalized motions of a two-dimensional airfoil-flap combination are

constructed. These relations are then transformed into the time domain to yield a state-space aerodynamic model. This method accounts for compressibility and unsteady effects due to free stream and blade-flap motions. The RFA approach was extended by Patt, Liu, and Friedmann [95, 116, 119] to calculate the chordwise pressure distribution, which is required in the acoustic calculation.

4.1.1 Doublet Lattice Method for Oscillatory Airloads

A two-dimensional double lattice method (DLM) [129] is first applied to generate lift, moment, and hinge moment responses to generalized oscillatory airfoil motions over a range of reduced frequencies and Mach numbers typical of the rotor environment. Using the compressible oscillatory response data generated by the DLM, oscillatory response quantities can be quickly calculated for any combination of reduced frequency, Mach number, and generalized airfoil motion, including flap motion. A brief description of this process follows:

Assume a normal velocity distribution represented by

$$W(x,t) = U\bar{w}(x)e^{i\omega t}, \tag{4.1}$$

and a surface pressure difference distribution given by

$$P(x,t) = \frac{1}{2}\rho U^2 \bar{p}(x)e^{i\omega t}, \tag{4.2}$$

where x represents a location on the chord of the airfoil which coincides with the x-axis,

with leading and trailing edges located at $x = -1$ and $x = 1$, respectively. The functions $w(x)$ and $p(x)$ represent dimensionless velocity and pressure quantities respectively. The functions $\bar{w}(x)$ and $\bar{p}(x)$ are related through the Possio integral equation, which is given by

$$\bar{w}(x) = \frac{1}{8\pi} \int_{-1}^{1} \bar{p}(\zeta) K(M, x - \zeta) d\zeta, \tag{4.3}$$

with kernel K given by

$$\begin{aligned} K(M,x) &= \frac{\pi k}{\beta} e^{-ikx} \left\{ e^{kx/\beta^2} \left(M \frac{|x|}{x} H_1^{(2)}(Mk|x|/\beta^2) - H_0^{(2)}(Mk|x|/\beta^2) \right) \right. \\ &\quad \left. + \frac{i2\beta}{\pi} \log(\frac{1+\beta}{M}) + i\beta^2 \int_0^{kx/\beta^2} \frac{kx}{2\beta^2} e^{iu} H_0^{(2)}(M|u|) du \right\}. \end{aligned} \tag{4.4}$$

The DLM is employed to obtain approximate solutions for $\bar{p}$ from Eq. 4.3 for a given normal velocity distribution $\bar{w}$. In the DLM, the airfoil chord is divided into N equal size segments, each containing a line of acceleration potential doublets at the segment quarter chord. Each line of doublets produces a force f per unit span at the quarter chord, acting normal to the airfoil surface. The doublet line strength corresponding to force f at the quarter chord of the j-th chord segment is given by $\frac{f_j}{4\pi\rho}$. The normal velocity induced by this doublet line at a point x_i on the airfoil chord is given by

$$\bar{w}_j(x_i) = \frac{f_j}{4\pi\rho} U^2 K(M, x_i - x_j), \tag{4.5}$$

where x_j is the location of the doublet line in the j-th segment. The total normal velocity induced at point x_i is given by the sum of the normal velocities induced by the N doublet

lines,

$$\bar{w}(x_i) = \sum_{j=1}^{N} \frac{f_j}{4\pi\rho} U^2 K(M, x_i - x_j). \tag{4.6}$$

Next, the force on the doublet line can be expressed as a pressure difference across the surface by taking

$$\frac{f_j}{4\pi\rho} U^2 = \frac{1}{8\pi} \bar{p}_j \Delta x, \tag{4.7}$$

where Δx is the length of the chord segment. Using Eq. 4.7, Eq. 4.6 can be rewritten as

$$\bar{w}_i = \sum_{j=1}^{N} D_{ij} \bar{p}_j, \tag{4.8}$$

where D_{ij} is given by

$$D_{ij} = \frac{1}{8\pi} \Delta x K(M, x_i - x_j). \tag{4.9}$$

The downwash $\bar{w}_i$ in Eq. 4.8 is taken at a point x_i corresponding to the $3/4$ chord point of the i-th chord segment. Taking the downwash at this point causes the Kutta condition to be satisfied. Equation 4.8 is then inverted, producing

$$\bar{p}_i = \sum_{j=1}^{N} A_{ij} \bar{w}_j, \tag{4.10}$$

where A_{ij} is the inverse of D_{ij}. The normal velocity distribution vector $\bar{w}$ depends upon the generalized airfoil motion being considered. The oscillatory pressure distribution represented by $\bar{p}_i$ is then used to calculate airfoil oscillatory response quantities corresponding to a particular generalized airfoil motion.

In summary, the DLM proceeds as follows: (1) The number of airfoil segments is

selected; (2) A reduced frequency and Mach number are selected; (3) The matrix D, given in Eq. 4.9, is calculated and then inverted to produce the matrix A; (4) Eq. 4.10 is then used to calculate the pressure distribution vector $\bar{p}$ for each generalized airfoil motion being considered; (5) The steps in this process are repeated until response quantities have been calculated for a sufficient number of Mach numbers and reduced frequencies.

4.1.2 Roger's Approximation

The RFA approach, which is based on a least squares method known as Roger's approximation [130], is employed to convert the tabulated frequency domain response data generated by the DLM into the time domain. This process is described below.

Consider an aerodynamic system which is represented in the Laplace domain by the expression

$$\mathbf{G}(\bar{s}) = \mathbf{Q}(\bar{s})\mathbf{H}(\bar{s}), \tag{4.11}$$

where $\mathbf{G}(\bar{s})$ and $\mathbf{H}(\bar{s})$ represent Laplace transforms of the generalized aerodynamic load and generalized motion vectors, respectively. Using the Least Squares approach, the aerodynamic transfer matrix $\mathbf{Q}(\bar{s})$ is approximated using a rational expression of the form

$$\tilde{\mathbf{Q}}(\bar{s}) = \mathbf{C}_0 + \mathbf{C}_1\bar{s} + \sum_{n=1}^{n_L} \frac{\bar{s}}{\bar{s} + \gamma_n}\mathbf{C}_{n+1}. \tag{4.12}$$

The n_L terms in the summation are aerodynamic lag terms and contain an associated set of poles γ_n. These poles are assumed to be positive valued to produce stable open loop roots. The accuracy and numerical efficiency of the approximation depend upon an appropriate

choice of the number of lag terms.

The elements of the coefficient matrices $\mathbf{C}_n$ are chosen such that they provide a best fit, in a least squares sense, to the oscillatory response data obtained using DLM. A high frequency constraint which constrains the approximation at $k = \infty$ to the piston theory response can be implemented. Furthermore, numerical optimization techniques are used to find the optimal poles such that the fitting error is minimized. The fitting process is described in detail in Ref. 108.

4.1.3 State Space Model

The arbitrary motions of the airfoil and flap are represented by the four generalized motions depicted in Fig. 4.1. These motions produce constant and linearly varying normal velocity distributions on the airfoil and flap, which can be expressed in terms of the classical pitch and plunge motions α and h, the flap deflection δ, and the freestream velocity U:

$$W_0 = U\alpha + \dot{h}, \tag{4.13}$$

$$W_1 = b\dot{\alpha}. \tag{4.14}$$

$$D_0 = U\delta_f, \tag{4.15}$$

$$D_1 = b\dot{\delta}_f. \tag{4.16}$$

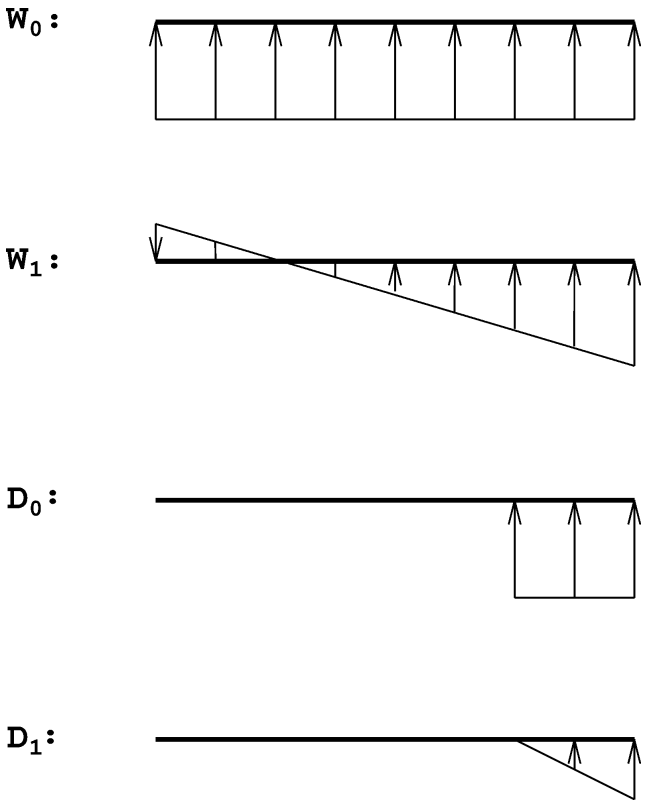

Figure 4.1: Normal velocity distribution corresponding to generalized airfoil and flap motions

A generalized motion vector $\mathbf{h}(t)$ and a generalized force vector $\mathbf{f}(t)$ are given by:

$$\mathbf{h} = \left\{ \begin{array}{c} W_0 \\ W_1 \\ D_0 \\ D_1 \end{array} \right\} \tag{4.17}$$

$$\mathbf{f} = \left\{ \begin{array}{c} C_L \\ C_M \\ C_{Hm} \end{array} \right\}. \tag{4.18}$$

In order to capture unsteady freestream effects [108], the derivation of the aerodynamic model is carried out in terms of reduced time $\bar{t}$, which is a nondimensional parameter representing the length in semi-chords that the airfoil has traveled.

$$\bar{t} = \frac{1}{b} \int_0^1 U(\tau) d\tau \tag{4.19}$$

The aerodynamic system can then be represented in the form given in Eq. 4.11 by taking $\mathbf{G}(\bar{s}) = \mathcal{L}[\mathbf{f}(\bar{t})U(\bar{t})]$ and $\mathbf{H}(\bar{s}) = \mathcal{L}[\mathbf{h}(\bar{t})]$.

To simplify the notation, the lag terms in Eq. 4.12 are rewritten in matrix form [108],

$$\sum_{n=1}^{n_L} \frac{\bar{s}}{\bar{s} + \gamma_n} \mathbf{C}_{n+1} = \mathbf{D} \left(\mathbf{I}\bar{s} - \mathbf{R} \right)^{-1} \mathbf{E}\bar{s}, \tag{4.20}$$

where

$$\mathbf{D} = \begin{bmatrix} \mathbf{I} & \mathbf{I} & \dots & \mathbf{I} \end{bmatrix}, \quad \mathbf{R} = - \begin{bmatrix} \gamma_1 \mathbf{I} & & & \\ & \gamma_2 \mathbf{I} & & \\ & & \dots & \\ & & & \gamma_{n_L} \mathbf{I} \end{bmatrix}, \quad \mathbf{E} = \begin{bmatrix} \mathbf{C}_2 \\ \mathbf{C}_3 \\ \vdots \\ \mathbf{C}_{n_L+1} \end{bmatrix}. \tag{4.21}$$

Using Eq. 4.20, the rational approximant $\tilde{\mathbf{Q}}(\bar{s})$ in Eq. 4.12 can be rewritten as

$$\tilde{\mathbf{Q}}(\bar{s}) = \mathbf{C}_0 + \mathbf{C}_1 \bar{s} + \mathbf{D} \left(\mathbf{I}\bar{s} - \mathbf{R} \right)^{-1} \mathbf{E}\bar{s}. \tag{4.22}$$

Eq. 4.22 is then substituted into Eq. 4.11, yielding

$$\mathbf{G}(\bar{s}) = \left(\mathbf{C}_0 + \mathbf{C}_1\bar{s} + \mathbf{D}\left(\mathbf{I}\bar{s} - \mathbf{R}\right)^{-1}\mathbf{E}\bar{s}\right)\mathbf{H}(\bar{s}). \tag{4.23}$$

The lag terms in Eq. 4.23 are then used to define a vector of aerodynamic states $\mathbf{X}_a(\bar{s})$ given by

$$\mathbf{X}_a(\bar{s}) = \left(\mathbf{I}\bar{s} - \mathbf{R}\right)^{-1}\mathbf{E}\bar{s}\mathbf{H}(\bar{s}). \tag{4.24}$$

Expressing Eq. 4.23 in terms of $\mathbf{X}_a(\bar{s})$ yields

$$\mathbf{G}(\bar{s}) = \mathbf{C}_0\mathbf{H}(\bar{s}) + \mathbf{C}_1\bar{s}\mathbf{H}(\bar{s}) + \mathbf{D}\mathbf{X}_a(\bar{s}). \tag{4.25}$$

Equations 4.24 and 4.25 are transformed to the time domain using the inverse Laplace transform. Converting from reduced time $\bar{t}$ to time t using the relation $\frac{d}{d\bar{t}} = \frac{b}{U(t)}\frac{d}{dt}$, yields

$$\dot{\mathbf{x}_a}(t) = \frac{U(t)}{b}\mathbf{R}\mathbf{x}_a(t) + \mathbf{E}\dot{\mathbf{h}}(t), \tag{4.26}$$

$$\mathbf{f}(t) = \frac{1}{U(t)}\left(\mathbf{C}_0\mathbf{h}(t) + \mathbf{C}_1\frac{b}{U(t)}\dot{\mathbf{h}}(t) + \mathbf{D}\mathbf{x}_a(t)\right), \tag{4.27}$$

The aerodynamic loads $\mathbf{f}(t)$ are a function of the aerodynamic states $\mathbf{x}(t)$, which are governed by the set of first order differential equations given by Eq. 4.26. Equations 4.27 and 4.26 are functions of the generalized airfoil and flap motions contained in the vector $\mathbf{h}(t)$.

To account for the large variations in Mach number encountered in rotary wing applications, rational approximants are generated at increments of Mach number over the range

of interest. The resulting coefficient matrices $\mathbf{C}_n(M)$ are then functions of Mach number and replace the original coefficients in Eqs. 4.26 – 4.27, yielding

$$\dot{\mathbf{x}_a}(t) = \frac{U(t)}{b}\mathbf{R}(M)\mathbf{x}_a(t) + \mathbf{E}(M)\dot{\mathbf{h}}(t), \tag{4.28}$$

$$\mathbf{f}(t) = \frac{1}{U(t)}\left(\mathbf{C}_0(M)\mathbf{h}(t) + \mathbf{C}_1(M)\frac{b}{U(t)}\dot{\mathbf{h}}(t) + \mathbf{D}(M)\mathbf{x}_a(t)\right). \tag{4.29}$$

4.1.4 Extension for Chordwise Pressure Calculation

In the extension of the RFA model for chordiwse pressure calculation described in Ref. 119, the oscillatory pressure distribution $\bar{p}_i$ given in Eq. 4.10 is saved prior to integration to obtain sectional airloads; a separate RFA procedure similar to what is described in Sections 4.1.2 and 4.1.3 for sectional airloads computation is then carried out at each chordwise location, using the corresponding oscillatory pressure data.

A generalized pressure vector $\mathbf{f}^p(t)$ is introduced:

$$\mathbf{f}^p = \begin{bmatrix} C_{P1} \\ C_{P2} \\ \vdots \\ C_{Pi} \\ \vdots \\ C_{Pn} \end{bmatrix}. \tag{4.30}$$

This pressure vector represents the pressure coefficients on panels in the chordwise direction of the airfoil as shown in Fig. 4.2. The pressure computations introduce new aero-

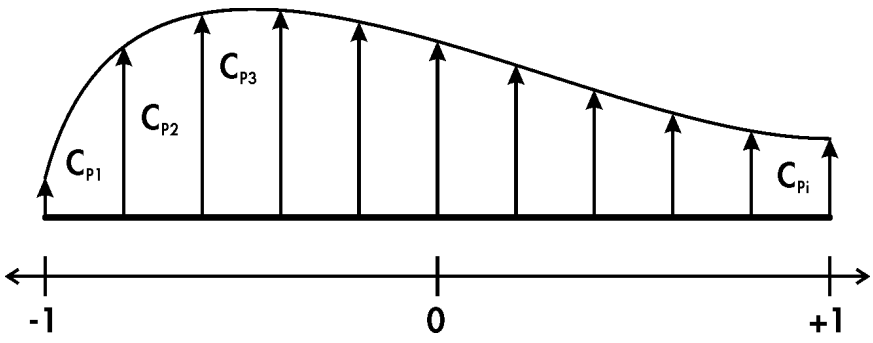

Figure 4.2: Airfoil chordwise pressure distribution

dynamic states $\mathbf{x}_a^p$; however, this computation is performed separately after the aeroelastic response solution is obtained, thus the additional computational cost for the pressure computations is minimized and the original aeroelastic solution procedure is kept intact. As a means of validation, the force and moment coefficients obtained by integrating the pressure vector $\mathbf{f}^p(t)$ are compared to the generalized force $\mathbf{f}(t)$ obtained from the original sectional RFA computation; typically with forty chordwise panels the sectional lift and moment coefficients can be reproduced within 5% when integrating pressure distribution over the chord.

The rational function approximations used to relate $\mathbf{f}^p(t)$ to $\mathbf{h}(t)$ are similar to those that relate $\mathbf{f}(t)$ to $\mathbf{h}(t)$. The final state space equations for pressure distribution are:

$$\dot{\mathbf{x}}_a^p(t) = \frac{U(t)}{b}\mathbf{R}(M)\mathbf{x}_a^p(t) + \mathbf{E}(M)\dot{\mathbf{h}}(t), \tag{4.31}$$

$$\mathbf{f}^p(t) = \frac{1}{U(t)}\left(\mathbf{C}_0^p(M)\mathbf{h}(t) + \mathbf{C}_1^p(M)\frac{b}{U(t)}\dot{\mathbf{h}}(t) + \mathbf{D}(M)\mathbf{x}_a^p(t)\right). \tag{4.32}$$

These equations can be compared to Eqs. 4.28 and 4.29 for sectional airloads. Note the difference is that in the sectional airloads computations, the generalized motion vector $\mathbf{h}$

is unknown and is obtained from the coupled aeroelastic response solution; whereas $\mathbf{h}$ is known from the aeroelastic response solution and is available for the pressure computations in Eqs. 4.31 and 4.32, representing the fact that the pressure computations are decoupled from the aeroelastic solution procedure.

4.2 Dynamic Stall Model for the Separated Flow Regime

Dynamic stall effects due to flow separation are modeled by a semi-empirical model based on a modified version of the ONERA dynamic stall model [32]. The modified aerodynamic state vector for each blade section consists of RFA attached flow states and ONERA separated flow states. Previous studies [30] have suggested that dynamic stall is an important contributor to vibration levels at high advance ratios($\mu \geq 0.35$).

In the ONERA model developed by Petot [121], the three second-order differential equations governing the separated flow states are:

$$\ddot{\Gamma}_{j2} + a_j.\frac{U}{b}\dot{\Gamma}_{j2} + r_j(\frac{U}{b})^2\Gamma_{j2} = -[r_j(\frac{U}{b})^2 V\Delta C_j + E_j.\frac{U}{b}\dot{W}_0], \tag{4.33}$$

where $j = l, m, d$ represent lift, moment, and drag respectively. The complete two-dimensional sectional airloads are given by:

$$L = L_A + L_S, \quad M = M_A + M_S, \quad D = D_A + D_S, \tag{4.34}$$

where L_A and M_A are the attached flow lift and moment calculated by the RFA approach

(Eq. 4.27). The separated flow quantities and the profile drag are given by:

$$L_S = \frac{1}{2}\rho c_b U \Gamma_{l2}, \tag{4.35}$$

$$M_S = \frac{1}{2}\rho c_b^2 U \Gamma_{m2}, \tag{4.36}$$

$$D_S = \frac{1}{2}\rho c_b U \Gamma_{d2}. \tag{4.37}$$

$$D_A = \frac{1}{2}\rho c_b U^2 C_{d0}, \tag{4.38}$$

The flow separation and reattachment criterion is based on the angle of attack and a correction similar to Prandtl-Glauert to account for compressibility. The critical angle of attack for separation and reattachment is $\alpha_{cr} = 17^o(1 - M^2)$. There are three measures of stall, one for each sectional airload. They can either be zero:

$$\Delta C_L = \Delta C_M = \Delta C_D = 0, \tag{4.39}$$

or take the following values if the flow has separated [30]:

$$\Delta C_L = (p_0 - 0.1M^4)(\alpha - \alpha_{cr}) - 0.7(1 - M)[e^{(-0.5+(1.5-M)M^2)(\alpha-\alpha_{cr})} - 1] \tag{4.40}$$

$$\Delta C_M = (-0.11 - 0.19e^{-40(M-0.6)^2})[e^{(-0.4-0.21arctan[22(0.45-M)])(\alpha-\alpha_{cr})} - 1] \tag{4.41}$$

$$\Delta C_D = (0.008 - 0.3)\left[1 - \left(\frac{25 - \alpha}{25 - \alpha_{cr}}\right)^{\frac{25-\alpha_{cr}}{18-2arctan(4M)}-\alpha_{cr}}\right] \tag{4.42}$$

where

$$p_0 = 0.1\frac{1-M^8}{\sqrt{1-M^2}}, \tag{4.43}$$

The separation criterion is based on the angle of attack, and three possible cases can occur.

1. Case 1: if $\alpha < \alpha_{cr} = 17^o(1-M^2)$, ΔC_L, ΔC_M and ΔC_D are 0.

2. Case 2: assume that at time $t = t_0$, $\alpha = \alpha_{cr}, \dot{\alpha} > 0$; then, ΔC_M and ΔC_D are given by Eqs. 4.41 – 4.42, and at time $t > t_0 + \Delta\tau$, ΔC_L is given by Eq. 4.40. The nondimensional lift delay is $\Delta\tau = 8$. As ΔC_L is different from zero, separated flow loads become substantial.

3. Case 3: when $\alpha < \alpha_{cr}$, the flow has reattached and ΔC_L, ΔC_M and ΔC_D are set to zero again and the separated flow loads quickly decrease to zero.

The ONERA model features 18 empirical coefficients, 6 each ($r_{j0}, r_{j2}, a_{j0}, a_{j2}, E_{j2}$) associated with lift ($j = l$), moment ($j = m$), and drag ($j = d$). These quantities can be found in Ref. 30

4.3 Free-Wake Model

This wake analysis is critical for properly capturing BVI effects on vibratory loads and noise. A detailed description of the characteristics and modeling of rotor wakes can be found in Ref. 91. The wake analysis has been extracted [28] from the comprehensive rotor

analysis code CAMRAD/JA [77, 78], and it has undergone significant improvements for the modeling of BVI noise [95, 116, 119].

The wake analysis consists of two elements: (1) a wake geometry calculation procedure including a free wake analysis developed by Scully [136], which determines the position of the vortices; (2) an induced velocity calculation procedure as implemented in CAMRAD/JA, which calculates the nonuniform induced velocity distribution at the blades.

4.3.1 Wake Geometry

The rotor wake is composed of two main elements: the tip vortex, which is a strong, concentrated vorticity filament generated at the tip of the blade; and the near wake, which is an inboard sheet of trailed vorticity that is much weaker and more diffused than the tip vortex. The wake vorticity is created in the flow field as the blade rotates, and then progresses with the local velocity of the fluid. The local velocity of the fluid consists of the free stream velocity, and the wake self induced velocity. Thus, the wake geometry calculation proceeds as follows: (1) the position of the blade generating the wake element is calculated, this is the point at which the wake vorticity is created; (2) the undistorted wake geometry is computed as wake elements are sent downstream from the rotor by the free stream velocity; (3) distortion of wake due to the wake self-induced velocity is computed and added to the undistorted geometry. The position of a generic wake element is identified by its current azimuth position ψ and its age ϕ_w. Age implies here the nondimensional time that has elapsed between the wake element's current position and the position where it was created. By carrying out this procedure, the position of a generic wake element is written

as:

$$\mathbf{r}_w(\psi, \phi_w) = \mathbf{r_b}(\psi - \phi_w) + \phi_w \mathbf{V_A} + \mathbf{D}(\psi, \phi_w) \tag{4.44}$$

where $\mathbf{r_b}(\psi - \phi_w)$ is the position of the blade when it generates the wake element, $\mathbf{V_A}$ is the free stream velocity, and $\mathbf{D}(\psi, \phi_w)$ is the wake distortion.

To evaluate the wake self-induced distortion $\mathbf{D}(\psi, \phi_w)$, a free wake procedure developed by Scully [136] is employed. This procedure is used only to calculate the distorted geometry of the tip vortices, which is the dominant feature of the rotor wake. The inboard vorticity is determined by a prescribed wake model [77] to save computational cost.

In the free wake geometry calculation, the distortion $\mathbf{D}$ is obtained by integrating in time the induced velocity at each wake element due to all the other wake elements. The induced velocity $\mathbf{q_I}$ is calculated at all wake elements for a given age ϕ_w, and all azimuth angles ψ. As the wake age increases by $\Delta\psi$, the distortion at time ψ is increased by the contribution of the induced velocity:

$$\mathbf{D}(\psi, \phi_w) = \mathbf{D}(\psi, \phi_w - \Delta\psi) + \Delta\psi \mathbf{q_I}(\psi) \tag{4.45}$$

To start this incremental computation, a value of $\mathbf{D}(\psi, 0)$ is required. At age $\phi_w = 0$, the wake element has just been generated from the blade tip, so it has no distortion:

$$\mathbf{D}(\psi, 0) = 0 \tag{4.46}$$

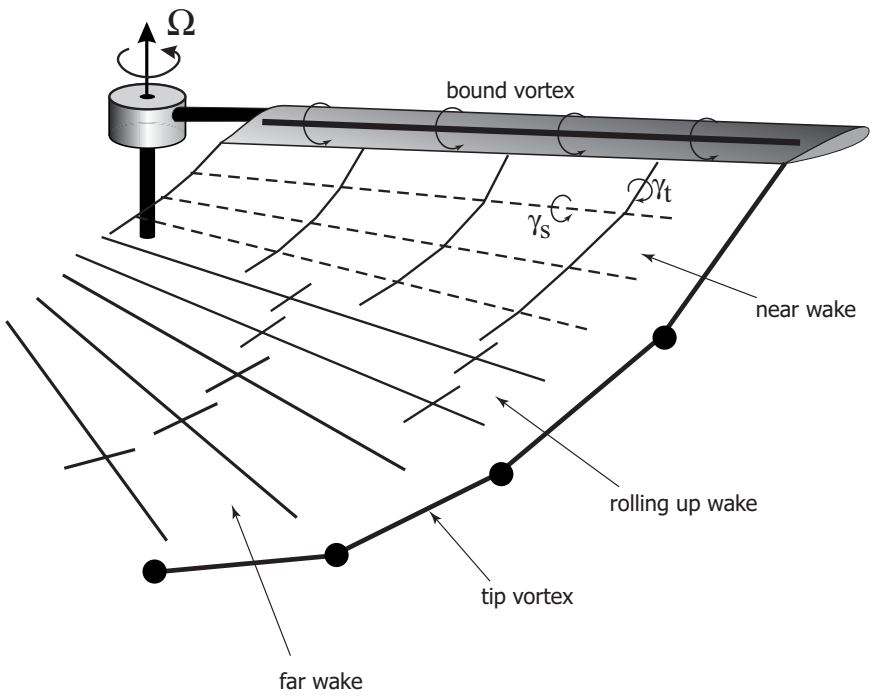

Figure 4.3: Vortex-lattice approximation for rotor wake model

4.3.2 Induced Velocity Calculation

The induced velocity calculation procedure, developed by Johnson [77], is based on a vortex-lattice approximation for the wake. The tip vortex elements are modeled by line segments with a small viscous core radius, while the near wake can be represented by vortex sheet elements or by line segments with a large core radius to eliminate large induced velocities. The near wake vorticity is generally retained for only a number K_{NW} of azimuth steps behind the blade. In this study, $K_{NW} = 4$. The wake structure is illustrated in Fig. 4.3.

Conservation of vorticity on a three-dimensional wing requires the bound circulation to be trailed into the wake from the blade tip and root. The lift and circulation are concentrated at the tip of the blade, since larger dynamic pressures are present in the tip region.

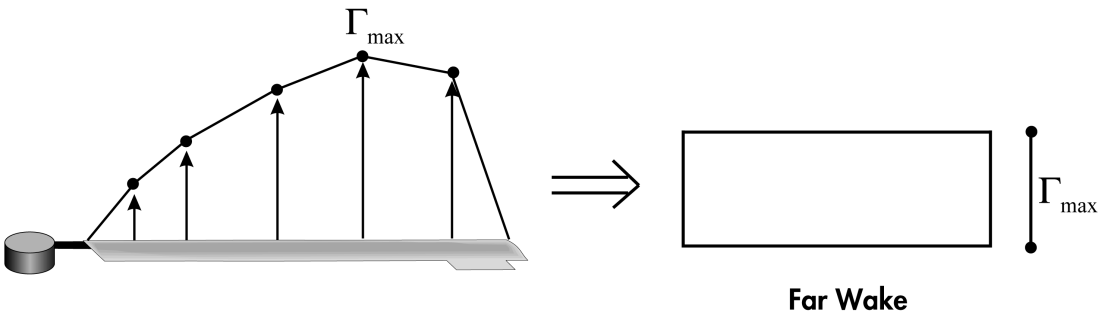

Figure 4.4: Single peak circulation distribution model and the resulting far wake approximation

Therefore, a strong concentrated tip vortex is generated. The vorticity in the tip vortex is distributed over a small but finite region, called the vortex core. The selection of a suitable value for the strength of the tip vortex is a delicate issue in wake modeling. Two models are available, depending on the spanwise distribution of the bound circulation. For helicopters in low speed forward flight, the bound circulation is positive along the entire span of the blade (Fig. 4.4). This is the single peak case. In the single peak model, the maximum value of the bound circulation over the blade span, $\Gamma_{\max}$, is selected for the tip vortex strength. For helicopters in high speed forward flight or under some means of active control, a spanwise circulation distribution with two peaks of opposite sign can be encountered. A large positive peak is generally located inboard and a smaller negative peak on the outboard section of blade (Fig. 4.5). The dual peak model is aimed at representing such a situation. The inboard and outboard peaks Γ_I and Γ_O, respectively, are identified, and the tip vortex strength assumes the value of the outboard peak.

Given the blade displacements and circulation distribution, the wake geometry is calculated. Once the wake geometry has been determined, the procedure calculates the influence

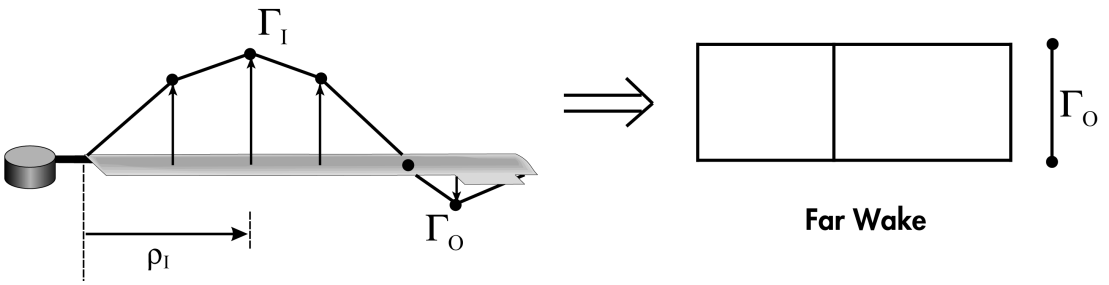

Figure 4.5: CAMRAD/JA dual peak model and the resulting far wake approximation

coefficients, which are stored in the influence coefficient matrix. The induced velocity distribution is obtained by conveniently multiplying the influence coefficient matrix times the circulation distribution:

$$\mathbf{q_I} = \sum_{j=1}^{J} \Gamma_{Oj} \mathbf{C}_{Oj} + \sum_{j=1}^{J} \Gamma_{Ij} \mathbf{C}_{Ij} + \sum_{j=1}^{K_{NW}} \sum_{i=1}^{M} \Gamma_{ij} \mathbf{C}_{NWij}, \tag{4.47}$$

where $\Gamma_{I_j}, \Gamma_{O_j}$ are the inboard and outboard peaks, respectively, at the azimuth j; J, M are the numbers of azimuth and spanwise stations, respectively, at which the induced velocity needs to be calculated; K_{NW} is the number of azimuth stations on which the near wake extends; $\mathbf{C}_{O_j}, \mathbf{C}_{I_j}$ and $\mathbf{C}_{NW_{ij}}$ represent the influence coefficient matrices which are based on the Biot-Savart law. For the single peak model, $\Gamma_{O_j} = \Gamma_{\max j}$ and $\Gamma_{I_j} = 0$.

4.3.3 Wake Modeling Improvements

As mentioned earlier, the fidelity of the wake model dictates the accuracy of BVI noise prediction. Therefore, a number of improvements have been made to the CAMRAD/JA wake model by Patt, Liu, and Friedmann [95, 116, 119] in order to obtain better correlation with the HART experimental data [148].

Wake Resolution

For accurate prediction of BVI noise, a 5° or finer azimuthal wake resolution is required, as compared to the much coarser 15° resolution that is often adequate for vibration reduction studies. The original CAMRAD/JA wake code which the present study is based on has a upper limit of 15° for the free wake analysis, probably due to the concerns about computer power at the time when the code was developed. This restriction was removed in the current wake code to allow for wake resolution of up to 2°. However, due to some numerical difficulties [136] the free wake model failed to converge for the resolutions higher than 3° and therefore the smallest resolution in the computation carried out in this study was 5° of azimuth, which proved to be adequate for prediction of BVI noise compared to the HART data [95, 116, 119].

Dual Vortex Roll-up

The free wake model taken from CAMRAD/JA was predicated on the assumption that the inboard vortices cannot roll up, such that either a vortex-sheet or an equivalent vortex-line model could be used to model the inboard vortices. This was not compatible with HART test data where significant increases in BVI noise levels for the "minimum vibration" case have been attributed to a dual vortex structure [147].

A dual vortex model was therefore incorporated by including a possible second inboard vortex line. This feature of the wake model becomes active only when the tip loading becomes negative, as shown in Fig. 4.6. The release point of this second vortex line is taken to be at the radial location r_I, where blade bound circulation becomes negative, and the

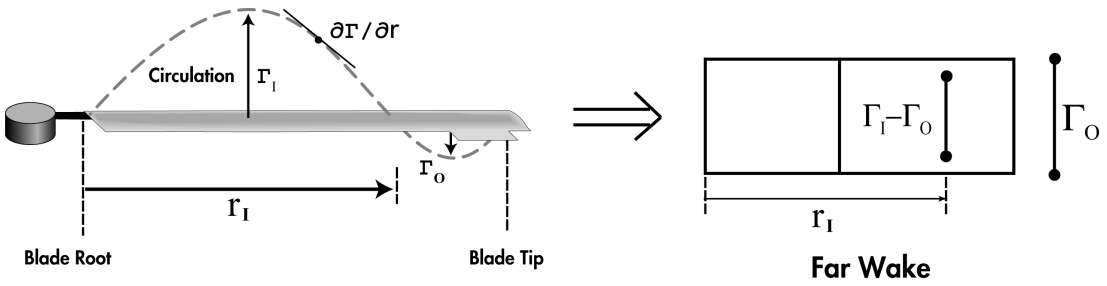

Figure 4.6: Improved dual peak model, leading to dual concentrated vortex lines

strength of this vortex is assumed to be $\Gamma_I - \Gamma_O$, where Γ_O, the outboard circulation peak, is negative. Furthermore, the free wake distortion computation routine was also modified to include the deformation of this second inboard vortex line, including its interaction with the outer tip vortices. This was realized by evaluating the self-induced velocities by both tip vortices and secondary vortices. Moreover, a threshold criteria, suggested in Ref. 124, can be employed to determine whether to have inboard vortex line rolled up. This is accomplished by requiring the radial gradient of the bound circulation $\partial\Gamma/\partial r$ at the inboard vortex release point r_I be greater than a specified threshold value that allows for roll-up of the inboard vortex. This represents the physical requirement that the shear in the wake be sufficiently strong so as to form a fully rolled-up, concentrated vortex.

4.4 Reverse Flow Model

In forward flight, there exists a reverse flow region on the retreating side of the rotor disk where the airflow encountered by the blade is flowing from the trailing edge to the leading edge. The boundary of this region on the blade span as a function of azimuth ψ and

advance ratio μ is given by

$$x_{rev}(\psi) = -(e_1 + \mu R \sin\psi). \tag{4.48}$$

This is illustrated schematically in Fig. 4.7. In the present analysis, it is assumed that the aerodynamic lift and moment are zero within the reverse flow region, and that the aerodynamic drag changes direction inside the reverse flow region, remaining parallel to the total air velocity. This is accomplished by multiplying the aerodynamic lift and moment expressions by the reverse flow parameter R_{LM}, and the drag expression by the reverse flow parameter R_D. These parameters are defined as follows:

$$R_{LM} = \begin{cases} 0 & for \quad 0 \leq x \leq x_{rev}(\psi) \\ 1 & for \quad x > x_{rev}(\psi) \end{cases}$$

$$R_D = \begin{cases} -1 & for \quad 0 \leq x \leq x_{rev}(\psi) \\ 1 & for \quad x > x_{rev}(\psi) \end{cases}$$

4.5 Sectional Airloads

Final expressions for the sectional airloads are obtained by combining the RFA aerodynamic model, the ONERA dynamic stall model, and the reverse flow model. For non-

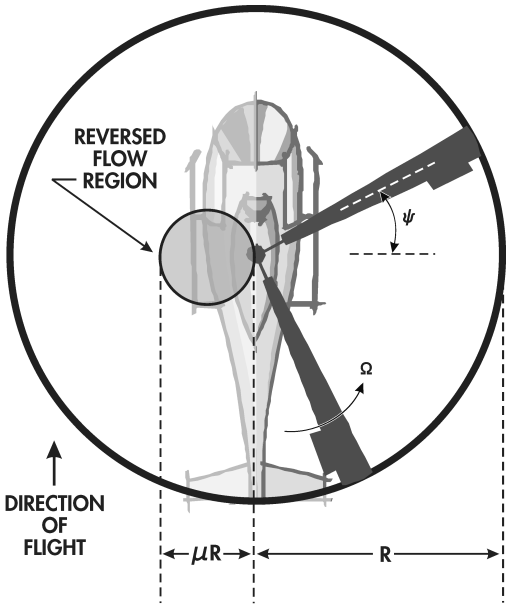

Figure 4.7: Reverse flow region

flapped sections, the sectional lift, moment, and drag are given by

$$L = \rho U^2 b \left(C_{L_A} + C_{L_S}\right) R_{LM}, \tag{4.49}$$

$$M = 2\rho U^2 b^2 \left(C_{M_A} + C_{M_S}\right) R_{LM}, \tag{4.50}$$

$$D = \rho U^2 b \left(C_{d0} + C_{D_S}\right) R_D. \tag{4.51}$$

where C_{L_A} and C_{M_A} are obtained from Eq. 4.29, C_{L_S}, C_{M_S}, and C_{D_S} are based on Eqs. 4.35, 4.36, and 4.37 respectively.

For flapped sections,

$$L = \rho U^2 b C_{L_A} R_{LM}, \tag{4.52}$$

$$M = 2\rho U^2 b^2 C_{M_A} R_{LM}, \tag{4.53}$$

$$D = \rho U^2 b C_{d0} R_D. \tag{4.54}$$

Flapped sections have an additional expression for the hinge moment given by

$$H_m = 2\rho U^2 b^2 C_{Hm}, \tag{4.55}$$

In addition, the following simple linear model is used to account for the effect of flap deflection on profile drag [30, 31]:

$$C_{d0} = 0.01 + 0.001\,|\delta_f| \tag{4.56}$$

To incorporate the aerodynamic model into the present analysis, the generalized airfoil and flap motions W_0, W_1, D_0, and D_1, the freestream velocity U, and angle of attack α need to be expressed in terms of the blade degrees of freedom and model parameters.

Recall that the generalized airfoil and flap motions are given by

$$W_0 = U\alpha + \dot{h}, \tag{4.57}$$

$$W_1 = b\dot{\alpha}. \tag{4.58}$$

$$D_0 = U\delta_f, \tag{4.59}$$

$$D_1 = b\dot{\delta}_f. \tag{4.60}$$

In helicopter applications, α, U, and $\dot{h}$ are interpreted in the following manner:

$$\alpha = \theta_G + \phi, \tag{4.61}$$

$$U = U_T, \tag{4.62}$$

$$-\dot{h} = U_P, \tag{4.63}$$

where θ_G is the geometric pitch angle composed of the control input and blade pretwist at the particular station, and U_T and U_P correspond to the components of freestream velocity approximately tangent and perpendicular to the hub plane, as illustrated in Fig. 4.8.

4.5.1 Blade Velocity Relative to Air

U_T and U_P can be expressed by (see Fig. 4.8)

$$U_T = U'_\eta \cos\theta - U'_\zeta \sin\theta \tag{4.64a}$$

$$U_P = U'_\eta \sin\theta + U'_\zeta \cos\theta \tag{4.64b}$$

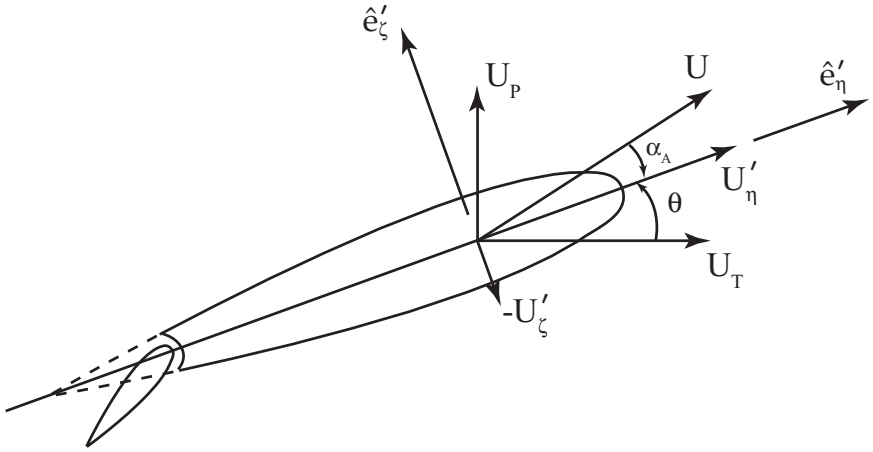

Figure 4.8: Schematic showing orientation of tangential and perpendicular air velocities

The velocity vector of a point on the elastic axis of the blade relative to air is

$$\mathbf{U} = \mathbf{V_{EA}} - \mathbf{V_A} = U'_x\hat{e}'_x + U'_\eta\hat{e}'_\eta + U'_\zeta\hat{e}'_\zeta \tag{4.65}$$

where $\mathbf{V_{EA}}$ is the velocity vector of a point on the elastic axis of the blade and $\mathbf{V_A}$ is the velocity vector of air due to forward flight and inflow. $\mathbf{V_{EA}}$ is given as [28]

$$\mathbf{V_{EA}} = V_x^{EA}\hat{e}_x + V_y^{EA}\hat{e}_y + V_z^{EA}\hat{e}_z \tag{4.66}$$

where

$$\begin{Bmatrix} V_x^{EA} \\ V_y^{EA} \\ V_z^{EA} \end{Bmatrix} = \begin{Bmatrix} \dot{u} + \Omega_y(h_z + w) - \Omega_z(h_y + v) + V_{bx} \\ \dot{v} + \Omega_z(h_x + x + u) - \Omega_x(h_z + w) + V_{by} \\ \dot{w} + \Omega_x(h_y + v) - \Omega_y(h_x + x + u) + V_{bz} \end{Bmatrix} \tag{4.67}$$

The velocity vector due to forward flight and inflow, $\mathbf{V_A}$, is

$$\mathbf{V_A} = \Omega R[\mu \cos\psi \hat{\mathbf{i}}_r - \mu \sin\psi \hat{\mathbf{j}}_r + \lambda_x(\psi, r)\hat{\mathbf{i}}_r + \lambda_y(\psi, r)\hat{\mathbf{j}}_r + \lambda_z(\psi, r)\hat{\mathbf{k}}_r] \tag{4.68}$$

where $\lambda_x(\psi, r), \lambda_y(\psi, r), \lambda_z(\psi, r)$ are the components of the induced velocity vector $\lambda(\psi, r)$ obtained from the wake analysis.

$\mathbf{V_A}$ can be expressed in the undeformed element coordinate system $(\hat{e}_x, \hat{e}_y, \hat{e}_z)$ using the following transformation

$$\begin{Bmatrix} V_x^A \\ V_y^A \\ V_z^A \end{Bmatrix} = \Omega R[T_{eb}][T_{br}] \begin{Bmatrix} \mu \cos\psi + \lambda_x(\psi, r) \\ -\mu \sin\psi + \lambda_y(\psi, r) \\ \lambda_z(\psi, r) \end{Bmatrix} \tag{4.69}$$

Combining Eqs. 4.65, 4.66 and 4.68, U'_η and U'_ζ can be obtained

$$\begin{Bmatrix} U'_x \\ U'_\eta \\ U'_\zeta \end{Bmatrix} = [T_{de}] \begin{Bmatrix} V_x^{EA} - V_x^A \\ V_y^{EA} - V_y^A \\ V_z^{EA} - V_z^A \end{Bmatrix} \tag{4.70}$$

Subsequently U_T and U_P can be obtained from Eq. 4.64.

4.5.2 Distributed Aerodynamic Loads

Lift is assumed to act normal to the total air velocity, and drag is assumed to act parallel to it, as illustrated in Fig. 4.8. The distributed aerodynamic loads are given in the deformed

curvilinear coordinate system $(\hat{e}'_x, \hat{e}'_\eta, \hat{e}'_\zeta)$ by

$$\mathbf{p_A} = p'_\eta \hat{e}'_\eta + p'_\zeta \hat{e}'_\zeta \tag{4.71}$$

$$\mathbf{q_A} = q'_x \hat{e}'_x \tag{4.72}$$

where

$$p'_\eta = L \sin \alpha_A - D \cos \alpha_A \tag{4.73}$$

$$p'_\zeta = L \cos \alpha_A + D \sin \alpha_A \tag{4.74}$$

$$q'_x = M \tag{4.75}$$

The blade local angle of attack α_A is given by

$$\alpha_A = -\tan^{-1}\left(\frac{U'_\zeta}{U'_\eta}\right) \tag{4.76}$$

The distributed aerodynamic loads can then be transformed to the undeformed element coordinate system $(\hat{e}_x, \hat{e}_y, \hat{e}_z)$

$$\mathbf{p_A} = p_x \hat{e}_x + p_y \hat{e}_y + p_z \hat{e}_z \tag{4.77}$$

$$\mathbf{q_A} = q_x \hat{e}_x + q_y \hat{e}_y + q_z \hat{e}_z \tag{4.78}$$

where

$$\begin{Bmatrix} p_x \\ p_y \\ p_z \end{Bmatrix} = [T_{de}]^T \begin{Bmatrix} 0 \\ p'_\eta \\ p'_\zeta \end{Bmatrix} \tag{4.79}$$

$$\begin{Bmatrix} q_x \\ q_y \\ q_z \end{Bmatrix} = [T_{de}]^T \begin{Bmatrix} q'_x \\ 0 \\ 0 \end{Bmatrix} \tag{4.80}$$

Chapter V

Acoustic Model

The acoustic formulation for several helicopter noise codes as well as the present study is based on the Ffowcs Williams-Hawkings (FW-H) equation [37], which is written in an inhomogeneous wave equation form

$$\frac{1}{c^2}\frac{\partial^2 p'}{\partial t^2} - \nabla^2 p' = \frac{\partial}{\partial t}[\rho_0 v_n |\nabla f| \delta(f) - \frac{\partial}{\partial x_i}[l_i |\nabla f| \sigma(f)] - \frac{\partial^2}{\partial x_i \partial x_j}[T_{ij} H(f)] \qquad (5.1)$$

The FW-H equation is derived by employing the conservation of mass and momentum for the fluid, which is valid for the entire three-dimensional space surrounding a moving body with arbitrary shape and motion. The rotational noise (thickness and loading noise) and BVI noise can be predicted with sufficient accuracy using the FW-H equation and neglecting the quadrupole source term.

5.1 Solution of the FW-H Equation

There exist a number of solutions to the FW-H equation [37], as documented in Ref. 34. One of Farassat's solutions known as Formulation 1A [35] has been implemented in several helicopter noise prediction codes due to its numerical efficiency.

Using Green's function of the wave equation in the unbounded domain $\delta(g)/4\pi r$, where

$$g = \tau - t + r/c \tag{5.2}$$

a retarded time solution to FW-H equation is obtained

$$4\pi p'(\mathbf{x},t) = \frac{1}{c}\frac{\partial}{\partial t}\int_{f=0}\left[\frac{\rho_0 c v_n + l_r}{r(1-M_r)}\right]_{\text{ret}} dS + \int_{f=0}\left[\frac{l_r}{r^2(1-M_r)}\right]_{\text{ret}} dS \tag{5.3}$$

To improve the speed and accuracy of the solution, mathematical manipulations are carried out to move the time derivative inside the first integral of Eq. 5.3 by using the following relation

$$\left.\frac{\partial}{\partial t}\right|_{\mathbf{x}} = \left[\frac{1}{1-M_r}\left.\frac{\partial}{\partial \tau}\right|_{\mathbf{x}}\right]_{\text{ret}} \tag{5.4}$$

this yields Formulation 1A

$$\begin{aligned} 4\pi p'_L(\mathbf{x},t) &= \frac{1}{c}\int_{f=0}\left[\frac{\dot{l}_i \hat{r}_i}{r(1-M_r)^2}\right]_{\text{ret}} dS + \int_{f=0}\left[\frac{l_r - l_i M_i}{r^2(1-M_r)^2}\right]_{\text{ret}} dS \\ &\quad + \frac{1}{c}\int_{f=0}\left[\frac{l_r(r\dot{M}_i\hat{r}_i + cM_r - cM^2)}{r^2(1-M_r)^3}\right]_{\text{ret}} dS \end{aligned} \tag{5.5a}$$

$$4\pi p'_T(\mathbf{x},t) = \int_{f=0}\left[\frac{\rho_0 v_n(r\dot{M}_i\hat{r}_i + cM_r - cM^2)}{r^2(1-M_r)^3}\right]_{\text{ret}} dS \tag{5.5b}$$

$$p'(\mathbf{x},t) = p'_L(\mathbf{x},t) + p'_T(\mathbf{x},t) \tag{5.5c}$$

where p'_L, p'_T, p' denotes the loading noise, thickness noise and overall noise, respectively.

5.2 BVI Noise Prediction

As mentioned in Chapter I, BVI noise dominates the low speed descent flight regime, and is characterized by its impulsiveness and high intensity. The frequency content of BVI noise falls mostly in the mid-frequency range, which is most sensitive to human hearing. A widely accepted definition of BVI noise frequency range is the sum of $6^{\text{th}} - 40^{\text{th}}$ harmonics of blade passage frequency [147].

Blade-vortex interaction noise is generated by unsteady pressure fluctuations on the blade induced by interaction with trailed vortices. More specifically, it originates primarily from the dipole or loading source term p'_L in Eq. 5.5. Because of its impulsiveness, the prediction of BVI noise requires high fidelity blade surface pressure, with a typical resolution of less than 5° in azimuth. The pressure distribution, both chordwise and spanwise, is provided by the aeroelastic calculation described in Chapter IV.

5.3 Modified WOPWOP Code

The present study is based on an extensively modified version of the helicopter aeroacoustic code WOPWOP [9] developed at NASA Langley and combines it with the previously described aeroelastic analysis code. The WOPWOP code implements Farassat's Formulation 1A(Eq. 5.5), and has been extensively validated [10, 12] for helicopter noise predictions.

The original version of WOPWOP requires blade harmonics and surface loading as input, which can be provided by either experiments or a suitable helicopter analysis code.

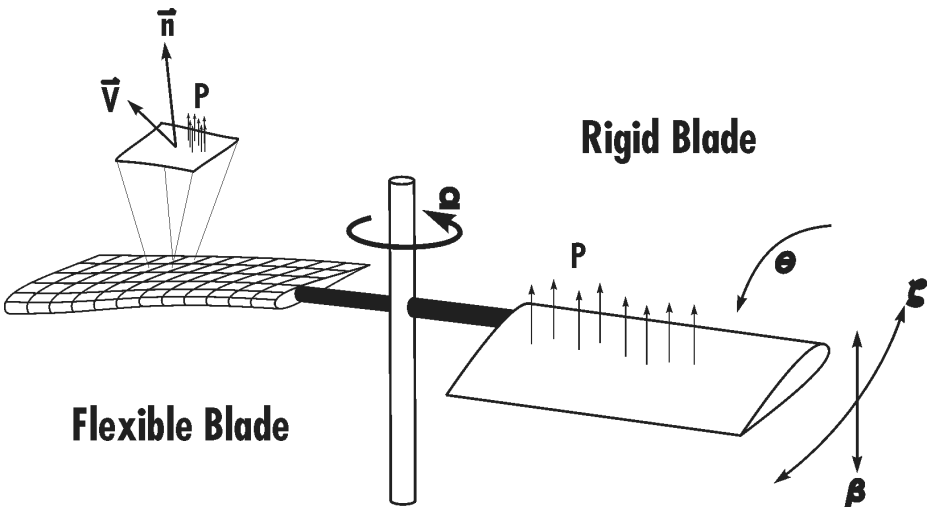

Figure 5.1: Rigid and flexible blade representations

A simple blade model based on the assumption of an offset hinged rigid blade has been used in the original WOPWOP code to generate the acoustic results. However, this simplified model is incompatible with the more realistic elastic blade described in Chapter III. In order to take into account the effects of blade flexibility, the blade dynamics in WOPWOP were replaced by the fully flexible blade model with partial span trailing edge flaps [116, 119]. This was accomplished by discretizing the blade into a number of individual panels as shown in Fig. 5.1. The acoustic code then calculates the contribution from each panel, each having its own velocity, normal vector and pressure distribution. The time domain response of each of these panels was obtained from the aeroelastic response analysis. This information, together with the unsteady pressure distribution on the panel, serves as the basis of the acoustic computations. Unlike some computational studies performed with WOPWOP [8], a surface pressure distribution is used in the acoustic calculation, such that no reduction to a chordwise compact loading is made. Tail rotor or engine noise was not considered in this study. Furthermore, aerodynamic effects of the fuselage have been

excluded, and thus the acoustic results represent the noise generated by the main rotor only. The combined aeroelastic/aeroacoustic solution methodology will be explained in Chap. VI.

Chapter VI

Solution Procedure

The chapter provides a description of the combined aeroelastic and acoustic solution procedure. The finite element discretized aeroelastic equations of motion described in Chap. III are solved using modal reduction based on eight modes, including an axial mode. This procedure has been developed in Ref. 174. Time domain solution of the coupled trim/aeroelastic equations is obtained following the development in Refs. 30 and 108. In the present study, a more general set of trim equations are derived which takes into account descending flight conditions. The acoustics and blade stresses are solved separately after the coupled trim/aeroelastic solution has been determined.

6.1 Free Vibration Analysis

The first step in the solution procedure is the calculation of the natural frequencies and mode shapes of the blade. The coupled equations of motion representing the free vibrations of the rotating blade are a set of nonlinear ordinary differential equations obtained from the finite element discretization described in Chapter III. The computation of the natural frequencies and mode shapes of the blade is based on the linear, undamped equations of motion in vacuum. The equations of motion for the typical element used to model the

straight portion of the blade are:

$$[M_i^F]\ddot{\mathbf{q}}_i + [K_i^F]\mathbf{q}_i = \mathbf{0}, \qquad \text{i=1,...,n-1 .} \tag{6.1}$$

The n-1 equations represented by Eq. 6.1 are then assembled using the standard finite clement assembly procedure. The assembled finite element equations of motion for the free vibrations of the blade are written as

$$[M^F]\ddot{\mathbf{q}}_i + [K^F]\mathbf{q}_i = \mathbf{0} \tag{6.2}$$

In Eqs. 6.1 and 6.2, the superscript F denotes matrices used in the free vibration analysis. The boundary conditions at the blade root for a cantilevered beam are imposed.

6.2 Modal Coordinate Transformation and Assembly Procedure

A preliminary step in the solution of the aeroelastic formulation is the modal coordinate transformation performed on the blade equations so as to reduce the number of degrees of freedom, and to assemble the various element matrices into global system mass, damping, and stiffness matrices as well as the system load vector. For the i-th clement, the modal coordinate transformation has the form:

$$\mathbf{q}_i = [Q_i]\mathbf{y} \tag{6.3}$$

where $\mathbf{y}$ is the vector of generalized modal coordinates, which becomes the new unknowns of the problem and has size N_m which is the number of modes used to perform the modal coordinate transformation. In this study, the following 8 modes are used: the first 3 flap modes, first 2 lead-lag modes, first 2 torsional modes, and the first axial mode.

The assembled stiffness, damping and mass matrices of the blade are obtained by summing the matrices of the individual elements after the modal coordinate transformation has been performed on each of these elements:

$$[K] = \sum_{i=1}^{n-1} [Q_i]^T [K_i][Q_i] \tag{6.4}$$

$$[C] = \sum_{i=1}^{n-1} [Q_i]^T [C_i][Q_i] \tag{6.5}$$

$$[M] = \sum_{i=1}^{n-1} [Q_i]^T [M_i][Q_i] \tag{6.6}$$

and the assembled load vector is given by:

$$\mathbf{F} = \sum_{i=1}^{n-1} [Q_i]^T \mathbf{F}_i \tag{6.7}$$

The effects of swept tips are not included in Eqs. 6.4 – 6.7 since only straight blades were considered in this study. The proper treatment of the local-to-global transformation for the swept tip element is provided in Ref. 174.

The assembled blade equations of motion in the modal space are a set of nonlinear,

coupled, ordinary differential equations written as:

$$[M(\mathbf{y})]\ddot{\mathbf{y}} + [C(\mathbf{y}, \dot{\mathbf{y}})] + [K(\mathbf{y}, \dot{\mathbf{y}}, \ddot{\mathbf{y}})]\mathbf{y} + \mathbf{F}(\mathbf{y}, \dot{\mathbf{y}}, \ddot{\mathbf{y}}) = \mathbf{0} \tag{6.8}$$

6.3 Treatment of the Axial Degree of Freedom

In the treatment of the axial degree of freedom, a *substitution approach* [174] is used to properly account for the centrifugal force and Coriolis coupling effects. In this approach, a new expression for the axial strain at the elastic axis, $\bar{\epsilon}_{xx}$, in terms of the axial inertia force is used to replace all the terms involving $\bar{\epsilon}_{xx}$ in the flap, lag and torsion equations, which is equivalent to the proper representation of the centrifugal force effects in these equations. Both the axial degree of freedom and the axial equation of motion are retained in the aeroelastic calculations. Also, the modal coordinate transformation should include an axial mode in order to properly account for the Coriolis coupling effect.

6.4 Coupled Trim/Aeroelastic Response Solution in Forward Flight

As described in Section 6.2, the assembled equations of motion have a total number of N_m equations to be solved, where N_m is the number of free-vibration natural modes. Additional equilibrium equations involving a set of trim parameters need to be satisfied for the helicopter to maintain steady flight conditions. Propulsive trim is considered in this study. Details on the wind tunnel trim procedure can be found in Ref. 95. These additional propulsive trim equations are solved with the aeroelastic problem in a fully coupled manner,

which is described next.

6.4.1 Time Domain Solution

The equations of motion are numerically integrated in time using a general purpose Adams-Bashforth ordinary differential equation (ODE) solver DE/STEP [137] capable of handling nonlinear system of equations. In order to use this ODE solver, the equations of motion must be cast in first-order state space form.

$$\dot{\mathbf{u}} = \mathbf{F}(\mathbf{u}; t), \tag{6.9}$$

The equations of motion for the elastic blade can be represented by the vector expression

$$\mathbf{f_b}(\mathbf{y}, \dot{\mathbf{y}}, \ddot{\mathbf{y}}, \mathbf{x_a}, \mathbf{q_d}, \mathbf{q_t}; \psi) = 0, \tag{6.10}$$

where $\mathbf{y}$ represents the vector of generalized coordinates, or modal participation; $\mathbf{x_a}$ represents the vector of RFA aerodynamic states, $\mathbf{q_d} = [\Gamma_{l2}\ \Gamma_{m2}\ \Gamma_{d2}]^T$ is a vector of dynamic stall states, and $\mathbf{q_t}$ represents the trim vector.

To convert Eq. (6.10) to first order form, define a mass matrix $\mathbf{M}$ given by

$$\mathbf{M} = \frac{\partial \mathbf{f_b}}{\partial \ddot{\mathbf{y}}}. \tag{6.11}$$

This allows Eq. (6.10) to be decomposed into the form

$$\mathbf{f_b} = \mathbf{g_b}(\mathbf{y}, \dot{\mathbf{y}}, \mathbf{x_a}, \mathbf{q_d}, \mathbf{q_t}; \psi) + \mathbf{M}(\mathbf{y}, \mathbf{q_t}; \psi)\ddot{\mathbf{y}}. \tag{6.12}$$

The values of $\mathbf{M}$ and $\mathbf{g_b}$ are calculated numerically. Solving Eq. (6.12) for $\ddot{\mathbf{y}}$ produces

$$\ddot{\mathbf{y}} = -\mathbf{M}^{-1}\mathbf{g_b}. \tag{6.13}$$

This can be written in first order state-variable form as follows:

$$\dot{\mathbf{y}}_\mathbf{b} = \begin{bmatrix} \mathbf{0} & \mathbf{I} \\ \mathbf{0} & \mathbf{0} \end{bmatrix} \mathbf{y_b} + \begin{Bmatrix} \mathbf{0} \\ -\mathbf{M}^{-1}\mathbf{g_b} \end{Bmatrix}, \tag{6.14}$$

where $\mathbf{y_b}$ is given by

$$\mathbf{y_b} = \begin{Bmatrix} \mathbf{y} \\ \dot{\mathbf{y}} \end{Bmatrix}. \tag{6.15}$$

Next, the attached flow aerodynamic state equations, Eq. 4.28, are provided in the form

$$\dot{\mathbf{x}}_\mathbf{a} = \mathbf{g_a}(\mathbf{y}, \dot{\mathbf{y}}, \ddot{\mathbf{y}}, \mathbf{x_a}, \mathbf{q_t}; \psi). \tag{6.16}$$

The dependence on $\ddot{\mathbf{y}}$ is eliminated by substituting Eq. 6.13 into Eq. 6.16, producing the reduced set of equations

$$\dot{\mathbf{x}}_\mathbf{a} = \mathbf{g_{aR}}(\mathbf{y}, \dot{\mathbf{y}}, \mathbf{x_a}, \mathbf{q_t}; \psi). \tag{6.17}$$

The separated flow governing equations, Eq. 4.33, can be written as

$$\ddot{\mathbf{q}}_\mathbf{d} = \mathbf{g}_\mathbf{d}(\mathbf{y}, \dot{\mathbf{y}}, \ddot{\mathbf{y}}, \mathbf{q}_\mathbf{d}, \ddot{\mathbf{q}}_\mathbf{d}, \mathbf{q}_\mathbf{t}; \psi). \tag{6.18}$$

Using Eq. 6.13 the reduced set of separated flow equations are

$$\ddot{\mathbf{q}}_\mathbf{d} = \mathbf{g}_{\mathbf{dR}}(\mathbf{y}, \dot{\mathbf{y}}, \mathbf{q}_\mathbf{d}, \ddot{\mathbf{q}}_\mathbf{d}, \mathbf{q}_\mathbf{t}; \psi). \tag{6.19}$$

Equation 6.19 can be written as

$$\dot{\mathbf{x}}_\mathbf{d} = \begin{bmatrix} \mathbf{0} & \mathbf{I} \\ \mathbf{0} & \mathbf{0} \end{bmatrix} \mathbf{x}_\mathbf{d} + \begin{Bmatrix} \mathbf{0} \\ \mathbf{g}_{\mathbf{dR}} \end{Bmatrix}, \tag{6.20}$$

where $\mathbf{x_d} = \left[\Gamma_{l2}\ \Gamma_{m2}\ \Gamma_{d2}\ \dot{\Gamma}_{l2}\ \dot{\Gamma}_{m2}\ \dot{\Gamma}_{d2}\right]^T$

Equations 6.14, 6.17, and 6.20 can be arranged into a system of coupled first order state variable equations

$$\begin{Bmatrix} \dot{\mathbf{y}} \\ \ddot{\mathbf{y}} \\ \dot{\mathbf{x}}_\mathbf{a} \\ \dot{\mathbf{q}}_\mathbf{d} \\ \ddot{\mathbf{q}}_\mathbf{d} \end{Bmatrix} = \begin{bmatrix} \mathbf{0} & \mathbf{I} & \mathbf{0} & \mathbf{0} & \mathbf{0} \\ \mathbf{0} & \mathbf{0} & \mathbf{0} & \mathbf{0} & \mathbf{0} \\ \mathbf{0} & \mathbf{0} & \mathbf{0} & \mathbf{0} & \mathbf{0} \\ \mathbf{0} & \mathbf{0} & \mathbf{0} & \mathbf{0} & \mathbf{I} \\ \mathbf{0} & \mathbf{0} & \mathbf{0} & \mathbf{0} & \mathbf{0} \end{bmatrix} \begin{Bmatrix} \mathbf{y} \\ \dot{\mathbf{y}} \\ \mathbf{x}_\mathbf{a} \\ \mathbf{q}_\mathbf{d} \\ \dot{\mathbf{q}}_\mathbf{d} \end{Bmatrix} + \begin{bmatrix} \mathbf{0} \\ -\mathbf{M}_\mathbf{b}^{-\mathbf{1}}\mathbf{g}_\mathbf{b} \\ \mathbf{g}_{\mathbf{aR}} \\ \mathbf{0} \\ \mathbf{g}_{\mathbf{dR}} \end{bmatrix}, \tag{6.21}$$

which can be numerically integrated in time from a given set of initial conditions and trim variables $\mathbf{q_t}$ using the ODE solver DE/STEP.

6.4.2 Rotor Hub Loads and Vibratory Loads

The resultant force and moment at the root of the blades are found by integrating the distributed inertial and aerodynamic loads [174] over the entire blade span in the rotating frame, then transforming these loads to the hub-fixed nonrotating system, and summing the contributions from each blade.

The resultant blade root loads for the k-th blade can be expressed in the $(\hat{\mathbf{i}}_r, \hat{\mathbf{j}}_r, \hat{\mathbf{k}}_r)$ system

$$\mathbf{F_{Rk}}(\psi_k) = F_{Rkx}(\psi_k)\hat{\mathbf{i}}_r + F_{Rky}(\psi_k)\hat{\mathbf{j}}_r + F_{Rkz}(\psi_k)\hat{\mathbf{k}}_r \tag{6.22}$$

$$\mathbf{M_{Rk}}(\psi_k) = M_{Rkx}(\psi_k)\hat{\mathbf{i}}_r + M_{Rky}(\psi_k)\hat{\mathbf{j}}_r + M_{Rkz}(\psi_k)\hat{\mathbf{k}}_r \tag{6.23}$$

where

$$\psi_k = \psi + \frac{2\pi(k-1)}{N_b}. \tag{6.24}$$

is the azimuth of the k-th blade for an N_b-bladed rotor.

Transforming $\mathbf{F_{Rk}}$ and $\mathbf{F_{Rk}}$ to the nonrotating, hub-fixed system $(\hat{\mathbf{i}}_{nr}, \hat{\mathbf{j}}_{nr}, \hat{\mathbf{k}}_{nr})$ and summing the contributions due to each blade, yields

$$\mathbf{F_H}(\psi) = F_{HX}(\psi)\hat{\mathbf{i}}_{nr} + F_{HY}(\psi)\hat{\mathbf{j}}_{nr} + F_{HZ}(\psi)\hat{\mathbf{k}}_{nr} \tag{6.25}$$

$$\mathbf{M_H}(\psi) = M_{HX}(\psi)\hat{\mathbf{i}}_{nr} + M_{HY}(\psi)\hat{\mathbf{j}}_{nr} + M_{HZ}(\psi)\hat{\mathbf{k}}_{nr} \tag{6.26}$$

In an N_b-bladed helicopter, N_b/rev is the dominant harmonic of vibratory loads transferred to the hub. Other harmonics of vibratory loads are also present, but these are of lesser

importance and are not considered in the active reduction problems addressed in this study. The quantities $\mathbf{F_{N_bcH}}$, $\mathbf{F_{N_bsH}}$, $\mathbf{F_{N_bcH}}$, and $\mathbf{F_{N_bsH}}$ represent the $\sin$ and $\cos$ components of the N_b/rev hub shears and moments, and are found using

$$\mathbf{F_{N_bcH}} = \frac{1}{\pi}\int_0^{2\pi} \mathbf{F_H}(\psi)\cos N_b\psi d\psi, \tag{6.27}$$

$$\mathbf{F_{N_bsH}} = \frac{1}{\pi}\int_0^{2\pi} \mathbf{F_H}(\psi)\sin N_b\psi d\psi, \tag{6.28}$$

$$\mathbf{M_{N_bcH}} = \frac{1}{\pi}\int_0^{2\pi} \mathbf{M_H}(\psi)\cos N_b\psi d\psi, \tag{6.29}$$

$$\mathbf{M_{N_bsH}} = \frac{1}{\pi}\int_0^{2\pi} \mathbf{M_H}(\psi)\sin N_b\psi d\psi. \tag{6.30}$$

The magnitude of the N_b/rev hub shear and moment components are given by

$$F_{N_b X} = \sqrt{\left(F_{N_b c XH}\right)^2 + \left(F_{N_b s XH}\right)^2} \tag{6.31}$$

$$F_{N_b Y} = \sqrt{\left(F_{N_b c YH}\right)^2 + \left(F_{N_b s YH}\right)^2} \tag{6.32}$$

$$F_{N_b Z} = \sqrt{\left(F_{N_b c ZH}\right)^2 + \left(F_{N_b s ZH}\right)^2} \tag{6.33}$$

$$M_{N_b X} = \sqrt{\left(M_{N_b c XH}\right)^2 + \left(M_{N_b s XH}\right)^2} \tag{6.34}$$

$$M_{N_b Y} = \sqrt{\left(M_{N_b c YH}\right)^2 + \left(M_{N_b s YH}\right)^2} \tag{6.35}$$

$$M_{N_b Z} = \sqrt{\left(M_{M_b c ZH}\right)^2 + \left(M_{N_b s ZH}\right)^2}. \tag{6.36}$$

The "H" subscripts on the resultants have been dropped for convenience.

6.4.3 Trim Equilibrium Equations

When enforcing the equilibrium at the rotor hub, the constant parts of the hub forces and moments are needed. Therefore the equilibrium at the hub results in a set of trim equations that is fully coupled with aeroelastic response solutions through the averaged hub forces and moments terms. The trim solution involves the calculation of parameters such as pilot control inputs (collective and cyclic pitch) and helicopter overall orientation (rotor angle of attack and roll angle).

The propulsive trim formulation is based on the procedure described in Ref. 28, which enforces six equilibrium equations of the helicopter in steady level flight, including three force and three moment equations. A simple tail rotor model has been included which affects the pitching and yawing moment equilibrium. In this study, the trim procedure was modified so that it can account for descending flight conditions, since BVI is most intensive during descent. The trim equations need to be solved in terms of six trim variables, represented by the vector $\mathbf{q_t}$

$$\mathbf{q_t} = \{\alpha_R, \theta_{\text{coll}}, \theta_{1c}, \theta_{1s}, \theta_{0t}, \phi_R\}^T, \tag{6.37}$$

The equilibrium equations are formulated in the nonrotating, hub-fixed system, as shown schematically in Fig. 6.1. Note the flight path angle θ_{FP} is defined positive for descending flight, as shown in the figure. The drag D_f is assumed to act parallel to the flight path. When $\theta_{\text{FP}} = 0$, we recover the set of equations given in Ref. 28 for level flight.

The trim equations are:

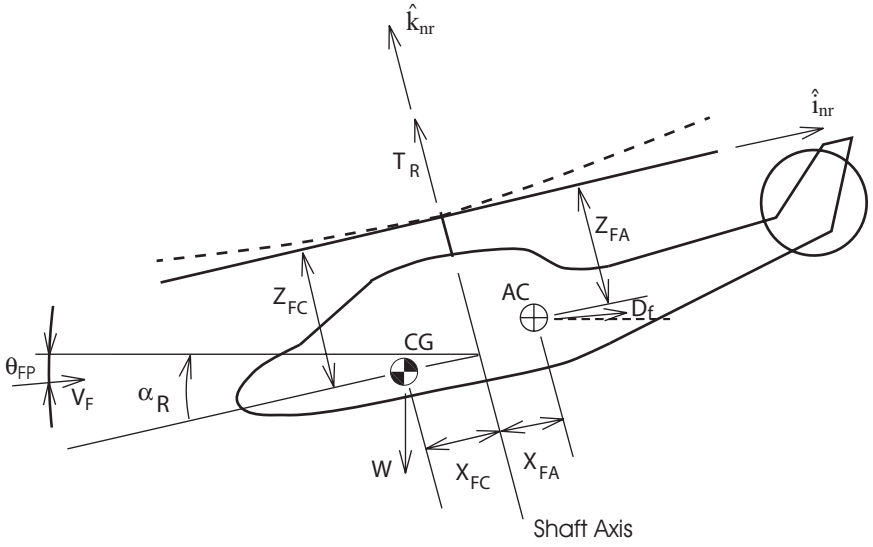

Figure 6.1: Schematic of helicopter used for trim analysis

Pitching Moment

Equilibrium about the $\hat{\mathbf{j}}_{nr}$ axis requires:

$$\overline{M}^{pt} + W_{_H}[-X_{FC}\cos\phi_R\cos\alpha_R + Z_{FC}\cos\phi_R\sin\alpha_R]$$

$$-D_f[-X_{FA}\sin(\alpha_R - \theta_{\rm FP}) + Z_{FA}\cos(\alpha_R - \theta_{\rm FP})] - Q_t \;=\; 0. \qquad (6.38a)$$

Rolling Moment

Equilibrium about the $\hat{\mathbf{i}}_{nr}$ axis requires:

$$\overline{M}^{rl} - Z_{FC}W_{_H}\sin\phi_R + T_t Z_t = 0. \qquad (6.38b)$$

where T_t is the tail rotor thrust and Z_t is the vertical distance between the hub axis and the center of the tail rotor.

Yawing Moment

Equilibrium about the $\hat{\mathbf{k}}_{nr}$ axis requires:

$$\overline{M}^{yw} - X_{FC} W_{_H} \sin\phi_R + T_t X_t = 0. \tag{6.38c}$$

where X_t is the horizontal distance between the hub axis and the center of the tail rotor.

Vertical Force

Equilibrium about the $\hat{\mathbf{k}}_{nr}$ axis requires:

$$\overline{F_T} - W_{_H} \cos\alpha_R \cos\phi_R - D_f \sin(\alpha_R - \theta_{\mathrm{FP}}) = 0. \tag{6.38d}$$

Longitudinal Force

Equilibrium about the $\hat{\mathbf{i}}_{nr}$ axis requires:

$$\overline{H} - W_{_H} \sin\alpha_R \cos\phi_R + D_f \cos(\alpha_R - \theta_{\mathrm{FP}}) = 0. \tag{6.38e}$$

Lateral Force

Equilibrium in the $\hat{\mathbf{j}}_{nr}$ direction requires:

$$\overline{Y} - W_{_H} \sin\alpha_R \cos\phi_R + T_t = 0. \tag{6.38f}$$

Aerodynamic Modifications for Descending Flight

Additional changes in the aerodynamic representation are also required to properly account for descent. The RFA model itself is valid for descending flight, however the velocity U must be redefined. To demonstrate the changes necessary, recall the generalized motions are given by:

$$\mathbf{h} = \left\{ \begin{array}{c} W_0 \\ W_1 \\ D_0 \\ D_1 \end{array} \right\} = \left\{ \begin{array}{c} U\alpha + \dot{h} \\ b\dot{\alpha} \\ U\delta \\ b\dot{\delta} \end{array} \right\}. \tag{6.39}$$

where α, U, and $\dot{h}$ are defined as follows:

$$\begin{aligned} \alpha &= \theta_G + \psi \\ U &= U_T \\ -\dot{h} &= U_P \end{aligned} \tag{6.40}$$

The definition of U_T and U_P is given in Chap. IV and is based on the flight conditions as well as blade dynamics. Recall from Eq. (4.65):

$$\mathbf{U} = \mathbf{V_{EA}} - \mathbf{V_A}, \tag{6.41}$$

The airflow velocity due to blade dynamics, $\mathbf{V_{EA}}$, has the same expression for descending flight, whereas the airflow velocity due to blade rotation, forward flight and inflow, $\mathbf{V_A}$, should be modified for descending flight. In level flight, $\mathbf{V_A}$ can be written in the nonrotating, hub-fixed system:

$$\mathbf{V_A} = \Omega R(\mu \hat{\mathbf{i}}_{\rm nr} - \lambda \hat{\mathbf{k}}_{\rm nr}) \tag{6.42}$$

where the advance ratio μ and inflow ratio λ are given by

$$\mu = \frac{V_F \cos\alpha_R}{\Omega R} \tag{6.43}$$

$$\lambda = \frac{V_F \sin\alpha_R + \nu}{\Omega R} \tag{6.44}$$

For descending flight, these equations must be modified by replacing α_R with $(\alpha_R - \theta_{\rm FP})$. Thus, the modified expressions for advance ratio μ and inflow ratio λ are:

$$\begin{aligned} \mu &= \frac{V_F \cos(\alpha_R - \theta_{\rm FP})}{\Omega R} \\ \lambda &= \frac{V_F \sin(\alpha_R - \theta_{\rm FP}) + \nu}{\Omega R} \end{aligned} \tag{6.45}$$

here ν is the induced inflow velocity. For the free wake analysis, it is replaced by a nonuniform inflow distribution. However, the components due to the velocity of flight $\mathbf{V_A}$ are the same as shown in Eq. (6.45).

The modified $\mathbf{V_A}$ due to descending flight is subsequently employed to obtain the definitions for U_P and U_T, as described in Section 4.5.1, which properly take into account the effects of descending flight. This approach is more general and recovers level flight formulations when flight path angel $\theta_{\mathrm{FP}} = 0$.

6.4.4 Solution of the Trim Equations

The trim equations are solved using an iterative procedure similar to an autopilot. The trim equations, Eqs. 6.38, can be written in the form:

$$\mathbf{f_t}(\mathbf{q_t}) = 0. \tag{6.46}$$

Let $\mathbf{R_{ti}}$ be the vector of trim residuals at the trim condition $\mathbf{q_{t_i}}$ at iteration i:

$$\mathbf{f_t}(\mathbf{q_{t_i}}) = \mathbf{R_{ti}}. \tag{6.47}$$

An iterative optimal control strategy is then used to reduce the value of $\mathbf{R_{ti}}$; based on the minimization of the performance index (see [28], Chap. 6):

$$J = \mathbf{R_{ti}^T R_{ti}}. \tag{6.48}$$

This algorithm resembles a global feedback controller used for vibration reduction. The trim parameters at the i^{th} iteration are then given by:

$$\mathbf{q_{t_i}} = -\mathbf{T_i^{-1}} \mathbf{R_{ti-1}} + \mathbf{q_{t_{i-1}}}, \tag{6.49}$$

where $\mathbf{T_i}$ is a transfer matrix describing the sensitivities of trim residuals to changes in the trim variables:

$$\mathbf{T_i} = \frac{\partial \mathbf{R_{ti}}}{\partial \mathbf{q_t}}. \tag{6.50}$$

$\mathbf{T_i}$ is computed using a finite difference scheme.

6.5 Blade Stresses

After the blade responses are obtained from the coupled trim/aeroelastic response solution, the stresses in the blade at any spanwise location can be recovered by using strain-displacement and constitutive relations. Solving for the stresses in this manner accounts for the complicated loading a blade encounters and is consistent with the structural dynamic model. The procedure for calculating stresses is as follows:

1. For a given azimuth angle, the displacements at any spanwise location are calculated by the aeroelastic response code.

2. The displacements are then substituted into the nonlinear strain-displacement relations giving the strains at any spanwise location.

3. Stresses are calculated by substituting Eq. 3.16 into the stress-strain relations given

by Eq. 3.18.

This calculation provides the blade stresses at any spanwise location and at any azimuth angle.

6.6 Acoustic Solution

The acoustic solution is obtained using the modified WOPWOP code, which needs the blade motions and the surface pressure distribution determined from the aeroelastic analysis as inputs. The theoretical basis for the acoustic calculations is given in Chap. V.

After the acoustic pressure time history at an observer location (such as the noise feedback locations on the helicopter or points on the carpet plane) is obtained, the discrete frequency components of the sound pressure are calculated using Fourier analysis. Blade-vortex interaction noise is then obtained by summing the frequency components of the $6^{th} - 40^{th}$ harmonics of the blade passage frequency (BPF). While BVI noise consists of many harmonics of radiated noise, the $6^{th} - 40^{th}$ harmonics of blade passage are dominant.

6.7 Hover Stability Analysis

In this study, the process for determining the hover stability of the blade is based on an extension of the method described in Ref. 174 which accounts for the RFA aerodynamic states [56]. As described in Ref. 174, the hover stability analysis proceeds as follows:

1. The non-linear static equilibrium solution of the blade is found for a given pitch

setting and uniform inflow, by solving a set of nonlinear algebraic equations. Note that uniform inflow is used only in the hover stability calculation. The forward flight analysis employs a free-wake model for inflow calculation.

2. The governing system of ordinary differential equations are linearized about the static equilibrium solution by writing perturbation equations and neglecting second-order and higher terms in the perturbed quantities. The linearized equations are rewritten in first-order state variable form.

3. The real parts of the eigenvalues of the first-order state variable matrix, $\lambda_k = \zeta_k + i\omega_k$, determine the stability of the system. If $\zeta_k \leq 0$ for all k, the system is stable.

However, in Ref. 174, the blade equations of motion were only a function of the blade response and trim parameters, i.e.,

$$\mathbf{f}_b(\mathbf{y}, \dot{\mathbf{y}}, \ddot{\mathbf{y}}, \mathbf{q_t}) = \mathbf{0} \tag{6.51}$$

where $\mathbf{y}$ is the vector of generalized modal coordinates representing the blade response and $\mathbf{q}_t$ is the vector of trim parameters which are uniform inflow and collective pitch for hover. In contrast, the governing equations in this study are given by Eqs. 6.10 and 6.17, which are functions of blade response *and* the RFA aerodynamic states. Note that the states associated with the dynamic stall model can be neglected for hover analysis. Equations 6.10 and 6.17 represent the coupled set of ordinary differential equations that govern the rotor blade system. Since these equations are coupled, the *combined* system must be linearized.

In the linearization process, perturbing Eq. 6.10 about the static equilibrium and neglecting the dynamic stall states and higher order terms gives

$$\left[\frac{\partial \mathbf{f}_b}{\partial \ddot{\mathbf{y}}}\right]_{\mathbf{q}_0} \Delta\ddot{\mathbf{y}} + \left[\frac{\partial \mathbf{f}_b}{\partial \dot{\mathbf{y}}}\right]_{\mathbf{q}_0} \Delta\dot{\mathbf{y}} + \left[\frac{\partial \mathbf{f}_b}{\partial \mathbf{y}}\right]_{\mathbf{q}_0} \Delta\mathbf{y} + \left[\frac{\partial \mathbf{f}_b}{\partial \mathbf{x}_a}\right]_{\mathbf{q}_0} \Delta\mathbf{x}_a = \mathbf{0} \tag{6.52}$$

where $\mathbf{q}_0$ is the static equilibrium vector and is given by

$$\mathbf{q}_0 = \begin{bmatrix} \mathbf{y}_0 \\ \dot{\mathbf{y}}_0 \\ \dot{\mathbf{x}}_{a0} \end{bmatrix} \tag{6.53}$$

The "0" subscript denotes static equilibrium solution.

From Eq. 6.12,

$$\left[\frac{\partial \mathbf{f}_b}{\partial \dot{\mathbf{y}}}\right]_{\mathbf{q}_0} = \left[\frac{\partial \mathbf{g}_b}{\partial \dot{\mathbf{y}}}\right]_{\mathbf{q}_0} \tag{6.54}$$

$$\left[\frac{\partial \mathbf{f}_b}{\partial \mathbf{y}}\right]_{\mathbf{q}_0} = \left[\frac{\partial \mathbf{g}_b}{\partial \mathbf{y}}\right]_{\mathbf{q}_0} \tag{6.55}$$

$$\left[\frac{\partial \mathbf{f}_b}{\partial \mathbf{x}_a}\right]_{\mathbf{q}_0} = \left[\frac{\partial \mathbf{g}_b}{\partial \mathbf{x}_a}\right]_{\mathbf{q}_0}. \tag{6.56}$$

Substituting Eqs. 6.54 – 6.56 and Eq. 6.11 into Eq. 6.52 gives

$$[\mathbf{M}]_{\mathbf{q}_0} \Delta\ddot{\mathbf{y}} + \left[\frac{\partial \mathbf{g}_b}{\partial \dot{\mathbf{y}}}\right]_{\mathbf{q}_0} \Delta\dot{\mathbf{y}} + \left[\frac{\partial \mathbf{g}_b}{\partial \mathbf{y}}\right]_{\mathbf{q}_0} \Delta\mathbf{y} + \left[\frac{\partial \mathbf{g}_b}{\partial \mathbf{x}_a}\right]_{\mathbf{q}_0} \Delta\mathbf{x}_a = \mathbf{0} \tag{6.57}$$

Solving for $\Delta\ddot{\mathbf{y}}$ yields

$$\Delta\ddot{\mathbf{y}} = -\mathbf{M}^{-1}\left[\frac{\partial \mathbf{g}_b}{\partial \dot{\mathbf{y}}}\right]_{\mathbf{q}_0}\Delta\dot{\mathbf{y}} - \mathbf{M}^{-1}\left[\frac{\partial \mathbf{g}_b}{\partial \mathbf{y}}\right]_{\mathbf{q}_0}\Delta\mathbf{y} - \mathbf{M}^{-1}\left[\frac{\partial \mathbf{g}_b}{\partial \mathbf{x}_a}\right]_{\mathbf{q}_0}\Delta\mathbf{x}_a. \tag{6.58}$$

Similarly, Eq. 6.17 can be linearized, yielding

$$\Delta\dot{\mathbf{x}}_a = \left[\frac{\partial \mathbf{g}_{\mathbf{aR}}}{\partial \dot{\mathbf{y}}}\right]_{\mathbf{q}_0}\Delta\dot{\mathbf{y}} + \left[\frac{\partial \mathbf{g}_{\mathbf{aR}}}{\partial \mathbf{y}}\right]_{\mathbf{q}_0}\Delta\mathbf{y} + \left[\frac{\partial \mathbf{g}_{\mathbf{aR}}}{\partial \mathbf{x}_a}\right]_{\mathbf{q}_0}\Delta\mathbf{x}_a. \tag{6.59}$$

Combining Eqs. 6.58 and 6.59 with the trivial perturbation equation $\Delta\dot{\mathbf{y}} = \Delta\dot{\mathbf{y}}$ into first-order state space form gives

$$\dot{\mathbf{z}} = [\mathbf{A}(\mathbf{q}_0)]\mathbf{z} \tag{6.60}$$

where

$$[\mathbf{A}(\mathbf{q}_0)] = \begin{bmatrix} \mathbf{0} & \mathbf{I} & \mathbf{0} \\ -\mathbf{M}^{-1}\left[\frac{\partial \mathbf{g}_b}{\partial \mathbf{y}}\right]_{\mathbf{q}_0} & -\mathbf{M}^{-1}\left[\frac{\partial \mathbf{g}_b}{\partial \dot{\mathbf{y}}}\right]_{\mathbf{q}_0} & -\mathbf{M}^{-1}\left[\frac{\partial \mathbf{g}_b}{\partial \mathbf{x}_a}\right]_{\mathbf{q}_0} \\ \left[\frac{\partial \mathbf{g}_{\mathbf{aR}}}{\partial \mathbf{y}}\right]_{\mathbf{q}_0} & \left[\frac{\partial \mathbf{g}_{\mathbf{aR}}}{\partial \dot{\mathbf{y}}}\right]_{\mathbf{q}_0} & \left[\frac{\partial \mathbf{g}_{\mathbf{aR}}}{\partial \mathbf{x}_a}\right]_{\mathbf{q}_0} \end{bmatrix} \tag{6.61}$$

and

$$\mathbf{z} \equiv \Delta\mathbf{y} = \begin{bmatrix} \Delta\mathbf{y} \\ \Delta\dot{\mathbf{y}} \\ \Delta\mathbf{x}_a \end{bmatrix} \tag{6.62}$$

As mentioned, the stability of the system is determined by the eigenvalues of $\mathbf{A}$. A comparison of aeroelastic stability results obtained with the approach described above, and those

obtained with the original analysis described in Ref. 174 is provided in Appendix B.

Chapter VII

Active/Passive Optimization

From the review in Chapter I, it is clear that a judicious combination of passive and active methods are necessary for optimum rotor blade design. In this study, the passive approach is based on structural optimization of the rotor blade, and active control is implemented with ACF's. Given the significant computational cost associated with the aeroelastic response computations, and that a global search of the design space is desired, SBO methods are used to facilitate a global search of the design space [55, 56, 59]. Active control is based on the variant of the HHC algorithm described in Ref. 96, 117, and 120. The passive optimization problem formulation, the various SBO approaches employed in this study, the active control algorithm, and the integration of the active and passive approaches into an active/passive optimization framework are described in this chapter.

7.1 Passive Optimization Problem Formulation

The formulation of the blade optimization problem in forward flight consists of several ingredients: the objective function, design variables, and constraints. The mathematical formulation of the optimization is stated as: Find the vector of design variables $\mathbf{D}$ which minimizes the *objective function*, i.e. $J(\mathbf{D}) \rightarrow \min$, subject to appropriate constraints.

7.1.1 Objective Functions

Vibration

The vibration objective function consists of a combination of the N_b/rev oscillatory hub shears and moments. For a four bladed rotor, the vibration objective function is given by

$$J_{_V} = K_S\sqrt{(F_{4X})^2 + (F_{4Y})^2 + (F_{4Z})^2} + K_M\sqrt{(M_{4X})^2 + (M_{4Y})^2 + (M_{4Z})^2} \qquad (7.1)$$

where K_S and K_M are appropriately selected weighting factors, and F_{4X} – M_{4Z} are given by Eqs. 6.31 – 6.36 with $N_b = 4$.

Noise

The noise objective function used in this study is given by [57]

$$J_{_N} = \sum \mathrm{SPL}_i,\ \forall i\ \ \text{such that}\ 20\log\left(\frac{\mathrm{SPL}_i}{P_0}\right) \geq T_{_{NL}} \qquad (7.2)$$

where SPL_i is the sound pressure calculated at the i^{th} grid point on the *carpet plane* depicted in Fig. 7.1, P_0 is a reference pressure, and $T_{_{NL}}$ is a threshold noise level in decibels. The sound pressure levels correspond to the $6^{th} - 40^{th}$ harmonics of the blade passage frequency since they are the most critical harmonics for BVI noise. Thus, the noise objective function represents the sum of all sound pressure levels which correspond to at least $T_{_{NL}}$ dB of noise. Equation 7.2 was formulated to capture the effects of high noise levels, i.e. $\geq T_{_{NL}}$, radiated over the entire far-field, while ensuring that less critical low noise levels

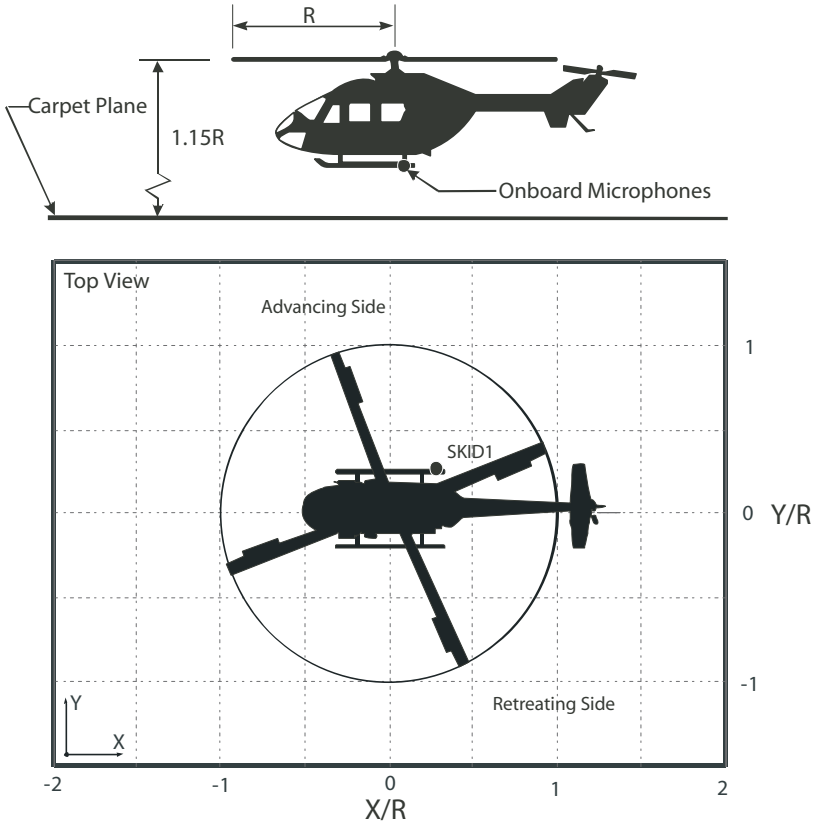

Figure 7.1: Carpet plane

do not dominate the objective function.

Power

The power, or performance, objective function is given by

$$J_P = \frac{\Omega}{2\pi} \int_0^{2\pi} -M_{H_Z}(\psi)\, \mathrm{d}\psi \ , \tag{7.3}$$

where M_{H_Z} is the total yawing moment about the hub. Equation 7.3 represents the instantaneous power required to drive the rotor at a constant angular velocity Ω averaged over one revolution. The effects of unsteadiness, compressibility, dynamic stall (if applicable),

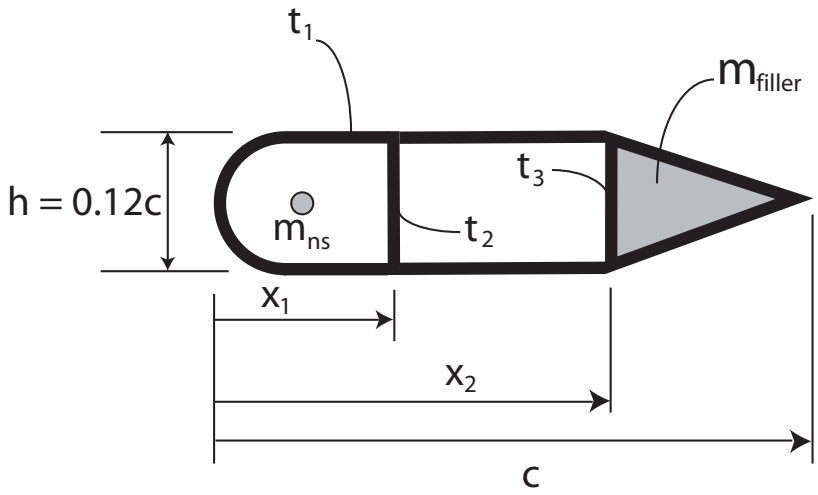

Figure 7.2: Simplified model of the blade's structural member

and the additional drag due to flap deflection are included in the calculation of M_{H_Z}. The engine must provide a torque equal to $-M_{H_Z}$ in order to maintain a constant angular velocity. The relation for J_P is a general expression which is valid for rotor blades with or without ACF's.

7.1.2 Design Variables

The vector of *design variables* $\mathbf{D}$ consists of the thicknesses t_1, t_2, t_3, and the non-structural mass m_{ns} located at the shear center, as shown in Fig. 7.2.

The following design variable configurations were considered in this study:

Configuration 1

The three thickness design variables were defined at the 0%, 25%, 50%, 75%, and 100% stations, while the non-structural mass design variable was defined at the 68% and 100% blade stations, resulting in a total of 17 design variables. These two blade stations

were chosen for the non-structural mass because previous studies have shown that non-structural masses are most effective for vibration reduction when they are distributed over the outboard 1/3 of the blade [45, 93]. The cross-sectional design variables were assumed to vary linearly between stations. The non-structural mass at the elastic axis inboard of the 68% station was set to zero for all configurations.

Configuration 2

The design variables were defined at two nodal locations – the 68% and 100% stations – resulting in a total of 8 design variables. The cross-sectional thicknesses at the root were fixed at baseline values, and the design variables varied linearly between the stations.

Configuration 3

The three thickness design variables were defined as constant within 4 equally sized spanwise sections, while the non-structural mass design variable was defined as constant between the 68% and 100% blade stations. Thus there were a total of 13 design variables in the passive optimization formulation based on Configuration 3.

Configuration 4

Configuration 4 is similar to the previous configuration, except that design variables representing the pretwist at the 50% and 100% stations – θ_1 and θ_2 respectively – are included. The pretwist at the root is fixed at a baseline value θ_0, and the twist is assumed to vary linearly between blade stations. Thus there are a total of 15 structural design variables.

The first configuration, which corresponds to the largest number of design variables, was used to evaluate the accuracy and effectiveness for optimization of the surrogate objective functions in Sections 8.1 and 8.2. In general, the larger the number of design variables, the more difficult it is to accurately approximate a function and to thoroughly search the design space for the optimum. Thus, among the various design variable configurations, Configuration 1 facilitates the most conservative evaluation of the performance of surrogate based optimization techniques. Configuration 2, which corresponds to the fewest design variables, is similar to that employed in Ref. 14 and was selected in order to conduct an initial evaluation of the EGO algorithm in Section 8.3. Configuration 3 represents a more realistic alternative to Configuration 1 since the design variables are assumed to be constant within several equally sized spanwise sections, as opposed to linearly interpolating between spanwise stations. The effectiveness of optimizing the spanwise mass and stiffness distribution for BVI noise reduction is demonstrated in Chapter X using this configuration. Finally, pretwist design variables were added in Configuration 4, which was used to generate the results in Chapter XI, since geometric parameters have been shown to affect the rotor power consumption.

7.1.3 Constraints

The design variables have *side constraints* to prevent them from reaching impractical values; these are stated as

$$\mathbf{D}_j^{(L)} \leq \mathbf{D} \leq \mathbf{D}_j^{(U)}, \qquad j = 1, 2, \ldots, N_{dv}. \tag{7.4}$$

In addition, four types of *behavior constraints*, given by

$$\mathrm{g}_i(\mathbf{D}) \leq 0, \qquad i = 1, 2, \ldots, N_c, \tag{7.5}$$

are placed on the design variables. The first type of behavior constraints are *frequency placement constraints*, which are prescribed upper and lower bounds on the fundamental flap, lag, and torsional frequencies of the blade. The frequency placement constraints on the fundamental flap frequency are written as

$$\mathrm{g}_{\text{flap}}(\mathbf{D}) = \frac{\omega_{F1}}{\omega_U} - 1 \leq 0 \tag{7.6}$$

and

$$\mathrm{g}_{\text{flap}}(\mathbf{D}) = 1 - \frac{\omega_{F1}}{\omega_L} \leq 0 \tag{7.7}$$

where ω_U and ω_L are the prescribed upper and lower bounds on the fundamental flap frequency. Similar constraints are placed on the lag and torsional frequencies, i.e. g_{lag} and $\mathrm{g}_{\text{torsion}}$. In addition, all blade frequencies must differ from integer multiples of the angular velocity – 1/rev, 2/rev, 3/rev, ..., etc. – to avoid undesirable resonances.

Another behavior constraint is an *autorotational constraint*, which ensures that mass redistributions produced during the optimization do not degrade the autorotational properties of the rotor. Several indices can be used to represent the autorotational properties of the blade; the one selected for this study is the requirement that the mass polar moment of

inertia of the rotor be at least 90% of its baseline value [14], which implies:

$$\mathrm{g}(\mathbf{D}) = 1 - \frac{I_P}{0.9 I_{P0}} \leq 0 \tag{7.8}$$

where I_P is the mass polar moment of inertia of the rotor when it is spinning about the shaft, and I_{P0} is the baseline value.

The third type of behavior constraints are *aeroelastic stability margin constraints* that can be stated as:

$$\mathrm{g}_k(\mathbf{D}) = \zeta_k + (\zeta_k)_{\min} \leq 0, \qquad k = 1, 2, \ldots, N_m \tag{7.9}$$

where N_m is the number of normal modes, ζ_k is the real part of the hover eigenvalue for the k^{th} mode, and $(\zeta_k)_{\min}$ is the minimum acceptable damping level for the k_{th} mode. It should be noted that the most critical modes for stability are usually the first and second lag modes.

The final behavior constraint is a *stress constraint* obtained by substituting the blade stresses into Von Mises' criterion, which is expressed mathematically as

$$\frac{2\sigma_{xx}^2 + 6(\sigma_{x\eta}^2 + \sigma_{x\zeta}^2)}{6} - \frac{\sigma_{allowable}^2}{3} \leq 0 \tag{7.10}$$

where σ_{xx}, $\sigma_{x\eta}$, and $\sigma_{x\zeta}$ are the axial and shear stresses, and $\sigma_{allowable}$ is the material yield stress divided by a factor of safety. At discrete values of the azimuth angle, Eq. 7.10 is evaluated at spanwise locations corresponding to the finite element nodes. The maximum

evaluation of Eq. 7.10 is used for the constraint, and is given as

$$\mathrm{g}(\mathbf{D}) = \mathrm{MAX}\left[\frac{2\sigma_{xx}^2 + 6(\sigma_{x\eta}^2 + \sigma_{x\zeta}^2)}{6} - \frac{\sigma_{allowable}^2}{3}\right] \leq 0 \tag{7.11}$$

where $\mathrm{MAX}[\ \ ]$ denotes the maximum value of Eq. 7.10 over each set of azimuth angle and blade stations at which it is evaluated. Therefore the stress constraint is enforced at the blade station and azimuth angle where the stress condition is most critical. The stress margin is given by

$$1 - \frac{\sqrt{\sigma_{xx}^2 + 3(\sigma_{x\eta}^2 + \sigma_{x\zeta}^2)}}{\sigma_{allowable}} \ . \tag{7.12}$$

A stress margin < 0 would correspond to a design which violates the stress constraint.

7.2 Global Sensitivity Analysis

The global sensitivity analysis (GSA), as proposed by Sobol [145], is used to estimate the effect of different design variables on the total variability of the objective function. The variability is a measure of how much the function changes due to changes in the design variables. In Sobol's approach, the significance of a design variable is quantified by calculating the contribution of the variable to the total variance of a function. The higher the variance caused by a variable, the more significant the variable is. The GSA separates the total variability in the objective function into contributions from *main effects*, i.e. variability due to each design variable alone, as well as contributions from interactions between all of the design variables. The advantages of conducting such an analysis include assessment of the importance of design variables and fixing non-essential variables during optimization,

thus reducing the dimensionality of the problem. A brief overview of the GSA is given below.

A function, $p(\mathbf{x})$, of a vector of independent input variables, $\mathbf{x}$ in domain [0, 1], is assumed and modeled as uniformly distributed random variables. The function can be decomposed into the sum of functions of increasing dimensionality given by

$$p(\mathbf{x}) = p_0 + \sum_{i=1}^{N_{dv}} p_i(x_i) + \sum_{1 \le i < j \le N_{dv}}^{N_{dv}} p_{ij}(x_i, x_j) + \ldots + p_{1,2,\ldots,N_{dv}}(x_1, x_2, \ldots, x_{N_{dv}}) \quad (7.13)$$

where

$$p_0 = \int_0^1 p(\mathbf{x})\, d\mathbf{x}\,. \quad (7.14)$$

It was shown in Ref. [145] that by enforcing the condition $\int_0^1 p_{i,\ldots,m}\, dx_k = 0$ for $k = i, \ldots, m$, the decomposition given by Eq. 7.13 is unique and the total variance of $p(\mathbf{x})$, $V(p)$, can be decomposed in a similar fashion:

$$V(p) = \sum_{i=1}^{N_{dv}} V_i + \sum_{1 \le i < j \le N_{dv}}^{N_{dv}} V_{ij} + \ldots + V_{1,2,\ldots,N_{dv}}\,, \quad (7.15)$$

where $V(p) = E[(p - p_0)^2]$, and $E[\ \ ]$ denotes the expected value operator. It can be shown that the partial variances in Eq. 7.15 are given by the following expressions:

$$\begin{aligned} V_i &= V(E[\,p\,|_{\,x_i}\,]) \\ V_{ij} &= V(E[\,p\,|_{\,x_i,x_j}\,]) - V_i - V_j \\ V_{ijk} &= V(E[\,p\,|_{\,x_i,x_j,x_k}\,]) - V_{ij} - V_{ik} - V_{jk} - V_i - V_j - V_k\,, \end{aligned} \quad (7.16)$$

and so on. In this notation, $V(E[\,p\,|_{\,x_i}\,])$ represents the expected value of p given the values of x_i. The contribution of x_i alone to the total variance is accounted for with V_i, while V_{ij}, V_{ijk}, and so on account for the variance due to interactions among x_i and the other design variables. Note that

$$E[\,p\,|_{\,x_i}\,] = \int_0^1 p_{_i}\, dx_i = 0 \tag{7.17}$$

and

$$V(E[\,p\,|_{\,x_i}\,]) = \int_0^1 p_{_i}^2\, dx_i\,. \tag{7.18}$$

The total contribution of the i^{th} design variable to the total variance is given as

$$V_i^{total} = V_{_i} + \sum_{j,j\neq i}^{N_{dv}} V_{_{ij}} + \sum_{j,j\neq i}^{N_{dv}} \sum_{k,k\neq i,j}^{N_{dv}} V_{_{ijk}} + \ldots\,. \tag{7.19}$$

Following Sobol's suggestion to reduce the computational complexity of calculating the global sensitivity of the function with respect to x_i, the set of design variables is divided into two subsets – the first subset contains only x_i, while the second contains all of the remaining design variables and is denoted as B. The total variance due to x_i can now be rewritten as

$$V_i^{total} = V_i + V_{i,B} \tag{7.20}$$

where $V_{i,B}$ is the measure of the variance that is dependent on interactions between x_i and all of the other design variables. The total variance due to the effects from all design variables is calculated from the following relation,

$$V(p) = V_i + V_B + V_{i,B} \tag{7.21}$$

where V_B is the partial variance corresponding to B.

Finally, *sensitivity indices* are calculated in order to quantify the significance of a design variable. For example, the first and second order sensitivity indices are given by

$$S_i = \frac{V_i}{V(p)} \tag{7.22}$$

and

$$S_{ij} = \frac{V_{ij}}{V(p)} \,. \tag{7.23}$$

The first order sensitivity index accounts for the main effects of a design variable. The effects of interactions among design variables are captured by the higher order sensitivity indices. For the i^{th} design variable, the total sensitivity index is given by

$$S_i^{total} = \frac{V_i^{total}}{V(p)} \,. \tag{7.24}$$

The relative significance of each design variable can be obtained by ranking each variable according to its respective total sensitivity index, with the most significant variables corresponding to higher indices.

7.3 Global Approximation Methods

In order to conduct a global search of the design space in a reasonable amount of time, it is necessary to use global approximation, or surrogate methods, in which the "true" objective function and expensive constraints are replaced with continuous functional rela-

tionships that can be evaluated quickly. To construct the surrogates, the objective function and constraints must first be evaluated over a set of design points. The surrogate is then generated by fitting the initial design points. Although function evaluations, which come from the expensive helicopter simulations, are needed to form the approximation, this initial investment of computer time is significantly less compared to global searches using non-surrogate based optimization methods. Once the surrogates have been obtained, they are used to replace the more expensive "true" objective function and constraints in the search for the optimum. As in the case of optimization, the GSA is also based on numerous evaluations of the objective function. Therefore, a surrogate must be used in place of the true objective function in the GSA; i.e. $p(\mathbf{x})$ from Eq. 7.13 is replaced with a surrogate.

The surrogate vibration objective function can be generated in two ways: (a) the vibratory hub shears and moments in Eq. 7.1 are replaced by surrogates which are used to build the surrogate objective function, as in Eq. 7.25, and (b) the overall output, $J_{_V}$, is approximated directly. Six responses need to be approximated in the first approach, and 1 response needs to be approximated in the second approach. Both methods were considered in this study.

$$\hat{J}_{_V} = K_S\sqrt{(\hat{F}_{4X})^2 + (\hat{F}_{4Y})^2 + (\hat{F}_{4Z})^2} + K_M\sqrt{(\hat{M}_{4X})^2 + (\hat{M}_{4Y})^2 + (\hat{M}_{4Z})^2}. \quad (7.25)$$

The surrogate noise and power objective functions are constructed by fitting the overall responses.

The stress constraint is the only constraint which requires a forward flight simulation, and is therefore the only computationally expensive constraint. Consequently, a surrogate

constraint is used in place of Eq. 7.11 during optimization. Descriptions of the methods for constructing the global approximations are given below.

7.3.1 Design of Computer Experiments

When the initial data set is produced by a deterministic computer code (as is the case in the vibration reduction problem), the term "design of computer experiments," is more appropriate than design of experiments [131, 140]. The distinction is necessary because in physical experiments there is measurement error and other random sources of noise that cannot be controlled, which affect the choice of the design point. However, in computer experiments, there is no random error; i.e., for a deterministic computer code, a given input will always yield the same output. Thus, the design of computer experiments need only be *space-filling*. Figure 7.3 illustrates the difference between a conventional design of experiment and a space-filling design. In the figure, locations of design points where experiments are to be conducted, which in this case represent design points where aeroelastic response simulations are performed, are shown for a design space which has two design variables.

A commonly used space-filling design is Latin hypercube sampling (LHS) [100]. In LHS, each design variable is partitioned into N_{sp} equally spaced sections, or strata. Every design variable D_i, where $i = 1, 2, ..., N_{dv}$, is sampled once in each strata, which forms N_{dv} vectors of size N_{sp}. The components of the N_{dv} vectors are then randomly combined to form an $N_{sp} \times N_{dv}$ matrix known as a Latin hypercube, where each row corresponds to a design point at which a computer experiment is performed. A major disadvantage of Latin hypercube sampling is that design points can cluster together due to the random process

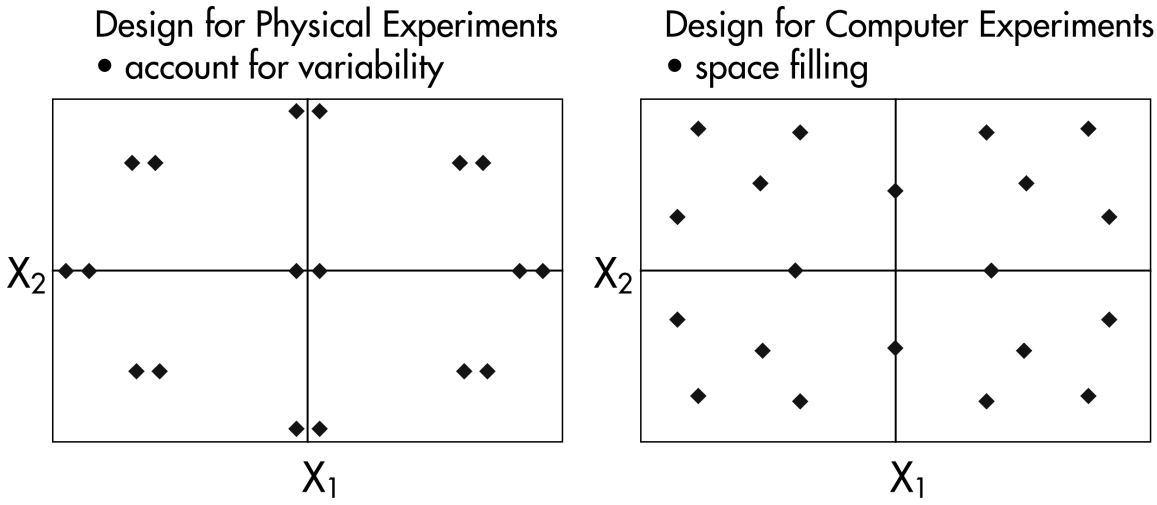

Figure 7.3: Design of physical experiment vs. design of computer experiment

by which design points are created. To prevent this, optimal Latin hypercube (OLH) [123] sampling is used in this study to ensure a more uniform (or space-filling) design of computer experiment. Optimal Latin hypercube sampling creates a more uniform design than conventional LHS by maximizing a spreading criteria, rather than randomly creating design points from the samples. Figure 7.4 illustrates the difference between a conventional Latin hypercube and an optimal Latin hypercube. In this study, the OLH algorithm from the iSIGHT software package was used [73, 85]. The OLH algorithm described in Ref. 73 is initialized with a conventional LH. An optimization algorithm is then employed in order to search over the various combinations of fitting points for the combination which results in the maximum of the minimum distance between any two points. Methods for fitting the data points in the OLH are described next.

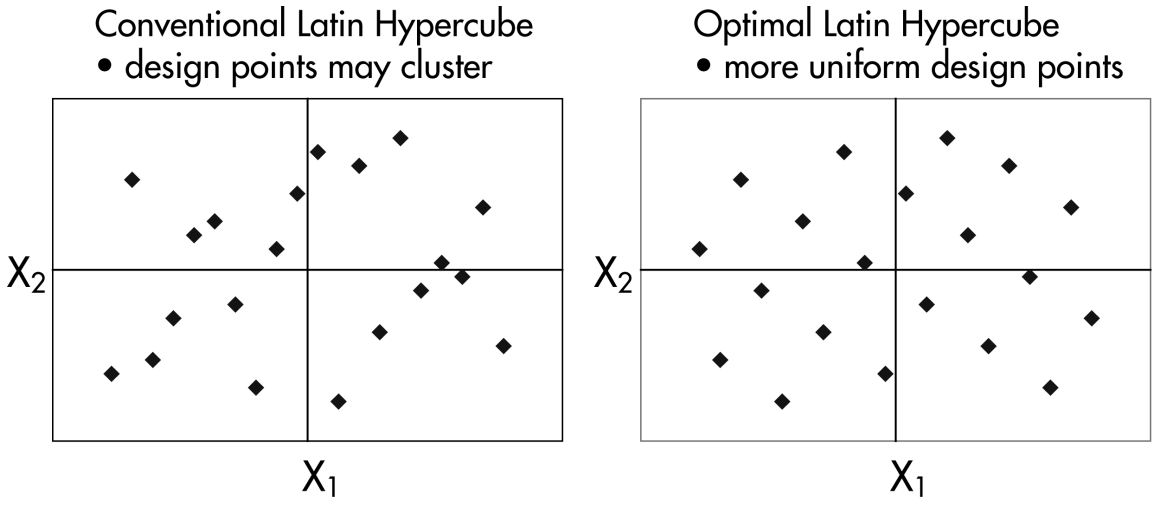

Figure 7.4: Conventional LH vs. Optimal LH in two dimensional design space

7.3.2 Polynomial Response Surfaces

Suppose a deterministic function of N_{dv} design variables needs to be approximated and has been evaluated at N_{sp} sample points. Sample point i is denoted $\mathbf{x}^{(i)} = (x_1^{(i)}, ..., x_{N_{dv}}^{(i)})$ and the associated response is given by $y_i = y(\mathbf{x}^{(i)})$ for $i = 1, ..., N_{sp}$. A polynomial regression approximation to $y(\mathbf{x})$ can be written as

$$y(\mathbf{x}) = \hat{y}(\mathbf{x}) + \epsilon_{\text{pr}} \tag{7.26}$$

where $\hat{y}(\mathbf{x})$ is the function chosen to approximate the true response $y(\mathbf{x})$, and ϵ_{pr} is the error associated with the approximation. It is important to note that the errors are assumed to be independent: i.e. the errors at two points close together will not necessarily be close. This assumption will be revisited when considering kriging. In this study, 2^{nd} order polynomials

are used for $\hat{y}(\mathbf{x})$. The least squares regression approximation is given as [72]

$$\hat{y}_{\text{poly}} = \beta_0 + \sum_{i=1}^{N_{dv}} \beta_i x_i + \sum_{i=1}^{N_{dv}} \sum_{j=1, i<j}^{N_{dv}} \beta_{ij} x_i x_j + \sum_{i=1}^{N_{dv}} \beta_{ii} x_i^2. \tag{7.27}$$

In addition to Eq. 7.27, a reduced term polynomial surrogate in which statistically insignificant terms are removed is considered. The t-statistic corresponding to a coefficient determines whether the coefficient is significantly different than zero, and thus statistically significant. The t-statistic for the coefficient β_{ij} is given by

$$tstat = \frac{\beta_{ij} - 0}{\text{SE}\left(\beta_{ij}\right)}, \tag{7.28}$$

where $\text{SE}\left(\beta_{ij}\right)$ is the standard error for the coefficient [107]. If $\beta_{ij} - 0 < \text{SE}\left(\beta_{ij}\right)$, i.e. a t-statistic less than 1, then the coefficient is not considered to be significantly different than zero. Thus, the reduced term polynomial is obtained by sequentially removing coefficients with t-statistics less than 1 from the full term polynomial.

7.3.3 Kriging

Kriging is based on the fundamental assumption that errors are correlated, which is in contrast to the assumption of independent or uncorrelated errors made in polynomial regression. This implies that one assumes the errors at two points close together will be close. In fact, the assumption that the errors are uncorrelated is only appropriate when the sources of error are random, such as in the case of measurement error or noise. In the case of deterministic computer simulations, there is no source of random error. Therefore, it is

more reasonable to assume that the error terms will be correlated and that this correlation is higher the closer two points are to each other. In kriging, the unknown function $y(\mathbf{x})$ is assumed to be of the form

$$y(\mathbf{x}) = f(\mathbf{x}) + Z(\mathbf{x}) \tag{7.29}$$

where $f(\mathbf{x})$ is an assumed function (usually polynomial form) and $Z(\mathbf{x})$ is a realization of a stochastic (random) process which is assumed to be a Gaussian process with zero mean and variance of σ^2_{var} (i.e. $Z(\mathbf{x})$ follows a normal, or Gaussian, distribution) [82, 132]. The function $f(\mathbf{x})$ can be thought of as a global approximation of $y(\mathbf{x})$, while $Z(\mathbf{x})$ accounts for local deviations which ensure that the kriging model interpolates the data points exactly. The covariance matrix of $Z(\mathbf{x})$, which is a measure of how strongly correlated two points are, is given by

$$\mathrm{Cov}[Z(\mathbf{x}^{(i)}), Z(\mathbf{x}^{(j)})] = \sigma^2_{var}\mathbf{R}_{\mathrm{krg}} \tag{7.30}$$

where each element of the $N_{sp} \times N_{sp}$ correlation matrix $\mathbf{R}_{\mathrm{krg}}$ is given by

$$(R_{\mathrm{krg}})_{ij} = R_{\mathrm{krg}}(\mathbf{x}^{(i)}, \mathbf{x}^{(j)}) \tag{7.31}$$

and $R_{\mathrm{krg}}(\mathbf{x}_i, \mathbf{x}_j)$ is a correlation function which accounts for the effect of each interpolation point on every other interpolation point. This function is called the spatial correlation function (SCF) and is chosen by the user. The most commonly used SCF is the Gaussian correlation function,

$$R_{\mathrm{krg}}(\mathbf{x}^{(i)}, \mathbf{x}^{(j)}) = \exp\left[-\sum_{k=1}^{N_{dv}} \vartheta_k |{x_k}^{(i)} - {x_k}^{(j)}|^{p_k}\right], \tag{7.32}$$

which is also employed in this study. The Gaussian SCF is dependent on the distance between two points. As two points move closer to each other, $|{x_k}^{(i)} - {x_k}^{(j)}| \rightarrow 0$, and Eq. 7.32 approaches unity which is the maximum value of the Gaussian SCF. In other words, the Gaussian SCF recovers the intuitive property that the closer two points are to each other, the greater the correlation between the points.

The fitting parameters ϑ_k and p_k are unknown correlation parameters which need to be determined. In order to determine these parameters, the form of $f(\mathbf{x})$ needs to be chosen.

Constant Trend Function

The most common choice for $f(\mathbf{x})$ is $f(\mathbf{x}) = \boldsymbol{\beta}$ where $\boldsymbol{\beta}$ is a constant. Previous studies have found that modeling with the SCF is so effective, that using a constant for the global behavior results in little loss of fidelity [82,131,132,142]. Another common simplification, is to fix all $p_k = 2$. When this simplification is combined with the constant global approximation, the approximation method is known as *ordinary kriging*. In the present study, kriging models where p_k are not fixed at 2 will be compared with ordinary kriging models.

In order to find ϑ_k and p_k, the generalized least square estimates of $\boldsymbol{\beta}$ and σ^2_{var}, denoted by $\hat{\boldsymbol{\beta}}$ and $\hat{\sigma}^2_{var}$ respectively, are employed [82, 132]:

$$\hat{\boldsymbol{\beta}} = (\mathbf{1}^{\mathrm{T}}(\mathbf{R}_{\mathrm{krg}})^{-1}\mathbf{1})^{-1}\mathbf{1}^{\mathrm{T}}(\mathbf{R}_{\mathrm{krg}})^{-1}\mathbf{y} \tag{7.33}$$

and

$$\hat{\sigma}^2_{var} = \frac{(\mathbf{y} - \mathbf{1}\hat{\boldsymbol{\beta}})^{\mathrm{T}}(\mathbf{R}_{\mathrm{krg}})^{-1}(\mathbf{y} - \mathbf{1}\hat{\boldsymbol{\beta}})}{N_{sp}} \tag{7.34}$$

where $\mathbf{1}$ is a vector populated by ones and $\mathbf{y}$ is a vector of observed function outputs at the interpolation points; both vectors are of length N_{sp}. With $\hat{\sigma}^2_{var}$ and $\hat{\boldsymbol{\beta}}$ known, ϑ_k and p_k are found such that a likelihood function is maximized [82, 132]. The likelihood function, given in Eq. 7.35, is a measure of the probability of the sample data being drawn from a probability density function associated with a Gaussian process. Since the stochastic process associated with kriging has been assumed to be Gaussian, one seeks the set of ϑ_k and p_k that maximize the probability that the interpolation points have been drawn from such a process.

$$-\frac{[N_{sp}\ln(\hat{\sigma}^2_{var}) + \ln|\mathbf{R}_{\text{krg}}|]}{2} \tag{7.35}$$

The maximum likelihood estimates (MLE's) of ϑ_k and p_k represent the "best guesses" [141] of the fitting parameters. Any values of ϑ_k and p_k would result in a surrogate which interpolates the sample points exactly, but the "best" kriging surrogate is found by optimizing the likelihood function. This auxiliary optimization process can result in significant fitting time depending on the size of the system. Due to the optimization process needed to create the kriging surrogate, kriging is only appropriate when the time needed to generate the interpolation points is much larger than the time to interpolate the data – which is the case in the helicopter vibration problem. With all parameters known, the kriging approximation to a function $y(\mathbf{x})$ can be written as [82, 131, 132, 142]

$$\hat{y}_{\text{krg}} = \hat{\boldsymbol{\beta}} + \mathbf{r}_{\text{krg}}(\mathbf{x})^{\text{T}}(\mathbf{R}_{\text{krg}})^{-1}(\mathbf{y} - \mathbf{1}\hat{\boldsymbol{\beta}}) \tag{7.36}$$

where

$$\mathbf{r}_{\mathrm{krg}}(\mathbf{x}) = \left[R_{\mathrm{krg}}(\mathbf{x}, \mathbf{x}^{(1)}), R_{\mathrm{krg}}(\mathbf{x}, \mathbf{x}^{(2)}), ..., R_{\mathrm{krg}}(\mathbf{x}, \mathbf{x}^{(N_{sp})})\right]^{\mathrm{T}} \tag{7.37}$$

The column vector $\mathbf{r}_{\mathrm{krg}}(\mathbf{x})$ of length N_{sp} is the correlation vector between an arbitrary point $\mathbf{x}$ and the interpolation points, $\mathbf{x}^{(1)}$, ... , $\mathbf{x}^{(N_{sp})}$.

Linear Trend Function

In addition to a constant trend function, kriging with a linear polynomial trend was considered; i.e.

$$f(\mathbf{x}) = \mathbf{f_x}^{\mathrm{T}}\boldsymbol{\beta} \tag{7.38}$$

where $\mathbf{f_x}^{\mathrm{T}}$ is a $1 \times N_{basis}$ vector, N_{basis} is the number of basis functions associated with the linear polynomial, and $\boldsymbol{\beta}$ is a $N_{basis} \times 1$ vector of coefficients. Similarly, $\mathbf{F}(\mathbf{x})$ can be defined as an $N_{sp} \times N_{basis}$ matrix where the i^{th} row corresponds to the evaluation of the N_{basis} functions at the i^{th} sample point. The generalized least square estimates of $\boldsymbol{\beta}$ and σ^2_{var} based on a linear trend function are given by:

$$\hat{\boldsymbol{\beta}} = (\mathbf{F}^{\mathrm{T}}(\mathbf{R}_{\mathrm{krg}})^{-1}\mathbf{F})^{-1}\mathbf{F}^{\mathrm{T}}(\mathbf{R}_{\mathrm{krg}})^{-1}\mathbf{y} \tag{7.39}$$

and

$$\hat{\sigma}^2_{var} = \frac{(\mathbf{y} - \mathbf{F}\hat{\boldsymbol{\beta}})^{\mathrm{T}}(\mathbf{R}_{\mathrm{krg}})^{-1}(\mathbf{y} - \mathbf{F}\hat{\boldsymbol{\beta}})}{N_{sp}} \tag{7.40}$$

The linear trend kriging approximation is

$$\hat{y}_{\text{krg}} = \mathbf{f_x}^{\text{T}}\hat{\boldsymbol{\beta}} + \mathbf{r}_{\text{krg}}(\mathbf{x})^{\text{T}}(\mathbf{R}_{\text{krg}})^{-1}(\mathbf{y} - \mathbf{F}\hat{\boldsymbol{\beta}}) \tag{7.41}$$

7.3.4 Radial Basis Function Interpolation

Radial basis function (RBF) interpolation is similar to kriging in the sense that they are based on Gaussian correlation functions. However, in this study RBF interpolation refers to an approximation method based on Gaussian correlation functions that does not include a constant global approximation term, unlike kriging. The method of RBF interpolation used in this study is based on the method employed in Ref. 143. A brief description of the methodology for generating the RBF surrogate is described next.

In RBF surrogates, the approximate response is a weighted sum of basis functions:

$$\hat{y} = \sum_{i=1}^{N_{sp}} w_i R_{\text{RBF}}\left(\left\|\mathbf{x} - \mathbf{x}^{(i)}\right\|\right) \tag{7.42}$$

where $R_{\text{RBF}}(*)$ is typically a non-linear function depending on the Euclidean distance (denoted by $\left\|\mathbf{x} - \mathbf{x}^{(i)}\right\|$) between two design points. The coefficients, w_i, are found such that the surrogate interpolates the initial data points. Thus, the following condition must be satisfied for $j = 1, ..., N_{sp}$:

$$y\left(\mathbf{x}^{(j)}\right) = \sum_{i=1}^{N_{sp}} w_i R_{\text{RBF}}\left(\left\|\mathbf{x}^{(j)} - \mathbf{x}^{(i)}\right\|\right) \tag{7.43}$$

By defining the vectors $\mathbf{w} = [w_1, w_2, ..., w_{N_{sp}}]^{\text{T}}$,

$\mathbf{y} = [y_1, y_2, ..., y_{N_{sp}}]$, and the $N_{sp} \times N_{sp}$ spatial correlation matrix $\mathbf{R}_{\mathrm{RBF}}$ with elements $(R_{\mathrm{RBF}})_{ij} = R_{\mathrm{RBF}}\left(|\mathbf{x}^{(i)} - \mathbf{x}^{(j)}|\right)$, Eq. 7.43 can be rewritten as

$$\mathbf{R}_{\mathrm{RBF}}\mathbf{w} = \mathbf{y}^{\mathrm{T}} \tag{7.44}$$

If the inverse of $\mathbf{R}_{\mathrm{RBF}}$ exists, then the weighting coefficients are

$$\mathbf{w} = (\mathbf{R}_{\mathrm{RBF}})^{-1}\mathbf{y}^{\mathrm{T}} \tag{7.45}$$

and the RBF surrogate is

$$\hat{y}_{RBF}(\mathbf{x}) = \mathbf{r}_{\mathrm{RBF}}\mathbf{w} = \mathbf{r}_{\mathrm{RBF}}(\mathbf{R}_{\mathrm{RBF}})^{-1}\mathbf{y}^{\mathrm{T}} \tag{7.46}$$

where

$$\mathbf{r}_{\mathrm{RBF}} = \left[R_{\mathrm{RBF}}\left(\left\|\mathbf{x} - \mathbf{x}^{(1)}\right\|\right), ..., R_{\mathrm{RBF}}\left(\left\|\mathbf{x} - \mathbf{x}^{(N_{sp})}\right\|\right)\right]. \tag{7.47}$$

As stated above, Eq. 7.46 shows that the RBF surrogate does not include a constant global approximation term, unlike Eq. 7.36 which includes $\hat{\boldsymbol{\beta}}$. Gaussian correlation functions of the form given by Eq. 7.48 are used for the basis functions in Eq. 7.42.

$$R_{\mathrm{RBF}}(\eta) = \exp(-\eta^2/2\tau^2_{\mathrm{RBF}}) \tag{7.48}$$

In this case, the dummy variable η would be $\left\|\mathbf{x} - \mathbf{x}^{(i)}\right\|$. The fitting parameter τ_{RBF} is found

by a process denoted as *leave-one-out cross validation*, which proceeds as follows:

1. The design variables are scaled to vary from 0 to 1. The possible values of τ_{RBF} are then spread over the domain $[10^{-1}, 10^{1}]$ on a logarithmic scale. This domain was used because the spatial correlation matrix did not become ill-conditioned during the fitting process with these bounds on τ_{RBF}.

2. For each value of τ_{RBF}, N_{sp} RBF models are created, leaving one interpolation point out each time, as if only $(N_{sp} - 1)$ interpolation points exist. Therefore, for each value of τ_{RBF}, N_{sp} evaluations of Eq. 7.46 are required and each evaluation involves the inversion of the $N_{sp} \times N_{sp}$ matrix $\mathbf{R}_{\text{RBF}}$. Since a large set of τ_{RBF} can lead to an excessive number of evaluations of Eq. 7.46, only 15 values for τ_{RBF} were considered so that the RBF remains computationally tractable.

3. The difference between the true response at the left out point and the response predicted at the left out point by the RBF model based on $(N_{sp} - 1)$ points is computed.

4. The value of τ_{RBF} that minimizes the sum of these residuals is selected as the fitting parameter.

7.3.5 Radial Basis Neural Networks

Radial basis neural networks (RBNN's) approximate a function as a weighted sum of radial basis functions, also known as neurons.

$$\hat{y}_{\text{RBNN}} = \sum_{i=1}^{N_{RBF}} \alpha_i R_{\text{RBNN}}(\mathbf{x}) \tag{7.49}$$

where $R_{\text{RBNN}}(\mathbf{x})$ is the response of the radial basis function at $\mathbf{x}$, and α_i is the weight associated with the radial basis function. In this study, the MATLAB routine *newrb* was used to construct the RBNN. Gaussian function's given by Eq. 7.50 are used for the neurons.

$$R_{\text{RBNN}}(\eta) = \exp(-\eta^2) \tag{7.50}$$

In this case, the dummy variable η would be $\left(\tau_{\text{RBNN}} \left\|\mathbf{x} - \mathbf{x}^{(i)}\right\|\right)$. The parameter τ_{RBNN} is inversely related to the user defined *spread* parameter, which controls the radius of influence for each neuron. Specifically, the radius of influence is the distance at which the output of a neuron reaches a certain small value corresponding to half of the spread parameter. A high spread would cause the neuron responses to be smooth, and a low spread would result in highly non-linear responses. The spread is set to 0.5 in this study. The number of radial basis functions and associated weights are determined by satisfying the user defined error *goal* for the mean square error in the approximation. The goal parameter is set to the square of 5% of the mean response in this study.

7.3.6 Weighted Average Surrogates

In addition to the individual surrogates described above, a weighted average surrogate based on the implementation described in Ref. 60 was employed. The weighted average model is formulated as a weighted sum of the polynomial, kriging, and RBNN surrogates, i.e.

$$\hat{y}_{\text{WTA}} = w_{\text{poly}}\hat{y}_{\text{poly}} + w_{\text{krg}}\hat{y}_{\text{krg}} + w_{\text{RBNN}}\hat{y}_{\text{RBNN}} \tag{7.51}$$

where w_{poly}, w_{krg}, and w_{RBNN} are the weights associated with each surrogate. Note that any number of the individual approximation methods could have been combined into a weighted average surrogate. The reasons for employing 2^{nd} order polynomials, kriging, and RBNN surrogates in the weighted average approach are as follows: (1) these are commonly used surrogates in engineering applications, (2) they offer a variety of parametric and non-parametric approaches [123], and (3) they differ in how the fitting parameters are selected. The weights are calculated in such a way that they (a) reflect the confidence in each individual surrogate and (b) filter out adverse effects associated with individual surrogates which represent the sample data well, but predict poorly at designs not included in the sample data. Furthermore, the weights in Eq. 7.51 are constrained to sum to 1 so that if all of the individual surrogates give the same output at some input, then the weighted surrogate will also recover this output. A weight scheme which satisfies these requirements is given below [60].

$$w_i = \frac{w_i^*}{\sum_i^{N_{sm}} w_i^*} \tag{7.52}$$

where

$$w_i^* = (E_i + d_1 E_{avg})^{d_2}, \quad d_1 < 1,\, d_2 < 0 \tag{7.53}$$

$$E_{avg} = \sum_i^{N_{sm}} E_i / N_{sm} \tag{7.54}$$

and N_{sm} is the number of surrogate models. The weights are based on a global data based error measure for each surrogate, denoted by E_i. In this study, the generalized mean square error (GMSE) based on leave-one-out cross-validation (also known as PRESS in the poly-

nomial response surface approximation terminology) is used as the error measure, and thus

$$E_i = \sqrt{GMSE_i}\,. \tag{7.55}$$

and

$$GMSE_i = \frac{1}{N_{sp}} \sum_{i=1}^{N_{sp}} \left(y_{_i} - \hat{y}_i^{(-i)}\right)^2 \tag{7.56}$$

where $\hat{y}_i^{(-i)}$ represents the prediction at $\mathbf{x}^{(i)}$ using the surrogate constructed with all sample points except $(\mathbf{x}^{(i)}, y_{_i})$. The advantage of cross-validation is that it provides a nearly unbiased estimate of the generalized error and the corresponding variance is reduced, when compared to split-sample, considering that every point gets to be in a test set once, and in a training set $(k-1)$ times, regardless of how the data is divided.

In Eq. 7.53, d_1 and d_2 are user defined parameters which control the relative influence of the individual surrogate error, E_i, and the average of the individual errors, E_{avg}, on the weight. Small values of d_1 and large negative values of d_2 result in high weights for the best individual surrogate, which satisfies the first goal mentioned above for determining the weights. Large values of d_1 and small negative values of d_2 result in more emphasis on the average of the error, which would protect against surrogates which may predict well at sample data points, but give poor predictions at unsampled locations in the design space. Based on a parametric study conducted in Ref. 60, setting $d_1 = 0.05$ and $d_2 = -1$, or $d_1 = 0.5$, $d_2 = -1$ has little effect on the weights. Since similar behavior was observed in this study, the results are presented for $d_1 = 0.05$ and $d_2 = -1$. Note that the intuitive property that the higher the error, the lower the weight corresponding to a surrogate is

recovered since $d_2 < 0$. It is worth noting that the optimum settings of d_1 and d_2 as well as the optimum choice of surrogates for use in the weighted average approach are important issues which are the subject of ongoing research and thus are beyond the scope of this thesis.

7.4 Passive Design Using Surrogate Based Optimization

In order to examine the effectiveness of surrogate based optimization (SBO) for rotor blade optimization, two approaches to utilizing the approximate objective functions were considered: (1) the one-shot approach was considered in order to compare the effectiveness of the surrogates without the benefit of updating search algorithms, and (2) an updating approach based on the EGO algorithm was used for single and multi-objective function optimization. Descriptions of these SBO approaches are given below.

7.4.1 One-shot Optimization

In the one-shot approach, the surrogate objective function is optimized directly. The predicted optimum design is then evaluated by the expensive aeroelastic response code in order to obtain the actual objective function value. There is no updating of the surrogate, regardless of the error in the predictions.

Multiple Surrogate Approach

Most research dealing with surrogate modeling and optimization has been concerned with choosing among different surrogates. However, the choice of the "best" surrogate model is determined by a number of factors, and once selected the choice of the "best" surrogate model is seldom reviewed. These factors include: the number of points used to construct the surrogate model (sampling density), the scheme used to select points (design of experiments), and parameters/nature of the surrogate model. Different surrogate models have been shown to perform well under different conditions and for different objectives. For instance, some studies have found that polynomials perform as well or better than other approximation methods, while others have concluded that radial basis function (RBF) interpolation or kriging are the best methods [38, 72, 114, 115, 141, 149]. Furthermore, the most accurate approximation method may not necessarily lead to the optimum design. Thus, a single approximation method has not distinguished itself as the most suitable for engineering applications.

As an alternative to seeking the "best" approximation method, there has been recent work on the collaborative use of an ensemble of surrogates [60]. The combination of multiple surrogates is motivated by our inability to find a unique solution to the non-linear inverse problem of identifying the model from a limited set of data [123] and essentially serves as an approach to account for the uncertainty in the choice of the appropriate approximation methods. Typically, the cost of obtaining data required for developing surrogates is high, so it is desirable to extract as much information as possible from the data. Although selecting the fitting parameters may require substantial effort for certain approximation

methods, surrogates can often be constructed without significant expense compared to the cost of acquiring data. Therefore, use of an ensemble of surrogates can prove to be a relatively inexpensive method of distilling correct trends from the data while protecting against poor surrogate models.

A multiple surrogate approach, including the weighted average model, is employed in this study in order to demonstrate some of the pitfalls associated with only using a single approximation method. The multiple surrogate approach is employed in a one-shot optimization framework. However, as noted in Section 1.5.3, this approach could be adapted into an updating scheme which explicitly accounts for prediction uncertainty.

7.4.2 EGO Algorithm

Once the surrogates are obtained, the one-shot approach is the simplest method for finding the optimum. However if the surrogate is not accurate everywhere in the design space, the optimization may lead to a poor design. Therefore, it is desirable to account for the uncertainty in the surrogate's predictions since promising designs could lie in regions where the surrogate is inaccurate. The Efficient Global Optimization (EGO) algorithm proposed by Jones et al. [82] is an alternative to the one-shot approach which accounts for uncertainty in the surrogate *and* is more efficient. In EGO, a small number of initial design points are used to fit kriging approximations of the objective function and expensive constraints. Based on the stochastic process nature of kriging, an expected improvement function (EIF) is created in order to facilitate the selection of additional sample points (infill samples) where expensive computer simulations are to be conducted. These sample

points are chosen to be where there is a high probability of producing a superior design over the current best design and/or where the predictions of the surrogate are unreliable due to a high amount of uncertainty. The infill samples represent a balance between the local consideration of finding an optimal design based on the surrogate's predictions, and the global consideration of sampling where there is much uncertainty in the surrogate's predictions.

Expected Improvement Based Search of the Design Space

Before forming the EIF it is necessary to derive an estimation of the error, or uncertainty, in the kriging model. The mean squared error (MSE) [82], at any point in the design space, of the kriging predictor can be written as

$$s^2(\mathbf{x}) = \hat{\sigma}^2_{var}\left[1 - \mathbf{r}^{\mathrm{T}}_{\mathrm{krg}}\mathbf{R}^{-1}_{\mathrm{krg}}\mathbf{r}_{\mathrm{krg}} + \frac{(1 - \mathbf{1}^{\mathrm{T}}\mathbf{R}^{-1}_{\mathrm{krg}}\mathbf{r}_{\mathrm{krg}})^2}{\mathbf{1}^{\mathrm{T}}\mathbf{R}^{-1}_{\mathrm{krg}}\mathbf{1}}\right]. \tag{7.57}$$

Equation 7.57 represents an approximation of the error in the kriging prediction at any design point. The advantage of Eq. 7.57 is that an estimate of the error, or uncertainty, in the kriging surrogate can be obtained without additional expensive function evaluations.

With the kriging model and the MSE defined, the EIF can be derived. For a minimization problem, the improvement over the current best design is written as

$$I = \max(y_{\min} - y(\mathbf{x}), 0) \tag{7.58}$$

where $y_{\min}$ is the best feasible design out of all of the sample points used to create the

surrogate. The expected improvement is simply the expected value of Eq. 7.58 [81], and can be written as

$$EIF(\mathbf{x}) = \begin{cases} \chi_1 + \chi_2 & \text{if } s > 0 \\ 0 & \text{if } s = 0 \end{cases} \tag{7.59}$$

where

$$\chi_1 = (y_{\min} - \hat{y}_{\text{krg}})\Phi_{\text{dist}}\left(\frac{y_{\min} - \hat{y}_{\text{krg}}}{s}\right) \tag{7.60}$$

and

$$\chi_2 = s\phi_{\text{den}}\left(\frac{y_{\min} - \hat{y}_{\text{krg}}}{s}\right). \tag{7.61}$$

The functions $\Phi_{\text{dist}}(*)$ and $\phi_{\text{den}}(*)$ represent the standard normal distribution function and the standard normal density function respectively.

The first term in the EIF, χ_1, is the difference between the current best objective function value and the predicted response at an arbitrary design, $\mathbf{x}$, multiplied by the probability that $y(\mathbf{x})$ is better than $y_{\min}$. This term is large where $\hat{y}_{\text{krg}}$ is likely to be better than $y_{\min}$. The second term, χ_2, is large where the error metric $s(\mathbf{x})$ is large and thus where there is much uncertainty in the surrogate's prediction. The design points with the highest expected improvement represent a balance between finding promising regions in the design space based on the surrogate's predictions (local search) and finding regions of high uncertainty in the surrogate's predictions (global search).

Weighted Expected Improvement Function

It is possible to control the balance between the local and global search characteristics of the EIF by weighting the two terms with a user defined parameter, w [144]. The weighted expected improvement function (WEIF) is given as

$$WEIF(\mathbf{x}) = \begin{cases} w\chi_1 + (1-w)\chi_2 & \text{if } s > 0 \\ 0 & \text{if } s = 0 \end{cases} \tag{7.62}$$

where $0 \leq w \leq 1$. Setting $w = 0$ would place more emphasis on searching in regions of the design space where there is much uncertainty in the surrogate's predictions, while $w = 1$ would emphasize locating designs which are predicted to be optimal. A value of $w = 0.5$ results in the same characteristics as the balanced search based on the EIF.

Implementation of the EGO Algorithm

In this study, the implementation of EGO, which is depicted in Fig. 7.5, proceeds as follows:

1. A small number of initial fitting points are generated using optimal Latin hypercube (OLH) sampling.

2. The initial fitting data is generated by evaluating the expensive objective function and constraints at each design in the OLH. This entails conducting a number of aeroelastic response simulations equal to the number of points in the OLH. Since each simulation corresponds to an independent rotor blade design, a number of simulations

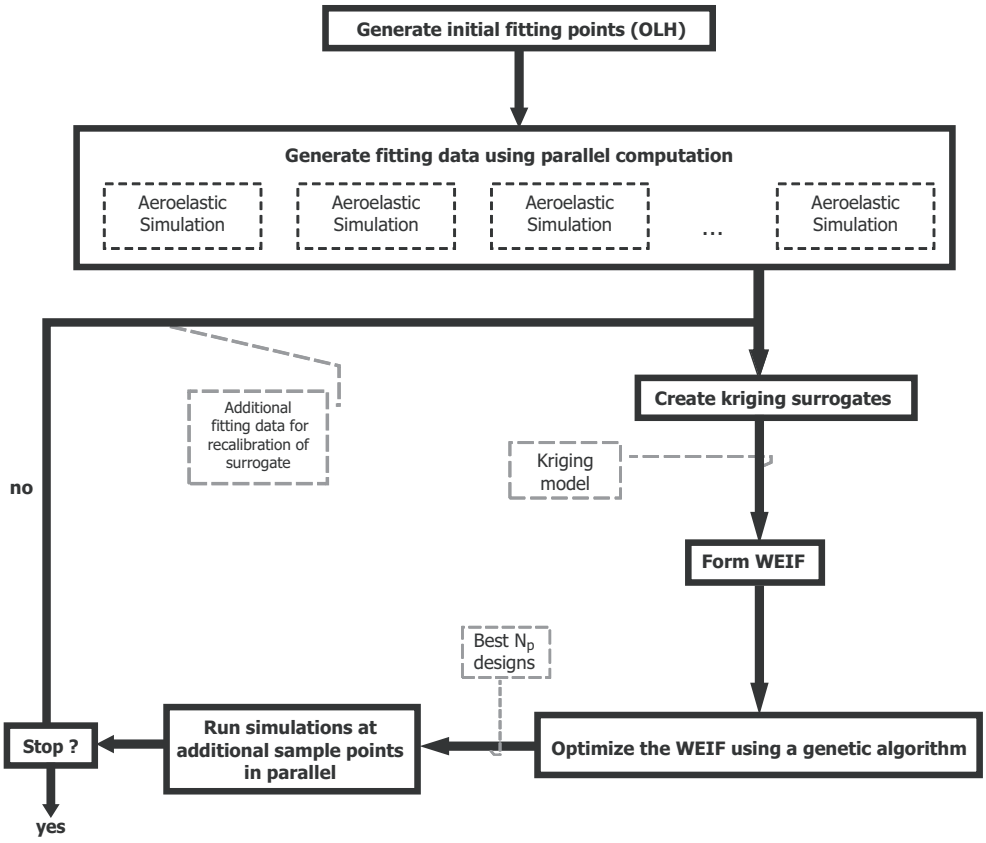

Figure 7.5: Efficient Global Optimization (EGO) algorithm

equal to the number of available processors are conducted in parallel until fitting data is generated for all designs in the OLH.

3. Kriging surrogates for the expensive objective function and constraints are generated from the fitting data.

4. The WEIF corresponding to the surrogate objective function is formed.

5. The WEIF, which is a continuous function of the design variables, is optimized to find the set of designs corresponding to the highest weighted expected improvement in the objective function. In this study, the Multi-Island Genetic Algorithm in iSIGHT [1] is used to optimize the WEIF while enforcing the constraints on the blade design.

6. From the genetic algorithm output file, the N_p best designs in terms of weighted expected improvement are selected, where N_p is the number of available processors. Simulations at each of the N_p best designs are run on individual processors in order to take advantage of parallel computation [143].

7. The stopping condition is checked. In this study, the algorithm is stopped if the best design from the current iteration is not better than the best design from the previous iteration. Other possible stopping criteria could be when a predefined amount of computer time elapses, or when the weighted expected improvement is low.

8. If the stopping condition is not reached, the kriging surrogates are refit after the additional fitting data is added to the initial data set, and the process of choosing additional sample points is repeated until the user defined stopping criterion is reached.

The advantages of such a method over the one-shot approach are (1) the chances of being led to a poor design due to errors in the surrogates are reduced by sampling in regions where there is much uncertainty in the surrogate's predictions, and (2) fewer expensive function evaluations are required since a smaller initial sample set is used and the EIF is used to select additional sample points in a more "intelligent" manner, as opposed to starting with a relatively large initial data set.

7.4.3 Surrogate Based Multi-objective Optimization

Since multiple objective functions are considered in this study, it is desirable to locate blade designs corresponding to the best trade-offs between the objective functions. The best

trade-off designs are *Pareto optimal* if no other designs can be found which correspond to superior objective function values for *all* objective functions. Each multi-objective problem considered in this study consists of two objective functions. To locate a set of Pareto optimal designs, two approaches were employed to extend EGO for multi-objective function optimization. The first approach is a weighted sum approach in which both objective functions are combined into a single objective function, i.e.

$$J_{\text{sum}} = W J_1 + (1 - W) J_2 \ . \tag{7.63}$$

Various values of $0 \leq W \leq 1$ are selected in order to convert the multi-objective function optimization problem into multiple single-objective function optimization problems. Thus, for each value of W, EGO is applied to J_{sum}. This approach is similar to ParEGO [84] except that W is not randomly selected for each iteration.

In the second approach, EGO is modified to locate the Pareto designs associated with the WEIF's. The modified EGO algorithm, which is depicted in Fig. 7.6, proceeds as follows:

1. A small number of initial fitting points are generated using optimal Latin hypercube (OLH) sampling.

2. As in the single objective EGO algorithm, the initial fitting data is generated by evaluating the expensive objective function and constraints at each design in the OLH using parallel computation.

3. Kriging surrogates for each of the N_{OF} expensive objective functions and constraints

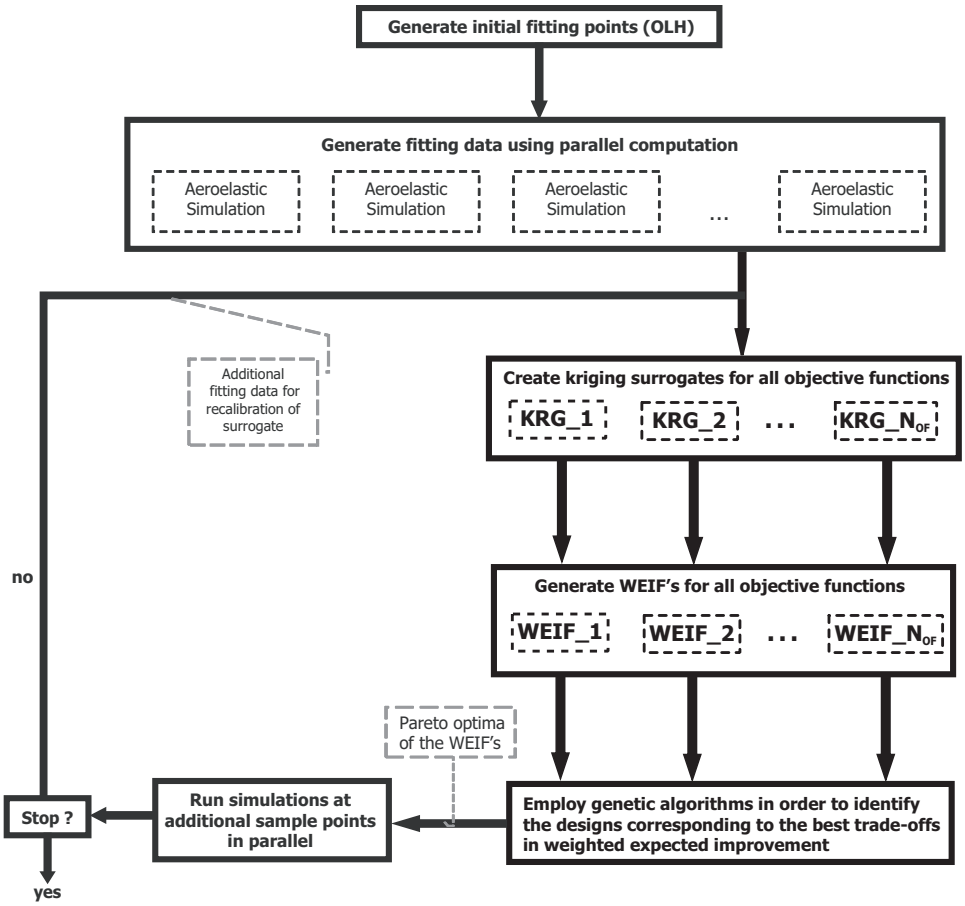

Figure 7.6: Multi-objective EGO algorithm

are generated from the fitting data, where N_{OF} is the number of objective functions.

4. Weighted expected improvement functions corresponding to all N_{OF} objective functions are generated.

5. Using genetic algorithms available in iSIGHT, the Pareto optima of the WEIF's are obtained; i.e. the designs corresponding to the best combinations of weighted expected improvement in the objective functions. The approach to employing genetic algorithms in order to identify the Pareto optima of the WEIF's is illustrated in Section 9.2.2.

6. Additional fitting data is generated by conducting simulations at each of the Pareto designs in parallel.

7. The stopping condition is checked. The algorithm is stopped if the additional sample points do not improve upon or add to the Pareto optima corresponding to the objective functions from the previous iteration.

8. If the stopping condition is not reached, the kriging surrogates are refit after the additional fitting data is added to the initial data set, and the process of choosing additional sample points is repeated until the user defined stopping criterion is reached.

In contrast to the method developed in Ref. 83, the approach described above is not based on a multi-objective extension of the EIF which was derived from statistical principles. However, it has two advantages over the approach proposed in Ref. 83: (1) it is a more straight forward extension since the EIF's derived in the single objective approach are used, and (2) the capability to control the balance of the search is maintained since the WEIF is used. It should be noted that a thorough comparison of the various approaches to applying EGO for multi-objective optimization, namely parEGO [84], Keane's formulation [83] and the approaches employed in this study has never been conducted; thus, it is unclear how well these methods perform relative to each other.

7.5 Active Control Algorithm

Active control of vibration and rotor power is based on the higher-harmonic control (HHC) algorithm [76]. The stability, robustness, and convergence properties of the algo-

rithm and a number of variants were explored in Ref. 117. The relaxed adaptive HHC variant detailed in Ref. 96 is employed in this study. The algorithm is based on a linear, frequency domain representation of helicopter response to control inputs. The input harmonics to the ACF consist of a combination of flap deflection angles having frequencies of 2, 3, 4 and $5/\mathrm{rev}$. Thus, the total flap deflection is a combination of these contributions:

$$\delta_f(\psi) = \sum_{N=2}^{5} \left[\delta_{Nc}\cos(N\psi) + \delta_{Ns}\sin(N\psi)\right], \tag{7.64}$$

where δ_{Nc} and δ_{Ns} are the control amplitudes.

The control strategy is based on the minimization of a performance index which is a quadratic function of the quantities that are being reduced, $\mathbf{z}_k$, and the control input amplitudes $\mathbf{u}_k$ [76, 117]:

$$J_{\text{ACF}}(\mathbf{z}_k, \mathbf{u}_k) = \mathbf{z}_k^{\mathrm{T}}\mathbf{Q}\mathbf{z}_k + \mathbf{u}_k^{\mathrm{T}}\mathbf{W}_{\mathrm{u}}\mathbf{u}_k \ . \tag{7.65}$$

In the case of vibration reduction,

$$\mathbf{z}_{k,\text{VR}} = \left[F_{4X} \ \ F_{4Y} \ \ F_{4Z} \ \ M_{4X} \ \ M_{4Y} \ \ M_{4Z}\right]^{\mathrm{T}} \ . \tag{7.66}$$

For noise reduction, $\mathbf{z}_k$ consists of the 6^{th} – 17^{th} harmonic components of BVI noise,

$$\mathbf{z}_{k,\text{NR}} = \left[N_{H06} \ \ N_{H07} \ \ N_{H08} \ \ \ldots \ \ N_{H17}\right]^{\mathrm{T}} \ . \tag{7.67}$$

Although BVI noise is made up of the 6^{th} – 40^{th} harmonics, the 6^{th} – 17^{th} harmonics dominate the overall sound pressure level. Using only this range shortens the length of the vector $\mathbf{z}_{k,\text{NR}}$, which reduces the computational cost associated with the active control algorithm considerably. This implementation has been found to work well for BVI noise reduction [120]. The noise components are measured at a microphone installed at the right rear landing skid, as shown in Fig. 7.1. Note that the objective function used for active noise reduction is measured at a microphone on a landing skid, as opposed to the carpet plane where the passive optimization objective function is calculated. The passive reduction objective function is based on noise levels in the carpet plane because the overall goal is to reduce far-field noise since this is what the observer hears. However, active on-blade controllers can only receive feedback information from a location on the helicopter.

For rotor power reduction,

$$\mathbf{z}_{k,\text{PR}} = \left[J_P\right] \ . \tag{7.68}$$

The optimal flap deflections are determined according to the control law described in Refs. 116 and 117, and can be written as

$$\mathbf{u}_{k+1} = -\left(\mathbf{T}^{\text{T}}\mathbf{Q}\mathbf{T} + \mathbf{W}_{\text{u}}\right)^{-1}\mathbf{T}^{\text{T}}\left(\mathbf{Q}\mathbf{z}_k - \mathbf{Q}\mathbf{T}\mathbf{u}_k\right) \tag{7.69}$$

The relationship between the flap deflections and the quantities which need to be reduced is quantified by the transfer matrix $\mathbf{T}$ given by $\mathbf{T} = \partial\mathbf{z}_k/\partial\mathbf{u}_k$. The subscript k refers to the k^{th} control update, reflecting the discrete-time nature of the controller; i.e. $\mathbf{z}_k$ and

$\mathbf{u}_k$ are recalculated at specific times $t_k = k\Delta t_k$ where Δt_k is the time interval between updates. In this study, Δt_k is set to 8 rotor revolutions, or settling revolutions, so that the system can reach a steady state. If the helicopter system cannot be perfectly represented by a linear model, the optimum control input will not be reached in a single step, and thus $\mathbf{u}_k$ must be updated in order to converge to the optimal control input [117]. Based on the implementations employed in Refs. 96 and 120, 8 control updates are used when considering BVI noise and vibration reduction, and 15 updates for vibration and power reduction.

Traditionally, Eq. 7.69 is rewritten in iterative form as

$$\mathbf{u}_{k+1} = \mathbf{u}_k + \Delta\mathbf{u}_k \tag{7.70}$$

In the relaxed HHC variant described in Ref. 117, a relaxation factor α_r is introduced, resulting in

$$\mathbf{u}_{k+1} = \mathbf{u}_k + \alpha_r\Delta\mathbf{u}_k \tag{7.71}$$

where $0 < \alpha_r < 1$. This range has been shown to enhance the robustness of the control algorithm at the expense of convergence speed [117]. In addition, the transfer matrix $\mathbf{T}$ is identified online following the adaptive HHC variant described in Ref. 117.

The $\mathbf{W}_{\mathrm{u}}$ matrix in Eq. 7.65 is used to enforce saturation limits on the flap deflections of $|\delta_{fmax}| \leq 4^\circ$, and is given by

$$\mathbf{W}_{\mathrm{u}} = c_{wu}\mathbf{I} \tag{7.72}$$

where c_{wu} is a scalar used to control the penalty on flap deflections and $\mathbf{I}$ is the identity matrix. If the flap deflections are overconstrained, then c_{wu} is reduced and a new optimal

control input is calculated. Similarly, c_{wu} is increased if the flap deflections are undercon-strained. Using the algorithm described in Ref. 22, c_{wu} is automatically iterated upon until the flap deflections converge to within $\pm 5\%$ of δ_{fmax}.

In this study, active control for BVI vibration and noise reduction, and vibration and power reduction at high advance ratios were considered.

BVI Induced Vibration and Noise Reduction

The vector $\mathbf{z}_k$ is obtained by combining $\mathbf{z}_{k,\text{VR}}$ and $\mathbf{z}_{k,\text{NR}}$ as

$$\mathbf{z}_k = \left[\begin{array}{c} \mathbf{z}_{k,\text{VR}} \\ \hline \mathbf{z}_{k,\text{NR}} \end{array}\right] . \tag{7.73}$$

In Eq. 7.65, $\mathbf{Q}$ is a diagonal weighting matrix. The weight matrices associated with vibration and noise reduction, $\mathbf{Q}_{\text{VR}}$ and $\mathbf{Q}_{\text{NR}}$, are combined as

$$\mathbf{Q} = \left[\begin{array}{cc} (W_\alpha) \cdot [\mathbf{Q}_{\text{VR}}] & 0 \\ 0 & (1 - W_\alpha) \cdot [\mathbf{Q}_{\text{NR}}] \end{array}\right], \tag{7.74}$$

where $0 \leq W_\alpha \leq 1$ is a user defined parameter which controls the emphasis of the controller.

Vibration and Power Reduction at High Advance Ratios

The vibration and power active control algorithm is formulated in a similar manner to the noise and vibration problem. The only differences are that $\mathbf{z}_{k,\text{NR}}$ and $\mathbf{Q}_{k,\text{NR}}$ would be

replaced with $\mathbf{z}_{k,\mathrm{PR}}$ and $\mathbf{Q}_{k,\mathrm{PR}}$ in Eqs. 7.73 and 7.74 respectively.

7.6 Active/Passive Approaches

Two approaches to integrating multi-objective passive optimization approaches based on EGO and active control techniques into an active/passive optimization framework were employed in this study: the *sequential approach* and the *combined approach*. In the sequential approach, structurally optimized blades are augmented with trailing edge flaps. While the structurally optimized designs correspond to the best passive objective function values without the benefits of active control, these designs will not necessarily result in the best possible objective function values when combined with active control. This was demonstrated in Ref. 178 for the case of vibration reduction. Therefore, as an alternative to sequential active/passive optimization, a combined approach is considered in which the blade/flap combination is optimized simultaneously. The optimum designs from the combined approach correspond to the best overall values of the passive objective functions when utilizing active control.

7.6.1 Sequential Active/Passive Approach

The sequential approach is implemented in two steps – (1) first, the blade is structurally optimized using the EGO algorithm, and (2) then partial span actively controlled trailing edge flaps (ACF's), in either dual servo-flap or single plain flap configurations, are added to the optimized designs. Based on the W_α setting, the control algorithm described in Section 7.5, which operates in a closed-loop mode, determines the flap deflections required for a

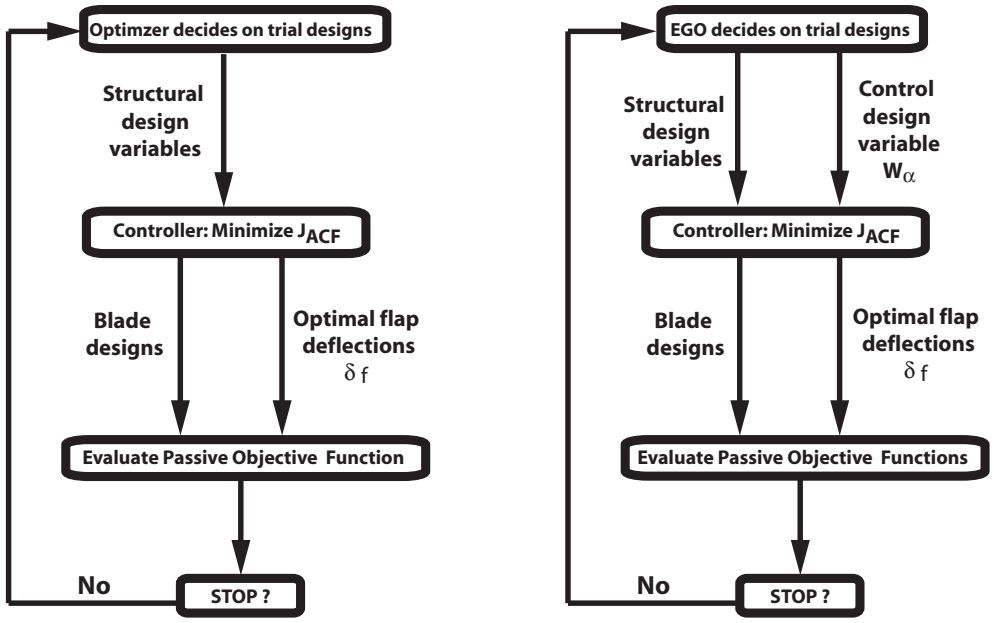

(a) Single objective **(b) Muli-objective**

Figure 7.7: Combined active/passive optimization algorithm

combination of vibration and noise reduction, or vibration and power reduction. Thus, in the sequential approach, active control is used to augment the characteristics of passively optimized blades.

7.6.2 Combined Active/Passive Approach

In this study, the combined active/passive approach employed in Ref. 178 was extended for application to multi-objective function optimization [58]. First, it is useful to understand how the single objective combined active/passive approach proceeds. For vibration reduction, the approach based on Ref. 178 is depicted in Fig. 7.7a and is characterized by the following steps:

1. The optimization algorithm selects a set of trial blade designs at which the passive

objective function needs to be evaluated. These designs are characterized by the structural design variables.

2. For each trial design, the active control algorithm determines the optimal control input for vibration reduction; i.e. the flap deflections which minimize J_{ACF}.

3. For each trial design, the flap is deflected according to the optimal control input $\delta_f(\psi)$ and the passive vibration objective function is evaluated.

4. The stopping condition is checked.

5. If the stopping condition has not been reached, the resulting values of the passive objective function are returned so that the optimization algorithm can determine the next set of trial designs, and step 1 is repeated.

In the single objective combined active/passive approach outlined above, an optimization algorithm is used to search the design space for the blade design such that the passive vibration function is reduced to the lowest possible value when the ACF's are deflected according to the optimal control law. For noise or power reduction, the passive vibration objective function would be replaced by the noise and performance objective functions given by Eqs. 7.2 and 7.3, and W_α would be set to 0.

Since vibration reduction was the only objective considered in Ref. 178, the control algorithm always selected the optimal control inputs for maximum vibration reduction; i.e. the flap deflections corresponding to $W_\alpha = 1$. However, in this study it is necessary to search the design space for the blade designs *and* the corresponding flap deflections which result in the best trade-offs between vibration and noise reduction, or vibration and power

reduction. Therefore, W_α is treated as an additional design variable since it affects how the flap is deflected. The multi-objective combined active/passive approach depicted in Fig. 7.7b proceeds as follows:

1. The multi-objective implementations of the EGO algorithm described in Section 7.4.3 are used to select a set of trial blade designs and corresponding W_α settings at which the passive objective functions need to be evaluated. In addition to the structural design variables, W_α is also treated as a design variable by the EGO algorithm. Each blade design and its corresponding W_α setting represents a potential Pareto optimal active/passive configuration.

2. For each blade design and its corresponding W_α setting, the active control algorithm determines the optimal flap deflections in order to minimize J_{ACF}.

3. For each trial design, the flap is deflected according to the optimal control input $\delta_f(\psi)$ and all of the passive objective functions are evaluated.

4. The stopping condition is checked. As described in Section 7.4.3, the algorithm is stopped if the trial active/passive configurations do not improve upon or add to the Pareto optima corresponding to the passive objective functions from the previous iteration.

5. If the stopping condition has not been reached, the resulting values of the passive objective function are returned so that the optimization algorithm can determine the next set of trial Pareto optimal active/passive configurations, and step 1 is repeated.

Thus, the multi-objective combined active/passive approach proceeds in a similar manner as the single objective method, except that W_α is treated as an additional design variable by the optimization algorithm and the algorithm is stopped if the current iteration fails to produce an active/passive configuration corresponding to a best trade-off combination of the passive objective functions.

Chapter VIII

Assessment of SBO Techniques for Vibration Reduction Under BVI Conditions

In order to evaluate the performance of SBO for passive blade design, the problem of vibration reduction under BVI conditions is considered. The accuracies of various approximation methods are compared. In addition, the surrogates were used to generate a vibration objective function which was used for optimization using a one-shot approach and the EGO algorithm. All optimized designs are compared to a baseline rotor blade which resembles an MBB BO-105 blade. This chapter is organized as follows: (1) in Section 8.1, the effectiveness of kriging, radial basis function interpolation, and polynomial regression surrogates are thoroughly investigated in order to determine if one method significantly outperforms the other, (2) the advantages of using a multiple surrogate approach are further investigated in Section 8.2, including their collaborative use in forming a weighted average model, and (3) the superiority of EGO over the one-shot approach is demonstrated in Section 8.3.

Table 8.1: Rotor and helicopter parameters

Dimensional Data	
$R = 4.91\,\mathrm{m}$	$\Omega = 425\,\mathrm{RPM}$
$m_0 = 5.57\,\mathrm{kg/m}$	
Non-Dimensional Data	
$N_b = 4$	$c_b = 0.05498R$
$\beta_p = 0.0^\circ$	$C_{do} = 0.01$
$\theta_{\mathrm{pt}} = 0^\circ$	$\theta_{\mathrm{FP}} = 6.5^\circ$
$\mu = 0.15$	$C_W = 0.005$
$\sigma = 0.07$	$C_{df} = 0.01$
$X_{FA} = 0.0$	$Z_{FA} = 0.3$
$X_{FC} = 0.0$	$Z_{FC} = 0.3$
MBB BO-105 Baseline Fundamental Frequencies	
$\omega_{L1} = 0.729$	$\omega_{F1} = 1.125$
$\omega_{T1} = 3.263$	

8.1 Evaluation of Various Approximation Methods

This section presents accuracy and robustness measures of the approximation methods that have been described, as well as vibration reduction results using surrogate objective functions. The blade is characterized by 17 design variables based on Configuration 1 (see Section 7.1.2). The helicopter configuration used in all computations is given in Table 8.1. The simulations are conducted at an advance ratio of 0.15 and descent angle of 6.5°, where high vibration levels due to strong blade vortex interaction (BVI) are encountered.

In addition to the information provided in Table 8.1, additional information that is needed for the fixed cross sectional parameters, objective function, constraints, and the finite element discretization of the blade is presented in the following pages. The material properties and the chordwise locations of the vertical walls are given in Table 8.2.

The weighting factors in the objective function, K_S and K_M, are selected to be 1. These weighting factors result in an objective function which represents the sum of the

Table 8.2: Fixed parameters defining the blade cross section

Aluminum Material Properties
$E = 70.7\,\mathrm{GPa}$
$\nu = 0.33$
$\rho_{\mathrm{struct}} = 2700\,\mathrm{kg/m^3}$
$\sigma_{_Y} = 324\,\mathrm{MPa}$
Non-structural Filler Mass Density
$\rho_{\mathrm{filler}} = 237.4\,\mathrm{kg/m^3}$
Locations of the Vertical Walls
$x_1 = 65.4\,\mathrm{mm}$ $\qquad$ $x_2 = 111.6\,\mathrm{mm}$

4/rev oscillatory hub shear resultant and the 4/rev oscillatory hub moment resultant in the hub-fixed non-rotating frame. For this study, the following side constraints are enforced:

$$1.0\,\mathrm{mm} \leq t_1 \leq 8.0\,\mathrm{mm} \tag{8.1}$$

$$1.0\,\mathrm{mm} \leq t_2, t_3 \leq 12.0\,\mathrm{mm} \tag{8.2}$$

$$0.0 \leq m_{ns}/m_0 \leq 0.25 \tag{8.3}$$

The upper and lower bounds used for the frequency placement constraints, /rev, are given below.

$$0.60 \leq \omega_{L1} \leq 0.80 \tag{8.4}$$

$$1.05 \leq \omega_{F1} \leq 1.20 \tag{8.5}$$

$$2.50 \leq \omega_{T1} \leq 6.50 \tag{8.6}$$

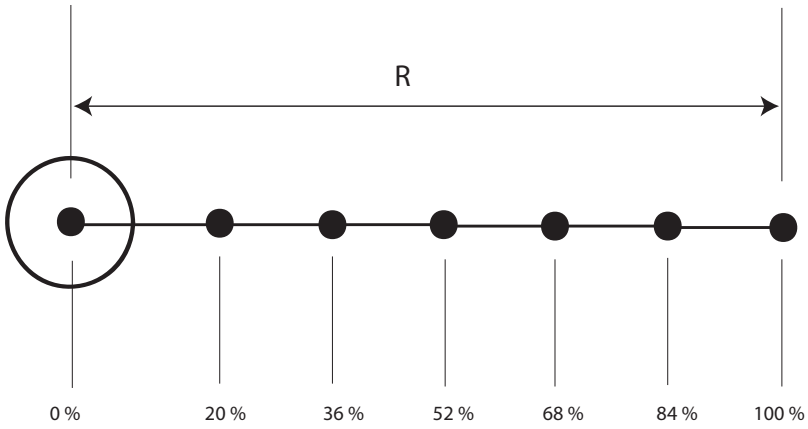

Figure 8.1: Finite element node locations

In the aeroelastic stability constraints given by Eq. 7.9, the minimum acceptable damping for all modes, $(\zeta_k)_{\min}$, is chosen to be 0.01. Additionally, the constraints are modified for the 2^{nd} lag mode, which can sometimes be slightly unstable. To prevent this situation, a small amount of structural damping is added to this mode. For this study, 0.5% structural damping is added to stabilize the 2^{nd} lag mode of the baseline blade. For the stress constraint, a factor of safety of 1.5 is used. The rotor blade was discretized by 6 finite element segments shown in Fig. 8.1.

8.1.1 Practical Implementation Details Associated with the Surrogates

Four approximation methods were compared: 2^{nd} order polynomials, RBF interpolation, ordinary kriging, and kriging where all p_k are not fixed at 2. Note that all kriging results in this section are based on a constant global trend function. The surrogates were fit to the sample data using MATLAB programs on a 3.2 GHz Xeon processor. The ordinary kriging surrogates were created with a freely available MATLAB kriging toolbox [98]. In the parameter estimation, a local optima of the likelihood function (Eq. 7.35) is sought.

Since this algorithm is only configured for ordinary kriging, a different MATLAB package is used for the more general kriging. The MATLAB package used for the more general kriging utilizes the global search algorithm DIRECT [80, 132] for optimization of the likelihood function. Since the DIRECT algorithm results in a more global optimization, the more general kriging algorithm requires more fitting time than the ordinary kriging algorithm.

Two sets of fitting points were used to build the surrogates – a 300 point optimum Latin hypercube (OLH) and a 500 point OLH. From the 300 point OLH, 283 points had converged trim solutions and were used to build the surrogates; while out of the 500 point OLH, 484 points had converged trim solutions. An unconverged trim solution is one in which the elements of the trim solution vector (Eq. 6.49) vary erratically with each iteration, which causes the trim residual vector (Eq. 6.47) to increase during the autopilot trim algorithm. The fitting times for each approximation method are given in Table 8.3. For the kriging surrogates, the majority of the fitting time is devoted to the maximum-likelihood parameter estimation, while for the RBF's, the leave-one-out cross validation method of finding the fitting parameter is responsible for most of the fitting time. The prediction time was much less than one second for each approximation method.

One of the advantages of surrogate based optimization with design of computer experiments is that each simulation corresponding to a design point in the OLH can be run independently of the others, and therefore the simulations can be run in parallel. The helicopter simulations were run on a Linux cluster of 1.8 – 2.4 Ghz Opteron processors. Using 40 processors, the 283 point data set required 53 hours to generate, while the 484 point data

Table 8.3: Surrogate fitting times

Surrogate	Sample Size	Fitting Time
Poly.	283	< 1 s
RBF	283	1.5 – 2 min.
Ord. krg.	283	15 – 20 s
Krg.	283	4 – 5 min.
Poly.	484	< 1 s
RBF	484	8 – 9 min.
Ord. krg.	484	50 s – 1 min.
Krg.	484	14 – 15 min.

set needed 82 hours.

8.1.2 Surrogate Accuracy Results

The predictive capabilities of the 2nd order polynomial response surfaces, kriging with the constant trend function, and radial basis function interpolations, were compared using the two sets of fitting points. In order to quantify the accuracy of the surrogates, two methods for calculating error were considered. The first method requires conducting additional simulations at test points which are independent of the fitting points, in order to test the predictions of the surrogates. The second method is based on leave-one-out cross validation and seeks to represent the error in the surrogate without conducting additional expensive simulations.

Errors Based on Additional Test Points

The first method for quantifying the error in the surrogates utilizes simulation data at test points which are not included in the optimum Latin hypercubes used to create the

surrogates. The predicted responses from the surrogates were then compared to the "actual" responses at the test points. The test points came from a 200 point OLH, of which 197 had converged trim solutions. None of the blade designs from the 197 test points were coincident with the blade designs from the two OLH's used to create the surrogates. Using the test points, the absolute percent error is given by

$$\varepsilon_i^{(tp)} = \frac{|y^{(i)} - \hat{y}^{(i)}|}{\bar{y}} \tag{8.7}$$

where $y^{(i)}$ is the "actual" response computed by the helicopter simulation, $\hat{y}^{(i)}$ is the response predicted by the surrogate at the i^{th} test point, and $\bar{y}$ is the mean of the absolute values of the responses from the 197 test points. Based on Eq. 8.7, the average percent error, maximum percent error, and minimum percent error are:

$$\varepsilon_{avg}^{(tp)} = \frac{\sum_{i=1}^{N_{tp}} \varepsilon_i^{(tp)}}{N_{tp}} \tag{8.8}$$

$$\varepsilon_{max}^{(tp)} = \text{Max}\left\{\varepsilon_1^{(tp)}, \ldots, \varepsilon_{N_{tp}}^{(tp)}\right\} \tag{8.9}$$

$$\varepsilon_{min}^{(tp)} = \text{Min}\left\{\varepsilon_1^{(tp)}, \ldots, \varepsilon_{N_{tp}}^{(tp)}\right\} \tag{8.10}$$

where N_{tp} is the number of test points. The minimum and maximum percent errors represent the best and worst predictive errors respectively. These error measures are localized since they only represent one point of the 197 test points, while the average percent error represents the surrogate's predictive capability over the entire design space since all 197 test points are included.

The average and maximum percent errors in the approximations of the hub shears and

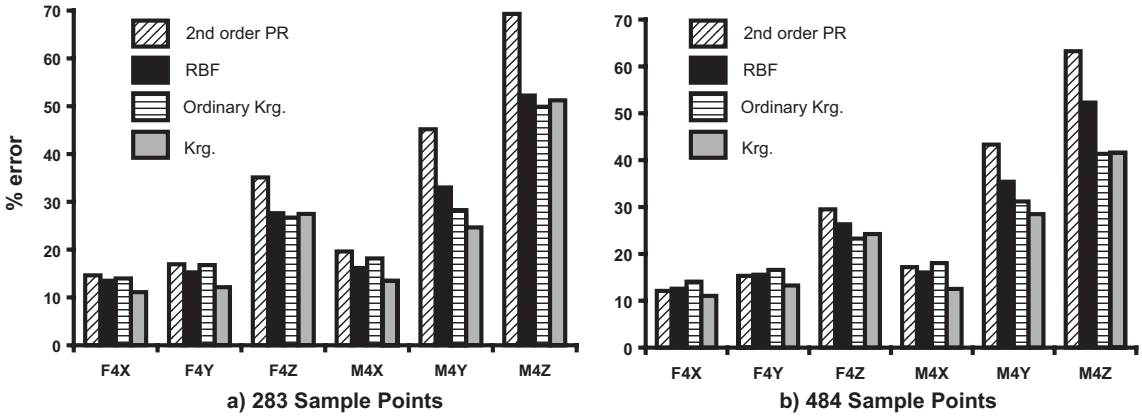

Figure 8.2: Average errors of the underlying vibratory loads, relative to mean responses

moments are given in Figs. 8.2 – 8.3 respectively. The minimum errors are very low – under 1% for each approximation method – and are not shown for the sake of brevity. Figure 8.2 shows that one of the kriging surrogates was the most accurate for every shear and moment in terms of average error, while the polynomial response surface generally had the highest average errors. Typically, the more general kriging surrogate had the lowest average errors, which ranged from $11-51\%$ with 283 sample points and $11-42\%$ with 484 sample points. Figure 8.2 shows that the kriging models are superior in terms of accurately modeling the hub shears and moments over the entire designs space, and that the kriging model which includes p_k in the maximum likelihood estimation generally outperformed the ordinary kriging model. Even though the more general kriging model typically has lower average errors than ordinary kriging, the differences are not large. The largest difference in error between the two kriging models occurred in the case of the M_{4X} surrogate based on 484 sample points, and was only 5.5%.

With the exception of the polynomial response surfaces, increasing the number of sam-

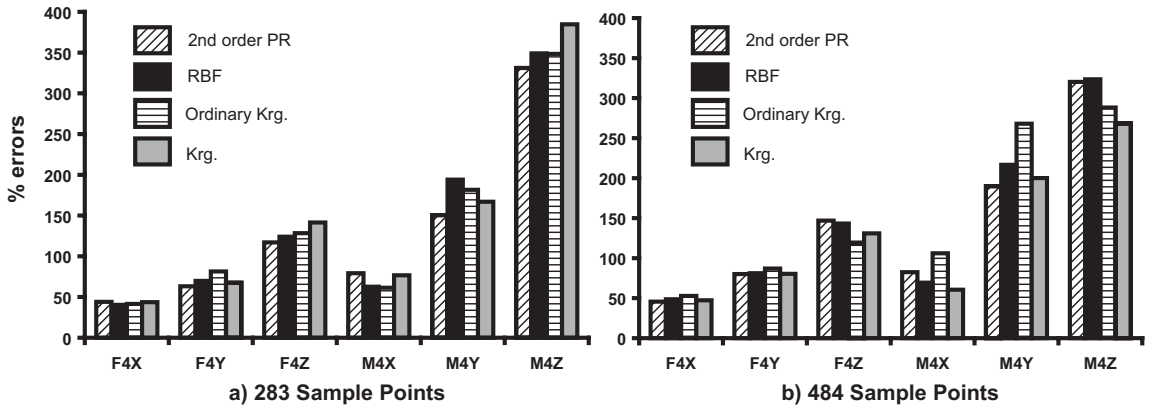

Figure 8.3: Maximum errors of the underlying vibratory loads, relative to mean responses

ple points did not always reduce the average errors in the approximate vibratory loads. In fact, for some surrogate vibratory loads, *higher* average errors were observed with the 484 sample set. The most drastic case is associated with the M_{4Y} surrogate in which the error for the more general kriging surrogate was 3.9% higher when using 484 sample points as opposed to 283. These results indicate that for the 17 dimensional design space, increasing the number of fitting points from 283 to 484 was not sufficient to significantly enhance the accuracy of the surrogates over the entire design space.

Figure 8.3 shows that all of the approximation methods are susceptible to high maximum errors, which range from $40 - 385\%$ for 283 sample points, and $46 - 324\%$ for 484 sample points. These results suggest that there are local regions in the design space where the surrogates are not reliable. Furthermore, increasing the number of sample points did not always reduce the maximum error, just as with average error.

The average and maximum errors in the surrogate objective function are given in Figs. 8.4 – 8.5. The surrogate objective functions were generated by two approaches: (a) combin-

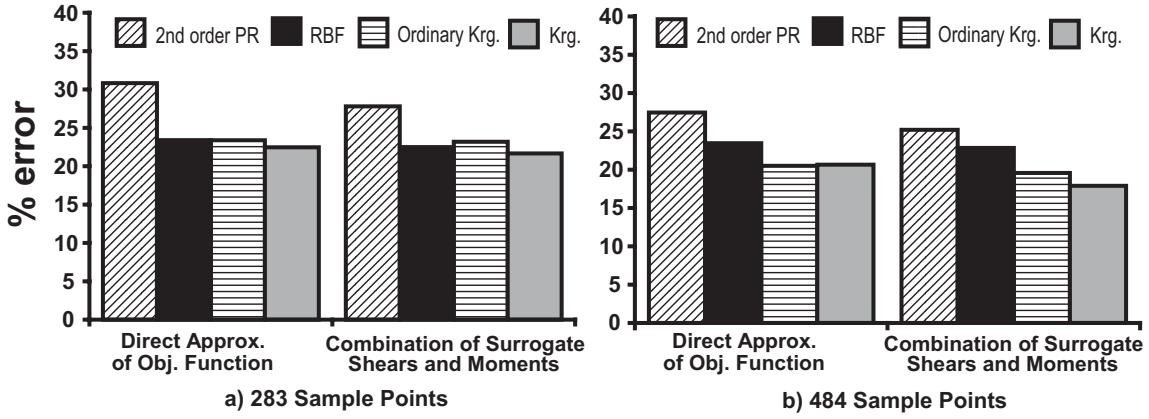

Figure 8.4: Average errors in the surrogate objective function, relative to mean responses

ing the surrogate hub shears and moments to form the approximate objective function as in Eq. 7.25 and (b) by directly fitting the outputs for J_V at the sample points. Figure 8.4 shows that constructing the surrogates from the approximate underlying responses results in slightly lower average errors for both sample sizes. The largest difference in average error between the two methods for creating the surrogate objective function was only 3.2% and occurred when using polynomials with 283 sample points.

Figure 8.5 shows that both methods of approximating the vibration objective function result in maximum errors above 100%, and thus both methods are susceptible to very high errors in local regions of the design space. However, in contrast to the results in Fig. 8.4 for average error, generating the surrogate objective function from the underlying vibratory hub loads did not always result in lower maximum errors. So approximating the underlying responses offered a small advantage for modeling the objective function over the entire design space, but neither method offered a clear advantage in terms of maximum error.

The errors in the approximate stress constraint (Eq. 7.11) are given in Figs. 8.6a and

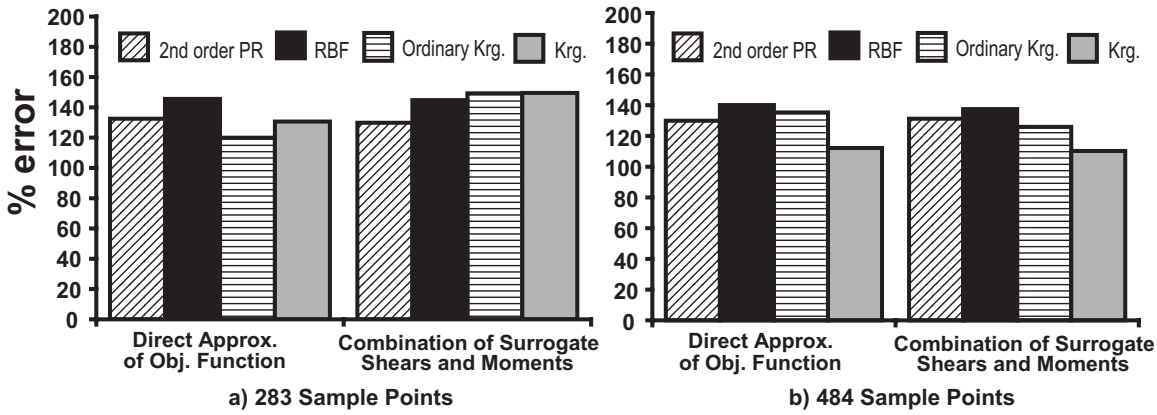

Figure 8.5: Maximum errors in the surrogate objective function, relative to mean responses

b. The ordinary kriging surrogate best approximates the constraint over the entire design space, with average errors of 35% using 283 sample points and 31% using 484 sample points. There are large maximum errors (over 300%) with all the approximation methods, thus the surrogate constraints may not be reliable in certain regions of the design space. The more general kriging surrogate has the highest average and maximum errors when using 484 sample points. This is because during the maximum-likelihood estimation of the fitting parameters, the correlation matrix (Eq. 7.31) became ill-conditioned, which has been known to occur [99], so the auxiliary optimization process used to find the fitting parameters could not be completed.

A comparison of the final fitting parameters for the two kriging models is given in Tables 8.4 – 8.7. The difference in fitting parameters shows that the two methods of kriging resulted in completely different surrogates.

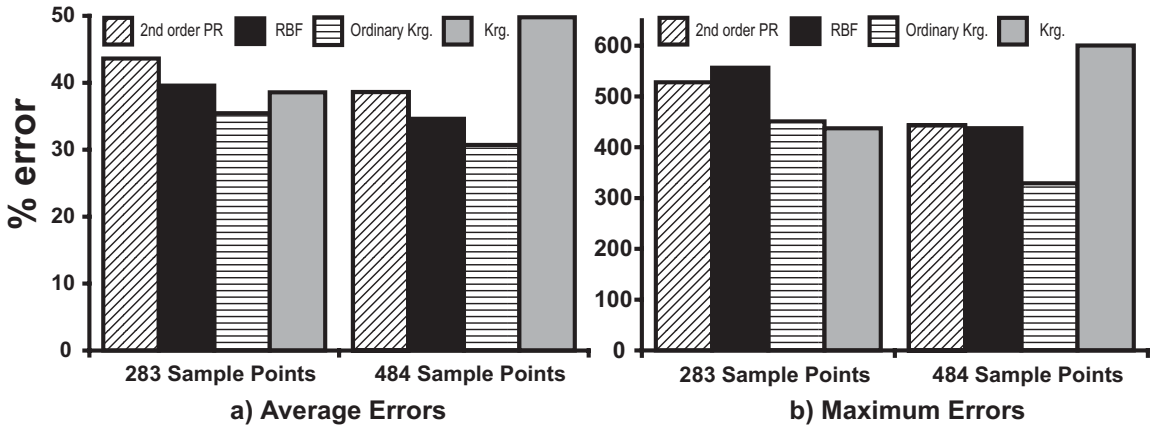

Figure 8.6: Errors in the surrogate stress constraint, relative to mean responses

Table 8.4: Fitting parameters for the ordinary kriging surrogates (283 sample points)

Parameter	$\mathbf{F_{4X}}$	$\mathbf{F_{4Y}}$	$\mathbf{F_{4Z}}$	$\mathbf{M_{4X}}$	$\mathbf{M_{4Y}}$	$\mathbf{M_{4Z}}$	**J**	**Stress Constraint**
ϑ_1	0.354	0.354	0.300	0.354	0.317	0.329	0.317	0.057
ϑ_2	0.258	0.258	0.216	0.258	0.235	0.235	0.219	0.030
ϑ_3	0.188	0.188	0.087	0.188	0.175	0.175	0.151	0.028
ϑ_4	0.137	0.137	0.130	0.177	0.139	0.130	0.112	0.028
ϑ_5	0.100	0.100	0.145	0.100	0.096	0.096	0.078	0.009
ϑ_6	0.073	0.073	0.035	0.073	0.072	0.072	0.055	0.020
ϑ_7	0.079	0.079	0.100	0.079	0.549	0.059	0.122	0.018
ϑ_8	0.039	0.039	0.030	0.039	0.039	0.044	0.099	0.017
ϑ_9	0.028	0.028	0.060	0.028	0.029	0.033	0.039	0.015
ϑ_{10}	0.035	0.024	0.232	0.035	0.556	0.540	0.065	0.100
ϑ_{11}	0.015	0.015	0.011	0.015	0.016	0.019	0.010	0.019
ϑ_{12}	0.011	0.011	0.187	0.011	0.012	0.534	0.042	0.013
ϑ_{13}	0.016	0.016	0.259	0.016	0.531	0.010	0.034	0.100
ϑ_{14}	0.010	0.010	0.030	0.013	0.010	0.011	0.019	0.028
ϑ_{15}	0.010	0.010	0.060	0.010	0.010	0.010	0.019	0.009
ϑ_{16}	0.010	0.010	0.019	0.012	0.010	0.010	0.019	0.016
ϑ_{17}	0.010	0.010	0.013	0.010	0.036	0.036	0.011	0.094

Table 8.5: Fitting parameters for the ordinary kriging surrogates (484 sample points)

Parameter	$\mathbf{F_{4X}}$	$\mathbf{F_{4Y}}$	$\mathbf{F_{4Z}}$	$\mathbf{M_{4X}}$	$\mathbf{M_{4Y}}$	$\mathbf{M_{4Z}}$	**J**	**Stress Constraint**
ϑ_1	0.354	0.354	0.289	0.354	0.317	0.538	0.289	0.056
ϑ_2	0.258	0.258	0.216	0.258	0.235	0.187	0.216	0.025
ϑ_3	0.188	0.188	0.161	0.188	0.175	0.134	0.161	0.022
ϑ_4	0.137	0.137	0.121	0.172	0.139	0.161	0.121	0.035
ϑ_5	0.100	0.100	0.090	0.100	0.096	0.070	0.090	0.025
ϑ_6	0.073	0.073	0.067	0.073	0.072	0.050	0.067	0.017
ϑ_7	0.079	0.079	0.097	0.079	0.059	0.075	0.201	0.022
ϑ_8	0.039	0.039	0.078	0.039	0.044	0.112	0.121	0.016
ϑ_9	0.028	0.028	0.028	0.046	0.029	0.045	0.028	0.005
ϑ_{10}	0.035	0.035	0.250	0.035	0.540	1.000	0.269	0.084
ϑ_{11}	0.015	0.015	0.016	0.015	0.016	0.010	0.016	0.011
ϑ_{12}	0.011	0.011	0.032	0.011	0.014	0.161	0.032	0.015
ϑ_{13}	0.016	0.016	0.482	0.016	0.531	0.145	0.216	0.100
ϑ_{14}	0.010	0.013	0.072	0.013	0.071	0.014	0.021	0.029
ϑ_{15}	0.010	0.010	0.034	0.010	0.010	0.058	0.031	0.015
ϑ_{16}	0.010	0.010	0.013	0.012	0.010	0.014	0.015	0.007
ϑ_{17}	0.010	0.010	0.040	0.010	0.036	0.030	0.040	0.037

Errors Based on Leave-One-Out Cross Validation

The second approach for quantifying the error is based on leave-one-out cross validation. In this procedure, the error is calculated as follows:

1. A single design point is removed from the OLH data used to fit the surrogate.

2. The surrogate is created using the remaining $(N_{sp} - 1)$ sample points.

3. The surrogate is evaluated at the left out design and compared to the actual response.

Thus, the cross validation error is given by

$$\varepsilon_i^{(cv)} = \frac{|y^{(i)} - \hat{y}^{(-i)}|}{\bar{y}} \tag{8.11}$$

Table 8.6: Fitting parameters for the more general kriging surrogates (283 sample points)

Parameter	$\mathbf{F_{4X}}$	$\mathbf{F_{4Y}}$	$\mathbf{F_{4Z}}$	$\mathbf{M_{4X}}$	$\mathbf{M_{4Y}}$	$\mathbf{M_{4Z}}$	**J**	**Stress Constraint**
ϑ_1	0.009	0.043	0.890	0.195	0.691	1.899	1.475	0.152
ϑ_2	0.006	0.006	0.006	0.012	0.071	0.026	0.016	0.152
ϑ_3	0.007	0.055	0.152	0.016	0.007	0.071	0.152	0.016
ϑ_4	0.691	1.475	0.152	1.475	2.445	0.251	1.475	0.152
ϑ_5	0.016	0.118	0.417	0.071	0.071	0.324	0.152	0.016
ϑ_6	0.033	0.043	0.006	0.118	0.417	0.071	0.152	0.152
ϑ_7	1.899	3.149	0.417	1.475	4.054	0.324	1.475	0.152
ϑ_8	0.152	0.251	0.055	0.071	0.016	0.152	0.152	0.016
ϑ_9	0.152	0.251	0.152	0.118	0.091	0.152	0.152	0.016
ϑ_{10}	0.152	0.324	1.899	0.324	4.054	1.475	1.475	1.475
ϑ_{11}	0.007	0.006	0.007	0.007	0.007	0.007	0.016	0.152
ϑ_{12}	0.016	0.007	0.324	0.007	0.091	0.324	0.152	0.016
ϑ_{13}	0.691	0.890	1.899	1.146	1.899	0.071	1.475	1.475
ϑ_{14}	0.016	0.055	0.091	0.033	0.152	0.007	0.152	0.152
ϑ_{15}	0.033	0.033	0.251	0.007	0.055	0.152	0.152	0.016
ϑ_{16}	0.016	0.071	0.033	0.152	0.033	0.009	0.016	0.152
ϑ_{17}	0.152	0.152	0.195	0.152	0.417	0.007	0.152	0.152
p_1	1.660	1.953	1.073	1.880	1.953	1.220	1.000	1.000
p_2	0.780	1.953	0.120	0.120	0.927	1.000	1.660	1.660
p_3	1.880	1.880	1.880	0.340	1.440	1.880	1.000	1.000
p_4	1.880	1.953	0.340	1.953	1.880	1.880	1.660	1.000
p_5	1.220	1.000	1.440	1.880	1.220	0.340	1.000	1.000
p_6	0.340	1.953	1.220	1.880	1.953	0.340	1.000	1.000
p_7	1.880	1.880	1.953	1.953	1.953	1.880	1.660	1.660
p_8	1.880	1.953	1.220	1.293	1.880	1.953	1.000	1.660
p_9	1.880	1.733	1.293	1.000	0.633	1.660	1.000	1.000
p_{10}	1.220	1.147	1.000	1.220	1.953	1.440	1.000	1.000
p_{11}	0.120	1.293	1.513	1.220	1.000	1.880	1.660	1.000
p_{12}	1.220	1.953	1.953	1.220	1.880	1.073	1.000	1.000
p_{13}	1.660	1.953	1.293	1.880	1.733	0.340	1.000	1.660
p_{14}	1.880	1.953	1.953	1.880	1.953	0.120	1.000	1.000
p_{15}	0.120	1.220	1.953	1.000	1.880	1.880	1.000	1.000
p_{16}	1.000	0.267	0.780	1.880	1.880	0.120	1.000	1.000
p_{17}	1.953	0.780	1.953	0.120	1.880	1.880	1.660	1.000

Table 8.7: Fitting parameters for the more general kriging surrogates (484 sample points)

Parameter	$\mathbf{F_{4X}}$	$\mathbf{F_{4Y}}$	$\mathbf{F_{4Z}}$	$\mathbf{M_{4X}}$	$\mathbf{M_{4Y}}$	$\mathbf{M_{4Z}}$	**J**	**Stress Constraint**
ϑ_1	0.016	0.016	0.890	0.537	0.417	4.054	1.475	0.016
ϑ_2	0.016	0.016	0.043	0.043	0.537	0.007	0.016	0.152
ϑ_3	0.152	0.152	0.152	0.033	0.071	0.417	0.016	0.016
ϑ_4	1.475	1.475	0.537	2.445	4.054	0.417	0.152	0.152
ϑ_5	0.152	0.152	0.118	0.071	0.006	0.152	0.152	0.152
ϑ_6	0.152	0.152	0.007	0.043	0.055	0.152	0.152	0.016
ϑ_7	1.475	1.475	0.691	3.149	1.475	0.691	1.475	0.152
ϑ_8	0.152	0.152	0.043	0.118	0.033	0.417	0.152	0.016
ϑ_9	0.152	0.152	0.152	0.324	0.043	0.152	0.152	0.152
ϑ_{10}	0.152	0.152	2.445	1.475	4.054	4.054	1.475	0.152
ϑ_{11}	0.016	0.016	0.118	0.033	0.007	0.071	0.152	0.152
ϑ_{12}	0.016	0.016	0.007	0.071	0.091	0.251	0.152	0.152
ϑ_{13}	0.152	0.152	1.899	0.890	1.475	0.691	1.475	0.016
ϑ_{14}	0.152	0.152	0.417	0.152	0.324	0.016	0.152	0.152
ϑ_{15}	0.016	0.152	0.324	0.026	0.016	0.006	0.152	0.152
ϑ_{16}	0.016	0.016	0.324	0.043	0.091	0.016	0.016	0.152
ϑ_{17}	0.016	0.152	0.152	0.033	0.020	0.043	0.152	0.152
p_1	1.000	1.660	1.440	0.340	1.293	1.807	1.000	1.000
p_2	1.000	0.340	1.953	1.880	1.660	1.953	0.340	1.000
p_3	1.000	1.000	1.807	0.340	0.707	1.880	1.660	1.000
p_4	1.660	1.660	0.560	1.953	1.733	1.953	1.000	1.000
p_5	1.000	1.660	1.660	1.440	1.660	1.880	1.000	1.000
p_6	1.660	1.660	1.880	0.780	0.927	0.120	1.660	1.000
p_7	1.660	1.660	1.293	1.880	1.293	1.953	1.000	1.000
p_8	1.000	1.000	1.733	1.880	1.367	1.880	1.000	1.000
p_9	1.000	1.660	1.953	1.880	1.880	0.340	1.000	1.000
p_{10}	1.000	1.000	1.880	1.733	1.953	1.953	1.000	1.000
p_{11}	1.000	1.660	0.487	1.513	1.880	0.633	1.000	1.000
p_{12}	1.000	1.660	1.880	1.880	1.953	1.293	1.000	1.000
p_{13}	1.660	1.000	1.660	1.953	1.953	1.587	1.660	1.000
p_{14}	1.000	1.000	1.807	0.707	1.000	1.293	1.000	1.000
p_{15}	1.000	1.660	1.880	1.220	1.220	1.440	1.660	1.000
p_{16}	1.660	1.000	0.340	1.880	1.807	1.807	1.000	1.000
p_{17}	1.000	1.000	1.880	1.880	1.880	1.953	1.000	1.000

where $\hat{y}^{(-i)}$ is the surrogate's prediction at the left out sample point when the surrogate is fit to the $(N_{sp}-1)$ remaining points. The average, maximum, and minimum leave-one-out cross validation errors can be written as:

$$\varepsilon_{avg}^{(cv)} = \frac{\sum_{i=1}^{N_{sp}} \varepsilon_i^{(cv)}}{N_{sp}} \tag{8.12}$$

$$\varepsilon_{max}^{(cv)} = \text{Max}\left\{\varepsilon_1^{(cv)}, \ldots, \varepsilon_{N_{sp}}^{(cv)}\right\} \tag{8.13}$$

$$\varepsilon_{min}^{(cv)} = \text{Min}\left\{\varepsilon_1^{(cv)}, \ldots, \varepsilon_{N_{sp}}^{(cv)}\right\} \tag{8.14}$$

The advantage of using leave-one-out cross validation is that a measure of the error can be obtained using only the simulated data used to create the surrogates, as opposed to conducting expensive simulations at additional test points which are only used to quantify error. However, leave-one-out cross validation errors represent the sensitivity of the surrogate to the left out designs, and may not adequately represent the error in the surrogate. Therefore, the purpose of comparing leave-one-out cross validation error with error based on additional test points is to determine whether the magnitude of error can be predicted without using additional test points. Note that the cross validation error in Eq. 8.11 is normalized by the mean responses from the 197 test points as in Eq. 8.7 so that errors based on Eqs. 8.7 and 8.11 can be directly compared.

The ratio of the leave-one-out cross validation errors to the errors based on test points are given in Tables 8.8 and 8.9 for the 6 surrogate hub shears and moments, the directly approximated objective function, and the surrogate stress constraint. Table 8.8 shows that the magnitude of the average error can be captured using leave-one-out cross validation,

Table 8.8: Ratio of average leave-one-out cross validation errors to average errors based on test points

Surrogate	**Sample Size**	$\mathbf{F_{4X}}$	$\mathbf{F_{4Y}}$	$\mathbf{F_{4Z}}$	$\mathbf{M_{4X}}$	$\mathbf{M_{4Y}}$	$\mathbf{M_{4Z}}$	**J**	**Stress Constraint**
Poly.	283	1.12	1.20	1.19	1.07	1.24	1.25	1.18	1.20
RBF	283	1.01	1.13	0.98	1.06	1.15	1.01	1.00	1.01
Ord. krg.	283	1.10	1.08	1.18	1.01	1.15	1.06	1.09	1.01
Krg.	283	1.06	1.16	0.96	1.15	1.40	1.01	1.05	1.00
Poly.	484	1.18	1.01	1.01	1.14	1.06	1.04	0.96	1.00
RBF	484	1.15	1.02	0.98	1.11	1.11	0.99	0.94	1.04
Ord. krg.	484	1.04	1.04	1.11	1.03	1.22	1.12	1.02	1.13
Krg.	484	1.07	0.98	1.06	1.31	1.15	1.12	1.04	0.96

with the largest difference occurring for the M_{4Y} kriging surrogate with 283 sample points where the cross validation error was 1.4 times larger than the error based on test points. Furthermore, the average cross validation error generally gave a more conservative (i.e. a ratio $>$ 1.0) estimate of the error over the entire design space.

Table 8.9 shows that leave-one-out cross validation also captured the magnitude of the maximum error, with the largest difference corresponding to the M_{4X} kriging surrogate with 484 sample points where the cross validation error was 3.22 times higher than the error based on test points. The maximum leave-one-out cross validation error was typically more conservative for the vibratory surrogates, but tended to underpredict the error in the stress constraint for the 484 point surrogates. So for the stress surrogate, whether or not the maximum cross validation error was a conservative measure of error was dependent on the number of sample points used to create the surrogate.

Table 8.9: Ratio of maximum leave-one-out cross validation errors to maximum errors based on test points

Surrogate	Sample Size	F_{4X}	F_{4Y}	F_{4Z}	M_{4X}	M_{4Y}	M_{4Z}	J	Stress Constraint
Poly.	283	1.38	1.47	1.84	1.08	1.74	1.11	1.31	1.10
RBF	283	1.29	1.21	1.55	1.45	1.33	1.08	1.25	1.08
Ord. krg.	283	1.18	1.08	1.31	1.75	1.38	1.05	1.35	1.26
Krg.	283	1.14	1.21	1.29	1.31	1.56	1.02	1.44	1.46
Poly.	484	1.04	0.90	1.02	1.33	0.89	1.03	0.94	0.60
RBF	484	1.35	1.08	1.04	3.07	1.36	1.28	1.23	0.68
Ord. krg.	484	1.07	1.08	1.16	1.62	1.33	1.41	1.37	0.76
Krg.	484	1.29	1.17	1.17	3.22	1.45	1.65	1.53	0.79

8.1.3 Robustness

In addition to the accuracy, another metric for quantifying the effectiveness of the surrogates is robustness, i.e. the capability of the approximation methods to accurately model different responses. The robustness measure indicates how sensitive the performance of an approximation method is to the type of response being modeled. The variance of the average and maximum error measures based on test points is used to quantify robustness [72]. The lower the variance, the more robust the approximation method. Figure 8.7 gives the variance of the errors for the 8 responses considered in this study: the 6 hub shears and moments, the overall objective function, and the stress constraint. Ordinary kriging is the most robust approximation method, and thus its performance fluctuates the least when modeling the responses in this study. Furthermore, the variance of each surrogate method, except the more general kriging, is lowered by increasing the number of sample points from 283 to 484. Therefore, for the responses considered in this study, increasing the number of sample points increases the robustness of the surrogates. This conclusion does not hold for

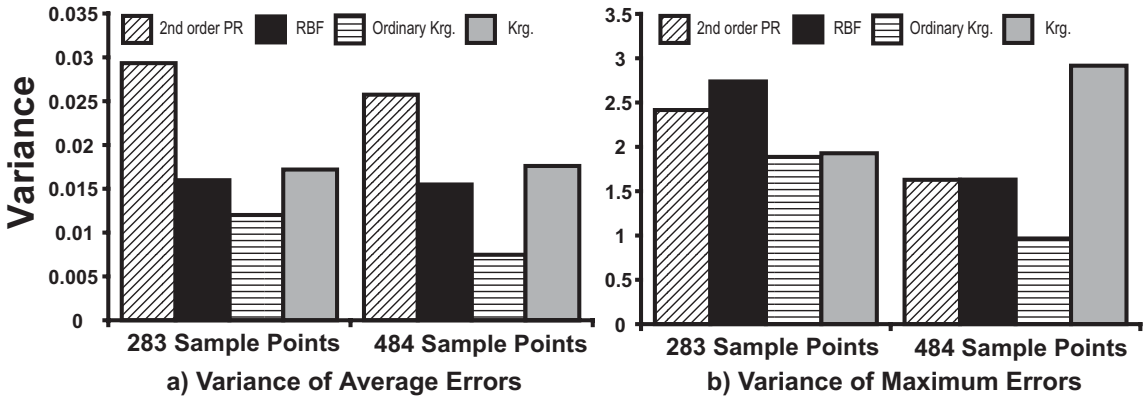

Figure 8.7: Variance of the average and maximum error measures (based on test points)

the more general kriging due to the ill-conditioned correlation matrix encountered when approximating the stress constraint.

8.1.4 Optimization Results

The surrogate based optimization (SBO) conducted in this study is *non-updating*, otherwise known as the one-shot approach, which means that the surrogate is not updated with objective function evaluations as the optimization progresses. While it is important to use an updating method so that optimization does not lead to regions of high uncertainty in the surrogate, the focus of this portion of the study was on the effectiveness of the approximation techniques and not on the search algorithm. Optimization of the surrogate objective functions was conducted with the Multi-Island Genetic Algorithm in iSIGHT [1]. It was necessary to include the surrogate stress constraint since optimizing without it led to designs for which stresses exceeded the Von Mises failure condition at the blade root. Helicopter simulations were conducted at the predicted optimum designs in order to obtain the "actual" amount of vibration reduction.

Table 8.10 gives the optimization results when using the underlying hub shears and moments to build the surrogate objective function. Note that vibration reduction is computed relative to the vibration levels of a baseline blade resembling an MBB BO-105 blade. Table 8.10 shows that all approximation methods lead to significant vibration reduction of over 50% and ordinary kriging leads to the best designs, with vibration reduction of 67.4% with 283 sample points and 66.1% with 484 sample points.

Table 8.11 shows that significant vibration reduction can also be achieved when directly approximating the objective function, however the amount of reduction was generally smaller than what is indicated by the results in Table 8.10. This is because by approximating the underlying responses, the behavior of the vertical shear F_{4Z} is captured, which is important since much of the reduction in the objective function is due to reduction of the vertical shear. The importance of approximating the vertical shear is illustrated in Fig. 8.8, in which the optimal vibratory loads from ordinary kriging surrogates using 283 sample points are compared with the MBB BO-105 baseline values. Figure 8.8 shows that approximating the underlying responses leads to 77% reduction of F_{4Z}, while approximating the overall objective function results in 67% reduction of the vertical shear. It is also clear from Fig. 8.8 that approximating the underlying responses results in higher values for the five other shears and moments compared to direct approximation of the objective function. Thus, approximating the underlying responses led to a superior design because capturing the behavior of the individual shears and moments leads to a more effective reduction of the vertical shear F_{4Z}.

Tables 8.10 and 8.11 also show that increasing the number of fitting points did not al-

Table 8.10: Comparison of predicted and "actual" vibration reductions using approximate underlying responses

Surrogate	**Sample Size**	**Predicted Reduction**	**Actual Reduction**	ω_{L1}	ω_{F1}	ω_{T1}
Poly.	283	100.0 %	66.4 %	0.664	1.067	5.032
RBF	283	100.0 %	55.2 %	0.605	1.064	3.783
Ord. krg.	283	92.6 %	67.4 %	0.611	1.060	4.583
Krg.	283	95.3 %	51.0 %	0.617	1.064	4.136
Poly.	484	100.0 %	58.9 %	0.602	1.059	3.953
RBF	484	100.0 %	57.7 %	0.600	1.059	4.165
Ord. krg.	484	94.9 %	66.1 %	0.616	1.061	4.483
Krg.	484	94.2 %	64.5 %	0.624	1.063	4.383

Table 8.11: Comparison of predicted and "actual" vibration reductions when directly approximating the objective function

Surrogate	**Sample Size**	**Predicted Reduction**	**Actual Reduction**	ω_{L1}	ω_{F1}	ω_{T1}
Poly.	283	394.4 %	64.4 %	0.605	1.061	4.325
RBF	283	132.8 %	51.9 %	0.600	1.060	4.054
Ord. krg.	283	144.4 %	63.8 %	0.615	1.061	4.404
Krg.	283	105.6 %	52.8 %	0.602	1.060	4.314
Poly.	484	222.4 %	45.0 %	0.622	1.063	3.956
RBF	484	136.4 %	52.2 %	0.602	1.061	3.958
Ord. krg.	484	162.8 %	54.7 %	0.613	1.061	4.283
Krg.	484	124.0 %	53.2 %	0.600	1.060	4.234

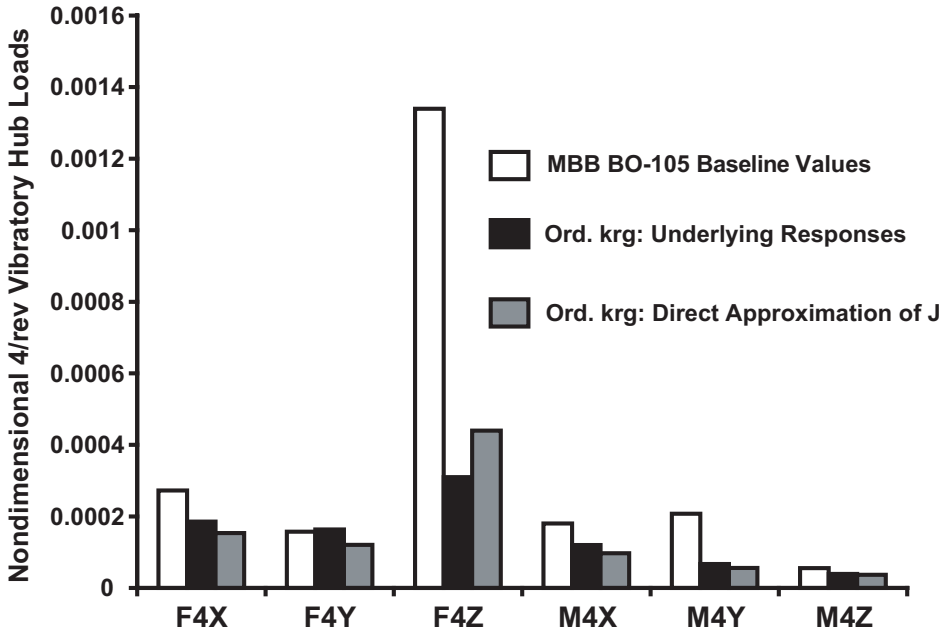

Figure 8.8: Comparison of the optimum vibratory loads when using surrogate underlying responses and when directly approximating the objective function

ways improve the optimum designs, and in some instances resulted in worse designs. This is probably due to the 283 sample set having a best feasible design with 52% vibration reduction, which was better than the 48% reduction associated with the best feasible design in the 484 data set. The polynomial surrogates were the most adversely affected by increasing the number of sample points. Furthermore, optimizing the surrogate did not always lead to a better design than the best design in the set of fitting points used to create the surrogates. This occurs because all of the surrogates are inaccurate at the optimum designs. For instance, Table 8.10 shows that optimizing the more general kriging surrogate based on 283 sample points led to 51% actual reduction, while the surrogate predicts 95.3% reduction. The discrepancy between the predicted reduction and the actual reduction shows that the surrogate is not accurate at the optimum design. Moreover, the optimum design is worse than the best feasible design from the OLH, which produced 52% reduction. So optimizing

the surrogate led to a region of the design space where the surrogate was not accurate, and the optimum design happened to be worse than the best feasible design from the fitting data. Although none of the surrogates accurately predict the amount of vibration reduction at the optimum designs, optimizing the surrogates generally led to superior designs than the best feasible designs in the optimum Latin hypercubes.

The fundamental rotating frequencies corresponding to the optimum designs are also given in Tables 8.10 and 8.11. No two optimum blade designs have the same set of fundamental frequencies, which means that each surrogate led to a different optimum blade design. These results suggest that, at the flight condition characterized by BVI induced vibrations, there are many local optima in the design space. Table 8.12 gives the predicted vibration reduction from each surrogate at all of the optimum designs from Table 8.10. The results from Table 8.12 show that every surrogate is capable of identifying designs with reduced vibration levels. Therefore, all of the surrogates are able to capture the fact that the objective function has many local optima, which would be important if it were desirable to obtain many prospective optimum designs in addition to the global optimum.

The optimum designs were checked for robustness to small perturbations by perturbing each design variable by $\pm 3\%$ from the optimum value, as done in Ref. 105. None of the perturbed designs resulted in more than 5% difference from the original objective function value, and there was an average change in objective function values of only 1.2% over all the perturbed designs. So the optimum designs were robust to small perturbations in the designs, which indicates that the regions around the optimum designs are reliable regions of reduced vibration designs.

Table 8.12: Predicted vibration reduction by each of the surrogates at all of the optimum designs from Table 8.10

Optimum	Sample Size	Predicted Reduction by Poly.	Predicted Reduction by RBF	Predicted Reduction by Ord. krg.	Predicted Reduction by Krg.
Poly.	283	100.0 %	83.3 %	15.5 %	95.2 %
RBF	283	69.3 %	100.0 %	24.4 %	72.7 %
Ord. krg.	283	21.5 %	40.9 %	92.6 %	70.7 %
Krg.	283	93.2 %	83.7 %	71.6 %	95.3 %
Poly.	484	100.0 %	84.1 %	61.3 %	74.5 %
RBF	484	63.2 %	100.0 %	34.1 %	58.0 %
Ord. krg.	484	74.1 %	62.7 %	94.9 %	72.5 %
Krg.	484	33.8 %	89.6 %	38.6 %	94.2 %

8.2 A Multiple Surrogate Approach

It is clear that none of the surrogates was the best in terms of all the evaluation metrics considered in Section 8.1. Therefore, the advantages of the collaborative use of multiple surrogates, including a weighted average model, as well as some pitfalls associated with only using a single surrogate, are explored in more detail in this section. The helicopter parameters are the same as those used to generate the results in Section 8.1. In this section, the following approximation methods were considered: (1) full and reduced term polynomial response surfaces, (2) kriging with a linear trend function and all $p_k = 2$, and (3) radial basis neural networks (RBNN).

The fitting times associated with each of the approximation methods are presented in Table 8.13. Note that the abbreviation "(red.)" indicates the use of reduced term polynomial surrogates (see Section 7.3.2). The individual surrogates were generated on 3.2 Ghz Xeon processors, while the 40 processors from the Linux cluster were used to generate the

Table 8.13: Fitting times associated with the approximation methods

Surrogate	Sample Size[1]	Fitting Time
Poly.	283	< 1 s
Poly(red.)	283	< 1 s
KRG	283	15 – 20 s
RBNN	283	30 – 50 s
Wtd. Avg.	283	7 – 10 min.
Wtd. Avg.(red.)	283	7 – 10 min.
Poly.	484	< 1 s
Poly(red.)	484	1 – 2 s
KRG	484	50 s – 1 min.
RBNN	484	1.5 – 2 min.
Wtd. Avg.	484	30 – 40 min.
Wtd. Avg.(red.)	484	30 – 40 min.

[1]The 283 and 484 sample points required 53 and 82 hours to generate respectively.

weighted average models. The leave-one-out cross validation error needed to generate the weighted models is suitable for parallel computation since the error at left out points can be calculated independently of the errors at the other points. These results demonstrate that constructing the surrogates in this study, including weighted average models, required little additional time compared to the time needed to generate the fitting data.

8.2.1 Weighted Average Surrogate Construction

The weight coefficients necessary to define the weighted average surrogates, which are determined according to Eq. 7.52, are given in Tables 8.14 – 8.15. The weight coefficients obtained when using the full term polynomial response surface are given in Table 8.14. Generally, the kriging surrogate has the highest weight for all responses and both sample sizes in Table 8.14. When the reduced term polynomial is used in place of the full term polynomial, as shown in Table 8.15, the polynomial is weighted the most for all responses

Table 8.14: Weight coefficients for the weighted average surrogates, with full term polynomial

Weight Coefficient	Sample Size	$\mathbf{F_{4X}}$	$\mathbf{F_{4Y}}$	$\mathbf{F_{4Z}}$	$\mathbf{M_{4X}}$	$\mathbf{M_{4Y}}$	$\mathbf{M_{4Z}}$	J	Stress Constraint
w_{poly}	283	0.407	0.395	0.322	0.374	0.306	0.291	0.333	0.353
w_{krg}	283	0.478	0.473	0.458	0.460	0.449	0.412	0.461	0.443
w_{RBNN}	283	0.115	0.132	0.219	0.167	0.245	0.297	0.206	0.205
w_{poly}	484	0.422	0.436	0.360	0.378	0.340	0.333	0.379	0.400
w_{krg}	484	0.449	0.422	0.425	0.448	0.405	0.381	0.419	0.424
w_{RBNN}	484	0.129	0.142	0.215	0.175	0.255	0.286	0.203	0.176

Table 8.15: Weight coefficients for the weighted average surrogates, with reduced term polynomial

Weight Coefficient	Sample Size	$\mathbf{F_{4X}}$	$\mathbf{F_{4Y}}$	$\mathbf{F_{4Z}}$	$\mathbf{M_{4X}}$	$\mathbf{M_{4Y}}$	$\mathbf{M_{4Z}}$	J	Stress Constraint
w_{poly}	283	0.497	0.493	0.431	0.472	0.406	0.401	0.443	0.433
w_{krg}	283	0.406	0.396	0.385	0.388	0.385	0.349	0.385	0.388
w_{RBNN}	283	0.097	0.110	0.183	0.140	0.209	0.250	0.172	0.179
w_{poly}	484	0.465	0.474	0.409	0.427	0.384	0.377	0.424	0.436
w_{krg}	484	0.415	0.394	0.393	0.413	0.378	0.356	0.388	0.399
w_{RBNN}	484	0.120	0.132	0.199	0.161	0.238	0.267	0.188	0.165

and sample sizes. The RBNN generally has the lowest weight. Since the RBNN corresponds to the highest leave-one-out cross validation errors, their responses are the most sensitive to the individual data points used to fit the model. This suggests that the poor performance of the RBNN is due to over-fitting of the data. Note that the reduced term polynomial could have been included with the other 3 surrogates in a single weighted average model. However, this would have introduced bias toward 2^{nd} order polynomials, while the focus of this study was to demonstrate the effectiveness of the weighted average approach using sufficiently distinct approximation methods.

8.2.2 Surrogate Accuracy Results

The predictive capabilities of the individual and weighted average surrogates were quantified using a set of data points not included in the construction of the surrogates. The predicted responses from the surrogates were then compared to the "actual" responses at the test points. The test points came from a 200 point OLH, of which 197 had converged trim solutions. None of the blade designs from the 197 test points were coincident with the blade designs from the two OLH's used to create the surrogates. Using the test points, the absolute percent error is given by

$$\varepsilon_i = \frac{|y^{(i)} - \hat{y}^{(i)}|}{\bar{y}} \tag{8.15}$$

where $y^{(i)}$ is the "actual" response computed by the helicopter simulation, $\hat{y}^{(i)}$ is the response predicted by the surrogate at the i^{th} test point. For the vibratory load errors, $\bar{y}$ is the mean of the absolute values of the responses from the 197 test points, while for the errors in the surrogate stress constraint,

$$\bar{y} = \frac{\sigma^2_{allowable}}{3} \ . \tag{8.16}$$

The average and maximum errors are given in Figs. 8.9 and 8.10 respectively for 7 responses – 6 underlying hub shears and moments and the stress constraint. Among the individual surrogates for each response, the lowest average errors range from $2 - 53\%$ and the highest average errors range from $5 - 69\%$ for the 283 sample set. By comparison, the average errors of the weighted average surrogates range from $2 - 53\%$ and always

correspond to lower errors than the worst approximation method. These results demonstrate that the weighted average surrogates performed as well as the best individual surrogates, while protecting against the poor performance of the worst approximation method for all 7 responses. A similar result is obtained for the 484 point sample set where the lowest average errors in Fig. 8.9(b) range from $3 - 55\%$ while the average errors of the weighted average surrogates range from $2 - 52\%$.

For the 283 point sample set, the kriging surrogate has the lowest average error of the individual surrogates for each response, while for some responses with the 484 point sample set, the polynomials correspond to the lowest average errors. So the choice of the "best" surrogate in terms of approximating over the entire design space is dependent on the sample size for the responses considered in this study. However, the weighted average surrogates performed as well as the best approximation methods regardless of sample size, which exemplifies the advantage of this approach: by using the weighted average surrogate approach, it is unnecessary to reconsider the identification of the most accurate approximation method each time a factor associated with the surrogates, such as sample size, is changed.

Similar to the results for average error, Fig. 8.10 shows that the weighted average surrogates typically perform as well as the best individual surrogate in terms of maximum error. For the 283 and 484 point sample sets, the lowest maximum errors among the individual surrogates are $32 - 331\%$ and $30 - 313\%$ respectively, while the weighted average surrogate maximum errors range from $37 - 368\%$ and $40 - 339\%$. It is worth noting that even though the weighted average surrogates are constructed using a global error measure – see

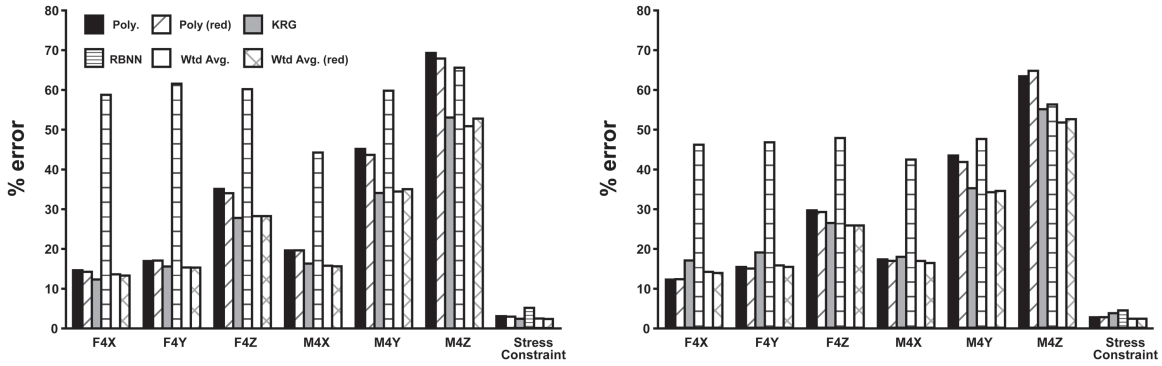

(a) 283 Sample Points (b) 484 Sample Points

Figure 8.9: Average errors of the underlying vibratory loads and stress constraint

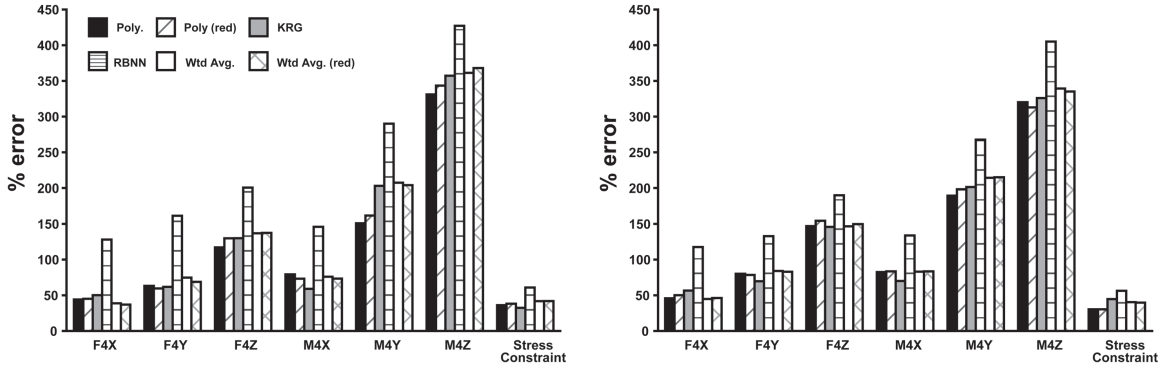

(a) 283 Sample Points (b) 484 Sample Points

Figure 8.10: Maximum errors of the underlying vibratory loads and stress constraint

Eq. 7.55 – they still perform well compared to the individual surrogate models in terms of maximum error, which is a local error measure.

The errors in the surrogate objective function are given in Figs. 8.11 and 8.12 for both methods of forming the approximate objective function. In terms of average error, kriging is the best individual approximation method, with $19 - 24\%$ errors for both sample sizes. For both methods of approximating the objective function and both sample sizes, the weighted average surrogates perform as well as the kriging surrogates in terms of average error. The largest difference in average error between the weighted average surrogates and the kriging surrogate is only 2% and occurs in the case of the 484 point data set when

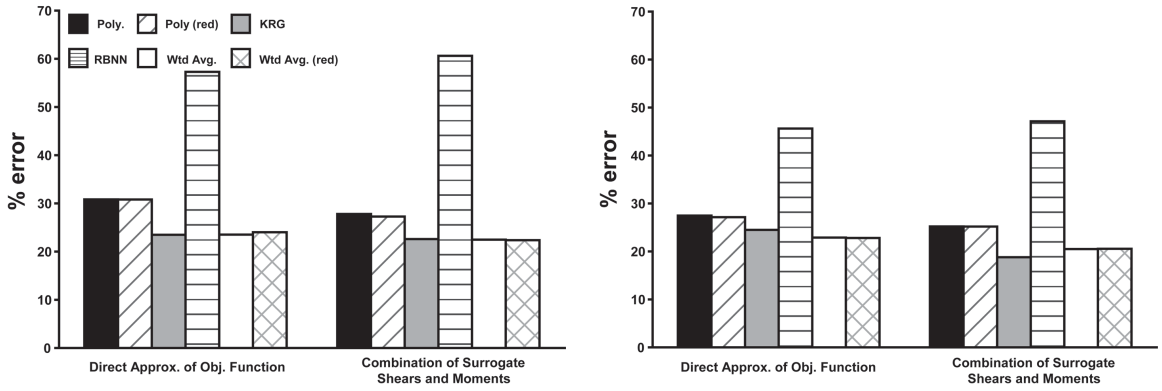

(a) 283 Sample Points (b) 484 Sample Points

Figure 8.11: Average errors in the surrogate objective function

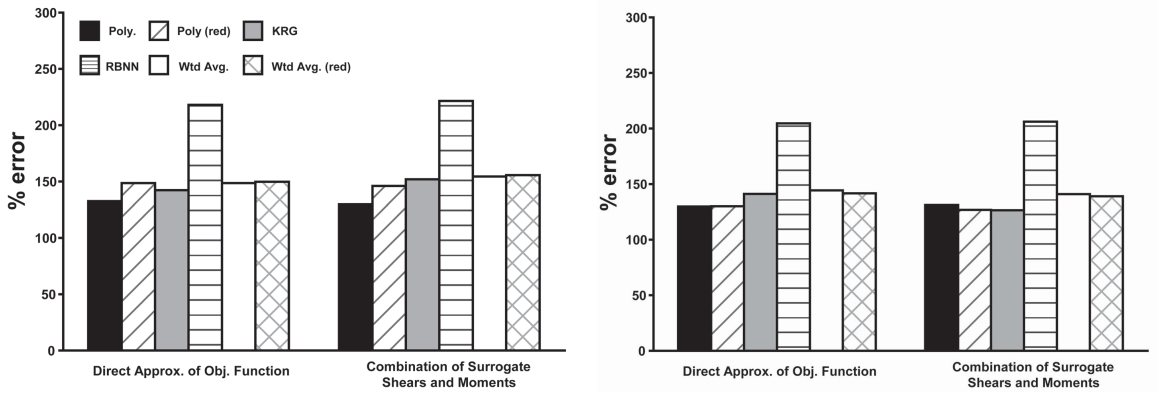

(a) 283 Sample Points (b) 484 Sample Points

Figure 8.12: Maximum errors in the surrogate objective function

combining the underlying responses to form the approximate objective function. In terms of maximum error, the weighted surrogates never produce an error more than 24% above the error from the best individual surrogate, and always perform better than the worst surrogate. So regardless of the method used to form the approximate objective function, the weighted average surrogates performed as intended.

A comparison of the errors in Figs. 8.9 through 8.12 with the weight coefficients in Tables 8.14 – 8.15 shows that the surrogate with the highest weight is not necessarily the most accurate when using test points to measure error. For example, consider the case of

approximating the overall objective function directly. The results in Table 8.15 indicate that reduced term polynomials are more accurate than kriging surrogates when using the GMSE as the global error measure. However, Fig. 8.11 shows that the kriging surrogates are more accurate than the reduced term polynomials in terms of the average error based on test points. This example illustrates a major issue with attempting to identify the most accurate individual surrogate for a given application: the most accurate approximation method may be dependent on the metric used to quantify error. This is not an issue with weighted average surrogates since they generally predict as accurately as the best individual surrogate, regardless of the metric used to quantify error.

It is interesting to note that increasing the sample size from 283 to 484 generally had little effect on the accuracy of the surrogates. This indicates that for the 17 dimensional design space, increasing the number of fitting points from 283 to 484 was not sufficient to significantly enhance the surrogates' predictions for the responses considered in this study.

8.2.3 Optimization Results

Optimization results based on surrogate objective functions and constraints are presented in this section. Optimization of the surrogate objective functions was conducted with the Multi-Island Genetic Algorithm in iSIGHT [1]. The genetic algorithm was set to run for 200,000 total objective function evaluations. This number was determined by numerical experimentation. Optimization of all surrogate objective functions for a given sample set were conducted in parallel since they can be optimized independently.

Table 8.16 gives the optimization results when using the underlying hub shears and

Table 8.16: Optimization results using surrogate underlying responses

Surrogate	Sample Size[1]	Optimization Time (hours)	Predicted Reduction	Actual Reduction	Actual Stress Margin	ω_{L1}	ω_{F1}	ω_{T1}
Poly.	283	3	100.0 %	66.4 %	0.017	0.671	1.062	5.036
Poly(red.)	283	3	100.0 %	67.3 %	0.014	0.641	1.059	4.679
KRG	283	3.5	94.2 %	59.0 %	0.008	0.613	1.059	4.176
RBNN	283	5	94.9 %	53.7 %	0.016	0.624	1.059	4.334
Wtd. Avg.	283	7	95.4 %	61.3 %	0.003	0.601	1.055	4.285
Wtd. Avg.(red.)	283	7	96.7 %	63.9 %	0.008	0.604	1.057	4.120
Poly.	484	3	100.0 %	58.9 %	0.006	0.608	1.056	3.958
Poly(red.)	484	3	100.0 %	62.2 %	0.007	0.603	1.056	3.919
KRG	484	4	87.0 %	68.7 %	0.008	0.621	1.058	4.560
RBNN	484	5	98.7 %	52.4 %	0.006	0.603	1.056	4.018
Wtd. Avg.	484	8	88.3 %	68.1 %	0.003	0.618	1.059	3.866
Wtd. Avg.(red.)	484	8	89.5 %	70.2 %	0.003	0.615	1.059	3.796

[1]The 283 and 484 sample points required 53 and 82 hours to generate respectively.

moments to build the surrogate objective function. Note that vibration reduction results are presented relative to the vibration levels of a baseline blade resembling an MBB BO-105 blade. The best individual surrogate differs with the sample size. For the 283 point sample set the reduced term polynomial produced the best design, with 67.3% vibration reduction, while for 484 points, kriging produced the best design, with 68.7% reduction. Significant vibration reduction is also obtained with the weighted average surrogates, which produce up to 63.9% vibration reduction with 283 sample points and up to 70.2% reduction with 484 sample points. The average of the Euclidean distances between all of the optimum designs corresponding to 283 sample points is equal to 40% of the distance between the two furthest corners of the design space. The maximum and minimum distances among the optimum designs are 56% and 13% of the distance between the two furthest corners respectively. Similarly, for the 484 point sample set, the average, maximum, and minimum Euclidean distances relative to the maximum dimension of the design space are 33%, 53%, and 8% respectively. These results indicate that optimization of the various surrogates led to designs in different regions of the design space.

Since optimization was conducted in parallel, 7 hours were needed to optimize all objective functions corresponding to 283 sample points in Table 8.16. By comparison, optimization of a single surrogate required at least 3 hours. So optimization of all surrogates required 4 additional hours, which is relatively insignificant compared to the 53 hours needed to generate the 283 sample points. Similar results for the 484 sample set are clear from Table 8.16.

Optimization results corresponding to direct approximation of the overall objective function are given in Table 8.17. The full term polynomial led to the best design among the individual surrogates for the 283 sample set, while the RBNN, which is the least accurate surrogate, led to the best design for the 484 point sample set. Furthermore, the full term polynomial is the worst single surrogate with 484 sample points. These results represent extreme examples in the sense that the best individual surrogate for one sample set is the worst surrogate for another sample set, and the least accurate surrogate led to the best design in one instance. Thus, optimizing the least accurate surrogate proved to be beneficial, especially considering it was relatively inexpensive to optimize all surrogates. The average, maximum, and minimum Euclidean distances relative to the maximum dimension of the design space are 33%, 51%, and 18% respectively for the 283 point data set, and 33%, 43%, and 18% respectively for the 484 point sample set.

Tables 8.16 and 8.17 show that among the individual surrogates, the approximation method which led to the best design depended on the sample size. Therefore, if the best individual approximation method based on one sample set were the only method used with the other sample set, inferior designs would be obtained compared to those found by op-

Table 8.17: Optimization results when directly approximating the objective function

Surrogate	Sample Size	Optimization Time (hours)	Predicted Reduction	Actual Reduction	Actual Stress Margin	ω_{L1}	ω_{F1}	ω_{T1}
Poly.	283	2	394.4 %	64.4 %	0.005	0.610	1.058	4.330
Poly(red.)	283	2	512.3 %	60.1 %	0.005	0.605	1.057	4.231
KRG	283	2	120.0 %	54.1 %	0.006	0.600	1.055	4.252
RBNN	283	4	93.9 %	57.4 %	0.009	0.602	1.055	4.420
Wtd. Avg.	283	4	234.9 %	70.5 %	0.008	0.604	1.055	4.538
Wtd. Avg.(red.)	283	4	221.7 %	65.0 %	0.000	0.604	1.059	3.871
Poly.	484	2	222.4 %	45.0 %	0.001	0.627	1.060	3.960
Poly(red.)	484	2	207.1 %	50.0 %	0.000	0.600	1.058	3.710
KRG	484	2	145.1 %	55.8 %	0.000	0.606	1.057	3.981
RBNN	484	4	97.4 %	67.5 %	0.000	0.631	1.057	4.670
Wtd. Avg.	484	4	116.7 %	67.6 %	0.010	0.620	1.057	4.602
Wtd. Avg.(red.)	484	4	129.2 %	58.8 %	0.008	0.625	1.056	4.380

timizing multiple surrogates. In addition, optimization of the weighted average surrogates produced superior designs than any of the individual approximation methods in some instances. So, given that optimization of multiple surrogates results in a small additional cost compared to the cost of generating the fitting data, optimization of multiple surrogates including weighted average models is superior to only considering a single surrogate.

The different fundamental blade frequencies presented in Tables 8.16 and 8.17, along with the Euclidean distances between optimum designs, demonstrate that optimization of multiple surrogates was useful for locating various reduced vibration designs in the BVI flight condition. Although all of the optimum designs in Tables 8.16 and 8.17 are different, they all result in significant reduction of the vertical shear, F_{4Z}, which is the primary mechanism for reducing the objective function corresponding to this flight condition. This is illustrated in Fig. 8.13, where the best and worst designs – 70.5% and 45.0% vibration reduction respectively – from Tables 8.16 and 8.17 are compared with the MBB BO-105 baseline vibratory loads. For these two designs, the vertical shear is reduced by 74% and 41% respectively. While the other vibratory loads are also reduced, the vertical shear is the

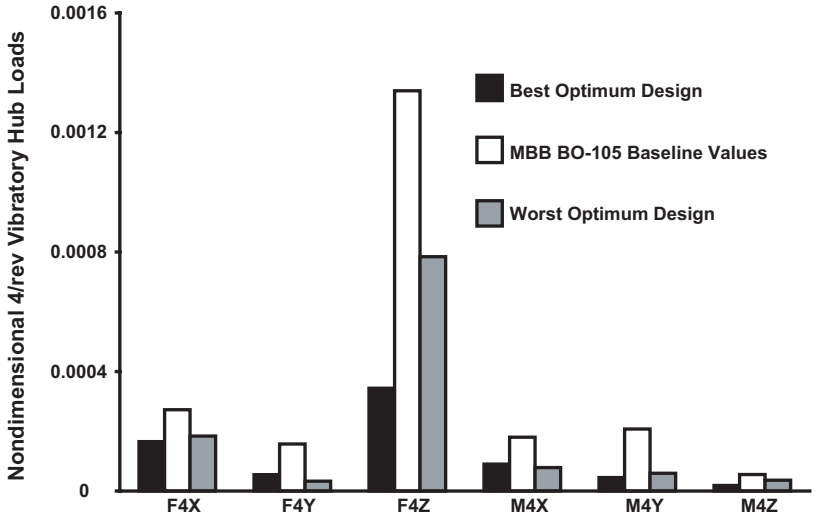

Figure 8.13: Comparison of the best and worst optimum designs

largest component and therefore its reduction is most critical for minimizing the objective function. Furthermore, all of the designs in Tables 8.16 and 8.17 correspond to stress margins < 0.02, which implies that the stresses in the optimum blades are relatively close to the allowable stress.

The significant differences in predicted and actual amounts of vibration reduction in Tables 8.16 and 8.17 indicate that the surrogates are inaccurate at their respective optimum designs. Furthermore, the surrogates were susceptible to predicting impractical amounts of vibration reduction, i.e. $\geq 100\%$. Thus it was critical for this problem to conduct simulations at each optimum design in order to obtain the actual amount of reduction. It is important to note that while the surrogates were not accurate everywhere in the design space, they still led to reduced vibration designs.

In order to illustrate the effects of errors in the individual surrogate constraints on optimization results, the predicted vibration reduction from each surrogate at all of the optimum designs from Table 8.17 are given in Table 8.18, along with predicted stress margins

Table 8.18: Predicted vibration reduction and stress margins by each of the surrogates

Optimum	Sample Size	Predicted Reduction & Stress Margin w/ Poly.	Predicted Reduction & Stress Margin w/ Poly(red.)	Predicted Reduction & Stress Margin w/ KRG	Predicted Reduction & Stress Margin w/ RBNN	Predicted Reduction & Stress Margin w/ Wtd. Avg.	Predicted Reduction & Stress Margin w/ Wtd. Avg.(red.)
Poly.	283	394% (0.0147)	341% (0.0080)	99% (0.0761)	91% (0.0001)	196% (0.0383)	205% (0.0324)
Poly(red.)	283	571% (-0.0002)	512% (0.0001)	115% (0.0083)	94% (-0.0191)	262% (-0.0003)	287% (-0.0002)
KRG	283	298% (-0.0180)	283% (-0.0098)	120% (0.0840)	91% (0.0005)	173% (0.0298)	187% (0.0275)
RBNN	283	427% (-0.0515)	300% (-0.0482)	90% (0.1141)	94% (0.0001)	203% (0.0295)	184% (0.0207)
Wtd. Avg.	283	484% (-0.0263)	417% (-0.0640)	119% (0.0407)	93% (0.0000)	235% (0.0083)	247% (-0.0130)
Wtd. Avg.(red.)	283	387% (0.0464)	378% (0.0435)	99% (0.0620)	92% (0.0002)	193% (0.0436)	222% (0.0427)
Poly.	484	222% (0.0076)	200% (0.0077)	72% (0.0074)	93% (-0.0386)	133% (-0.0007)	130% (-0.0002)
Poly(red.)	484	215% (0.0047)	207% (0.0045)	82% (0.0056)	93% (-0.0379)	135% (-0.0025)	137% (-0.0022)
KRG	484	108% (0.0001)	104% (0.0003)	145% (0.0068)	90% (-0.0426)	120% (-0.0044)	118% (-0.0043)
RBNN	484	48% (-0.0149)	37% (-0.0012)	104% (0.1076)	97% (0.0004)	81% (0.0380)	75% (0.0410)
Wtd. Avg.	484	154% (-0.0286)	146% (-0.0223)	102% (0.0625)	78% (0.0060)	117% (0.0152)	116% (0.0154)
Wtd. Avg.(red.)	484	185% (-0.0002)	185% (0.0005)	86% (0.0045)	91% (-0.0108)	124% (-0.0001)	129% (0.0002)

in parentheses. While all surrogate objective functions predict that each optimum design is a reduced vibration design, some designs were missed due to errors in the surrogate constraints. For example, among the individual approximation methods based on 283 sample points, the full term polynomial surrogate objective function predicts that the optimum design corresponding to the RBNN results in 427% reduction, which is superior to the 394% predicted reduction corresponding to its own optimum. However, as indicated by the stress margin, the full term polynomial surrogate stress constraint incorrectly predicts that the RBNN optimum design yields. Thus, inaccuracies in the surrogate constraints may lead away from designs which are predicted to have better objective function values.

Table 8.18 also illustrates how the errors in the surrogate objective functions may lead to inferior designs. For example, the kriging surrogate stress constraint based on 283 sample points correctly predicts that the full term polynomial design, which is superior to the kriging optimum in terms of actual vibration reduction, is feasible. However, the kriging surrogate objective function predicts that the superior design corresponds to 99% vibration reduction, while predicting 120% reduction for the inferior kriging optimum. Therefore,

the kriging surrogate objective function led to an inferior design compared to the full term polynomial because it incorrectly predicted that the kriging optimum was better than the full term polynomial optimum.

8.2.4 Global Sensitivity Analysis Results

The variability in the surrogate objective functions due to the most significant design variables are presented in this section. All results in this section are based on direct approximation of the overall objective function. Figures 8.14 – 8.18 shows the contributions to the total variability from main effects and interactions among design variables. Design variables which are predicted to account for less than 3% of the total variability are considered to be relatively unimportant, and therefore are not shown. In addition, Figs. 8.14 – 8.18 also give the total variability from all of the depicted design variables, as well as the total variability from the remaining design variables which individually account for less than 3% of the variance. Note that results generated with RBNN's are not depicted because all design variables were predicted to account for $5 - 9\%$ of the total variability. Thus, the GSA based on RBNN's predicts that all of the design variables essentially have equal importance. However, this does not preclude the use of weighted average surrogates in GSA since they are different functions than the RBNN's given that relatively little weight is placed on the RBNN's.

From Figs. 8.14 – 8.18 it is clear that the GSA predicts t_1 at the 25%, 50%, and 100% blade stations are the three most important design variables, no matter what sample size or approximation method is used in the analysis. However, beyond this observation, the

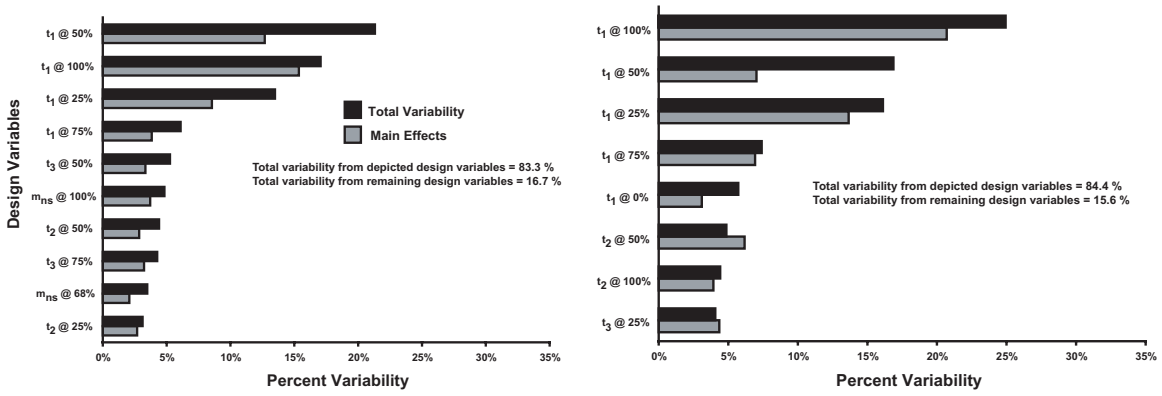

(a) Poly., 283 sample points (b) Poly., 484 sample points

Figure 8.14: Contribution to the variability in the objective function from the most significant design variables using full term polynomial surrogates

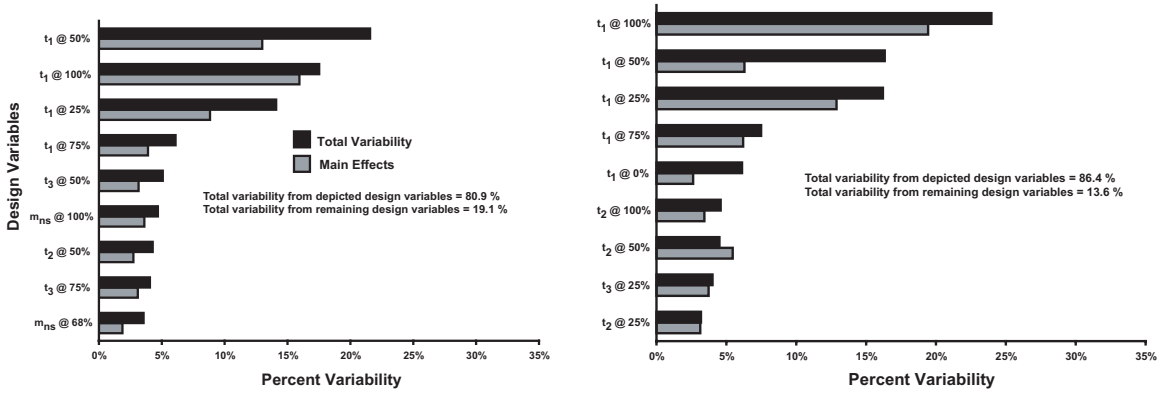

(a) Poly.(red), 283 sample points (b) Poly.(red), 484 sample points

Figure 8.15: Contribution to the variability in the objective function from the most significant design variables using reduced term polynomial surrogates

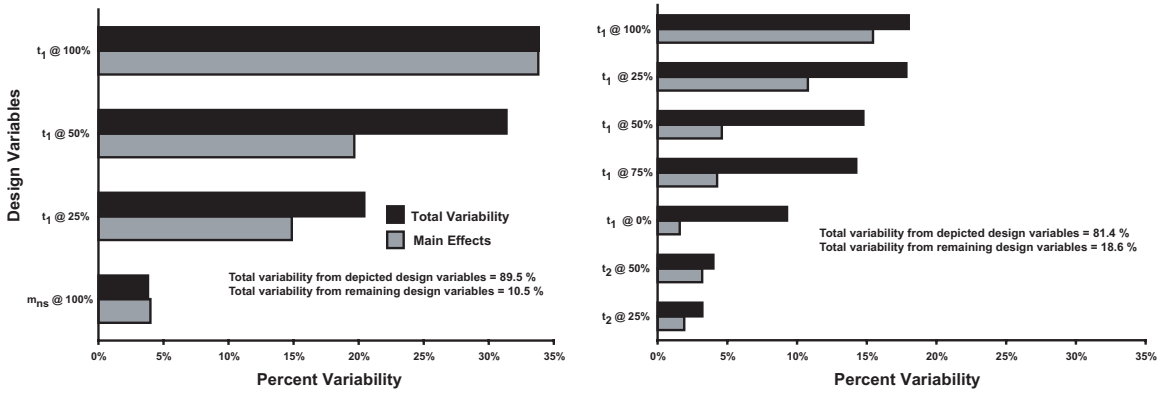

(a) KRG, 283 sample points (b) KRG, 484 sample points

Figure 8.16: Contribution to the variability in the objective function from the most significant design variables using kriging surrogates

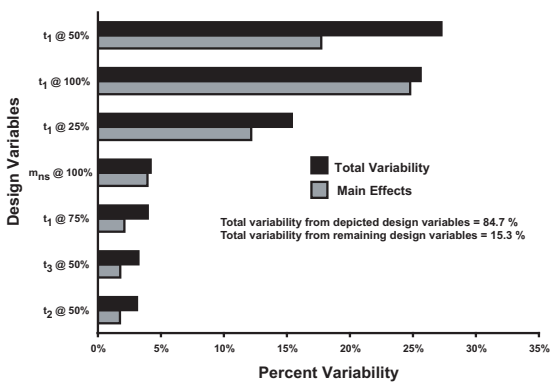

(a) Wtd. Avg., 283 sample points

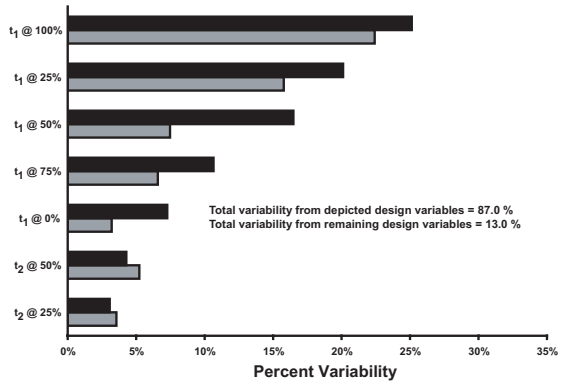

(b) Wtd. Avg., 484 sample points

Figure 8.17: Contribution to the variability in the objective function from the most significant design variables using weighted average surrogates with the full term polynomial

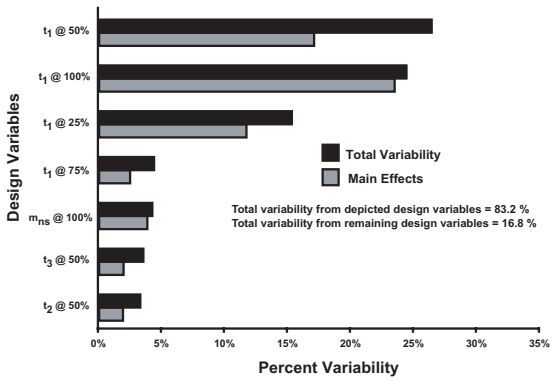

(a) Wtd. Avg.(red), 283 sample points

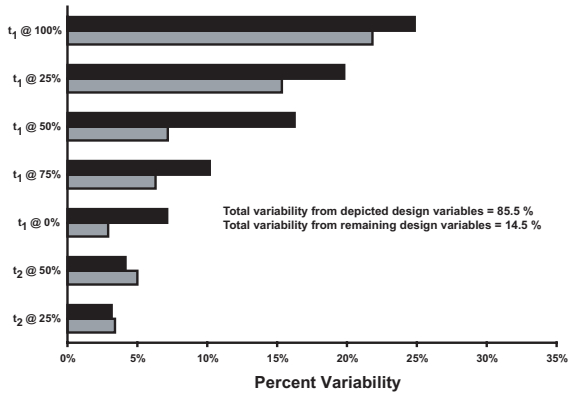

(b) Wtd. Avg.(red), 484 sample points

Figure 8.18: Contribution to the variability in the objective function from the most significant design variables using weighted average surrogates with the reduced term polynomial

results of the global sensitivity analysis are highly dependent on the sample size and the approximation method. For instance, using the kriging surrogate and 283 sample points, t_1 at the 50% station is predicted to be the second most important variable. In contrast, this variable accounts for the third most variability in the objective function when using 484 sample points to create the surrogate. Furthermore, increasing the number of sample points changes which variables the GSA determines to be the most important for each surrogate. Comparing the results corresponding to the kriging surrogate with the other surrogates in Figs. 8.14 - 8.18 with 283 sample points illustrates the effect of using different surrogates. The kriging surrogate predicts that only 4 variables are significant and account for 89.5% of the total variability, while GSA with the other surrogates predicts that 7 – 10 design variables are significant.

In order to verify that the unimportant variables according to the GSA have little effect on the predictive capabilities of the surrogates, the surrogates were reconstructed after eliminating the unimportant design variables and the errors using the 197 test points were compared to the errors when all of the design variables were included in the fitting process. The results of this comparison are summarized in Table 8.19, which gives the ratios of the reconstructed surrogates' errors to the errors obtained when using all of the design variables. The most extreme application of the GSA occurs in the case of kriging with 283 sample points, in which 13 of the 17 design variables were considered unimportant. In this case, the average error of the 4 dimensional kriging surrogate was 13.9% higher than the 17 dimensional kriging surrogate, while the maximum error was essentially the same. Other than the case of kriging with 283 sample points, the reconstructed surrogates after the GSA

Table 8.19: Ratio of errors after unimportant design variables are eliminated

Surrogate used in GSA	Sample Size	Number of Eliminated Variables	Ratio of Average Errors	Ratio of Maximum Errors
Poly	283	7	0.822	1.025
Poly(red)	283	8	0.787	0.971
KRG	283	13	1.139	1.023
Wtd. Avg.	283	10	1.030	0.878
Wtd. Avg.(red)	283	10	1.014	0.880
Poly	484	9	0.917	0.980
Poly(red)	484	8	0.930	1.015
KRG	484	10	0.951	0.896
Wtd. Avg.	484	10	1.043	0.811
Wtd. Avg.(red)	484	10	1.048	0.838

were only slightly less accurate or even *more* accurate – i.e. ratios less than 1 – than the original surrogates. For example, the reduced term polynomial based on 283 sample points is 21.3% more accurate than the original surrogate in terms of average error. Instances in which the reconstructed surrogates are more accurate suggest that the eliminated variables are unimportant since they impair the predictive capabilities of the surrogates when included.

The GSA was also utilized to refine the search for the optimum with each surrogate. After the unimportant design variables were removed, the reconstructed surrogates were optimized. The unimportant variables were fixed at their original optimum values from optimization when all variables were included in the surrogate construction. The results of this analysis are given in Table 8.20. Using the GSA to refine the optimization search generally resulted in superior designs to the original optimal designs. The most significant improvement occurred in the case of kriging surrogates based on 484 sample points, where the refined search led to an additional 13.8% vibration reduction. The weighted average

Table 8.20: Optimization results after GSA

Surrogate	Sample Size	Actual Reduction (all variables)	Actual Reduction (after GSA)	Actual Stress Margin (after GSA)	ω_{L1}	ω_{F1}	ω_{T1}
Poly.	283	64.4 %	70.4 %	0.005	0.623	1.058	4.521
Poly(red)	283	60.1 %	66.9 %	0.003	0.621	1.057	4.454
KRG	283	54.1 %	58.0 %	0.017	0.640	1.058	5.139
Wtd. Avg.	283	70.5 %	60.2 %	0.004	0.602	1.057	4.071
Wtd. Avg.(red)	283	65.0 %	64.8 %	0.003	0.613	1.059	3.952
Poly.	484	45.0 %	52.4 %	0.006	0.626	1.057	4.346
Poly(red)	484	50.0 %	60.7 %	0.008	0.618	1.056	4.512
KRG	484	55.8 %	69.6 %	0.001	0.606	1.055	4.569
Wtd. Avg.	484	67.6 %	63.9 %	0.006	0.608	1.056	4.395
Wtd. Avg.(red)	484	58.8 %	65.1 %	0.004	0.616	1.056	4.497

surrogates were the only models in which the refined optimization did not always produce a better design. The failure of the refined search based on GSA to lead to better designs in the case of some of the weighted average surrogates does not necessarily mean that the GSA led to the removal of important design variables. Rather, this suggests that the original optimization over all 17 design variables found the best design based on the weighted average surrogates' responses, and refining the search is unlikely to lead to better designs.

8.3 Efficient Global Optimization of Helicopter Rotor Blades

In this section, optimization results using EGO with a weighted expected improvement function are compared to one-shot optimization results. The results are based on the helicopter parameters and BVI flight condition described in Section 8.1. Since the purpose of this section is to evaluate the performance of EGO, a simplified helicopter model consisting of the reduced design variable Configuration 2 (see Section 7.1.2) and no stress constraint was considered. Ordinary kriging (see Section 7.3.3) was used since the results in Section

8.1 indicate that the more general kriging offers no clear advantage. To start the EGO algorithm, an optimum Latin hypercube (OLH) of 100 design points was generated. Since the computational cost of evaluating the actual constraints is low, the constraints at each point in the OLH were evaluated first. Designs that violated the constraints were removed from the data set so that expensive forward flight simulations would not be wasted. From the 100 point OLH, 53 blade designs were feasible and had converged trim solutions. In addition, OLH's of 250 and 500 points, resulting in 143 and 284 feasible designs respectively, were used to obtain one-shot optimization results.

For each iteration of the EGO algorithm, the 25 best designs from the genetic algorithm optimization of the WEIF were selected for parallel computation; i.e $N_p = 25$ in Fig. 7.5. In addition, a variation of the EGO algorithm was considered in which the infill sample points for each iteration were the 25 best designs from direct optimization of the surrogate objective function using a genetic algorithm; these results are referred to as "GA updating". In order to ensure that each of the 25 designs were different, the following criterion was used: a design was considered to be different from another if there was at least a 0.5 mm difference in *any* of the thickness design variables or if there was a difference of at least 5% of the baseline cross-sectional mass in any of the non-structural mass design variables. Each simulation took about 6 hours to complete on a Linux cluster with 1.8 GHz Opteron processors. The EGO algorithm was run for at least 2 iterations and was stopped if the best design from the current iteration was not better than the best blade design from previous iterations. Optimization of the WEIF and the surrogate objective function was conducted with the Multi-Island Genetic Algorithm in the iSIGHT [85] software package.

Table 8.21: One-shot optimization results

# of feasible designs from the OLH	Best % Vibration Reduction from the OLH	Actual % Vibration Reduction at the One-shot Optimum Design
53	18.52%	4.50%
143	41.60%	17.47%
284	53.39%	33.58%

All optimization results are compared to a baseline blade with cross-sectional properties resembling an MBB BO-105 blade, which is considered to have good vibration characteristics.

Table 8.21 shows the results for one-shot optimization of kriging surrogates built from OLH's with 53, 143 and 284 design points, compared to the best design in each OLH. For all three kriging models in Table 8.21, the optimum design returned by the genetic algorithm optimization is *worse* than the best design in the OLH used to create the surrogate. This is because at certain designs, the kriging surrogates predict a negative value for the vibration objective function, which is not realistic given Eq. 7.1. So when the surrogates are minimized directly, the optimization algorithm will move toward regions with negative objective function values, even though the surrogates are inaccurate in these regions. This illustrates the danger of directly optimizing a surrogate for a function with behavior that is difficult to capture: if the surrogate is not accurate everywhere in the design space, direct optimization may lead to a region in the design space with inferior designs.

Efficient Global Optimization results based on updating the surrogate model with additional blade designs selected by the WEIF and the genetic algorithm are shown in Table 8.22 and Fig. 8.19. Table 8.22 summarizes the amount of vibration reduction achieved,

Table 8.22: Vibration Reduction using EGO

EGO Setting	**Number of Function Evaluations**	**% Vibration Reduction**
$w = 0.0$	72	55.15%
$w = 0.2$	128	65.18%
$w = 0.4$	128	45.00%
$w = 0.5$	153	54.55%
$w = 0.6$	128	44.09%
$w = 0.8$	178	64.53%
$w = 1.0$	153	54.35%
GA updating	178	54.68%

while Fig. 8.19 shows the best value of the vibration objective function after each iteration of the EGO algorithm. The results presented in Table 8.22 and Fig. 8.19 were generated by applying EGO to the vibration objective function with the user defined parameter w set to 0.0, 0.2, 0.4, 0.5, 0.6, 0.8, or 1.0. For each application of EGO, w was held fixed and the algorithm was run until the stopping condition was reached.

The results for $w = 0.5$ would also be the results if an unweighted expected improvement function were considered. For $w = 0.5$, the maximum amount of vibration reduction is 54.55%, and the algorithm finishes after 153 objective function evaluations. This is clearly superior to the 53.39% vibration reduction obtained with 284 objective function evaluations. This comparison indicates that the expected improvement function is effective in reducing the number of function evaluations needed to find optimum designs compared to using a relatively large number of sample points from a space-filling scheme. Other than $w = 0.4$ and $w = 0.6$, every weight setting resulted in vibration reduction greater than 53.39%, and with less function evaluations than the 284 in Table 8.21. Therefore, other than at $w = 0.4$ and $w = 0.6$, the WEIF was superior to the one-shot approach. Furthermore, settings of $w = 0.2$ and $w = 0.8$ resulted in the best designs with 65.18%

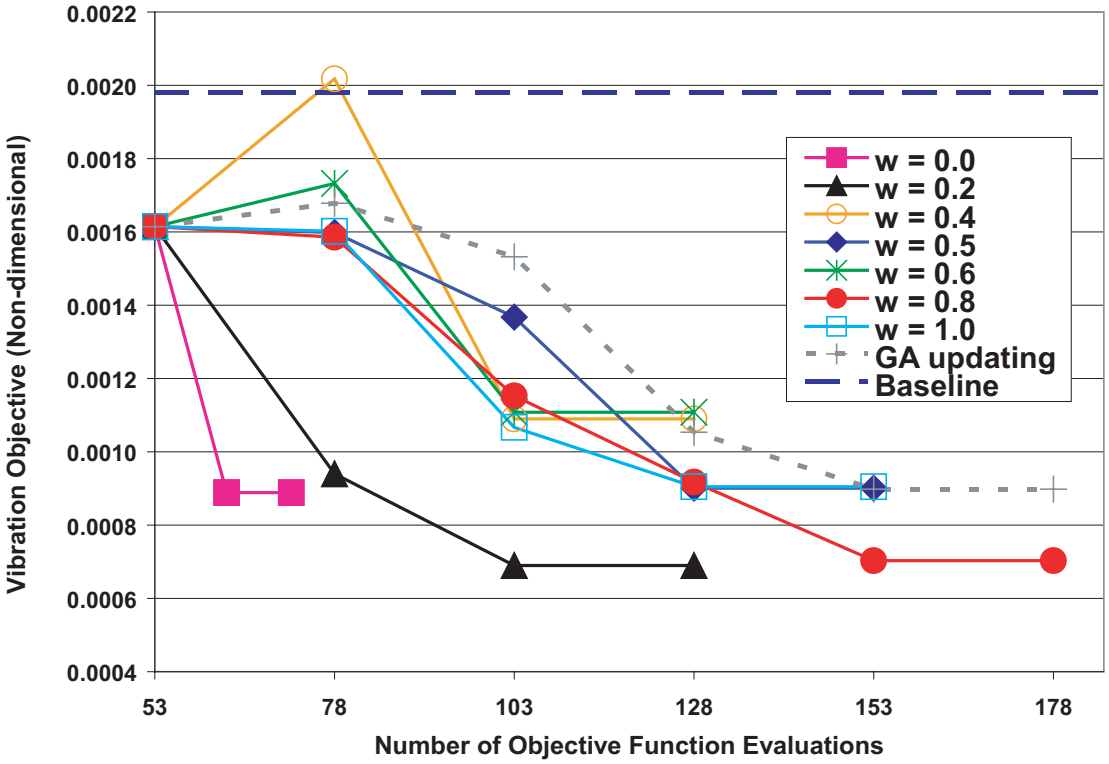

Figure 8.19: Change in the objective function during EGO

and 64.53% reduction respectively. The problem considered in this study is an example of a situation in which a promising design was located in a region of high uncertainty, and with a more global setting of $w = 0.2$, the EGO algorithm was able to locate it. Note that in the results for $w = 0$, the surrogate is not updated with 25 additional sample points each iteration because only 10 out of the 25 designs returned from the genetic algorithm optimization of the WEIF in the first iteration had converged trim solutions, while only 9 designs had converged trim solutions in the second iteration. Thus for $w = 0$, only 19 total sample points were added to the initial 53 points from the OLH, resulting in a total of 72 complete objective function evaluations.

The importance of accounting for uncertainty is further illustrated by comparing the results in Fig. 8.19 for $w = 0.8$ and 1.0 with the results corresponding to genetic algorithm

(GA) updating. For $w = 0.8$, a superior design is found compared to the best design from GA updating. Thus even a small weighting on the global search characteristics was beneficial compared to a purely local search. The setting of $w = 1.0$ results in essentially the same amount of vibration reduction as the GA updating, but in 1 less iteration of EGO. Therefore, the $w = 1.0$ setting resulted in a more efficient optimization algorithm than GA updating. This can be explained by examining the normal distribution term (which is an explicit function of the uncertainty measure $s(\mathbf{x})$) in Eq. 7.62, since this term accounts for the only difference between optimization of the WEIF with $w = 1.0$ and direct optimization of the surrogate objective function $\hat{y}_{\text{krg}}$. For an amount of predicted reduction given by $y_{\min} - \hat{y}_{\text{krg}}$, the normal distribution function will be high for low values of $s(\mathbf{x})$ and vice versa. Therefore, maximization of $(y_{\min} - \hat{y}_{\text{krg}})\Phi_{\text{dist}}(\frac{y_{\min} - \hat{y}_{\text{krg}}}{s})$ will favor blade designs which are predicted to lower vibrations *and* at which the uncertainty in the surrogate's predictions is low. In contrast, direct optimization of the surrogate objective function using the genetic algorithm will favor designs which are predicted to lower vibration, but the uncertainty in the surrogate's predictions is not explicitly accounted for. Thus the inclusion of the uncertainty measure during optimization accounted for the improved efficiency of the EGO algorithm when using a setting of $w = 1.0$ compared to the GA updating.

Figures 8.20a – h show the design variables corresponding to the best designs as EGO progresses. These results show that for this problem, the change in design variables during EGO is different for each weight setting, and thus the performance of EGO is sensitive to the weight setting. Even though all weight settings resulted in significant vibration reduction, each setting led to a different optimum design. This suggests that there are numerous

local optima in the vibration objective function at this flight condition.

Figures 8.21a – f show the variation of the vibratory shears and moments corresponding to the best designs as the EGO algorithm progresses. Every weight setting resulted in designs with significant reduction (over 70%) in the vertical shear F_{4Z}, while other vibratory components increased for some weight settings. Figure 8.22 compares the baseline hubloads with those corresponding to the best design from EGO. In Fig. 8.22 it is clear that the vertical shear is the dominant vibratory component of the baseline blade, and therefore the majority of the reduction in the objective function comes from the significant reduction in the vertical shear.

The errors in the surrogates are given after each iteration of EGO in Fig. 8.23. The errors were calculated by comparing the predicted response of the surrogates to the actual response at 427 test points, which were obtained by combining the sample data of the 143 point and 284 point OLH's from Table 8.21. The errors in the surrogates tend to increase as additional sample points were added during the optimization. This is because only regions of high expected improvement are sampled in EGO, which led to a decline in the predictive capabilities of the surrogate in regions of low expected improvement. Although the accuracies diminished slightly, the more global weightings of $w = 0.0$ and $w = 0.2$ had negligible effects on the accuracy of the surrogates, which is not surprising since the goal of using more global weightings is to reduce the uncertainty, or error, in the surrogate.

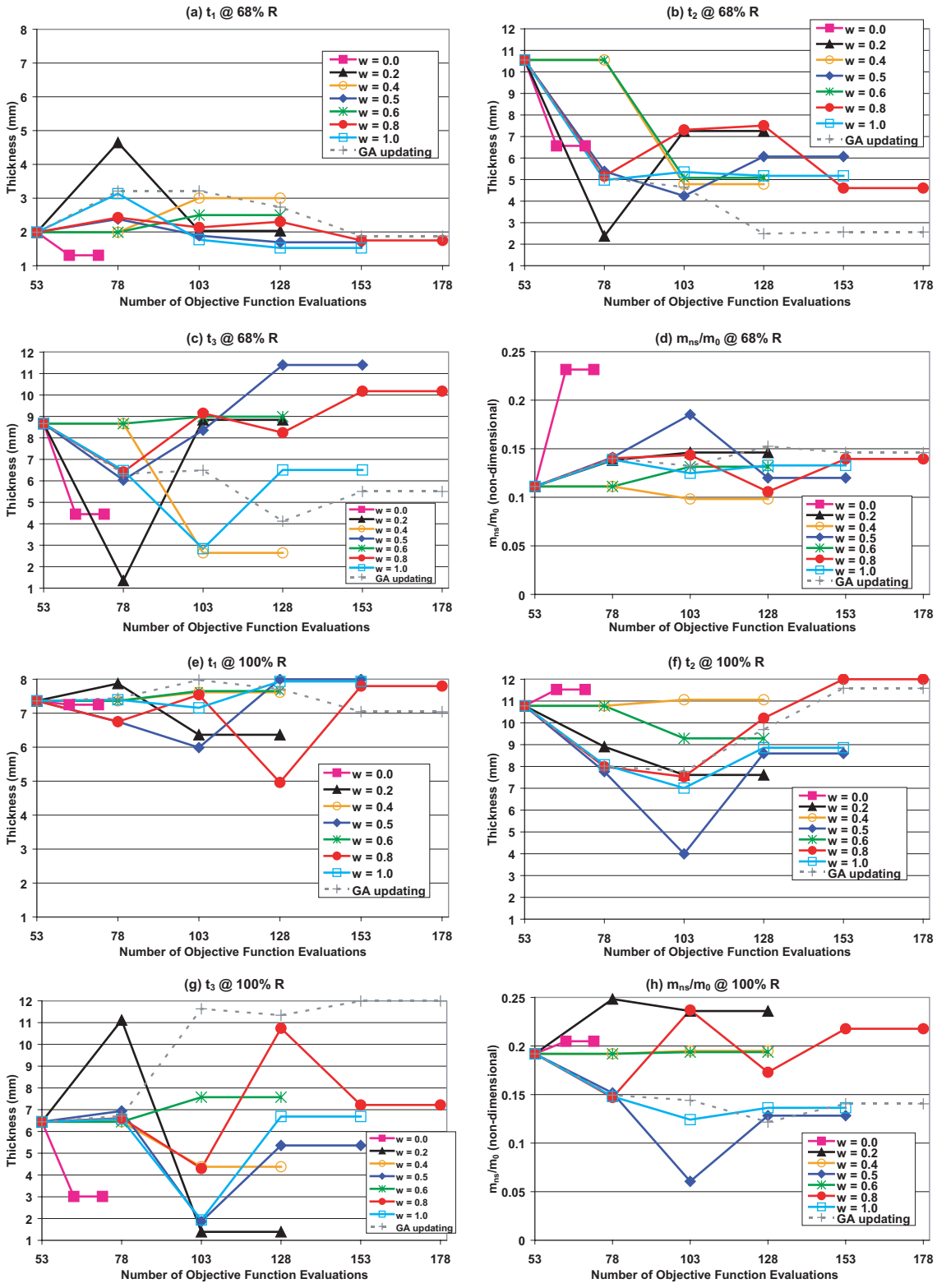

Figure 8.20: Change in the best blade design during EGO

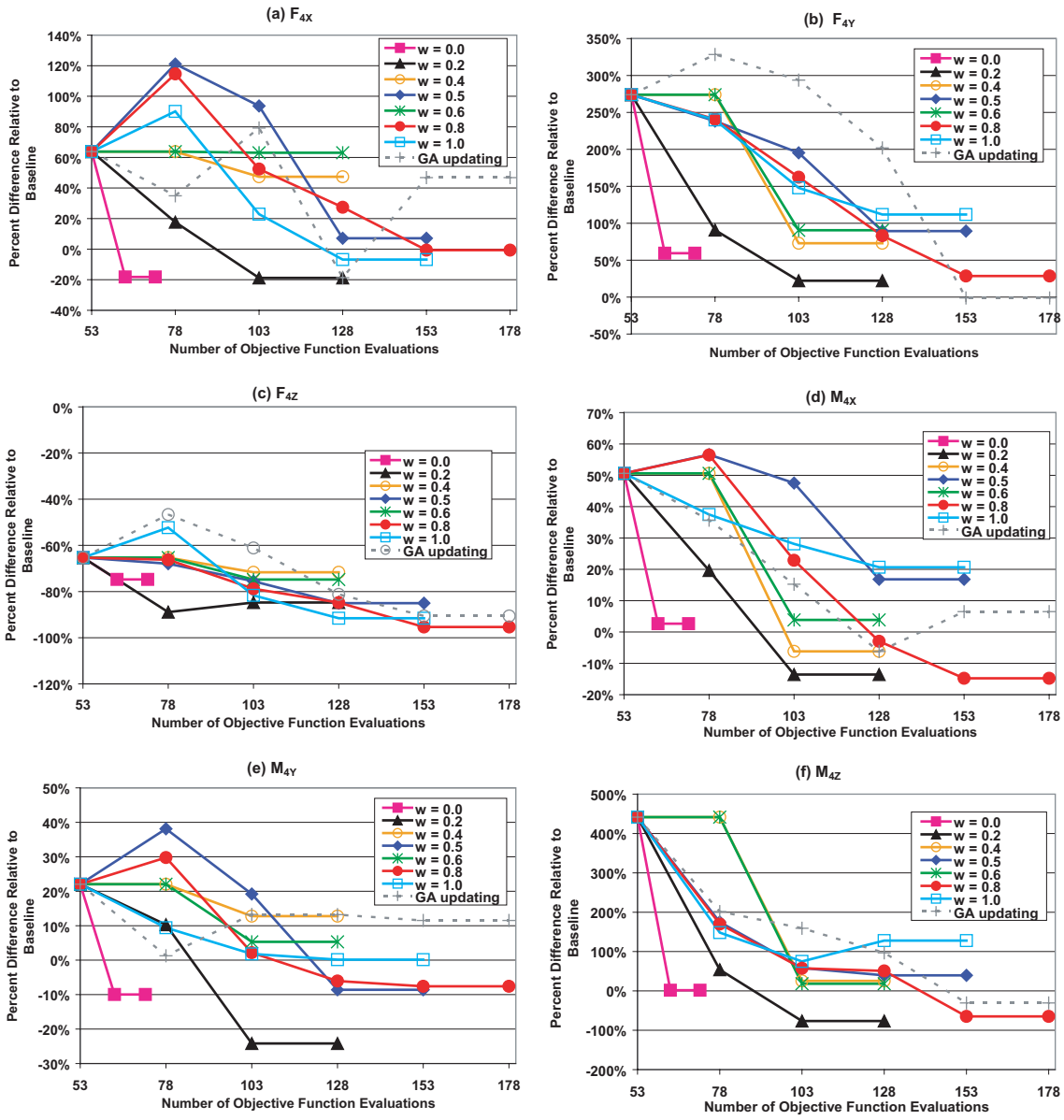

Figure 8.21: Change in the vibratory loads at the best designs during EGO

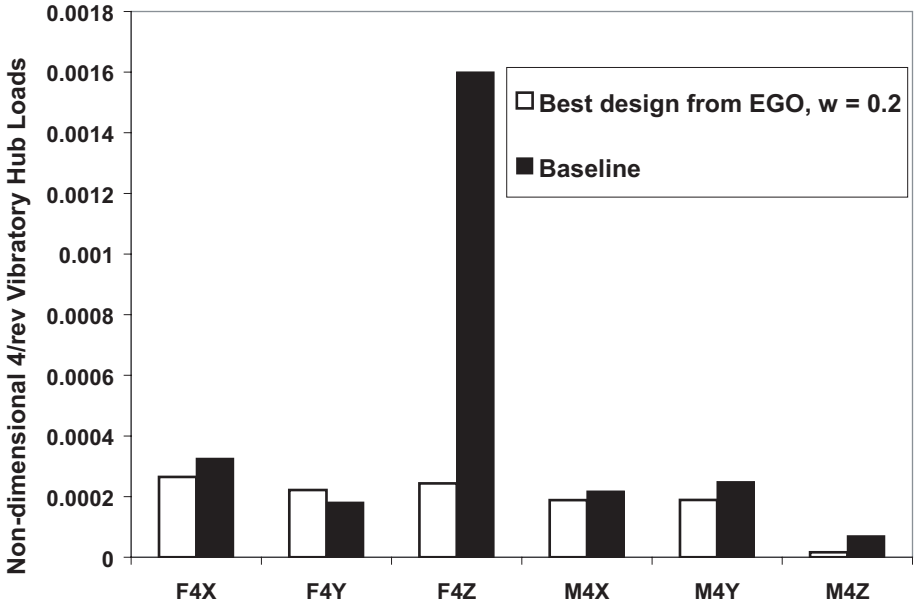

Figure 8.22: Comparison of the vibratory loads of the best design from EGO and the baseline blade

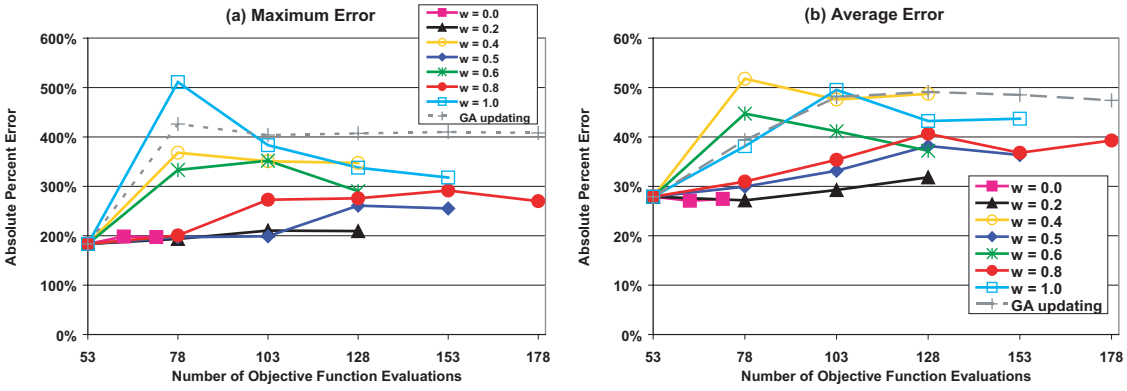

Figure 8.23: Errors in the surrogates after each iteration of EGO

Chapter IX

Vibration Reduction Over the Entire Flight Envelope

In this chapter, SBO was used to optimize the blade at low advance ratios, where BVI induced vibrations dominate, as well as high advance ratios where dynamic stall induced vibrations are critical. These flight regimes are the most critical in terms of helicopter vibrations. Therefore, it is imperative that advanced rotor blade designs address vibration characteristics at both flight conditions. The two objective functions given by Eq. 7.1 evaluated in the BVI regime, and the dynamic stall regime, are denoted J_{BVI} and J_{DS} respectively. All multi-objective function optimization results in this study were generated using the EGO-based approaches described in Section 7.4.3. The goal in treating this problem in a multi-objective manner, which had not been considered in previous studies, was to identify a Pareto optimal design suitable for vibration reduction over the entire flight envelope. The helicopter configuration and flight condition parameters used in all the computations are given in Table 9.1, and the 17 design variables based on Configuration 1 were

Table 9.1: Rotor and helicopter parameters for both flight conditions

Rotor Data	
$R = 4.91\,\mathrm{m}$	$\Omega = 425\,\mathrm{RPM}$
$N_b = 4$	$c_b = 0.05498R$
$\beta_p = 2.5^\circ$	$C_{do} = 0.01$
$\theta_{\mathrm{pt}} = -8^\circ$	$C_W = 0.005$
$\sigma = 0.07$	$C_T/\sigma = 0.0714$
$X_{FA} = 0.0$	$Z_{FA} = 0.3$
$X_{FC} = 0.0$	$Z_{FC} = 0.3$
$C_{df} = 0.01$	
BVI Flight Condition	
$\mu = 0.15$	$\theta_{\mathrm{FP}} = 6.5^\circ$
Dynamic Stall Flight Condition	
$\mu = 0.35$	$\theta_{\mathrm{FP}} = 0^\circ$
MBB BO-105 baseline blade	
$\omega_{L1} = 0.729$	$\omega_{F1} = 1.125$
$\omega_{T1} = 3.263$	

used to generate the results.

9.1 Single Objective Function Optimization Results

Efficient Global Optimization results using the weighted expected improvement function are given in this section. For each iteration of the EGO algorithm, the 20 best designs from the genetic algorithm optimization of WEIF were selected for parallel computation. Twenty designs were selected based on the number of available processors; i.e. $N_p = 20$. Each BVI simulation required about 6 hours to complete on a Linux cluster with 1.8 - 2.4 GHz Opteron processors, while each dynamic stall simulation required 8 hours. The EGO algorithm was used for 2 iterations with $w = 0.2$, followed by iterations with $w = 0.8$. The algorithm was terminated once the iterations with $w = 0.8$ failed to improve upon the best

design from the previous iteration. This weight scheme was selected for two reasons: (1) so that the EGO algorithm would focus on a more global search initially and then switch to a more local search within regions of high probability of improvement, and (2) because these weights were shown to be effective for BVI vibration reduction in Section 8.3. Optimization of the WEIF was conducted with the Multi-Island Genetic Algorithm from iSIGHT. All optimization results are compared to a baseline blade with cross-sectional properties resembling an MBB BO-105 blade.

To start EGO for the BVI objective function, an optimum Latin hypercube (OLH) of 100 design points was generated. From the 100 point OLH, 95 blade designs had converged trim solutions. Figure 9.1 shows the best feasible value of the vibration objective function after each EGO iteration when optimizing under the BVI flight condition. In addition, Fig. 9.1 depicts the objective function corresponding to vibration levels in the dynamic stall regime that result from the best designs for the BVI flight condition. Using EGO, 73.9% vibration reduction was achieved for the BVI flight condition. The best design under BVI conditions also corresponds to 10.7% vibration reduction in the dynamic stall regime. These results indicate that it is possible to design a blade with reduced vibrations under both intense blade-vortex interaction and dynamic stall.

Two OLH's were considered for initializing the optimization of the dynamic stall objective function. The first was the same OLH used for optimization of the BVI objective function. However, the best blade design from the 100 point OLH corresponded to a 17% *increase* of the dynamic stall objective function. Thus, in the dynamic stall regime, regions in the design space corresponding to reduced vibration were not sampled with the 100 point

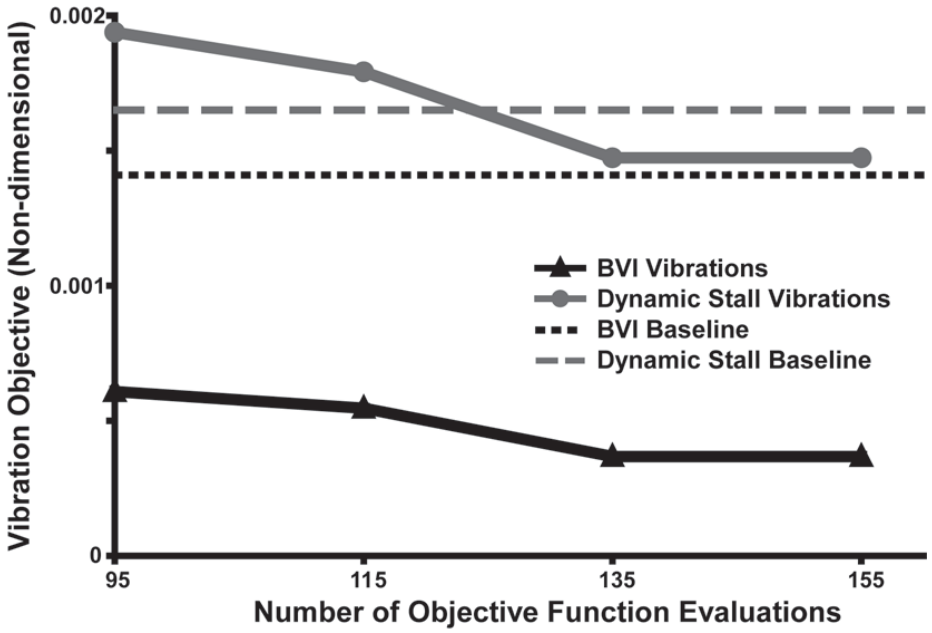

Figure 9.1: Changes in the objective functions corresponding to optimization for the BVI flight condition

OLH. Therefore, a 200 point OLH was considered for initialization of the EGO algorithm in order to increase the chance of sampling in regions of reduced vibration. Although more of the design space was sampled than with the 100 point OLH, the best design from the 200 point OLH corresponded to a 19% increase of the objective function.

The best values of the dynamic stall regime objective function after each iteration of EGO are shown in Fig. 9.2a and b. The best design in the dynamic stall regime corresponds to 27.6% vibration reduction with the 100 point OLH, and 29.2% reduction with the 200 point OLH. In the BVI regime, the 100 and 200 point OLH's lead to 28.3% and 36.9% vibration reduction respectively. So the 200 point OLH led to minimal improvement of the dynamic stall objective function compared to the 100 point OLH, and moderate improvement of the BVI objective function.

Figures 9.1 and 9.2 show that the space-filling nature of OLH's results in significant

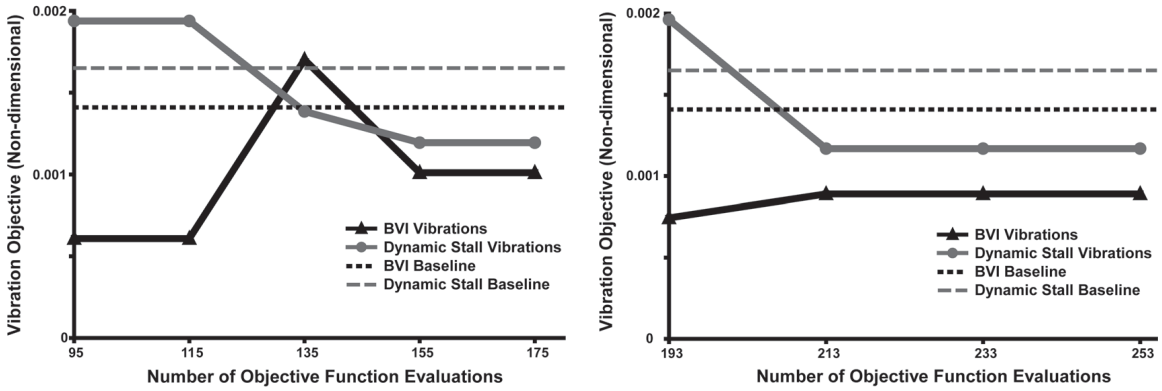

(a) 100 point OLH (b) 200 point OLH

Figure 9.2: Changes in the objective function corresponding to optimization for the dynamic stall flight condition

vibration reduction in the BVI regime. Under BVI conditions, 57% vibration reduction was achieved using the best design of the initial 95 sample points from the space-filling OLH. However, the same design from the OLH corresponds to a 17% increase of vibration levels in the dynamic stall regime. In contrast to the BVI flight condition, the EGO algorithm is not initialized with a reduced vibration design in the dynamic stall regime. Therefore, the dynamic stall optimization results show that the EGO algorithm is capable of finding reduced vibration designs even when initialized with poor designs. Furthermore, the dynamic stall objective function was more difficult to optimize in the sense that one more EGO iteration with the 100 point OLH compared to the BVI objective function was required.

In order to demonstrate the superiority of EGO to the one-shot optimization approach for the dynamic stall regime, a kriging surrogate based on a 400 point OLH – 372 had converged trim solutions – was constructed and optimized directly. One-shot optimization led to a design corresponding to a 10% *increase* in the dynamic stall objective function. Because of the error in the surrogate's predictions, one-shot optimization led to a design

which is predicted to be a low vibration design, but in reality is a poor design. By comparison, Fig. 9.2b shows that EGO led to 29% vibration reduction with 253 objective function evaluations. Thus, in the dynamic stall regime, EGO led to a better design with 119 fewer expensive objective function evaluations compared to the one-shot approach. By emphasizing regions in the design space where there is much uncertainty in the surrogate's predictions, i.e. a setting of $w = 0.2$, EGO was able to locate a design which one-shot optimization failed to because of errors in the surrogate objective function. These results illustrate that (a) beginning with a relatively small number of function evaluations compared to the one-shot approach and using the WEIF to update in an "intelligent" manner results in the superior efficiency of EGO, and (b) accounting for the uncertainty in the surrogate during optimization results in a more global search which can lead to designs that the one-shot approach misses. Similar results demonstrating the superiority of the EGO algorithm for optimization in the BVI regime are provided in Section 8.3.

9.2 Multi-objective Function Optimization Results

The results in Figs. 9.1 and 9.2 indicate that it is possible to find designs which reduce vibrations in both flight conditions. However, the best design for one flight condition was not the best design for the other. In order to find the "best" design for both flight conditions, multi-objective function optimization techniques are necessary. Therefore, the weighted sum and modified EGO approaches described in Section 7.4.3 are employed to locate the *Pareto* optimum designs. A design is considered to be Pareto optimal, or non-dominated, if no design exists which has superior objective function values for *all* objective functions.

9.2.1 Weighted Sum Approach

The following values of W were considered: 0.0, 0.25, 0.50, 0.75 and 1.0. Setting $W = 0$ corresponds to optimization of the BVI objective function, and $W = 1$ emphasizes the dynamic stall vibration objective. The surrogate dynamic stall objective function based on the 200 point OLH was used in the multi-objective function optimizations. Note that the results in Figs. 9.1 and 9.2b correspond to $W = 0$ and $W = 1$ respectively. Similar to the results in Figs. 9.1 and 9.2, 20 local optima of the WEIF were selected for updating after each iteration of EGO. However, for values of W other than 0 or 1, helicopter simulations in both flight regimes must be conducted for each of the 20 local optima. Therefore, for each iteration of EGO with $W \neq 0, 1$, 40 expensive objective function evaluations were necessary. Among all of the designs which were located after conducting EGO at the various W settings, the "best" designs were selected by identifying the Pareto optima.

The amount of vibration reduction corresponding to the Pareto optimal designs are given in Table 9.2. It is clear from Table 9.2 that a single design which is best for both flight conditions does not exist, and trade-offs are necessary in order to select the "best" design among the Pareto points. There is relatively little difference in the BVI objective function for the 5 Pareto optimal designs corresponding to $44.4 - 48.1\%$ BVI vibration reduction. In contrast, the differences in the dynamic stall objective function are larger for these 5 designs, which vary between 19.6 – 31.9% reduction of the dynamic stall objective function. Furthermore, these 5 designs have similar fundamental frequencies which suggests that these designs are in the same region of the design space. These results indicate that within this region of the design space, larger amounts of vibration reduction

Table 9.2: Pareto optimal designs from the weighted sum approach

Vibration Reduction in BVI Regime	**Vibration Reduction in Dynamic Stall Regime**	ω_{L1}	ω_{F1}	ω_{T1}
73.9%	10.7%	0.614	1.065	4.849
48.1%	19.6%	0.600	1.056	4.189
47.9%	20.3%	0.600	1.057	4.090
45.0%	22.0%	0.601	1.057	4.076
44.8%	29.1%	0.601	1.058	3.999
44.4%	31.9%	0.601	1.057	3.997

in the dynamic stall regime can be achieved with relatively little increase in BVI induced vibrations.

It is interesting to note that the optimum design corresponding to $W = 1.0$ is *not* a Pareto optima. With $W = 1$, a design corresponding to 36.9% vibration reduction in the BVI regime and 29.2% reduction in the dynamic stall regime was found. However, this design is dominated by the design in Table 9.2 corresponding to 44.4% reduction in the BVI regime and 31.9% reduction in the dynamic stall regime. This occurs because of the error in the approximate objective function. While the design corresponding to $W = 1$ is *predicted* to be the best blade design for the dynamic stall flight condition, it is not *actually* the best design.

9.2.2 Modified EGO approach

The WEIF Pareto front was obtained using two genetic algorithms available in iSIGHT – the Neighborhood Cultivated Genetic Algorithm (NCGA) and the Multi Island Genetic Algorithm (MIGA) [1]. The NCGA, which is based on the approach described in Ref. 180, is a multi-objective algorithm which is formulated to locate the entire Pareto front. How-

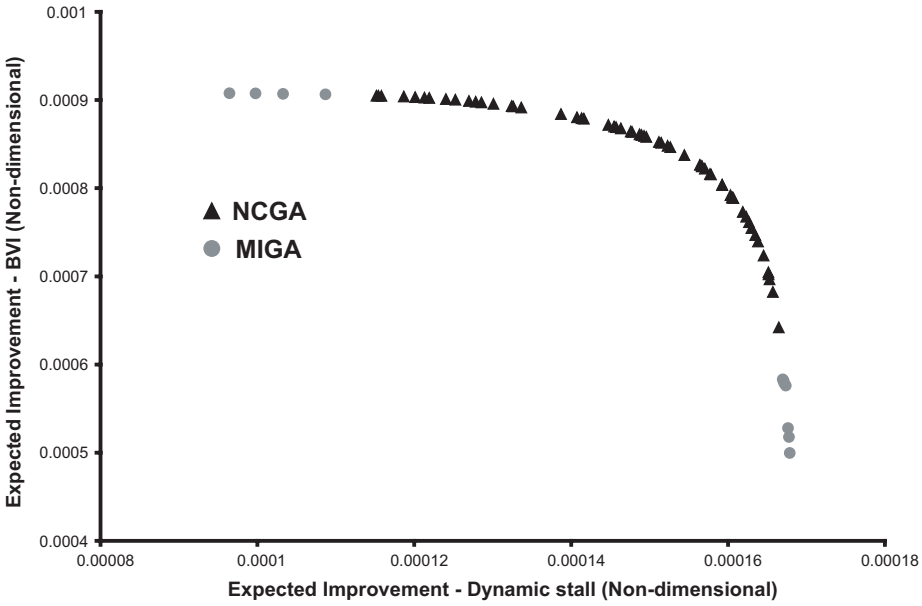

Figure 9.3: Weighted expected improvement Pareto front

ever, it was found that the NCGA was not as effective as MIGA, which is a single objective algorithm, for locating designs on the ends of the Pareto front. This is depicted in Fig. 9.3, in which the Pareto optimal designs corresponding to both WEIF's are shown for one iteration of the modified EGO approach. The output data from the NCGA approach, and the MIGA approach which was used to optimize each WEIF individually, were combined and filtered for the overall expected improvement Pareto front. It is clear from Fig. 9.3 that both approaches contributed to the Pareto front. Therefore, for all multi-objective results in this thesis, NCGA and MIGA were applied to the WEIF's corresponding to each iteration, and the Pareto points from the combined output data were selected. This adds no additional cost to the problem since the three individual optimizations – (1) NCGA applied to both WEIF's, (2) MIGA applied to the BVI WEIF, and (3) MIGA applied to the dynamic stall WEIF – can be conducted in parallel.

As in the previous results, the first two iterations of the modified EGO algorithm were

run with a WEIF setting of $w = 0.2$. A setting of $w = 0.8$ was used for subsequent iterations, and the algorithm was stopped once it could not find additional Pareto optimal designs. The modified EGO approach located a single Pareto optimum corresponding to 71.1% and 26.3% reduction of the BVI and dynamic stall objective functions respectively, and fundamental frequencies of $\omega_{L1} = 0.601$, $\omega_{F1} = 1.055$, $\omega_{T1} = 4.671$. This design represents an excellent trade-off since it corresponds to vibrations which are only 2.8% higher than the best design for the BVI regime, and 5.6% higher than the best design for the dynamic stall regime. These results illustrate the importance of treating this problem in a multi-objective manner since this design would have been overlooked if the blade was optimized for only one flight condition. In general, the modified EGO approach will return multiple Pareto designs, just as in the weighted sum approach. However, only a single Pareto point was returned in this case because the design is such an excellent trade-off design that it dominated all other designs located by the modified algorithm.

The Pareto designs from the two approaches are compared in Fig. 9.4, in which the designs returned by both multi-objective function optimization approaches are plotted in the objective function space. It is clear from Fig. 9.4 that three of the designs located by the weighted sum approach are not *actual* Pareto points since they are dominated by the design located by the modified EGO approach. Figure 9.4 also provides an approximate representation of the *Pareto front* which was obtained by connecting the 4 *actual* Pareto designs from both approaches. The Pareto front shows that neither method of utilizing EGO for multi-objective function optimization distinguished itself as the best, since both methods located designs on the Pareto front which the other was unable to find. Therefore,

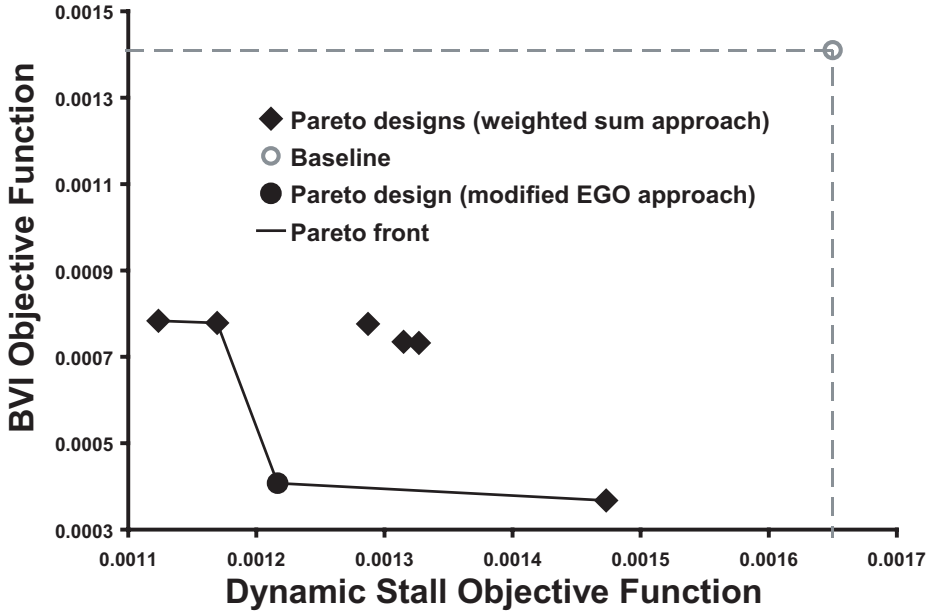

Figure 9.4: Pareto optimal designs plotted in the objective function space

the results in this study indicate that the most effective way in which to utilize EGO for locating Pareto designs is to use *both* the weighted sum approach and the modified EGO approach.

9.3 Vibratory Loads Corresponding to the Best Designs

The vibratory loads corresponding to the best designs in the BVI and dynamic stall regimes, as well as the "best" trade-off design, are shown in Figs. 9.5a and b. The design identified by the modified EGO approach was selected as the "best" trade-off design since its vibration characteristics are similar to the best designs for both flight conditions. Figure 9.5a shows that the baseline vertical shear is the most significant vibratory load in the BVI regime. Therefore, the reduction of the vertical shear is the dominant mechanism for reducing the overall BVI objective function. By optimizing the BVI objective function, the

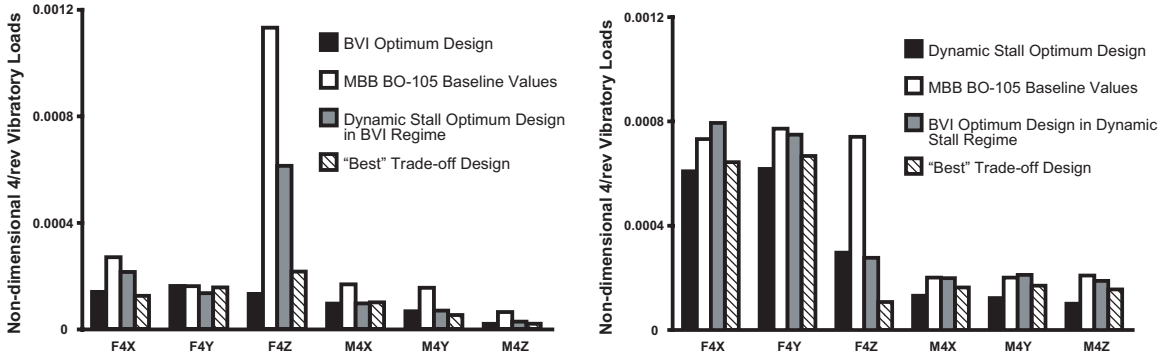

(a) BVI regime, $\mu = 0.15$ (b) Dynamic stall regime, $\mu = 0.35$

Figure 9.5: Vibratory loads in the BVI and dynamic stall flight regimes

vertical shear is reduced by 88%. On the other hand, the best design from optimizing the dynamic stall objective function results in 46% reduction of the vertical shear in the BVI regime, while the trade-off design results in 81% reduction of the vertical shear.

Figure 9.5b shows that no single vibratory load dominates the dynamic stall objective function. Rather, all three hub shear components make substantial contributions to the objective function. The best design in the dynamic stall regime alleviates vibration by reducing all three shears by $17 - 60\%$. In contrast, the best design from optimizing the BVI objective function lowers vibrations in the dynamic stall regime by reducing the vertical shear by 63%. Similar to the best design for the dynamic stall regime, the trade-off design alleviates vibration by reducing the three shears by $12 - 85\%$. So in both flight regimes, the BVI optimum blade design achieves vibration alleviation by significantly reducing the vertical shear, while the dynamic stall optimum and trade-off design reduce all three shears.

Chapter X

Active/Passive BVI Vibration and Noise Reduction

Vibration and noise reduction results using the EGO and active control algorithms are presented in this chapter. The helicopter parameters given in Table 9.1 corresponding to the BVI flight condition were used for all results. The blade was characterized by the 13 design variables described in Configuration 3. Furthermore, a relaxed autorotational constraint was employed in which the blade must maintain 80% of the mass polar moment of inertia of the baseline blade, and the lower bound on the fundamental lead-lag frequency constraint was set to 0.50/rev. For all noise reduction results, $P_0 = 20\ \mu\mathrm{Pa}$ and the threshold noise level was set to $T_{_{NL}} = 110\ \mathrm{dB}$ since the highest noise levels in the carpet plane corresponding to the baseline blade were greater than 110 dB.

10.1 Passive Optimization Results

Efficient Global Optimization results using the WEIF are given in this section. The EGO algorithm was initialized with 200 data points and the initial iterations were run with a weight setting of $w = 0.2$. Once EGO failed to improve upon the best design from the previous iteration, the weight setting was changed to $w = 0.8$. The EGO algorithm was stopped once the iterations with $w = 0.8$ failed to improve upon the best design from the

previous iteration. The weighted sum approach to multi-objective function optimization was conducted with the following values of W: 0.0, 0.25, 0.50, 0.75 and 1.0. All optimization results are compared to a baseline blade with cross-sectional properties resembling an MBB BO-105 blade. The best trade-off designs from both multi-objective function optimization approaches described in Section 7.4.3 were combined into a data set which is filtered for the final Pareto optimal designs.

The amount of vibration and noise reduction for the best trade-off, or Pareto optimal designs are given in Table 10.1 along with the fundamental frequencies which characterize the blade designs. The best vibration design corresponds to 66.8% reduction of the vibration objective function and 37.6% noise reduction, while the best noise design corresponds to a 3.7% increase in vibration levels and a 62.6% reduction in noise relative to the baseline blade. Among the best trade-off designs, the maximum noise levels in the carpet plane are $1.3 - 2.8$ dB lower than the baseline design. These results indicate that it is possible to passively design a blade for simultaneous vibration and noise reduction, although the best design for vibration is not the best design for noise. Therefore, as in many multi-objective function optimization problems, there is no single best design.

The Pareto front, which is obtained by plotting the 20 Pareto optimal designs from Table 10.1 in the objective function space, is shown in Fig. 10.1. Figure 10.1 illustrates that, among the Pareto optimal designs, a significant reduction in one objective function is associated with a significant increase in the other objective function. These results indicate that passive reduction of BVI induced vibration and noise is characterized by strong trade-offs between the two objectives.

Table 10.1: Best trade-off designs

Design Identifier	Vibration Reduction	Noise Reduction	Reduction of Max. Noise Level in Carpet Plane (dB)	ω_{L1} (/rev)	ω_{F1} (/rev)	ω_{T1} (/rev)
P1	66.8%	37.6%	1.3	0.609	1.054	4.675
P2	66.3%	38.7%	1.4	0.632	1.058	4.694
P3	65.9%	39.3%	1.6	0.577	1.050	4.677
P4	65.4%	39.3%	1.8	0.593	1.051	4.855
P5	65.0%	41.0%	1.8	0.597	1.052	4.828
P6	63.4%	44.4%	1.7	0.634	1.057	4.852
P7	61.9%	44.5%	1.6	0.638	1.057	4.858
P8	57.1%	47.4%	1.9	0.656	1.061	4.603
P9	22.8%	47.5%	2.1	0.553	1.048	4.640
P10	15.4%	51.1%	2.5	0.704	1.066	5.602
P11	14.8%	52.0%	2.4	0.609	1.054	4.675
P12	10.1%	52.6%	2.7	0.655	1.062	5.054
P13	9.6%	54.0%	2.4	0.751	1.072	5.750
P14	9.1%	54.1%	2.6	0.662	1.063	5.348
P15	8.3%	54.4%	2.6	0.696	1.066	5.120
P16	6.1%	57.3%	2.8	0.683	1.066	5.522
P17	1.3%	58.5%	2.4	0.698	1.067	5.451
P18	0.3%	59.4%	2.5	0.703	1.068	5.488
P19	-2.9%	59.8%	2.7	0.766	1.073	5.860
P20	-3.7%	62.6%	2.6	0.669	1.062	5.048

The vibratory loads corresponding to the best vibration and noise designs are shown in Fig. 10.2. The baseline vertical shear, F_{4Z}, is the most significant vibratory load in the BVI regime. Therefore, the significant reduction in the overall objective function associated with the best vibration design is due to a 70% decrease in the vertical hub shear. The best noise design results in a 58% reduction of the vertical shear. However, in contrast to the best vibration design, F_{4X}, F_{4Y}, and M_{4Z} are increased by $191 - 592\%$. Because of this, the overall vibration objective function associated with the best noise design is increased by 3.7% in spite of the significant alleviation of the vertical hub shear.

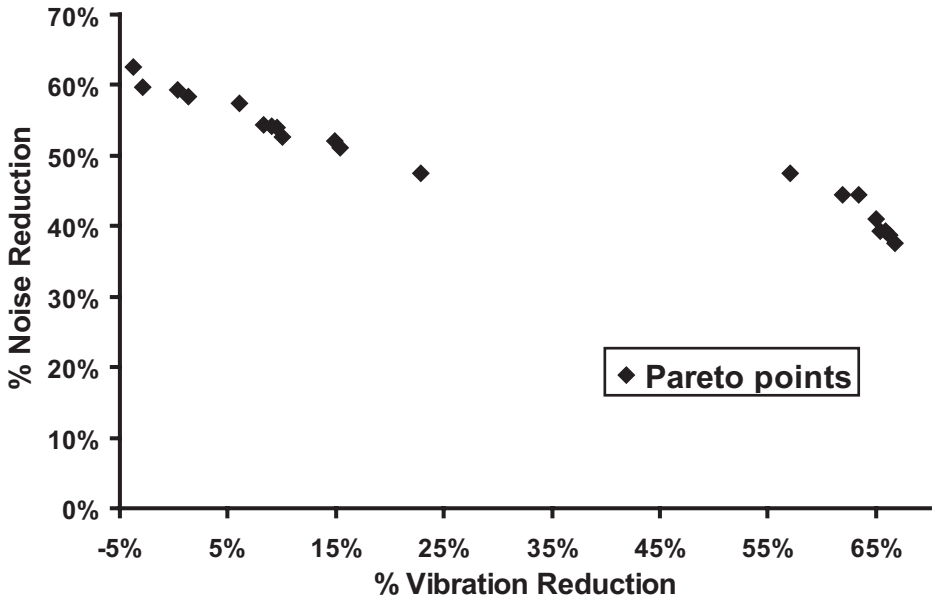

Figure 10.1: Vibration and noise Pareto front

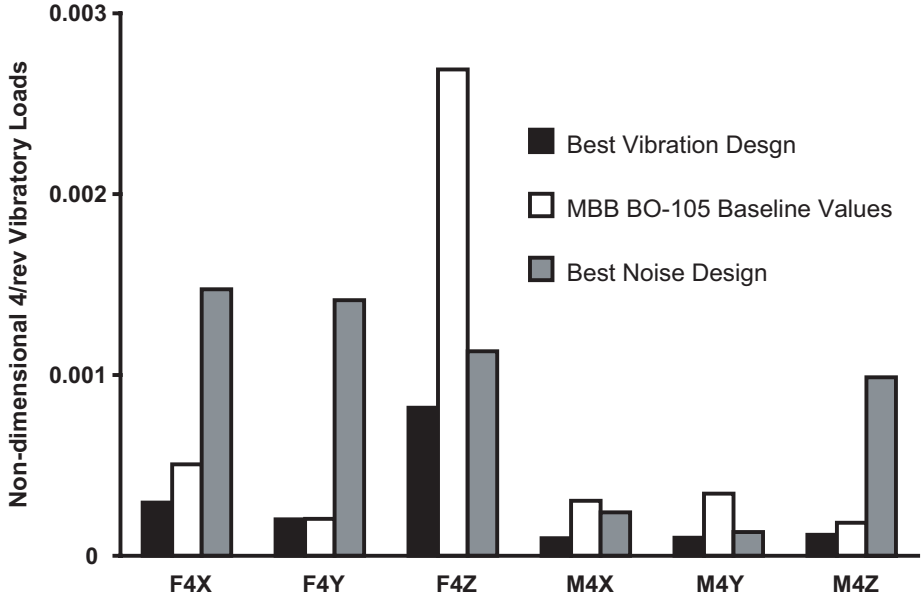

Figure 10.2: Vibratory loads corresponding to the best vibration and noise designs

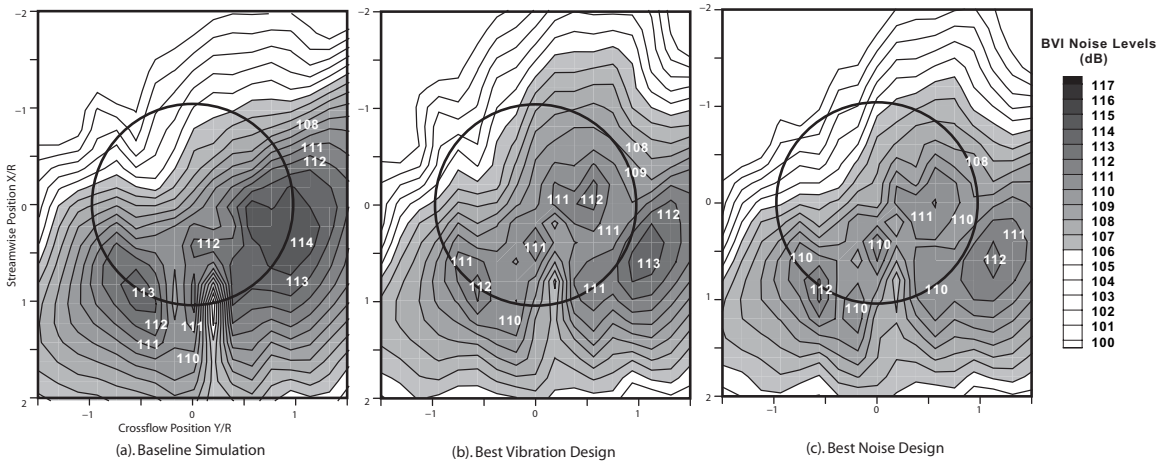

Figure 10.3: Noise levels corresponding to the best passive designs

The noise levels in the carpet plane associated with the baseline, best vibration, and best noise designs are shown in Fig. 10.3. Figure 10.3 shows that the best vibration and noise designs both correspond to decreased noise levels throughout the carpet plane. The best vibration design results in a 1.3 dB reduction of the maximum noise level on the advancing side, and a 1.4 dB decrease on the retreating side. Similarly, the best noise design corresponds to a 2.6 dB and 1.6 dB reduction of maximum noise levels on the advancing and retreating sides respectively. These results demonstrate that the noise objective function introduced in this study is effective for locating designs which correspond to lower noise levels on the advancing and retreating sides of the carpet plane.

10.2 Sequential Active/Passive Optimization Results

The active/passive results given in this section were generated by adding actively controlled flaps (ACF's) to the best trade-off designs. Active control was implemented for vibration reduction, noise reduction, and simultaneous reduction. The dual servo-flap con-

Table 10.2: Dual servo-flap configuration

$c_c = 0.25c_b$	$m_c = 0.0625m_0$
Inboard flap	
$x_c = 0.72R$	$L_c = 0.06R$
Outboard flap	
$x_c = 0.92R$	$L_c = 0.06R$

figuration (see Fig. 1.2a) employed for all active/passive results is given in Table 10.2.

For active control of vibration, the weighting matrix $\mathbf{Q}_{\text{VR}}$ employed in Refs. 120 and 41 was used,

$$\mathbf{Q}_{\text{VR}} = \begin{bmatrix} 1 & 0 & 0 & 0 & 0 & 0 \\ 0 & 1 & 0 & 0 & 0 & 0 \\ 0 & 0 & 1 & 0 & 0 & 0 \\ 0 & 0 & 0 & 10 & 0 & 0 \\ 0 & 0 & 0 & 0 & 10 & 0 \\ 0 & 0 & 0 & 0 & 0 & 10 \end{bmatrix}. \tag{10.1}$$

The active/passive results associated with vibration control are given in Table 10.3. The vibration and noise reduction results correspond to the passive objective functions so that direct comparisons can be made with the results obtained with only passive reduction. Designs P13, P14, and P16 are omitted from Table 10.3 since these blades, when combined with the flaps, produce infeasible designs. These designs were on the boundary of the hover stability constraint and addition of the flaps was sufficient to result in a violation of the constraint. The active/passive configurations set for vibration control result in an addi-

Table 10.3: Active/passive results associated with vibration control

Design Identifier	Vibration Reduction	Noise Reduction	Change in Max. Noise Level due to Active Control (dB)
P1	91.2%	60.7%	-1.0
P2	90.0%	66.7%	-1.3
P3	90.5%	53.6%	+0.1
P4	89.7%	60.9%	-0.1
P5	90.8%	57.9%	-0.3
P6	86.9%	57.7%	-0.4
P7	83.9%	54.3%	-0.5
P8	89.1%	62.5%	+0.2
P9	51.0%	59.3%	-0.8
P10	52.8%	56.0%	+0.7
P11	49.4%	62.2%	-0.5
P12	44.2%	69.9%	-0.3
P15	38.6%	60.1%	+0.4
P17	21.7%	73.7%	-0.6
P18	20.7%	71.8%	-0.7
P19	32.4%	80.0%	-0.5
P20	12.3%	75.6%	-0.2
MBB	76.1%	25.2%	-1.0

tional $16-37\%$ vibration reduction compared to the Pareto optimal designs without ACF's. In the case of the lowest vibration active/passive design P1, which corresponds to a 91.2% decrease in vibration, the controller provides an additional 24.4% vibration reduction compared to the original passive optimum. Although the 76.1% vibration reduction associated with the MBB baseline blade with ACF's is significant, it is still inferior to P1. These results demonstrate that ACF's can significantly augment the vibration characteristics of structurally optimized blades, and that an active/passive approach to vibration reduction is superior to only passive or only active approaches.

For each of the active/passive designs, an additional $5-28\%$ noise reduction compared to the passive designs was observed when controlling for vibration. Although the noise

objective function, which represents high noise levels over the entire carpet plane, was decreased by the presence of the flaps, maximum noise levels in the carpet plane were not decreased for every design. For instance, adding flaps to design P10 and controlling for vibration resulted in a 0.7 dB increase in the maximum noise level compared to P10 without flaps.

Note that for some of the active/passive designs, controlling for vibration increased the active control noise objective function, i.e. the noise level at the microphone located on the skid increased, despite a reduction in the passive noise objective function. A good example of this is design P6 where the noise at the microphone was increased by 1.1 dB when controlling for vibration, yet the passive noise objective function and maximum noise level in the carpet plane were reduced by 13% and 0.4 dB respectively when compared to P6 without flaps. This indicates that the noise levels at the microphone are not strongly correlated to noise levels in the carpet plane for all of the blade designs.

For noise reduction, equal weighting was placed on each SPL harmonic, thus the diagonal components of $\mathbf{Q}_{\text{NR}}$ were identical. Active/passive results representing control for noise reduction are given in Table 10.4. An additional $7-46\%$ noise reduction compared to the passive optimum designs was achieved by adding flaps and controlling noise. Although the passive noise objective function was decreased by adding flaps to each of the optimized designs, the maximum noise levels were not always reduced. For instance, adding flaps to case P15 and controlling for noise increased the maximum noise level by 0.3 dB compared to the maximum noise level associated with design P15 without flaps. Therefore, for some designs, controlling noise produced noise reduction over the entire carpet plane at the cost

Table 10.4: Active/passive results associated with noise control

Design Identifier	Vibration Reduction	Noise Reduction	Change in Max. Noise Level due to Active Control (dB)
P1	67.7%	76.9%	-1.4
P2	64.5%	73.6%	-1.4
P3	37.8%	63.5%	0.0
P4	62.5%	71.7%	-0.1
P5	65.5%	65.9%	-0.2
P6	71.8%	63.6%	-1.0
P7	66.1%	64.5%	-0.8
P8	64.2%	66.5%	-0.1
P9	16.9%	61.4%	-0.7
P10	5.8%	60.1%	+0.1
P11	-8.5%	71.2%	-0.8
P12	-4.4%	74.7%	-0.2
P15	1.68%	64.9%	+0.3
P17	-22.5%	72.7%	-0.8
P18	-12.3%	71.0%	-0.5
P19	-25.9%	74.8%	-0.1
P20	-20.5%	70.0%	+0.2
MBB	23.0%	91.2%	-2.9

of slight increases in the maximum noise level.

Actively controlled flaps combined with the baseline blade produced the most significant noise reduction, despite the fact that the baseline blade without flaps has higher noise levels than all of the passively optimized blades. It should be noted that the flaps reduce noise at the microphone location by $0.1 - 1.1$ dB when combined with the Pareto optimal designs. By comparison, the controller reduced noise at the microphone by 3.8 dB with the MBB BO-105 baseline blade. This behavior can be attributed to the fact that the Pareto optimal designs presented in Table 10.1 are all much stiffer in torsion than the baseline blade. Therefore the flaps have a smaller effect on the blade responses of the optimized designs compared to the baseline blade, and thus less influence on noise levels. These results

suggest that in order to obtain the *best* active/passive configuration for noise reduction, the blade/flap combination has to be optimized simultaneously. This would likely result in a design which is softer in torsion.

In order to further understand the cause of the additional noise reduction when flaps are added to the optimized designs, noise levels were calculated for the active/passive configurations with flap deflections set to zero. These results are presented in Table 10.5. In addition to the noise reduction associated with zero flap deflection, Table 10.5 also provides the change in the noise objective function due to non-zero flap deflections associated with control for vibration and noise. The change in noise attributed to non-zero flap deflections was calculated by subtracting the noise objective function corresponding to zero flap deflection from the noise objective function values associated with non-zero flap deflections. It is clear from Table 10.5 that non-zero flap deflections contribute relatively little to noise reduction for the optimized designs. For instance, adding flaps to design P1 with $\delta_f = 0^\circ$ results in a 58.3% decrease in the noise objective function compared to the baseline blade, and an additional 18.6% noise reduction was obtained by deflecting the flaps for noise reduction. So most of the total noise reduction was due to the aerodynamic contributions from the extra chord length added by the undeflected flaps. The effect of non-zero flap deflections for the other optimized designs was less than what was observed in the case of P1. In contrast to the optimized designs, the flap deflection is the dominant source of noise reduction for the torsionally softer baseline blade. These results show that although the high torsional stiffnesses of the optimum designs limit the ability of the controller to reduce noise, the presence of the flaps still contribute to noise reduction due to the extra

Table 10.5: Effect of flap deflection on noise reduction

Design Identifier	Noise Reduction with $\delta_f = 0°$	Change in Noise due to Control of Vibration	Change in Noise due to Control of Noise
P1	58.3%	-2.4%	-18.6%
P2	62.5%	-4.2%	-11.1%
P3	49.5%	-4.2%	-14.1%
P4	58.3%	-2.5%	-13.3%
P5	59.5%	+1.5%	-6.5%
P6	50.7%	-7.0%	-12.9%
P7	55.0%	+0.7%	-9.4%
P8	64.1%	+1.6%	-2.5%
P9	56.4%	-2.9%	-5.0%
P10	58.3%	+2.3%	-2.4%
P11	66.4%	+4.2%	-4.8%
P12	70.6%	+0.7%	-4.1%
P15	60.8%	+0.7%	-4.1%
P17	72.0%	-1.7%	-0.7%
P18	69.3%	-2.5%	-1.7%
P19	72.8%	-7.1%	-2.0%
P20	66.1%	-9.5%	-3.9%
MBB	26.7%	+1.4%	-64.5%

chord length with $\delta_f = 0°$. It should be noted that the extra chord length associated with the undeflected flaps essentially represents a modification of the planform geometry. The resulting noise reduction is consistent with the studies documented in Ref. 172 in which modification of the planform geometry has been shown to be effective for reducing noise. If a plain flap configuration were used, instead of the servo-flap configuration employed in this study, the beneficial noise characteristics associated with the modified blade planform would not be present.

For simultaneous reduction,

$$\mathbf{Q}_{\text{NR}} = \begin{bmatrix} 100 & \dots & 0 \\ \vdots & \ddots & 0 \\ 0 & 0 & 100 \end{bmatrix}. \tag{10.2}$$

and $W_\alpha = 0.5$. The weights in $\mathbf{Q}_{\text{NR}}$ were set to higher values compared to $\mathbf{Q}_{\text{VR}}$ so as to avoid a controller dominated by vibration reduction. It was found that without placing higher weights on $\mathbf{Q}_{\text{NR}}$ compared to $\mathbf{Q}_{\text{VR}}$, the controlled simultaneous reduction would be dominated by vibration reduction.

The results corresponding to controlled simultaneous vibration and noise reduction are given in Table 10.6. For each design, simultaneously controlled reduction led to superior vibration reduction compared to the results presented in Table 10.4 corresponding to control for noise. However, control for simultaneous reduction did not always produce superior reduction of the passive noise objective function compared to the results associated with control for vibration. For instance, control for simultaneous reduction with design P2 resulted in 62.8% reduction of the passive noise objective function, while control for vibration decreased noise by 66.7%. However, the simultaneous reduction controller reduced noise at the skid microphone by 0.8 dB while control for vibration resulted in a 0.6 dB *increase* at the feedback location. Similar results were observed for each of the designs for which control for simultaneous reduction failed to produce superior noise reduction compared to control for vibration. Therefore, the simultaneous reduction control algorithm did not fail. Rather, reduction of the active control noise objective function, i.e. noise at

Table 10.6: Active/passive results associated with control for simultaneous reduction

Design Identifier	Vibration Reduction	Noise Reduction	Change in Max. Noise Level due to Active Control (dB)
P1	74.8%	67.5%	-1.1
P2	73.0%	62.8%	-1.2
P3	77.6%	62.7%	-0.1
P4	67.1%	58.9%	+0.1
P5	75.1%	67.1%	-0.3
P6	73.3%	59.2%	-0.9
P7	72.7%	67.2%	-1.0
P8	65.7%	66.7%	-0.1
P9	24.8%	60.7%	-0.8
P10	15.7%	57.0%	-0.8
P11	14.8%	67.4%	+0.4
P12	6.3%	72.2%	-0.7
P15	8.1%	67.1%	-0.1
P17	5.5%	75.2%	+0.2
P18	-0.6%	68.5%	-0.7
P19	4.2%	71.4%	-0.6
P20	-6.4%	68.8%	-0.3
MBB	54.2%	75.8%	-2.6

the skid microphone, did not always correlate with reduction of noise levels over the entire carpet plane.

The Pareto optimal active/passive designs from Tables 10.3, 10.4, and 10.6 are presented in Table 10.7. The designs in Table 10.7 correspond to the best trade-offs with respect to the passive vibration and noise objective functions. Although there is no single blade/flap configuration which corresponds to the lowest vibration and noise levels, P1 is the most versatile design since one can control for vibration, noise, or simultaneous reduction and the results would be Pareto optimal. A blade/flap configuration with the versatility exhibited by P1 would be an attractive choice for a blade designer.

The noise levels in the carpet plane corresponding to P1 are shown in Fig. 10.4. From

Table 10.7: Best active/passive designs

Design Identifier	Control for	Vibration Reduction	Noise Reduction
P1	Vibration	91.2%	60.7%
P2	Vibration	90.0%	66.7%
P5	Simult.	75.1%	67.1%
P1	Simult.	74.8%	67.5%
P1	Noise	67.7%	76.9%
P19	Vibration	32.4%	80.0%
MBB	Noise	23.0%	91.2%

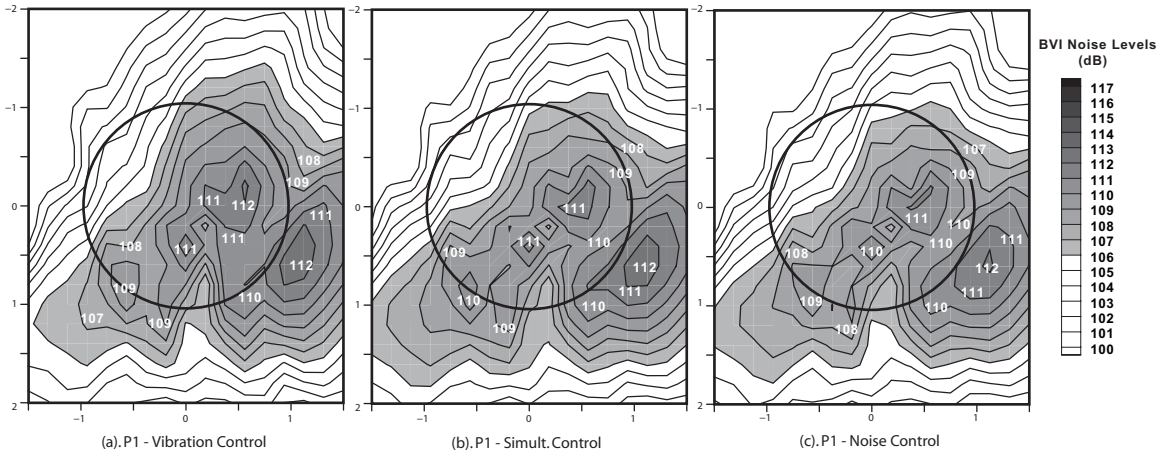

Figure 10.4: Noise levels corresponding to the P1 active/passive configurations

comparison with Fig. 10.3a it is clear that the P1 blade/flap combination results in lower noise levels relative to the baseline design without flaps. The maximum noise levels on the advancing side for each active/passive variation of P1 are reduced by $2.3-2.7$ dB compared to the baseline design, while $3.2 - 3.8$ dB reduction is observed on the retreating side.

Figure 10.5 displays the vibratory loads associated with the P1 active/passive combinations. The vertical shear is reduced by $73 - 97\%$ compared to the baseline. These results along with those in Fig. 10.4 demonstrate that the P1 active/passive design would have excellent vibration and noise characteristics relative to the baseline design in the BVI flight

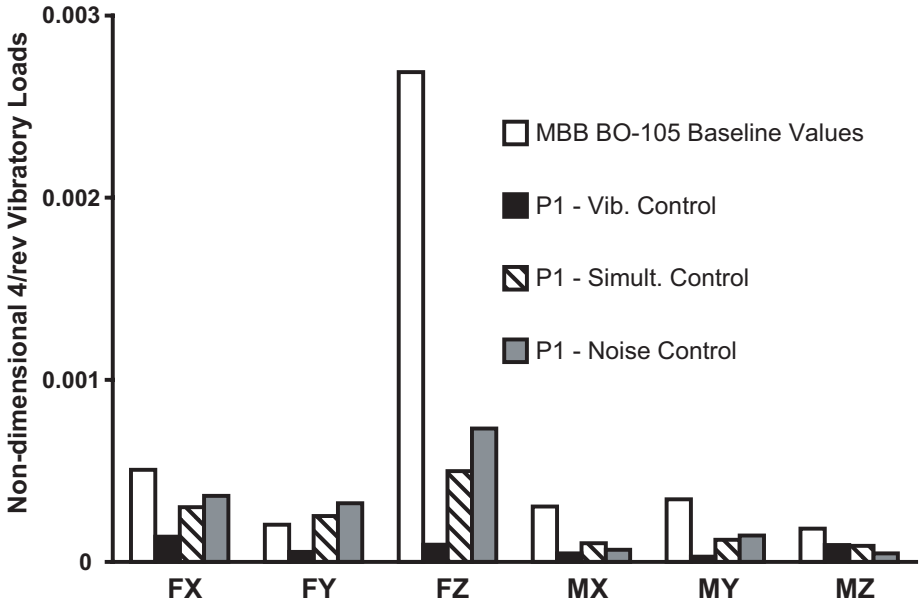

Figure 10.5: Vibratory loads corresponding to the P1 active/passive configurations

regime, regardless of whether one chooses to control for vibration, noise, or simultaneous reduction.

Chapter XI

Active/Passive Vibration Reduction and Performance Enhancement

The helicopter configuration and flight condition parameters used to generate all of the results in this section are given in Table 11.1. The simulations are conducted at a level flight condition with an advance ratio of $\mu = 0.35$. High vibration levels due to dynamic stall are encountered at this flight condition. The blade was characterized by the 15 structural design variables described in Configuration 4 (see Section 7.1.2). The relaxed autorotational and lead-lag frequency constraints described in the opening paragraph of Chapter X were used. The active/passive results were generated by employing a single plain flap, as depicted in Fig. 1.2b.

11.1 Passive Optimization Results

Efficient Global Optimization results using the weighted expected improvement function are given in this section. The EGO algorithm was initialized with 200 data points and the initial iterations were run with a weight setting of $w = 0.2$. Once EGO failed to improve upon the best design from the previous iteration, the weight setting was changed to $w = 0.8$. The EGO algorithm was stopped once the iterations with $w = 0.8$ failed to

Table 11.1: Rotor and helicopter parameters for $\mu = 0.35$

Rotor Data	
$R = 4.91\,\mathrm{m}$	$\Omega = 425\,\mathrm{RPM}$
$N_b = 4$	$c = 0.05498R$
$\beta_p = 2.5^\circ$	$C_{do} = 0.01$
$\theta_0 = 5.6^\circ$	$C_W = 0.005$
$\sigma = 0.07$	$C_T/\sigma = 0.0714$
$X_{FA} = 0.0$	$Z_{FA} = 0.3$
$X_{FC} = 0.0$	$Z_{FC} = 0.3$
$C_{df} = 0.01$	$m_0 = 5.57\,\mathrm{kg/m}$
Flight Condition	
$\mu = 0.35$	$\theta_{\mathrm{FP}} = 0^\circ$
MBB BO-105 baseline blade	
$\omega_{L1} = 0.729$	$\omega_{F1} = 1.125$
$\omega_{T1} = 3.263$	
$\theta_1 = 1.6^\circ$	$\theta_2 = -2.4^\circ$

improve upon the best design from the previous iteration. The weighted sum approach to multi-objective function optimization was conducted with the following values of W: 0.0, 0.25, 0.50, 0.75 and 1.0. All optimization results are compared to a baseline blade with cross-sectional properties resembling an MBB BO-105 blade.

The amount of vibration and power reduction for the best trade-off, or Pareto optimal designs are given in Table 11.2 along with the fundamental frequencies and pretwist design variables which characterize the blade designs. The best vibration design corresponds to 34.2% reduction of the vibration objective function and a 13.9% *increase* in power consumption, while the best power design corresponds to a 30.4% increase in vibration levels and 3.30% performance enhancement relative to the baseline blade. These results demonstrate that there are strong trade-offs between the two objectives at this flight condition.

Table 11.2: Best trade-off designs

Design Identifier	Vibration Reduction	Power Reduction	ω_{L1} (/rev)	ω_{F1} (/rev)	ω_{T1} (/rev)	θ_1	θ_2
P1	34.24%	-13.91%	0.776	1.074	5.997	$-2.36°$	$1.15°$
P2	9.82%	2.64%	0.589	1.052	4.163	$3.62°$	$-2.36°$
P3	-27.00%	2.95%	0.705	1.068	5.503	$3.24°$	$-0.41°$
P4	-30.06%	3.08%	0.658	1.062	5.548	$4.00°$	$-0.98°$
P5	-30.36%	3.26%	0.657	1.062	5.530	$4.00°$	$-0.91°$
P6	-30.43%	3.30%	0.655	1.061	5.540	$4.00°$	$-0.91°$

Despite the strong trade-offs, the multi-objective function optimization approach based on EGO led to a design corresponding to 9.8% vibration reduction and 2.64% performance enhancement. The trade-off design P2, which corresponds to simultaneous reduction of the two objectives, would not have been located without employing multi-objective function optimization techniques.

The vibratory loads corresponding to the best vibration and power designs, as well as the trade-off design P2, are shown in Fig. 11.1. It is clear from Fig. 11.1 that the three hub shears are the dominant components of the overall vibration objective function. The best vibration design reduces the overall objective function by decreasing F_{4X} and F_{4Y} by 48% and 32% respectively. In contrast, there is little difference between the baseline values of F_{4X} and F_{4Y} and those corresponding to P2. For P2, the overall vibration objective function is decreased due to the 20% reduction of the vertical shear F_{4Z}. In the case of the best power design, the $23 - 64\%$ increase in the hub shears along with the 277% increase in M_{4Z} result in the significant vibration penalty associated with optimization for power reduction.

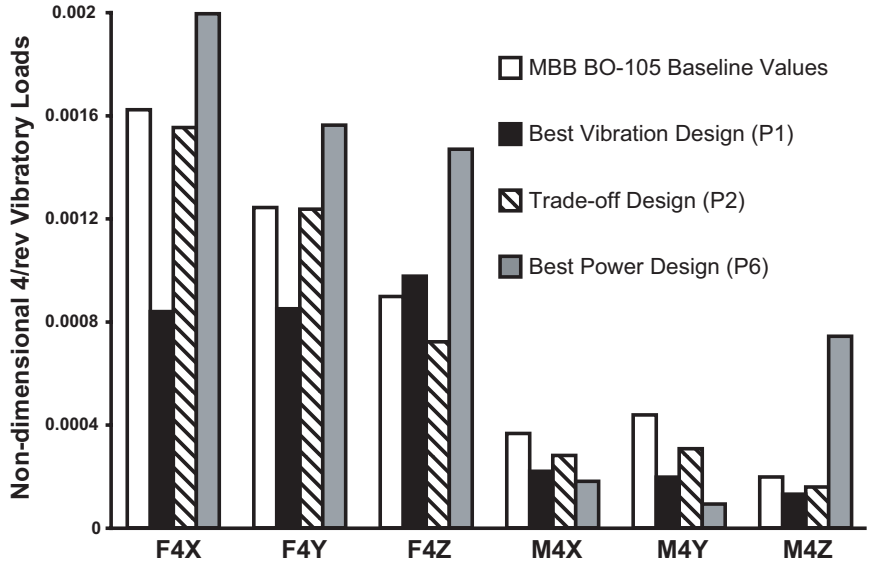

Figure 11.1: Vibratory loads corresponding to the passively optimized designs

11.2 Sequential Active/Passive Optimization Results

The active/passive results were generated by adding a single plain flap, as depicted in Fig. 1.2b, to the six trade-off designs. The flap is centered at the 75% blade station and has a total spanwise dimension of $0.12R$ and a chordwise dimension of $0.20c_b$. The diagonal components of $\mathbf{Q}_{\text{VR}}$ and $\mathbf{Q}_{\text{PR}}$ were set to 1. For each of the Pareto optimal designs, active control was implemented for W_α settings of 0.0, 0.25, 0.50, 0.75 and 1.0. Thus, there were a total of 30 active/passive configurations in the sequential approach.

The results associated with the best trade-offs from the 30 active/passive configurations are given in Table 11.3. Compared to the best vibration design from passive optimization, up to 22.8% additional vibration reduction was obtained by using active control. However, even when augmenting P1 with active control, the high power consumption could not be significantly reduced and remained substantially higher than the baseline value. By augmenting P5 with active control, up to 0.25% additional power reduction was achieved

Table 11.3: Best trade-off configurations obtained from the sequential approach

Design Identifier	W_α	**Vibration Reduction**	**Power Reduction**
P1	1.00	57.07%	-14.12%
P1	0.75	51.37%	-14.07%
P1	0.50	50.20%	-13.77%
P1	0.25	41.24%	-13.64%
P2	1.00	27.62%	3.06%
P2	0.50	27.45%	3.09%
P2	0.25	27.35%	3.13%
P2	0.00	0.76%	3.24%
P5	0.25	-27.33%	3.39%
P5	0.00	-56.04%	3.55%

compared to the best power design without active control. However, the P5 active/passive configurations correspond to a $27.3 - 56.0\%$ increase in vibration levels.

Although the performance characteristics of the best vibration design could not be significantly augmented by using active control, and vice versa, the sequential approach resulted in increased levels of simultaneous reduction with P2. The active/passive P2 configurations with W_α settings of 1.0, 0.50, and 0.25, resulted in an additional $17.5-17.8\%$ vibration reduction and $0.42 - 0.49\%$ performance enhancement. Note that P2 with $W_\alpha = 0.75$ was not among the best trade-offs because setting $W_\alpha = 1.0$ resulted in lower vibration and power levels. Although a setting of $W_\alpha = 0.75$ emphasizes rotor power reduction compared to $W_\alpha = 1.0$, the control algorithm may not always result in the optimal control input [96].

Table 11.4: Active/passive results associated with the combined approach

Design Identifier	W_α	Vibration Reduction (controlled)	Power Reduction (controlled)	Vibration Reduction (uncontrolled)	Power Reduction (uncontrolled)	ω_{L1} (/rev)	ω_{F1} (/rev)	ω_{T1} (/rev)	θ_1	θ_2
C1	0.51	25.55%	-0.96%	-4.34%	-0.53%	0.782	1.077	5.568	-1.61°	-3.06°
C2	0.25	19.10%	1.46%	2.30%	1.61%	0.747	1.070	5.998	2.68°	1.48°
C3	0.75	16.49%	2.70%	-6.02%	1.76%	0.603	1.053	4.279	1.73°	-2.80°
C4	0.60	-11.86%	3.17%	-44.36%	3.59%	0.652	1.062	5.539	3.52°	0.18°
C5	0.45	-53.04%	5.97%	-81.35%	5.93%	0.570	1.054	4.852	3.43°	2.17°

11.3 Combined Active/Passive Optimization Results

The best trade-off configurations from the combined active/passive approach are given in Table 11.4. In addition to the total amounts of vibration and power reduction obtained with active control, the uncontrolled levels are also provided. Note that C5 corresponds to 5.93% uncontrolled power reduction, which is superior to P6. Therefore, a design that should have been located with the passive approach was missed. This indicates that conducting additional EGO iterations in the passive approach would lead to improved designs.

Other than C5, the designs in Table 11.4 are inferior in terms of vibration and power compared to at least one of the configurations found from the sequential approach. Therefore, as in the case of the passive approach, additional iterations with the combined approach were necessary to locate the best designs. Since it was apparent that optimal active/passive configurations were missed, W_α settings of 0.0, 0.25, 0.50, 0.75 and 1.0 were considered for each of the blade designs corresponding to C1 – C5. This is equivalent to conducting a local search of the design space in the vicinity of the best designs returned from a global search.

The resulting 25 active/passive configurations from the combined approach were compared to those from the sequential approach and the Pareto optimal configurations were

Table 11.5: Best trade-off designs obtained from both active/passive approaches

Design Identifier	W_α	Vibration Reduction	Power Reduction
P1	1.00	57.07%	-14.12%
P1	0.75	51.37%	-14.07%
P1	0.50	50.20%	-13.77%
P1	0.25	41.24%	-13.64%
C1	1.00	36.85%	-1.40%
C2	1.00	36.50%	1.17%
C2	0.75	30.49%	1.28%
P2	1.00	27.62%	3.06%
P2	0.50	27.45%	3.09%
P2	0.25	27.35%	3.13%
P2	0.00	0.76%	3.24%
C4	0.50	-24.65%	3.36%
P5	0.25	-27.33%	3.39%
C4	0.25	-32.98%	3.49%
C5	0.75	-52.03%	5.94%
C5	0.50	-52.99%	5.99%
C5	0.00	-83.68%	6.09%

identified. These results are provided in Table 11.5. The presence of C1, C2, C4, and C5 among the best trade-offs in Table 11.5 demonstrates that the combined approach led to useful configurations which would have been overlooked if only sequential optimization were employed. For instance, C2 corresponds to a 2.30% and 1.61% reduction in vibration and power respectively without the benefits of active control. By comparison, P2 corresponds to 9.82% and 2.64% reductions in vibration and power respectively, and thus is superior to C2 in terms of passive characteristics. Therefore, when employing the sequential approach, C2 would have been eliminated because it is not Pareto optimal in terms of the passive vibration and power objectives. However, when using active control with $W_\alpha = 1$, an additional 34.2% vibration reduction relative to the uncontrolled design is obtained, compared to 17.8% with P2. Thus, C2 is superior to P2 in terms of the total amount of vibration reduction which can be achieved with active control.

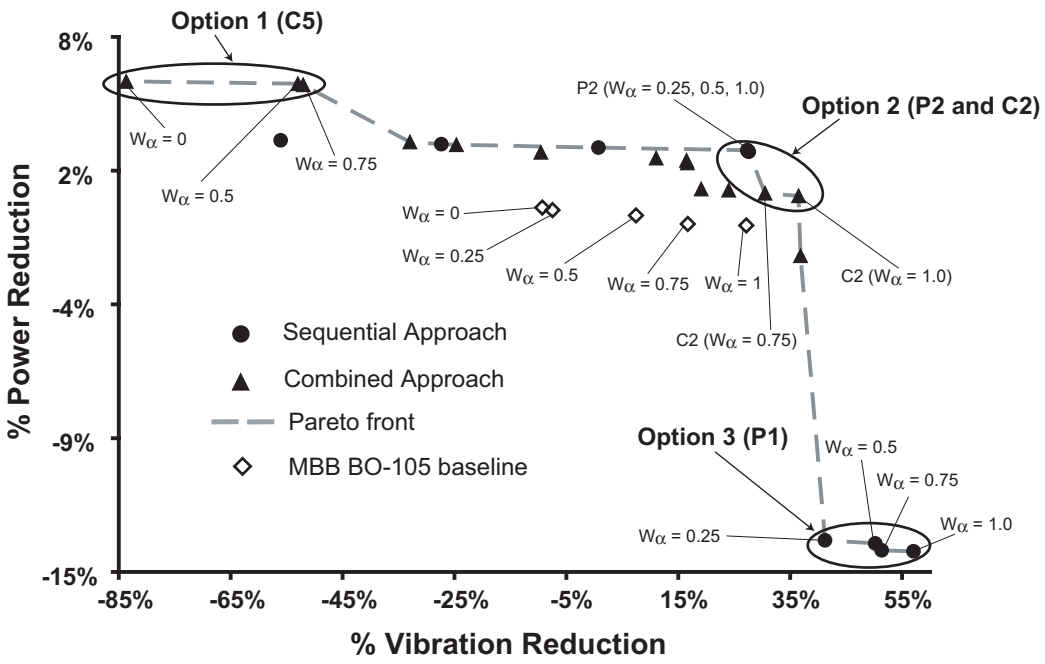

Figure 11.2: Vibration and power Pareto front

The active/passive configurations from the sequential and combined approaches, along with the active control results corresponding to the baseline design with W_α settings of 0.0, 0.25, 0.50, 0.75 and 1.0, are plotted in the objective function space in Fig. 11.2. The Pareto front is obtained by connecting each of the best trade-off points in Table 11.5.

The following design options are apparent when moving from left to right on the Pareto front:

Option 1: The designer can select design C5, which would result in $5.94 - 6.09\%$ performance enhancement. However, depending on W_α, there is a $52 - 84\%$ increase in vibration levels associated with the lowest power option.

Option 2: Significant levels of vibration reduction and performance enhancement can be obtained by selecting the C2 or P2 trade-off designs. While the Pareto optimal ac-

tive/passive configurations based on C2 correspond to $2.9 - 6.0\%$ more vibration reduction than P2, P2 results in $1.8 - 2.1\%$ less power consumption. Note that the P2 configurations appear as a single point in Fig. 11.2 because there is little difference in the vibration and performance characteristics when setting $W_\alpha = 0.25$, 0.5, or 1.0 for this design. Furthermore, it is unlikely that one would set W_α to 0 with P2 since this would result in only an additional 0.11% power reduction at the expense of a 26.6% increase in vibration compared to using $W_\alpha = 0.25$.

Option 3: The best vibration option would be to select P1, which would result in $41.2 - 57.1\%$ vibration reduction depending on the W_α setting. However, the $13.6 - 14.1\%$ degradation in performance compared to the baseline design would substantially increase the cost of implementing such a design.

The trade-offs obtained with the MBB BO-105 baseline design are also plotted in Fig. 11.2. All of the baseline active/passive configurations are inferior to those corresponding to option 2. For example, it is clear that C2 with $W_\alpha = 1$ corresponds to superior levels of both vibration reduction (further to the right in Fig. 11.2) and power reduction (higher in Fig. 11.2) than any of the baseline active/passive configurations.

Chapter XII

Conclusions and Recommendations for Future Research

Effective means for optimum rotor design subject to multiple objectives are presented in this study. The primary goal was to demonstrate the effectiveness of active/passive optimization based on SBO combined with an ACF system. The novel contributions of this study consist of the application of several SBO approaches to rotor blade design combined with the treatment of multi-objective optimization applications. Specifically, the results of this study demonstrated the effectiveness of treating (1) vibration reduction over the entire flight envelope, (2) BVI induced vibration and noise reduction, and (3) vibration reduction and performance enhancement in a multi-objective manner. In order to accomplish the optimization goals of this study, a modified EGO algorithm which proved to be effective for locating excellent trade-off designs was employed, and a combined active/passive approach which is suitable for multi-objective optimization was developed.

12.1 Conclusions

The results presented in this study demonstrated the effectiveness of surrogate based optimization for helicopter rotor blade design. In particular, the EGO algorithm effectively located optimum designs in terms of vibration, noise, and power reduction. Furthermore,

the results demonstrated that the vibration, noise, and performance characteristics of structurally optimized blades can be significantly augmented by utilizing actively controlled trailing edge flaps. The principal conclusions and observations of this study are:

1. Among the individual approximation methods considered, kriging was the most effective method for approximating BVI induced vibratory loads over the entire design space, and for locating an optimum blade design. The high maximum errors suggest that none of the approximation methods considered in this study can be used for precise predictions of vibrations everywhere in the design space, at least without adding more interpolation points. However, they were still useful in finding improved designs.

2. Since no single approximation method distinguished itself as the best in terms of the various metrics considered in this study, optimization of multiple surrogates, including the weighted average surrogates, was an effective method for locating reduced vibration blade designs which would have been overlooked if only a single surrogate was employed. Feasible designs ranging from $45 - 70.5\%$ BVI induced vibration reduction were located with this approach.

3. Regardless of the sample sizes considered, and whether the surrogate objective function was formed by approximating the underlying vibratory loads, or by directly approximating the overall response, the performance of the weighted average surrogates was comparable to the best individual method in terms of average error, and performed better than the worst approximation method in terms of maximum error.

4. It is possible to locate superior blade designs and enhance the predictive capabilities of the surrogates by eliminating design variables which are determined to be unimportant using GSA.

5. The results demonstrate that it is important to explicitly account for the uncertainty in the surrogate's predictions during optimization and that the weighted expected improvement function can lead to superior designs in fewer expensive function evaluations for vibration reduction under BVI and dynamic stall conditions.

6. The EGO algorithm can be used effectively for multi-objective function optimization by considering two approaches: (1) a weighted sum approach in which the two objective functions are combined into a single objective function, and (2) an approach in which the EGO algorithm is modified to update the surrogate objective functions with the Pareto optimal designs corresponding to the expected improvement functions. It was advantageous to utilize both approaches since each method located Pareto designs that the other did not.

7. The best design for the BVI regime differs from the best design for the dynamic stall regime. Therefore it is necessary to identify the designs corresponding to the best trade-offs, i.e. the Pareto optimal designs, which can be used to obtain the "best" blade design. By treating the problem in a multi-objective manner, an excellent trade-off design with vibration characteristics similar to the best designs for each flight condition was located.

8. The results demonstrate that the passive noise objective function introduced in this

study is effective for locating designs which correspond to lower noise levels on the advancing and retreating sides of the carpet plane, and that optimization of the blade's mass and stiffness distribution is an effective means of BVI induced noise reduction.

9. The characteristics of a structurally optimized blade can be significantly augmented by adding ACF's. An active/passive approach based on ACF's and SBO led to a versatile active/passive configuration corresponding to $67.7\% - 91.2\%$ vibration reduction, $60.7 - 76.9\%$ noise reduction over the carpet plane, and a $2.3 - 2.7$ dB decrease in the maximum BVI noise level. Two designs corresponding to significant levels of vibration and power reduction at $\mu = 0.35$ were identified using the sequential and combined active/passive approaches: the first decreases vibration and power levels by $30.5 - 36.5\%$ and $1.2 - 1.3\%$ respectively, and the second corresponds to $27.4 - 27.6\%$ vibration reduction and $3.06 - 3.13\%$ performance enhancement.

12.2 Recommendations for Future Research

While this study represents the most comprehensive investigation of helicopter rotor blade multi-objective optimization carried out to date, significant research topics remain and need to be considered. Continued research on the development of improved models combined with surrogate based optimization may produce the quiet, "jet smooth" helicopters sought after by civilian and military agencies.

Since this study represents the first application of multi-objective active/passive optimization to rotor blade design, a simplified model of an isotropic cross-section was justi-

fied so as to be able to focus on the effectiveness of SBO. Future studies should examine more practical blade cross-sections employing composite construction. Composite materials have the potential for aeroelastic tailoring due to composite couplings that are not available in isotropic materials. To this end, the structural dynamic model used in this study has been combined with the composite cross-sectional analysis VABS (Variational Asymptotic Beam Sectional Analysis) [15, 42]. A detailed description of the resulting blade model, as well as the advantages of using VABS as the cross-sectional analysis, are provided in Appendix A. Furthermore, geometric design variables, such as tip sweep/anhedral, spanwise chord distribution, and airfoil shape, should be included in order to explore all of the options available for advanced rotor blade designs.

In addition to improving the blade model, additional research is required to demonstrate the effectiveness of active/passive optimization. The present study was limited to passive vibration reduction over the entire flight envelope, active/passive vibration and noise reduction at low advance ratios, and active/passive vibration and power reduction at high advance ratios. However, optimum rotor design must account for all of these objectives over the entire flight envelope. Therefore, active/passive optimization for improved vibration, noise, and performance characteristics over the entire flight envelope should be considered. To this end, high-speed impulsive noise modeling capability needs to be addressed. In addition, an improved model of the unsteady drag due to flap deflection needs to be developed so that accurate predictions of required rotor power can be obtained.

From the perspective of SBO, focusing on applications in which it is not computationally feasible to obtain accurate surrogates would prove beneficial since many complicated

engineering design applications are likely to fall under this category. While the EGO algorithm represents a major step in this direction, the question of how best to use EGO for multi-objective function optimization remains unexplored. A thorough comparison of the limited number of existing methods [83, 84], the modified EGO approach employed in this study, and any other multi-objective frameworks which account for surrogate prediction uncertainty, would be extremely beneficial to the engineering design community.

Finally, the multiple surrogate approach could potentially overcome the main drawback associated with EGO – namely that the measure of the surrogate's prediction uncertainty in the expected improvement function is obtained from a single approximation method, which may not produce an accurate measure of error [81]. As an alternative, regions of high uncertainty can be identified by using multiple surrogates [60]. Such an uncertainty measure could then be combined with a metric representing improvement over the current best design into a function with similar properties as the EIF. Thus a multiple surrogate approach, with an intelligent updating scheme, may prove to be an extremely effective optimization algorithm, particularly when surrogates with limited accuracy are used.

Appendix A

An Improved Cross-Sectional Analysis for the Structural Dynamic Model

Over the past 25 years, significant advances have been made toward accurate modeling of composite blades with arbitrary cross-sectional geometry and material distribution. Particularly, Hodges and coworkers [15, 23, 65, 66, 122] have developed a beam model which accounts for all of the non-classical effects mentioned above, while requiring significantly less computational effort than a direct three dimensional (3-D) solution based on a nonlinear finite element discretization of the structure.

In the approach developed by Hodges et al., dimensional reduction of the 3-D elasticity equations representing the slender structure is performed by means of an asymptotic approximation, which results in a 1-D beam model. The dimensional reduction is based on the presence of a small parameter associated with the slender structure, namely the inverse of the blade's aspect ratio, which is used to split the 3-D structural dynamic problem into two independent problems with different spatial scales: a 2-D problem at the cross-section, and a 1-D problem along the longitudinal dimension. The 1-D problem defines the beam equations of motion, given in terms of 1-D deformations – i.e. axial, bending, torsion, and shear deformation – under applied loads, while the solution of the 2-D problem

provides cross-sectional stiffness and inertia constants which depend on the material distribution and cross-sectional geometry. Since the 1-D beam equations of motion are based on geometrically exact kinematics, the formulation is appropriate for large displacement analysis. The cross-sectional coefficients needed as inputs to the 1-D beam solver come from the 2-D finite element code VABS (Variational Asymptotic Beam Sectional Analysis), which accounts for arbitrary in and out-of-plane cross-sectional warping. Although warping displacements are much smaller than the 1-D beam deformations, accurate modeling of the warping is important since the stress field is a function of warping derivatives which may not be small [65]. The work by Hodges et al. represents the state of the art in computationally efficient structural modeling of a composite rotor blade.

Although the cross-sectional analysis described in Chapter III can account for arbitrary cross-sectional geometries and material distributions, in-plane stresses and warping were neglected. In VABS, the in-plane stresses are not neglected since it has been shown that the uniaxial stress assumption can lead to significant errors in the torsional rigidity for some composite cross-sections [171]. Furthermore, the out-of-plane warping deformation associated with the structural model from Refs. 88 and 174 is based on the St. Venant solution of a tip-loaded prismatic beam, as opposed to the more general warping displacements modeled in VABS. Another advantage of VABS is that the variational-asymptotic approach provides a powerful tool for extending basic theory, e.g. the solution of the coupled electroelastic beam problem, which is applicable to rotor blades with embedded piezocomposites, and the treatment of non-classical cross-sectional deformations associated with rotor blades with adaptive airfoils [112, 113]. In both cases, however, the 1-D beam equations

needed to be modified to account for the additional effects.

Clearly, it is desirable to upgrade the blade model described in Chapter III with VABS. Although VABS was designed to be used with the geometrically exact formulation described in Ref. 65, it has been used to calculate the cross-sectional properties needed as inputs for other rotorcraft analysis codes [67, 106]. However, there are two differences associated with the blade model developed by Yuan and Friedmann [174] and the other models with which VABS has been coupled: (1) the amplitude of the out-of-plane warping is represented as a spanwise degree of freedom in the Yuan and Friedmann (YF) model, and (2) there are cross-sectional constants associated with the YF model which are not computed in the VABS formulation. Therefore, the purpose of this appendix is to demonstrate that VABS can be used as the cross-sectional analysis associated with the YF blade model in spite of the differences between the formulations.

A.1 Comparison of Cross-Sectional Analyses

In order to determine the compatibility between the cross-sectional properties calculated by VABS and those needed as inputs to the YF blade model, it is useful to understand the similarities and differences between the two formulations. Therefore, this section provides comparisons between the strain relations, constitutive relations, the resulting strain energy relations, and the kinetic energy relations associated with the two formulations. The strain and kinetic energy relations are functions of the cross-sectional coefficients associated with each model. Note that in the following sections, the notation used in Chapter III is changed to facilitate a convenient comparison with the VABS formulation.

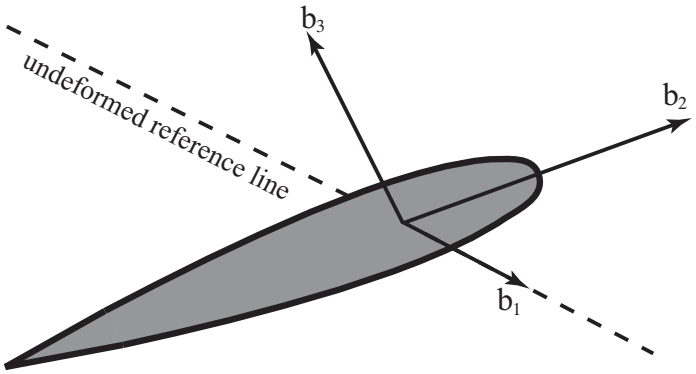

Figure A.1: Undeformed coordinate system

A.1.1 Strain Relations

Consider a beam idealized as a reference line, with a cross-section depicted in Fig. A.1. A coordinate system parallel to the orthogonal unit vectors $\mathbf{b}_i$ for $i = 1, 2, 3$ is fixed at each point along the undeformed reference line, where $\mathbf{b}_1$ is tangent to the reference line and $\mathbf{b}_2$, $\mathbf{b}_3$ are orthogonal to $\mathbf{b}_1$. The coordinates x_2, and x_3 correspond to the $\mathbf{b}_2$, $\mathbf{b}_3$ unit vectors, while x_1 denotes the axial location of the cross-section.

The non-zero components of the strain tensor in the $\mathbf{b}_i$ system associated with the YF blade model, i.e. Eqns. 3.15a – c, can be written in a notation consistent with VABS as follows:

$$\begin{aligned}\Gamma_{11}^{(Y)} = \quad & \gamma_{11} \quad + w_{1,1}^{(Y)} + k_1 \left(x_3 w_{1,2}^{(Y)} - x_2 w_{1,3}^{(Y)} \right) - x_2 \left(\bar{\kappa}_3 - 2\gamma_{12,1} + 2k_1 \gamma_{13} \right) \\ & - \quad x_3 \left(-\bar{\kappa}_2 - 2\gamma_{13,1} - 2k_1 \gamma_{12} \right) + \frac{1}{2} \left(x_2^2 + x_3^2 \right) \bar{\kappa}_1^2 \end{aligned} \tag{A.1}$$

$$2\Gamma_{12}^{(Y)} = 2\gamma_{12} + w_{1,2}^{(Y)} - x_3 \bar{\kappa}_1 \tag{A.2}$$

$$2\Gamma_{13}^{(Y)} = 2\gamma_{13} + w_{1,3}^{(Y)} + x_2 \bar{\kappa}_1 \ , \tag{A.3}$$

where the (Y) superscript denotes association with the YF blade model, and $(\ )_{,i}$ denotes a derivative with respect to the x_i coordinate. In Eqs. A.1 – A.3, the 1-D axial and shear strain measures at the reference line, which are functions of the x_1 coordinate only, are given by γ_{11}, γ_{12}, and γ_{13} respectively. The initial twist is denoted by k_1. The out-of-plane warping displacements w_1 are functions of x_1, x_2, and x_3. In the YF model,

$$w_1^{(Y)}(x_1, x_2, x_3) = \alpha(x_1)\,\Psi(x_2, x_3)\ , \tag{A.4}$$

where $\alpha(x_1)$ is the unknown 1-D warping amplitude and $\Psi(x_2, x_3)$ is the 2-D warping shape function. The warping shape functions are based on the St. Venant solution of a tip-loaded prismatic beam [88] and thus are known for a given cross-section.

The 1-D "moment strains" [65], $\bar{\kappa}_i$, are with respect to a coordinate system parallel to the $\mathbf{T}_i$ basis vectors shown in Fig. A.2 and represent the differences between the deformed and initial states of the twist and bending curvatures. The elastic twist is given by $\bar{\kappa}_1$, while $\bar{\kappa}_2$ and $\bar{\kappa}_3$ are the moment strains corresponding to bending. Since the helicopter rotor blade is assumed to have no initial curvature in the YF model, the bending moment strains are equal to the deformed bending curvatures.

In the VABS formulation, the moment strains are written with respect to the $\mathbf{B}_i$ coordinate system and denoted by κ_i. The $\mathbf{T}_i$ and $\mathbf{B}_i$ systems differ due to transverse shear deformation since $\mathbf{T}_1$ is tangent to the deformed reference line, while $\mathbf{B}_1$ is normal to the deformed cross-section. With the assumption of no initial bending curvature, the elastic twist and the deformed bending curvatures in the $\mathbf{T}_i$ system are transformed to the $\mathbf{B}_i$

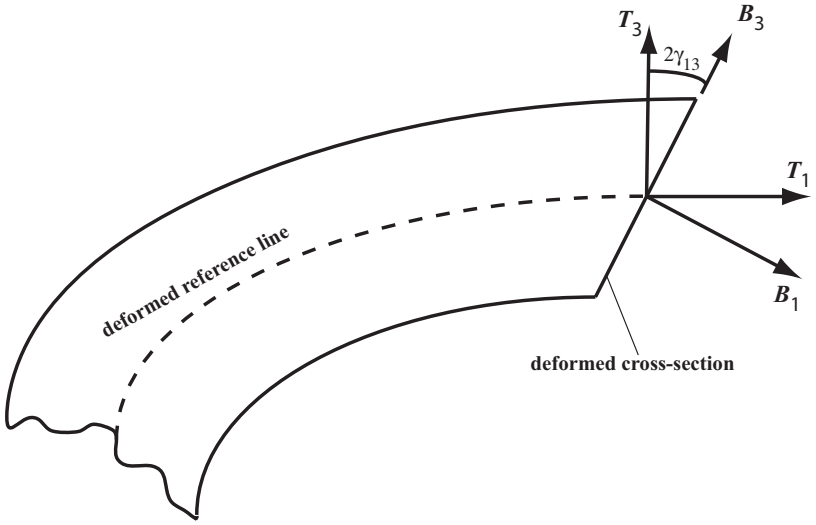

Figure A.2: Coordinate systems which differ due to transverse shear deformations

coordinate system by [170]:

$$\bar{\kappa}_1 = \kappa_1 \tag{A.5}$$

$$\bar{\kappa}_2 = \kappa_2 - 2\gamma_{13,1} - 2k_1\gamma_{12} \tag{A.6}$$

$$\bar{\kappa}_3 = \kappa_3 + 2\gamma_{12,1} - 2k_1\gamma_{13} \ . \tag{A.7}$$

The YF strain relations can be rewritten in a form which is consistent with the VABS formulation by substituting Eqs. A.5 – A.7 into Eqs. A.1 – A.3, resulting in

$$\Gamma_{11}^{(Y)} = \gamma_{11} + w_{1,1}^{(Y)} + k_1\left(x_3 w_{1,2}^{(Y)} - x_2 w_{1,3}^{(Y)}\right) - x_2\kappa_3 + x_3\kappa_2 + \frac{1}{2}\left(x_2^2 + x_3^2\right)\kappa_1^2 \tag{A.8}$$

$$2\Gamma_{12}^{(Y)} = 2\gamma_{12} + w_{1,2}^{(Y)} - x_3\kappa_1 \tag{A.9}$$

$$2\Gamma_{13}^{(Y)} = 2\gamma_{13} + w_{1,3}^{(Y)} + x_2\kappa_1 \ . \tag{A.10}$$

Note that $\Gamma_{22}^{(Y)} = \Gamma_{23}^{(Y)} = \Gamma_{33}^{(Y)} = 0$ since in-plane warping is neglected in the YF model.

From Ref. 65, the strain relations corresponding to VABS' "Generalized Timoshenko model" with the "trapeze effect" are given by

$$\begin{aligned}\Gamma_{11}^{(V)} = \quad & \gamma_{11} \quad + w_{1,1}^{(V)} + k_1 \left(x_3 w_{1,2}^{(V)} - x_2 w_{1,3}^{(V)} \right) - x_2 \kappa_3 + x_3 \kappa_2 \\ & + \quad \frac{1}{2} \left(x_2^2 + x_3^2 \right) \kappa_1^2 + \text{H.O.T.}\end{aligned} \tag{A.11}$$

$$2\Gamma_{12}^{(V)} = 2\gamma_{12} + w_{1,2}^{(V)} - x_3 \kappa_1 + f_{12} \left(w_2^{(V)}, w_3^{(V)} \right) + \text{H.O.T.} \tag{A.12}$$

$$2\Gamma_{13}^{(V)} = 2\gamma_{13} + w_{1,3}^{(V)} + x_2 \kappa_1 + f_{13} \left(w_2^{(V)}, w_3^{(V)} \right) + \text{H.O.T.} \tag{A.13}$$

$$\begin{aligned}\Gamma_{22}^{(V)} &= f_{22} \left(w_2^{(V)} \right) + \text{H.O.T.} \neq 0, \; \Gamma_{23}^{(V)} = f_{23} \left(w_2^{(V)}, w_3^{(V)} \right) + \text{H.O.T.} \neq 0, \\ \Gamma_{33}^{(V)} &= f_{33} \left(w_3^{(V)} \right) + \text{H.O.T.} \neq 0,\end{aligned} \tag{A.14}$$

where the (V) superscript denotes association with VABS, f_{ij} represent the contributions from the in-plane warping to the strain field, and H.O.T. refers to higher order terms which are present in the VABS formulation but are not accounted for in the YF strain relations.

In VABS, the warping displacements are discretized over the cross-section using the finite element approach. The VABS warping displacements can be written as

$$w_i^{(V)} (x_1, x_2, x_3) = S_{ij} (x_2, x_3) V_j (x_1) , \; i = 1, 2, 3 \text{ and } j = 1, 2, \ldots, N_V \; . \tag{A.15}$$

In Eq. A.15, S_{ij} are 2-D finite element shape functions, V_j are the nodal values of the

warping displacement over the cross-section, and N_V is the number of nodal degrees of freedom. In contrast to the YF formulation, the VABS warping displacements are not assumed to be in the shape of the St. Venant warping function $\Psi(x_2, x_3)$. Since the shape of the warping is not assumed, VABS treats warping displacements in a more general manner than the YF model.

The H.O.T.'s in Eqs. A.11 – A.13 consist of nonlinearities in the 1-D strain measures, such as γ_{11}^2 and $\kappa_2\kappa_3$ for example, and couplings between the warping displacements and the 1-D strain measures. Such H.O.T.'s were neglected in the derivation of the YF strain equations. However, $\frac{1}{2}\left(x_2^2 + x_3^2\right)\kappa_1^2$ was retained in the YF formulation since it accounts for a higher order extension-torsion coupling known as the "trapeze effect," which is known to be important for helicopter rotor blade modeling due to the large centrifugal forces.

From comparison of Eqs. A.8 – A.10 with Eqs. A.11 – A.14, its is clear that there are three differences in the strain relations associated with the VABS and YF formulations:

1. VABS treats out-of-plane warping in a more general manner, thus $w_1^{(V)} \neq w_1^{(Y)}$.

2. The effects of in-plane warping on the strain field are accounted for in VABS.

3. VABS includes higher order couplings between the 1-D strain measures, and coupling between the 1-D strain measures and warping displacements, which are neglected in the YF formulation.

A.1.2 Constitutive Relations

The constitutive relation for an anisotropic material given by Eqn. 3.17 can be rewritten as

$$\boldsymbol{\sigma}^{(V)} = \mathbf{D}\boldsymbol{\Gamma}^{(V)} \tag{A.16}$$

where

$$\boldsymbol{\sigma}^{(V)} = [\sigma_{11} \;\; \sigma_{12} \;\; \sigma_{13} \;\; \sigma_{22} \;\; \sigma_{23} \;\; \sigma_{33}]^T \tag{A.17}$$

$$\boldsymbol{\Gamma}^{(V)} = [\Gamma_{11} \;\; 2\Gamma_{12} \;\; 2\Gamma_{13} \;\; \Gamma_{22} \;\; 2\Gamma_{23} \;\; \Gamma_{33}]^T, \tag{A.18}$$

and $\mathbf{D}$ is the 6×6 symmetric compliance matrix. The VABS constitutive relation is based on Eq. A.16. In contrast, the YF model employs the uniaxial stress assumption, i.e. $\sigma_{22} = \sigma_{23} = \sigma_{33} = 0$. After neglecting the in-plane stresses, the constitutive relation associated with the YF model given by Eq. 3.18 is rewritten as

$$\boldsymbol{\sigma}^{(Y)} = \mathbf{Q}\boldsymbol{\Gamma}^{(Y)} \tag{A.19}$$

where

$$\boldsymbol{\sigma}^{(Y)} = [\sigma_{11} \;\; \sigma_{12} \;\; \sigma_{13}]^T \tag{A.20}$$

$$\boldsymbol{\Gamma}^{(Y)} = [\Gamma_{11} \;\; 2\Gamma_{12} \;\; 2\Gamma_{13}]^T, \tag{A.21}$$

and $\mathbf{Q}$ is a 3×3 symmetric matrix. Expressions for $\mathbf{Q}$ in terms of the $\mathbf{D}$ matrix's elements can be found in Ref. 174. Although the uniaxial stress assumption was considered valid for composite thin-walled structures in Ref. 174, it was demonstrated in Refs. 65 and

171 that this simplification may lead to significant errors in the torsional rigidity of a thin-walled composite boxbeam. Therefore, while the uniaxial stress simplification may lead to acceptable results for some composite cross-sections, the only way to ensure correct results for all cases is to employ a formulation, such as the one associated with VABS, which does not neglect in-plane stresses.

A.1.3 Strain Energy Relations

The relation for strain energy, U, is

$$2U = \int_0^L \iint_A \mathbf{\Gamma}^T \boldsymbol{\sigma} \, \mathrm{d}A \, \mathrm{d}x_1, \tag{A.22}$$

where L is the length of the beam, and A is the cross-sectional area of the structural member. Substitution of Eqs. A.4, A.8, A.9, A.10, and A.19 into Eq. A.22 gives the strain energy associated with the YF model:

$$2U^{(Y)} = \int_0^L \boldsymbol{\epsilon}_Y^T \mathbf{Y} \boldsymbol{\epsilon}_Y \, \mathrm{d}x_1, \tag{A.23}$$

where

$$\boldsymbol{\epsilon}_Y = \begin{bmatrix} \gamma_{11} & 2\gamma_{12} & 2\gamma_{13} & \kappa_1 & \kappa_2 & \kappa_3 & \kappa_1^2 & \alpha & \alpha_{,1} \end{bmatrix}^T, \tag{A.24}$$

and $\mathbf{Y}$ is a 9×9 symmetric matrix containing integrals over the cross-section which are provided in Ref. 174. The elements of $\mathbf{Y}$ are needed as inputs for the YF model, and are computed by the 2-D finite element cross-sectional analysis described in Ref. 88. To facilitate a straight forward comparison with the VABS strain energy relation, Eq. A.23 can

be rewritten as

$$2U^{(Y)} = 2\int_0^L \left(u_1^{(Y)} + u_2^{(Y)} + u_\alpha^{(Y)}\right) \mathrm{d}x_1 \tag{A.25}$$

where

$$u_1^{(Y)} = \frac{1}{2}\begin{bmatrix} \gamma_{11} \\ 2\gamma_{12} \\ 2\gamma_{13} \\ \kappa_1 \\ \kappa_2 \\ \kappa_3 \end{bmatrix}^T \begin{bmatrix} Y_{11} & Y_{12} & Y_{13} & Y_{14} & Y_{15} & Y_{16} \\ Y_{12} & Y_{22} & Y_{23} & Y_{24} & Y_{25} & Y_{26} \\ Y_{13} & Y_{23} & Y_{33} & Y_{34} & Y_{35} & Y_{36} \\ Y_{14} & Y_{24} & Y_{34} & Y_{44} & Y_{45} & Y_{46} \\ Y_{15} & Y_{25} & Y_{35} & Y_{45} & Y_{55} & Y_{56} \\ Y_{16} & Y_{26} & Y_{36} & Y_{46} & Y_{56} & Y_{66} \end{bmatrix} \begin{bmatrix} \gamma_{11} \\ 2\gamma_{12} \\ 2\gamma_{13} \\ \kappa_1 \\ \kappa_2 \\ \kappa_3 \end{bmatrix} \tag{A.26}$$

$$u_2^{(Y)} = \kappa_1^2\left(Y_{17}\gamma_{11} + 2Y_{27}\gamma_{12} + 2Y_{37}\gamma_{13} + Y_{47}\kappa_1 + Y_{57}\kappa_2 + Y_{67}\kappa_3 + \frac{Y_{77}}{2}\kappa_1^2\right) \tag{A.27}$$

$$u_\alpha^{(Y)} = \begin{bmatrix} \alpha \\ \alpha_{,1} \end{bmatrix} \begin{bmatrix} Y_{18} & \dots & \frac{Y_{88}}{2} & Y_{89} \\ Y_{19} & \dots & Y_{89} & \frac{Y_{99}}{2} \end{bmatrix} \boldsymbol{\epsilon}_Y. \tag{A.28}$$

The VABS strain energy is a function of the following 1-D parameters: γ_{11}, $2\gamma_{12}$, $2\gamma_{13}$, κ_1, κ_2, κ_3 and V_j, i.e.

$$2U^{(V)} = f\left(\gamma_{11}, 2\gamma_{12}, 2\gamma_{13}, \kappa_1, \kappa_2, \kappa_3, V_j\right). \tag{A.29}$$

From Eqs. A.23 and A.24, it is clear that $U^{(Y)}$ is similar in form to $U^{(V)}$ in the sense that $U^{(Y)}$ is a function of γ_{11}, $2\gamma_{12}$, $2\gamma_{13}$, κ_1, κ_2, κ_3, and the 1-D warping variable α. However,

in VABS the variational asymptotic method is applied in order to obtain an approximation of $U^{(V)}$ which is *not* a function of the 1-D warping variables, i.e.

$$2U^{(V)} \cong 2\tilde{U}^{(V)} = \tilde{f}\left(\gamma_{11}, 2\gamma_{12}, 2\gamma_{13}, \kappa_1, \kappa_2, \kappa_3\right), \tag{A.30}$$

where $\tilde{U}^{(V)}$ and $\tilde{f}$ are the approximations of $U^{(V)}$. The approximation of $U^{(V)}$ is obtained by minimizing the strain energy with respect to warping, which results in *warping recovery relations* for the nodal displacements V_j. The warping recovery relations are functions of the 1-D strain measures, γ_{11}, $2\gamma_{12}$, $2\gamma_{13}$, κ_1, κ_2, and κ_3.

In the original VABS strain energy $U^{(V)}$, the contribution due to warping is associated with the cross-sectional parameters multiplying V_j. However, in the approximate VABS strain energy, $\tilde{U}^{(V)}$, the contributions from warping are accounted for by a new set of cross-sectional parameters which multiply γ_{11}, $2\gamma_{12}$, $2\gamma_{13}$, κ_1, κ_2, and κ_3. Therefore, by approximating $U^{(V)}$ with $\tilde{U}^{(V)}$, the strain energy associated with warping displacements is accounted for by the terms multiplying the 1-D strain measures. Details on the application of the variational asymptotic method and the resulting expressions are given in Chapter 4

of Ref. 65. From Ref. 65, the VABS strain energy is given by

$$
\begin{aligned}
2\tilde{U}^{(V)} = & \int_0^L \begin{bmatrix} \gamma_{11} \\ 2\gamma_{12} \\ 2\gamma_{13} \\ \kappa_1 \\ \kappa_2 \\ \kappa_3 \end{bmatrix}^T \begin{bmatrix} H_{11} & H_{12} & H_{13} & H_{14} & H_{15} & H_{16} \\ H_{12} & H_{22} & H_{23} & H_{24} & H_{25} & H_{26} \\ H_{13} & H_{23} & H_{33} & H_{34} & H_{35} & H_{36} \\ H_{14} & H_{24} & H_{34} & H_{44} & H_{45} & H_{46} \\ H_{15} & H_{25} & H_{35} & H_{45} & H_{55} & H_{56} \\ H_{16} & H_{26} & H_{36} & H_{46} & H_{56} & H_{66} \end{bmatrix} \begin{bmatrix} \gamma_{11} \\ 2\gamma_{12} \\ 2\gamma_{13} \\ \kappa_1 \\ \kappa_2 \\ \kappa_3 \end{bmatrix} \mathrm{d}x_1 \\
& + \quad 2\int_0^L \begin{bmatrix} \gamma_{11} \\ \kappa_1 \\ \kappa_2 \\ \kappa_3 \end{bmatrix}^T (\gamma_{11}\mathbf{A} + \kappa_1\mathbf{B} + \kappa_2\mathbf{C} + \kappa_3\mathbf{D}) \begin{bmatrix} \gamma_{11} \\ \kappa_1 \\ \kappa_2 \\ \kappa_3 \end{bmatrix} \mathrm{d}x_1, \qquad \text{(A.31)}
\end{aligned}
$$

where $\mathbf{A}$, $\mathbf{B}$, $\mathbf{C}$, and $\mathbf{D}$ are symmetric 4×4 matrices. Note that the strain energy terms associated with $\mathbf{A}$, $\mathbf{B}$, $\mathbf{C}$, and $\mathbf{D}$ are higher order functions of the 1-D strain measures than the terms associated with $\mathbf{H}$. The $\mathbf{H}$, $\mathbf{A}$, $\mathbf{B}$, $\mathbf{C}$, and $\mathbf{D}$ matrices are output by VABS. In order to compare with $U^{(Y)}$, Eq. A.31 can be rewritten as

$$
2\tilde{U}^{(V)} = 2\int_0^L \left(u_1^{(V)} + u_2^{(V)} + u_{H.O.T.}^{(V)} \right) \mathrm{d}x_1 \,, \qquad \text{(A.32)}
$$

where

$$u_1^{(V)} = \frac{1}{2}\begin{bmatrix} \gamma_{11} \\ 2\gamma_{12} \\ 2\gamma_{13} \\ \kappa_1 \\ \kappa_2 \\ \kappa_3 \end{bmatrix}^T \begin{bmatrix} H_{11} & H_{12} & H_{13} & H_{14} & H_{15} & H_{16} \\ H_{12} & H_{22} & H_{23} & H_{24} & H_{25} & H_{26} \\ H_{13} & H_{23} & H_{33} & H_{34} & H_{35} & H_{36} \\ H_{14} & H_{24} & H_{34} & H_{44} & H_{45} & H_{46} \\ H_{15} & H_{25} & H_{35} & H_{45} & H_{55} & H_{56} \\ H_{16} & H_{26} & H_{36} & H_{46} & H_{56} & H_{66} \end{bmatrix} \begin{bmatrix} \gamma_{11} \\ 2\gamma_{12} \\ 2\gamma_{13} \\ \kappa_1 \\ \kappa_2 \\ \kappa_3 \end{bmatrix} \tag{A.33}$$

$$u_2^{(V)} = \kappa_1^2 \left[\left(A_{22} + 2B_{12} \right) \gamma_{11} + B_{22}\kappa_1 + \left(2B_{23} + C_{22} \right) \kappa_2 + \left(2B_{24} + D_{22} \right) \kappa_3 \right] \tag{A.34}$$

$$u_{H.O.T.}^{(V)} = \begin{bmatrix} \gamma_{11} \\ \kappa_1 \\ \kappa_2 \\ \kappa_3 \end{bmatrix}^T \left(\gamma_{11}\mathbf{A} + \kappa_1\mathbf{B} + \kappa_2\mathbf{C} + \kappa_3\mathbf{D} \right) \begin{bmatrix} \gamma_{11} \\ \kappa_1 \\ \kappa_2 \\ \kappa_3 \end{bmatrix} - u_2^{(V)}. \tag{A.35}$$

Using the strain energy relations given in Eqs. A.25 – A.28 for the YF formulation, and Eqs. A.32 – A.35 for VABS, a direct comparison of the cross-sectional parameters associated with both models can be made. The comparison is organized into three categories – (1) terms which are present in both model, (2) terms which are present in VABS' strain energy relation, but are not accounted for in the YF model, and (3) terms present in the YF model, but are not included in the VABS formulation.

A.1.4 Strain Energy Terms Present in Both Models

A comparison of Eqs. A.26 and A.27 with Eqs. A.33 and A.34 shows that

$$Y_{ij} \Leftrightarrow H_{ij} \quad \text{for } i,j = 1,\ldots,6 \tag{A.36}$$

$$Y_{17} \Leftrightarrow A_{22} + 2B_{12} \tag{A.37}$$

$$Y_{47} \Leftrightarrow B_{22} \tag{A.38}$$

$$Y_{57} \Leftrightarrow 2B_{23} + C_{22} \tag{A.39}$$

$$Y_{67} \Leftrightarrow 2B_{24} + D_{22} \tag{A.40}$$

In Eqs. A.36 – A.40, "$\Leftrightarrow$" denotes that the cross-sectional parameters multiply the same 1-D strain measures. It is important to use "$\Leftrightarrow$" instead of "$=$" because the cross-sectional parameters will not be equal to one another in general. There are two reasons the cross-sectional parameters in Eqs. A.36 – A.40 will not be equal:

1. In the constitutive relations associated with the YF model, the in-plane stresses are neglected; thus Eq. A.19 is substituted into Eq. A.22 in order to derive the strain energy relation. However, VABS does not make the uniaxial stress simplification. Therefore, the VABS strain energy relation is obtained by substituting Eq. A.16 into Eq. A.22.

2. The 1-D warping variables are eliminated from the VABS strain energy formulation, which results in $\tilde{U}^{(V)}$. In effect, VABS accounts for the strain energy due to in an

out-of-plane warping in the $\mathbf{H}$, $\mathbf{A}$, $\mathbf{B}$, $\mathbf{C}$, and $\mathbf{D}$ matrices, which multiply the 1-D strain measures and are functions of S_{ij}. However, the warping strain energy in the YF model is retained in terms of the 1-D out-of-plane warping amplitude α and the cross-sectional coefficients Y_{i8} and Y_{i9}, which are functions of Ψ.

A.1.5 Strain Energy Terms Present in VABS, but not in the YF model

The higher order VABS strain energy terms, $u^{(V)}_{H.O.T.}$, are not accounted for in the YF model. The strain energy contribution from $u^{(V)}_{H.O.T.}$ is due to the H.O.T.'s retained in the VABS strain relations.

A.1.6 Strain Energy Terms Present in the YF Model, but not in VABS

A comparison of Eqs. A.27 and A.34 shows that VABS does not output cross-sectional coefficients which correspond to Y_{27}, Y_{37} and Y_{77}. Such terms were neglected in the VABS strain energy formulation [65]. In addition, VABS does not calculate cross-sectional properties which correspond to the Y_{i8} and Y_{i9} terms present in $u^{(Y)}_{\alpha}$. Instead, VABS accounts for the strain energy due to warping within the $\mathbf{H}$, $\mathbf{A}$, $\mathbf{B}$, $\mathbf{C}$, and $\mathbf{D}$ matrices.

A.1.7 Kinetic Energy Relations

The kinetic energy cross-sectional properties calculated by VABS are given in Eqs. A.41 – A.46,

$$m \equiv \iint_A \rho \, \mathrm{d}A \tag{A.41}$$

$$m_{x_2} \equiv \iint_A \rho x_2 \, \mathrm{d}A \tag{A.42}$$

$$m_{x_3} \equiv \iint_A \rho x_3 \, \mathrm{d}A \tag{A.43}$$

$$I_{m_{22}} \equiv \iint_A \rho x_3^2 \, \mathrm{d}A \tag{A.44}$$

$$I_{m_{33}} \equiv \iint_A \rho x_2^2 \, \mathrm{d}A \tag{A.45}$$

$$I_{m_{23}} \equiv \iint_A \rho x_2 x_3 \, \mathrm{d}A \tag{A.46}$$

where ρ is the material density. The YF model requires the same kinetic energy cross-sectional parameters given by Eqs. A.41 – A.46 as inputs. In addition, the YF model also requires cross-sectional properties associated with the kinetic energy due to warping velocities [174]. Since warping velocity is neglected in the VABS formulation [65], VABS will not output cross-sectional properties associated with kinetic energy due to warping.

A.2 The YF/VABS Blade Model

In the previous section, the similarities and differences between the two cross-sectional analyses were specified. This section provides a description of how the similarities can be used to couple VABS with the YF model, and justification for why the differences between the cross-sectional formulations do not prevent the coupling. The capabilities and limitations of the YF/VABS model will be described in terms of the cross-sectional analysis, the solution of the 1-D beam displacements, and recovery of cross-sectional warping displacements and stresses.

A.2.1 Cross-Sectional Analysis

In order to couple VABS with the YF model, the cross-sectional parameters in the YF strain energy formulation are replaced with their VABS counterparts. This implies that the Y_{ij} terms in Eqs. A.36 – A.40 are replaced with the corresponding right hand side terms. The warping cross-sectional properties, Y_{i8} and Y_{i9}, as well as Y_{27}, Y_{37}, and Y_{77} are set to zero since there are no VABS counterparts. The YF warping cross-sectional coefficients need to be set to zero in order to avoid "double counting" of the strain energy due to warping since VABS already accounts for warping in the $\mathbf{H}$, $\mathbf{A}$, $\mathbf{B}$, $\mathbf{C}$, and $\mathbf{D}$ matrices. Even though strain energy contributions associated with Y_{27}, Y_{37}, Y_{77} and $u^{(V)}_{H.O.T.}$ are not accounted for in the YF/VABS model, the YF/VABS formulation represents an accurate representation of the "actual" strain energy since the unaccounted for terms are higher order functions of the 1-D strain measures compared to the terms which are accounted for. For example, Y_{27} is associated with the shear-twist coupling $\kappa_1^2\gamma_{12}$, which is higher order than the $\kappa_1\gamma_{12}$ term corresponding to H_{24}.

This process of replacing appropriate coefficients in the YF model with equivalent VABS parameters and setting various cross-sectional coefficients equal to zero will result in a "hybrid" strain energy formulation which will be different from $U^{(Y)}$ and $\tilde{U}^{(V)}$. In certain regards, the YF/VABS hybrid strain energy will be more accurate for composite beam modeling than the original YF formulation based on the cross-sectional analysis from Ref. 88 since in-plane stresses and warping are accounted for, and out-of-plane warping is treated in a more general manner by VABS. Furthermore, the loss in accuracy compared to the original YF and VABS strain energy formulations is due to the neglect of higher order

terms, and thus is expected to be insignificant.

The YF/VABS kinetic energy cross-sectional parameters are taken directly from the VABS outputs for Eqs. A.41 – A.46 since the YF model requires these coefficients. The kinetic energy parameters associated with warping velocities are set to zero since VABS does not account for warping inertia. However, the kinetic energy contribution from warping is not expected to be significant. Therefore, since higher order strain energy terms and warping inertia are not considered to be significant, the differences between the two formulations do not prohibit coupling of VABS with the YF model.

A.2.2 Solution of 1-D Beam Displacements

Using the VABS cross-sectional outputs as inputs to the YF model based on the procedure described above does not require modification of the 1-D kinematics associated with the YF model. This implies that the strain-displacement relations employed in Ref. 174 are retained, and the 1-D beam displacements – axial, bending, torsion, and shear deformation – are solved for by the finite element method described in Section 3.6. Since the strain-displacement relations are based on the ordering scheme described in Ref. 174, the YF/VABS model is only valid for moderate deflection analysis, which is sufficient for most helicopter rotor blade applications.

A.2.3 Recovery of Cross-Sectional Warping Displacements

Since Y_{i8} and Y_{i9} are set to zero in the YF/VABS model, the out-of-plane warping amplitude α is eliminated from the finite element discretized equations of motion. Therefore,

warping must be calculated using the VABS warping recovery relations. The warping recovery relations approximate V_j as functions of γ_{11}, $2\gamma_{12}$, $2\gamma_{13}$, κ_1, κ_2, and κ_3 using the variational asymptotic approach [65]. In the YF/VABS model, warping displacements are obtained from the VABS warping recovery relations as follows:

1. The beam 1-D displacements are solved for using the finite element approach.

2. The 1-D strain measures are recovered by substituting the displacements into the YF strain-displacement relations.

3. The 1-D strain measures are substituted into the VABS warping recovery relations, which yield in and out-of-plane warping displacements.

It is worth noting that by eliminating the 1-D variable α, the capability to model restrained warping, i.e. constraining warping displacements at the boundary to be zero, is lost. Without a 1-D variable associated with warping, there is no way to enforce boundary conditions on the warping displacements at the root. However, accounting for restrained warping is generally not considered to be critical for composite closed cross-sections [65, 156], even though exceptions are known to exist [126]. In the most extreme example presented by [126], a moderate error of 11% was observed in the prediction of the tip twist deformation when neglecting restrained warping effects. Furthermore, the Vlasov-type approach to restrained warping available in VABS is only appropriate for open cross-sections and may produce errors if used for closed section modeling, e.g. Ch. 7 of Ref. 65, and therefore is not used with the YF/VABS model. Thus, the YF/VABS model is suitable for rotor blade analysis since helicopter rotor blades are modeled as closed cross-

sections. Furthermore, accounting for restrained warping effects associated with closed sections would likely produce only moderate gains in accuracy at most.

A.2.4 Stress Recovery

The YF/VABS strain field is recovered by substituting the 1-D strain measures and cross-sectional warping derivatives into Eqs. A.11 – A.14. Note that the contributions from in-plane warping are included in the YF/VABS strain field since VABS accounts for in-plane warping. Stresses are obtained by substituting Eqs. A.11 – A.14 into Eq. A.16 instead of Eq. A.19 since VABS accounts for in-plane stresses.

It should be noted that a higher order beam theory would be needed to impose zero beam strains at the root and therefore the current approach will only provide an accurate estimation of the cross-sectional stress distributions away from the boundary.

A.3 Validation Results for the YF/VABS Model

In this section, results from the YF/VABS model are compared with experimental data and other analysis codes. The YF/VABS model was validated by considering displacements and stresses due to static loading, as well as calculation of vibratory hubloads in forward flight . Additional validation results can be found in Ref. 42. As in Refs. 67 and 68, the trapeze effect was treated by setting $A_{22} = H_{55} + H_{66}$ and all other elements of $\mathbf{A}$, $\mathbf{B}$, $\mathbf{C}$, and $\mathbf{D}$ to zero for all results. This is consistent with the YF model, in which $Y_{17} = Y_{55} + Y_{66}$.

A.3.1 Displacements and Stresses Under Static Loading

The YF/VABS static analysis capability is validated by considering a prismatic composite cantilevered beam, loaded by a vertical tip force. The YF/VABS results were compared with experimental data from Ref. 104 and results generated by NLABS (Nonlinear Active Beam Solver, [113]), which is based on the geometrically exact kinematic formulation for which VABS was designed. Details on the experimental setup can be found in Ref. 15 and 104. The static displacement results in Fig. A.3 correspond to two composite cross-sections: (1) a symmetric layup, $[45^\circ/0^\circ]_{3s}$ which exhibits bending-torsion coupling, and (2) an anti-symmetric layup, $[20^\circ/-70^\circ/-70^\circ/20^\circ]_{2a}$ which exhibits extension-twist coupling. The YF/VABS model compares well with the experimental results and NLABS until the loading is large enough to cause deflections over 10% of the beam length. This is expected since the ordering scheme used to simplify the YF strain-displacement relation is based on the assumption that the maximum bending deflections are on the order of 10 – 20% of the beam's length [174]. These results demonstrate that the YF/VABS model is valid for moderate deflection analysis, while a geometrically exact formulation is necessary to accurately model large deflections.

Figure A.4 shows the axial stress distribution at the midspan section calculated by NLABS, YF/VABS, and a 3-D finite element solution using the MSC.NASTRAN linear static solver for the symmetric layup and a tip force of 0.0044 N, which is well within the moderate deflection regime. The NASTRAN model contains over 2 million degrees of freedom and requires 25 GB of memory and 8 hours of simulation time on a 3.2 Ghz Xeon processor. By comparison, NLABS and YF/VABS require less than 1 minute of simula-

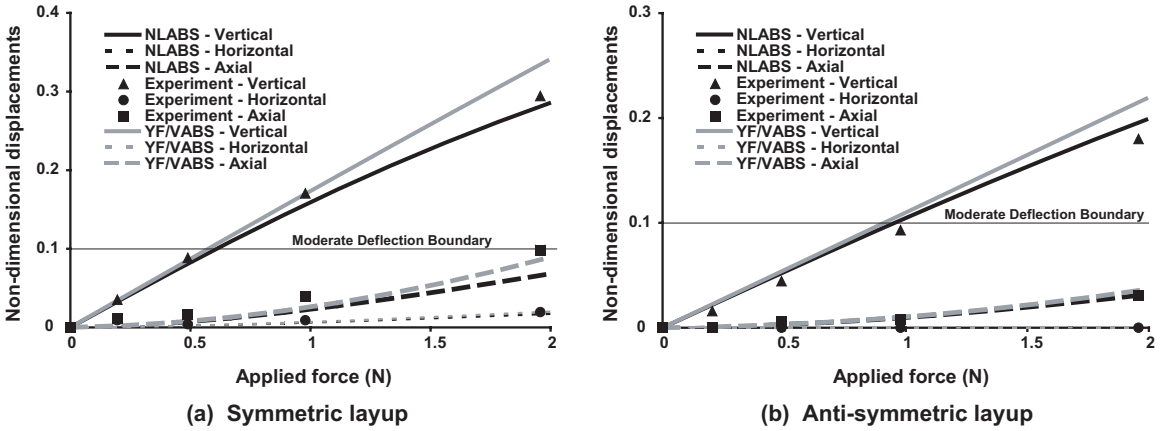

Figure A.3: Composite beam displacements, non-dimensionalized by the beam length

tion time. Figure A.4 illustrates that the cross-sectional stress distributions calculated by YF/VABS and NLABS yield similar agreement with the NASTRAN results for moderate deflection analysis.

A.3.2 Vibratory Hubloads in Forward Flight

Using the rotor and helicopter parameters from Ref. 175, the 4/rev vibratory hub shears and moments were calculated for a double-cell composite blade depicted in Fig. A.5 at an advance ratio of 0.30. The ply angles in the middle vertical wall and the inner half of the rear vertical wall were oriented at Λ_{v}, while ply angles in the remaining walls were set to zero. The vibratory hubloads calculated by YF/VABS are compared with the YF model in Fig. A.6 for various values of Λ_{v}. It is clear from Fig. A.6 that YF/VABS and the YF model predict similar trends in vibratory loads as Λ_{v} is varied. Furthermore, the differences in hub shears range from $0.1 - 8.7\%$ relative to the YF values, and $0.01 - 8.2\%$ for the hub moments. These results suggest that the VABS cross-sectional analysis will result in small to moderate differences in the vibratory loads compared to the model based on the

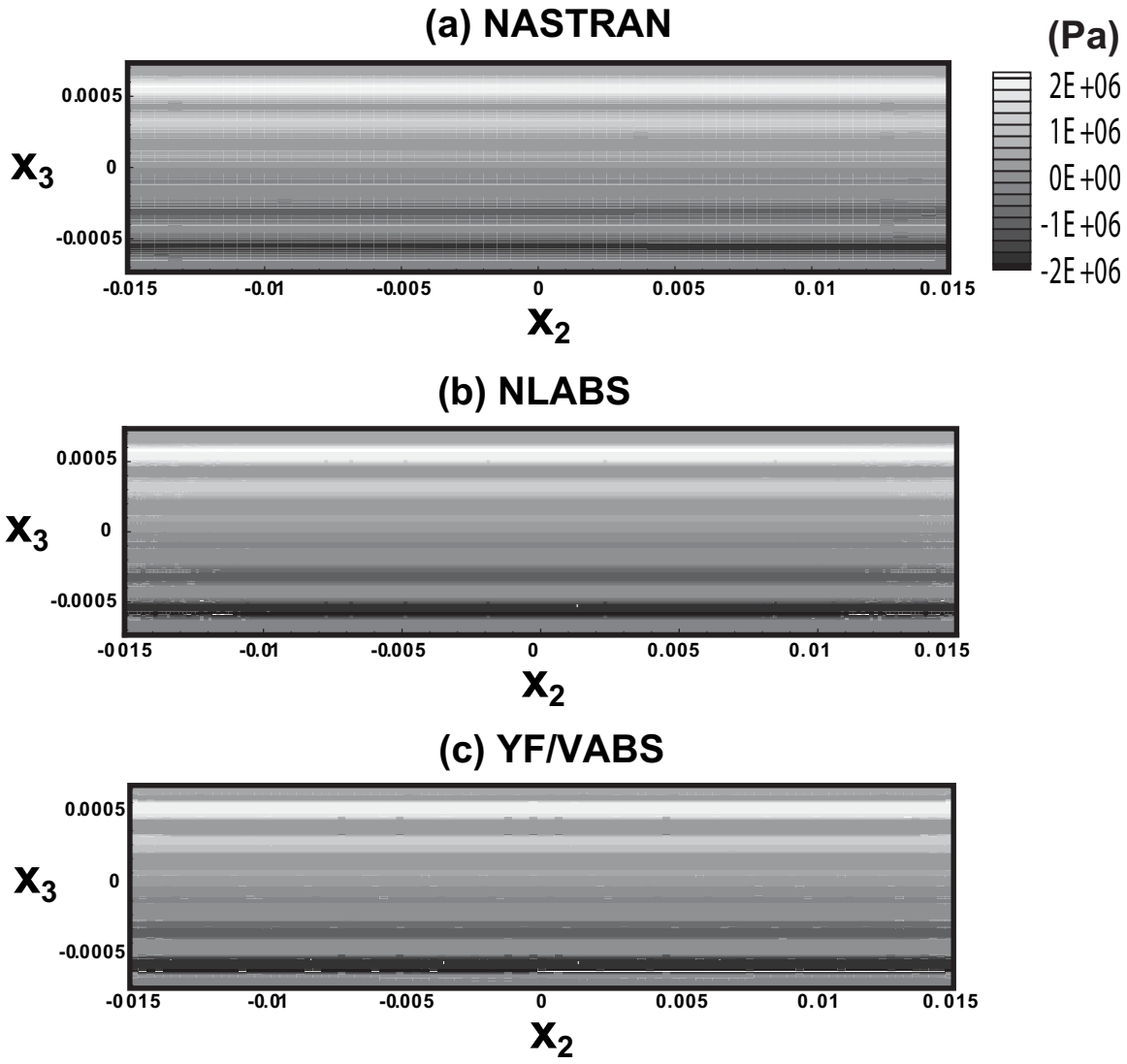

Figure A.4: Axial stress distributions (σ_{11}) corresponding to the symmetric layup

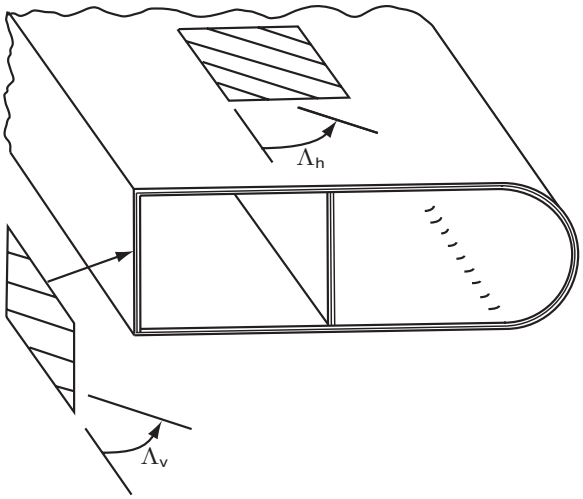

Figure A.5: Double-cell cross-section

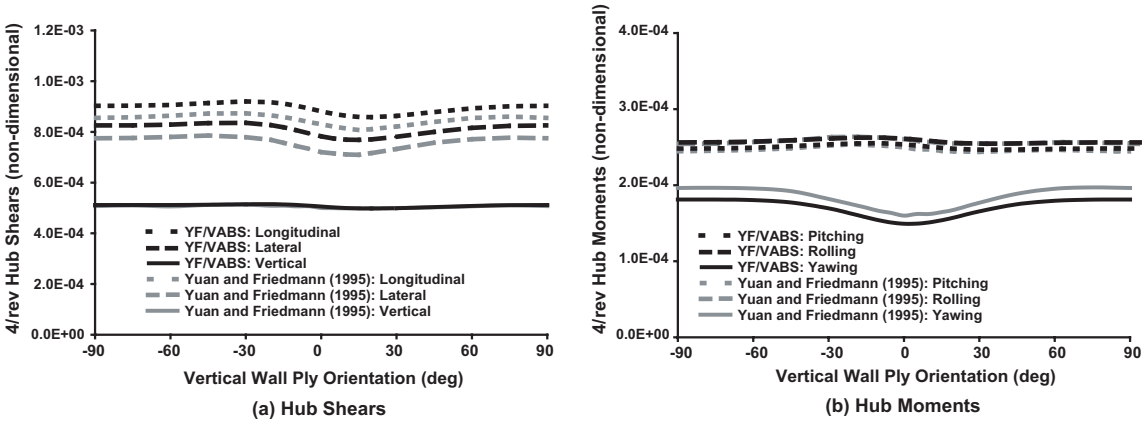

Figure A.6: Comparison of vibratory hubloads as a function of Λ_v

cross-sectional analysis described in Ref. 88.

A.4 Summary

The results demonstrate that VABS is suitable for coupling with the moderate deflection composite blade model described in Ref. 174, in spite of the differences between the formulations. Compared to the original YF blade model, YF/VABS will (1) output a more accurate stress field due to the more general treatment of warping, and (2) will accurately

compute the elastic stiffness quantities for composite cross-sections in which the neglect of in-plane stresses would produce large errors.

Appendix B

Comparison of Aeroelastic Stability Eigenvalues with RFA and Quasi-steady Aerodynamic Models in Hover

In this appendix, hover stability eigenvalues calculated with the RFA aerodynamic model using the approach described in Section 6.7 are presented. The eigenvalues obtained with the RFA model are compared to those based on a relatively simple quasi-steady, incompressible aerodynamic model employed in Ref. 174. The quasi-steady model is based on Greenberg's extension of Theodorsen's theory [62]. The results were generated using the MBB BO-105 baseline rotor described in Table 8.1 for $0.01 \leq C_T/\sigma \leq 0.10$.

B.1 Root Locus Eigenvalues

Figure B.1 provides the root loci when using RFA and quasi-steady aerodynamics. It is clear from Fig. B.1a and b that the presence of unsteadiness and compressibility effects in the RFA model results in little difference in the real and imaginary parts of the eigenvalues associated with the 1^{st} and 2^{nd} lead-lag modes. Over the range of C_T/σ which was considered, the relative differences in the lead-lag eigenvalues compared to the quasi-steady values vary from $0.003 - 0.5\%$ for the imaginary parts, and $0.5 - 5.3\%$ for the real parts.

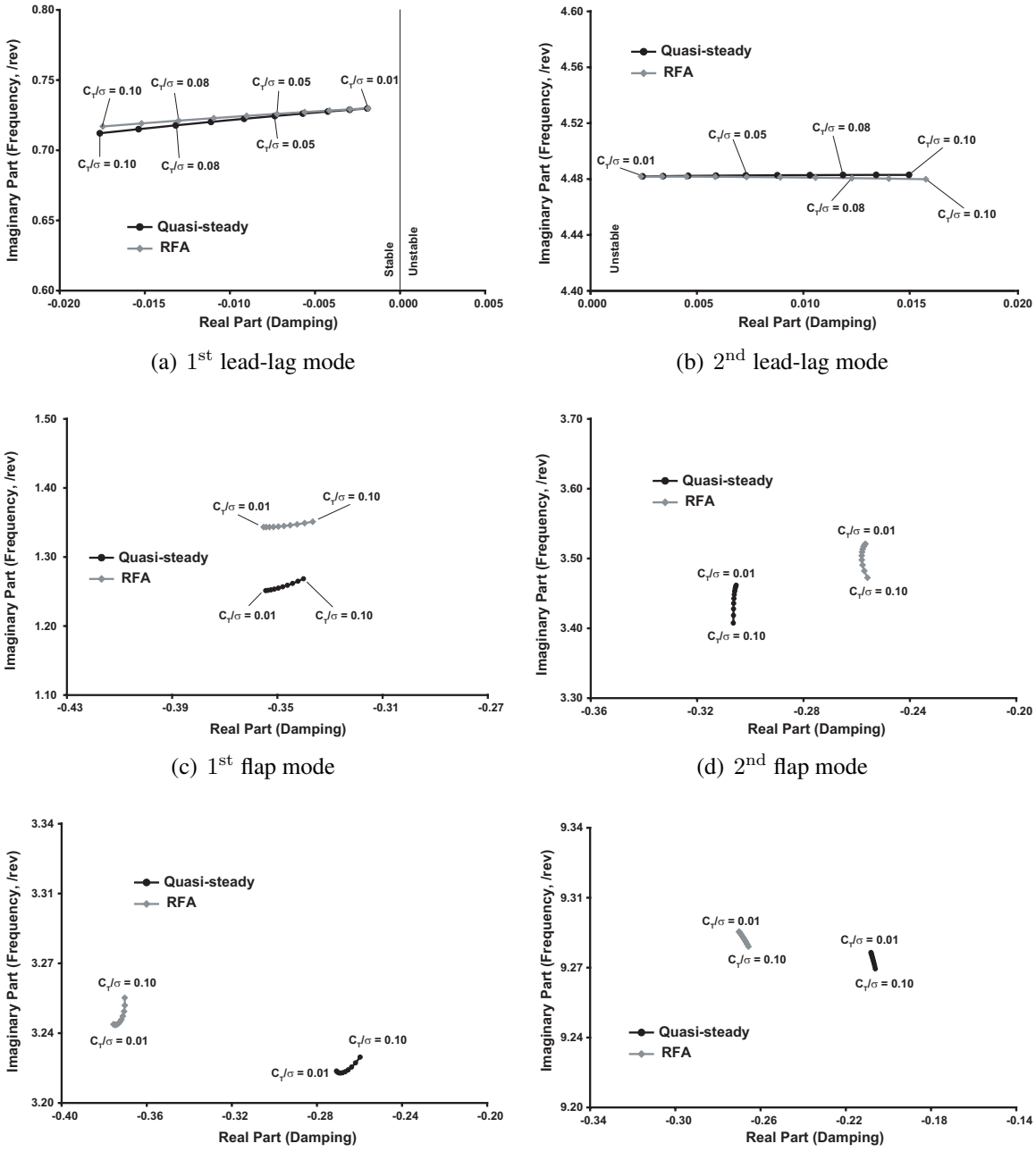

(a) 1^{st} lead-lag mode

(b) 2^{nd} lead-lag mode

(c) 1^{st} flap mode

(d) 2^{nd} flap mode

(e) 1^{st} torsion mode

(f) 2^{nd} torsion mode

Figure B.1: Root locus eigenvalues as a function of C_T/σ

The real parts of the 1^{st} flap mode eigenvalues calculated with the RFA model are all within 1% of the values obtained with the quasi-steady model. However, as depicted in Fig. B.1c, there is a noticeable difference in the imaginary parts. The differences between the imaginary parts of the 1^{st} flap mode range from $6.5 - 7.4\%$. In contrast to the 1^{st} flap mode, there are significant differences of $16 - 17\%$ in the real parts of the 2^{nd} flap mode eigenvalues. The differences in the 2^{nd} flap mode imaginary parts are all under 2%.

The largest differences between the hover stability eigenvalues correspond to the torsion modes, which are depicted in Figs. B.1e and f. For each value of C_T/σ, there is about 40% and 30% difference between the real parts calculated by the RFA and quasis-steady models for the 1^{st} and 2^{nd} torsion modes respectively. The differences in the imaginary parts are all under 1%.

B.2 Summary

The results in this appendix indicate that the effects of unsteadiness and compressibility can significantly affect the calculated real parts of the hover stability eigenvalues associated with the 2^{nd} flap mode and the 1^{st} and 2^{nd} torsion modes. In contrast, there was little difference between the RFA and quasi-steady models in terms of the imaginary parts of the eigenvalues.

Bibliography

[1] "iSIGHT Version 9.0 Reference Guide,". Engenious Software Inc.

[2] N. Alexandrov, J. E. Dennis Jr., R. M. Lewis, and V. Torczon. "A Trust Region Framework for Managing the use of Approximate Models in Optimization,". *Structural Optimization*, 15(1):16 – 23, 1998.

[3] T. Aoyama, C. Yang, and S. Saito. "Numerical Analysis of Active Flap for Noise Reduction Using Overlapped Grid Method,". *Journal of the American Helicopter Society*, 52(3):189 – 200, 2007.

[4] J. D. Baeder and B. W. Sim. "Blade-Vortex Interaction Noise Reduction by Active Trailing-Edge Flaps,". In *Proceedings of the 54th Annual Forum of the American Helicopter Society*, Washington, DC, May 1998.

[5] A. Bagai. *Contributions to the Mathematical of Rotor Flow-Fields Using a Pseudo-Implicit Free-Wake Analysis*. PhD Dissertation, University of Maryland, 1995.

[6] G. Bir and I. Chopra, *University of Maryland Advanced Rotor Code (UMARC) Theory Manual*. University of Maryland, technical report um-aero 94-18 edition, July 1994.

[7] A. J. Booker, J. E. Dennis Jr., P. D. Frank, D. B. Serafini, V. Torczon, and M. W. Trosset. "A Rigorous Framework for Optimization of Expensive Functions by Surrogates,". *Structural Optimization*, 17:1–13, 1999.

[8] D. D. Boyd, T. F. Brooks, C. L. Burley, and J. R. Jolly. "Aeroacoustic Codes for Rotor Harmonic and BVI Noise - Camrad.Mod1/HIRES,". *Journal of the American Helicopter Society*, 45(2):63–89, April 2000.

[9] K. S. Brentner, *A Computer Program Incorporating Realistic Blade Motions and Advanced Acoustic Formulation*. NASA Technical Memorandum, Vol. 87721 1986.

[10] K. S. Brentner and F. Farassat. "Helicopter Noise Prediction: The Current Status and Future Direction,". *Journal of Sound and Vibration*, 170(1):79–96, 1994.

[11] K. S. Brentner and F. Farassat. "Modeling Aerodynamically Generated Sound of Helicopter Rotors,". *Progress in Aerospace Sciences*, 39:83–120, 2003.

[12] K. S. Brentner and F. Farassat. "Modeling Aerodynamically Generated Sound of Helicopter Rotors,". *Progress in Aerospace Sciences*, 39(2–3):83–120, February–April 2003.

[13] R. Celi. "Recent Applications of Design Optimization to Rotorcraft – A Survey,". *Journal of Aircraft*, 36(1):176–189, January-February 1999.

[14] R. Celi and P. P. Friedmann. "Structural Optimization with Aeroelastic Constraints of Rotor Blades with Straight and Swept Tips,". *AIAA Journal*, 28(5):928–936, 1990.

[15] C. E. S. Cesnik and D. H. Hodges. "VABS: A New Concept for Composite Rotor Blade Cross-Sectional Modeling,". *Journal of the American Helicopter Society*, 42(1):27–38, Jan. 1997.

[16] B. D. Charles, H. Tadghighi, and A. Hassan. "Higher Harmonic Actuation of Trailing-Edge Flaps for Rotor BVI Noise Control,". In *Proceedings of the 52nd Annual Forum of the American Helicopter Society*, Washington, DC, June 1996.

[17] V. C. P. Chen, K. Tsui, R. B. Barton, and M. Meckesheimer. "A Review on Design, Modeling, and Applications of Computer Experiments,". *IIE Transactions*, 38:273 – 291, 2006.

[18] R. P. Cheng and R. Celi. "Optimum 2/Rev Inputs for Improved Rotor Performance,". In *Proceedings of the American Helicopter Society Northeast Region Active Controls Technology Conference*, Fairfield County,Connecticut, October 2000.

[19] R. P. Cheng, C. Theodore, and R. Celi. "Effects of Two/rev Higher Harmonic Control on Rotor Performance,". *Journal of the American Helicopter Society*, 48(1):18–27, January 2003.

[20] I. Chopra. "Status of Application of Smart Structures Technology to Rotorcraft Systems,". *Journal of the American Helicopter Society*, 45(4):228–252, October 2000.

[21] K. Collins, J. Bain, L. Sankar, T. A. Egolf, R. D. Janakiram, K. Brentner, and L. Lopes. "Pareto Frontier Method for Multi-disciplinary Optimization of Helicopter Rotors,". In *American Helicopter Society's Specialist's Conference on Aeromechanics*, San Francisco, CA, Jan. 23 – 25 2008.

[22] R. Cribbs and P. P. Friedmann. "Actuator Saturation and Its influence on Vibration Reduction by Actively Controlled Flaps,". In *Proceedings of the 42nd AIAA/ASME/ASCE/AHS/ACS Structures, Structural Dynamics and Materials Conference*, Seattle, WA, April 2001. AIAA Paper No. 2001-1467.

[23] D. A. Danielson and D. H. Hodges. "Nonlinear Beam Kinematics by Decomposition of the Rotation Tensor,". *Journal of Applied Mechanics*, 54:258–262, jun 1987.

[24] I. Das and J. E. Dennis. "A Closer Look at Drawbacks of Minimizing Weighted Sums of Objectives for Pareto Set Generation in Multicriteria Optimization Problems,". *Structural Optimization*, 14(1):63 – 69, 1997.

[25] A. Datta and W. Johnson. "An Assessment of the State-of-the-art in Multidisciplinary Aeromechanical Analyses,". In *American Helicopter Society's Specialist's Conference on Aeromechanics*, San Francisco, CA, Jan. 23 – 25 2008.

[26] M. W. Davis and W. H. Weller. "Helicopter Rotor Dynamics Optimization with Experimental Verification,". *Journal of Aircraft*, 28(1):38 – 48, 1991.

[27] S. Dawson, F. K. Straub, E. Booth, and M. Marcolini. "Wind Tunnel Test of an Active Flap Rotor: BVI Noise and Vibration Reduction,". In *Proceedings of the 51st Annual Forum of the American Helicopter Society*, pages 381–392, Fort Worth, TX, May 1995.

[28] M. de Terlizzi. *Blade Vortex Interaction and Its Alleviation Using Passive and Active Control Approaches*. PhD Dissertation, UCLA, 1999. Mechanical and Aerospace Engineering.

[29] K. Deb, S. Agrawal, S. Pratap, and T. Meyarivan. "A Fast and Elitist Multiobjective Genetic Algorithm: NSGA-II,". *IEEE Transactions on Evolutionary Computation*, 6(2):182 – 197, April 2002.

[30] G. Depailler. *Alleviation of Dynamic Stall Induced Vibrations on Helicopter Rotors Using Actively Controlled Flaps*. PhD Dissertation, University of Michigan, 2002. Aerospace Engineering.

[31] G. Depailler and P. P. Friedmann. "Alleviation of Dynamic Stall Induced Vibrations Using Actively Controlled Flaps,". In *58th Annual Forum of the American Helicopter Society*, Montreal, Canada, June 2002.

[32] G. Depailler and P. P. Friedmann. "Reductions of Vibrations Due to Dynamic Stall in Helicopters Using an Actively Controlled Flap,". In *Proceedings of the 43rd AIAA/ASME/ASCE/AHS/ACS Structures, Structural Dynamics and Materials Conference*, Denver, CO, April 2002. AIAA Paper No. 2002-1431.

[33] B. Enenkl, V. Klöppel, D. Preissler, and P. Jänker. "Full Scale Rotor with Piezoelectric Actuated Blade Flaps,". In *Proceedings of the Twenty-Eighth European Rotorcraft Forum*, Bristol, UK, September 2002.

[34] F. Farassat. "Linear Acoustic Formulas for Calculation of Rotating Blade Noise,". *AIAA Journal*, 19(9), September 1981.

[35] F. Farassat and G. P. Succi. "The Prediction of Helicopter Rotor Discrete Frequency Noise,". *Vertica*, 7(4):309–320, May 1983.

[36] A. Farhang-Mehr and S. Azarm. "Bayesian Meta-Modelling of Engineering Design Simulations: A Sequential Approach with Adaptation to Irregularities in the Response Behaviour,". *International Journal for Numerical Methods in Engineering*, 62:2104 – 2126, 2005.

[37] J. E. Ffowcs Williams and D. L. Hawkings. "Sound Generation by Turbulence and Surfaces in Arbitrary Motion,". *Philosophical Transactions of Royal Soc. London, Series A*, 264(1151):321–342, May 1969.

[38] J. Forsberg and L. Nilsson. "On Polynomial Response Surfaces and Kriging for use in Structural Optimization of Crashworthiness,". *Structural and Multidisciplinary Optimization*, 29(3):232 – 243, 2005.

[39] P. P. Friedmann. "Helicopter Vibration Reduction Using Structural Optimization with Aeroelastic/Multidisciplinary Constraints – A Survey,". *Journal of Aircraft*, 28(1):8–21, January 1991.

[40] P. P. Friedmann. "Rotary Wing Aeroelasticity - Current Status and Future Trends,". *AIAA Journal*, 42(10):1953–1972, October 2004.

[41] P. P. Friedmann, M. de Terlizzi, and T. F. Myrtle. "New Developments in Vibration Reduction with Actively Controlled Trailing Edge Flaps,". *Mathematical and Computer Modelling*, 33:1055–1083, 2001.

[42] P. P. Friedmann, B. Glaz, and R. Palacios. "A Moderate Deflection Composite Helicopter Rotor Blade Model with an Improved Cross-Sectional Analysis,". *International Journal of Solids and Structures*, 2008. to appear.

[43] P. P. Friedmann and D. H. Hodges. "Rotary Wing Aeroelasticity - A Historical Perspective,". *Journal of Aircraft*, 40(6):1019–1046, November 2003.

[44] P. P. Friedmann and T. A. Millott. "Vibration Reduction in Rotorcraft Using Active Control: A Comparison of Various Approaches,". *Journal of Guidance, Control, and Dynamics*, 18(4):664–673, July-August 1995.

[45] P. P. Friedmann and P. Shanthakumaran. "Optimum Design of Rotor Blades for Vibration Reduction in Forward Flight,". *Journal of the American Helicopter Society*, 29(4):70 – 80, 1984.

[46] J. C. Fu and L. Wang. "A Random-Discretization Based Monte Carlo Sampling Method and Its Applications,". *Methodology and Computing in Applied Probability*, 4:5 – 25, 2002.

[47] M. Fulton and R. A. Ormiston. "Small-Scale Rotor Experiments with On-Blade Elevons to Reduce Blade Vibratory Loads in Forward Flight,". In *Proceedings of the 54th Annual Forum of the American Helicopter Society*, pages 433–451, Washington, DC, May 1998.

[48] R. Ganguli. "Optimal Design of a Low Vibration Helicopter Rotor Using Response Surface Approximation,". *Journal of Sound and Vibration*, 258(2):327 – 344, 2002.

[49] R. Ganguli. "Survey of Recent Developments in Rotorcraft Design Optimization,". *Journal of Aircraft*, 41(3):493–510, May-June 2004.

[50] R. Ganguli and I. Chopra. "Aeroelastic Optimization of a Helicopter Rotor to Reduce Vibration and Dynamic Stresses,". *Journal of the Aircraft*, 12(4):808 – 815, July – Aug. 1996.

[51] R. Ganguli and I. Chopra. "Aeroelastic Optimization of a Helicopter Rotor with Two-Cell Composite Blades,". *Journal of the American Helicopter Society*, 34(4):835 – 841, April 1996.

[52] S. E. Gano, J. E. Renaud, J. D. Martin, and T. W. Simpson. "Update Strategies for Kriging Models Used in Variable Fidelity Optimization,". *Structural and Multidisciplinary Optimization*, 32(4):287 – 298, Oct. 2006.

[53] S. E. Gano, J. E. Renaud, and B. Sanders. "Hybrid Variable Fidelity Optimization Using a Kriging-Based Scaling Function,". *AIAA Journal*, 43(11):2422 – 2430, Nov. 2005.

[54] W. Gerstenberger, R. A. Wagner, B. Kelley, and C. W. Ellis. "The Rotary Round Table: How Can Helicopter Vibrations be Minimized,". *Journal of the American Helicopter Society*, 2(3), July 1957.

[55] B. Glaz, P. P. Friedmann, and L. Liu. "Efficient Global Optimization of Helicopter Rotor Blades for Vibration Reduction in Forward Flight,". In *11th AIAA/ISSMO Multidisciplinary Analysis & Optimization Conference*, pages 1 – 20, Portsmouth, VA, September 6-8 2006. AIAA Paper 2006-6997.

[56] B. Glaz, P. P. Friedmann, and L. Liu. "Surrogate Based Optimization of Helicopter Rotor Blades for Vibration Reduction in Forward Flight,". *Structural and Multidisciplinary Optimization*, 35(4):341 – 363, April 2008.

[57] B. Glaz, P. P. Friedmann, and L. Liu. "Vibration and Noise Reduction of Helicopter Rotors Using an Active/Passive Approach,". In *American Helicopter Society's Specialist's Conference on Aeromechanics*, San Francisco, CA, Jan. 23 – 25 2008.

[58] B. Glaz, P. P. Friedmann, and L. Liu. "Vibration Reduction and Performance Enhancement of Helicopter Rotors Using an Active/Passive Approach,". In *49th AIAA/ASME/ASCHE/AHS/ASC Structures, Structural Dynamics & Materials Conference*, pages 1 – 18, Schaumburg, IL, April 7 – 10 2008. AIAA Paper 2008-2178.

[59] B. Glaz, T. Goel, L. Liu, P. P. Friedmann, and R. T. Haftka. "Application of a Weighted Average Surrogate Approach to Helicopter Rotor Blade Vibration Reduction,". In *48th AIAA/ASME/ASCE/AHS/ACS Structures, Structural Dynamics and Materials Conference*, pages 1 – 25, Honolulu, HI, April 23 – 26 2007. AIAA Paper 2007-1898.

[60] T. Goel, R. T. Haftka, W. Shyy, and N. V. Queipo. "Ensemble of Surrogates,". *Structural and Multidisciplinary Optimization*, 33:199 – 216, 2007.

[61] T. Goel, R. Vaidyanathan, R. T. Haftka, W. Shyy, N. V. Queipo, and K. Tucker. "Response Surface Approximation of Pareto Optimal Front in Multi-objective Optimization,". *Computer Methods in Applied Mechanics and Engineering*, 196:879 – 893, 2007.

[62] J. M. Greenberg, *Airfoil in Sinusoidal Motion in a Pulsating Stream*. NACA TN-1326, 1947.

[63] Hariharan, N., and Leishman, J. G. "Unsteady Aerodynamics of a Flapped Airfoil in Subsonic Flow by Indicial Concepts,". *Journal of Aircraft*, 33(5):855 – 868, September-October 1996.

[64] C. J. He and D. A. Peters. "Optimization of Rotor Blades for Combined Structural, Dynamic, and Aerodynamic Properties,". *Structural Optimization*, 5:37 – 44, 1992.

[65] D. H. Hodges. *Nonlinear Composite Beam Theory*, AIAA, Reston, VA, 2006.

[66] D. H. Hodges, A. R. Atilgan, C. E. S. Cesnik, and M. V. Fulton. "On a Simplified Strain Energy Function for Geometrically Nonlinear Behavior of Anisotropic Beams,". *Composites Engineering*, 2:513–526, 1992.

[67] D. H. Hodges, H. Saberi, and R. A. Ormiston. "Development of Nonlinear Beam Elements for Rotorcraft Comprehensive Analyses,". *Journal of the American Helicopter Society*, 52(1):36–48, Jan. 2007.

[68] D. H. Hodges and W. Yu. "A Rigorous, Engineer-friendly Approach for Modeling Realistic, Composite Rotor Blades,". *Wind Energy*, 10:179–193, 2007.

[69] T. Homma and A. Saltelli. "Importance Measures in Global Sensitivity Analysis of Nonlinear Models,". *Reliability Engineering and Systems Safety*, 52:1–17, 1996.

[70] D. Huang, T. T. Allen, W. I. Notz, and N. Zeng. "Global Optimization of Stochastic Black-Box Systems via Sequential Kriging Meta-Models,". *Journal of Global Optimization*, 34:441 – 466, 2006.

[71] S. A. Jacklin. "Second Test of a Helicopter Individual Blade Control System in the NASA Ames 40 by 80 Foot Wind Tunnel,". In *Proceedings of the 2nd International American Helicopter Society Aeromechanics Specialists Conference*, Bridgeport, CT, October 1995.

[72] R. Jin, W. Chen, and T. W. Simpson. "Comparative Studies of Metamodeling Techniques Under Multiple Modeling Criteria,". *Structural and Multidisciplinary Optimization*, 23:1 – 13, 2001.

[73] R. Jin, W. Chen, and A. Sudjianto. "An Efficient Algorithm for Constructing Optimal Design of Computer Experiments,". *Journal of Statistical Planning and Inference*, 134(1):268 – 287, 2005.

[74] W. Johnson, *Comprehensive Analytical Model of Rotorcraft Aerodynamics and Dynamics, Part I: Analysis Development*. NASA Technical Manual TM 81182, 1980.

[75] W. Johnson. *Helicopter Theory*, Dover, 1980.

[76] W. Johnson, *Self-Tuning Regulators for Multicyclic Control of Helicopter Vibrations*. NASA Technical Paper 1996, 1982.

[77] W. Johnson, *CAMRAD/JA - A Comprehensive Analytical Model of Rotorcraft Aerodynamics and Dynamics, Vol I. Theory Manual*. Johnson Aeronautics, Palo Alto, CA, 1988.

[78] W. Johnson, *CAMRAD/JA - A Comprehensive Analytical Model of Rotorcraft Aerodynamics and Dynamics, Vol II. Users' Manual*. Johnson Aeronautics, Palo Alto, CA, 1988.

[79] W. Johnson and A. Datta. "Requirements for Next Generation Comprehensive Analysis of Rotorcraft,". In *American Helicopter Society's Specialist's Conference on Aeromechanics*, San Francisco, CA, Jan. 23 – 25 2008.

[80] D. R. Jones. "The DIRECT global optimization algorithm,". *Encyclopedia of Optimization*, 1:431 – 440, 2001.

[81] D. R. Jones. "A Taxonomy of Global Optimization Methods Based on Response Surfaces,". *Journal of Global Optimization*, 21:345 – 383, 2001.

[82] D. R. Jones, M. Schonlau, and W. J. Welch. "Efficient Global Optimization of Expensive Black-Box Functions,". *Journal of Global Optimization*, 13:455 – 492, 1998.

[83] A. J. Keane. "Statistical Improvement Criteria for Use in Multiobjective Design Optimization,". *AIAA Journal*, 44(4):879 – 891, April 2006.

[84] J. Knowles. "ParEGO: A Hybrid Algorithm with On-line Landscape Approximation for Expensive Multiobjective Optimization Problems,". *IEEE Transactions on Evolutionary Computation*, 10(1):50 – 66, Feb. 2005.

[85] P. N. Koch, J. P. Evans, and D. Powell. "Interdigitation for Effective Design Space Exploration using iSIGHT,". *Structural and Multidisciplinary Optimization*, 23(2):111 – 126, 2002.

[86] P. N. Koch, T. W. Simpson, and F. Mistree. "Statistical Approximations for Multidisciplinary Design Optimization: The Problem of Size,". *Journal of Aircraft*, 36(1):275 – 286, January-February 1999.

[87] N. A. Koratkar and I. Chopra. "Wind Tunnel Testing of a Smart Rotor Model with Trailing Edge Flaps,". *Journal of the American Helicopter Society*, 47(4):263 – 272, October 2002.

[88] J. B. Kosmatka. *Structural Dynamic Modeling of Advanced Composite Propellers by the Finite Element Method*. PhD Dissertation, UCLA, 1986. Mechanical and Aerospace Engineering.

[89] J. B. Kosmatka and P. P. Friedmann. "Vibration Analysis of Composite Turbopropellers Using a Nonlinear Beam-Type Finite-Element Approach,". *AIAA Journal*, 27(11):1606–1614, November 1989.

[90] J. Lee and P. Hajela. "Parallel Genetic Algorithm Implementation in Multidisciplinary Rotor Blade Design,". *Journal of Aircraft*, 33(5):962 – 969, Sept. – Oct. 1996.

[91] J. G. Leishman. *Principles of Helicopter Aerodynamics*, Cambridge University Press, Second edition, 2006.

[92] J. G. Leishman and T. S. Beddoes. "A Generalized Model for Unsteady Aerodynamic Behavior and Dynamic Stall Using the Indicial Method,". In *42nd Annual Forum of the American Helicopter Society*, pages 243 – 265, Washington D.C., 1986.

[93] J. W. Lim and I. Chopra. "Aeroelastic Optimization of a Helicopter Rotor,". *Journal of the American Helicopter Society*, 34(1):55 – 62, 1989.

[94] J. W. Lim and I. Chopra. "Aeroelastic Optimization of a Helicopter Rotor Using an Efficient Sensitivity Analysis,". *Journal of Aircraft*, 28(1):29 – 37, January 1991.

[95] L. Liu. *BVI Induced Vibration and Noise Alleviation by Active and Passive Approaches*. PhD Dissertation, University of Michigan, 2005. Aerospace Engineering.

[96] L. Liu, P. P. Friedmann, I. Kim, and D. S. Bernstein. "Vibration Reduction and Performance Enhancement in Rotorcraft Using Active Flaps at High Advance Ratios,". In *47th AIAA/ASME/ASCHE/AHS/ASC Structures, Structural Dynamics & Materials Conference*, pages 1 – 21, Newport, RI, May 1-4 2006. AIAA Paper 2006-1861.

[97] R. G. Loewy. "Helicopter Vibrations: A Technological Perspective,". *Journal of the American Helicopter Society*, 29(4):4 – 30, October 1984.

[98] S. N. Lophaven, H. B. Nielsen, and J. Søndergaard, *A Matlab Kriging Toolbox, Version 2.0*. Informatics and Mathematical Modeling, DTU, 2002. Technical Report IMM-TR-2002-12.

[99] J. D. Martin and T. W. Simpson. "Use of Kriging Models to Approximate Deterministic Computer Models,". *AIAA Journal*, 43(4):853 – 863, April 2005.

[100] M. D. McKay, R. J. Beckman, and W. J. Conover. "A Comparison of Three Methods for Selecting Values of Input Variables in the Analysis of Output from a Computer Code,". *Technometrics*, 21(2):239–245, May 1979.

[101] A. Messac and A. A. Mullur. "A Computationally Efficient Metamodeling Approach for Expensive Multiobjective Optimization,". *Optimization and Engineering*, 9(1):37 – 67, March 2008.

[102] J. H. Milgram, I. Chopra, and F. K. Straub. "Rotors with Trailing Edge Flaps: Analysis and Comparison with Experimental Data,". *Journal of the American Helicopter Society*, 43(4):319–332, October 1998.

[103] T. A. Millott and P. P. Friedmann, *Vibration Reduction in Helicopter Rotors Using an Actively Controlled Partial Span Trailing Edge Flap Located on the Blade*. NASA CR 4611, June 1994.

[104] P. Minguet and J. Dugundji. "Experiments and Analysis for Composite Blades Under Large Deflections, Part I – Static Behavior,". *AIAA Journal*, 28(9):1573–1579, Sept. 1990.

[105] S. Murugan and R. Ganguli. "Aeroelastic Stability Enhancement and Vibration Suppression in a Composite Helicopter Rotor,". *Journal of Aircraft*, 42(4):1013 – 1024, July-August 2005.

[106] S. Murugan, R. Ganguli, and D. Harursampath. "Effects of Structural Uncertainty on Aeroelastic Response of Composite Helicopter Rotor,". In *48th AIAA/ASME/ASCE/AHS/ACS Structures, Structural Dynamics and Materials Conference*, pages 1–18, Honolulu, HI, April 23-26 2007. AIAA Paper 2007-2298.

[107] R. H. Myers and D. C. Montgomery. *Response Surface Methodology: Process and Product Optimization Using Designed Experiments*, Wiley, New York, 1995.

[108] T. F. Myrtle. *Development of an Improved Aeroelastic Model for the Investigation of Vibration Reduction in Helicopter Rotors using Trailing Edge Flaps*. PhD Dissertation, University of California, Los Angeles, 1998. Mechanical and Aerospace Engineering.

[109] T. F. Myrtle and P. P. Friedmann. "Application of a New Compressible Time Domain Aerodynamic Model to Vibration Reduction in Helicopters Using an Actively Controlled Flap,". *Journal of the American Helicopter Society*, 46(1):32–43, January 2001.

[110] M. Orr, *MATLAB Functions for Radial Basis Function Networks*. Institute for Adaptive and Neural Computation, Division of Informatics,, Edinburgh University, Edinburgh EH8 9LW Scotland, UK, 1999.

[111] A. B. Owen. "Orthogonal Arrays for Computer Experiments, Integration and Visualization,". *Statistica Sinica*, 2:439 – 452, 1992.

[112] R. Palacios and C. E. S. Cesnik. "Cross-Sectional Analysis of Non-Homogeneous Anisotropic Active Slender Structures,". *AIAA Journal*, 43(12):2624–2638, December 2005.

[113] R. Palacios and C. E. S. Cesnik. "A Geometrically-Nonlinear Theory of Active Composite Beams with Deformable Cross Sections,". *AIAA Journal*, 46(2):439–450, February 2008.

[114] K. Palmer and M. Realff. "Metamodeling Approach to Optimization of Steady-State Flowsheet Simulations - Model Generation,". *Transactions of the Institution of Chemical Engineers*, 80(7):760 – 772, Oct. 2002.

[115] K. Palmer and M. Realff. "Optimization and Validation of Steady-State Flowsheet Simulation Metamodels,". *Transactions of the Institution of Chemical Engineers*, 80(7):773 – 782, Oct. 2002.

[116] D. Patt. *Simultaneous BVI Noise, and Vibration Reduction in Rotorcraft using Actively-Controlled Flaps and Including Performance Considerations*. PhD Dissertation, University of Michigan, 2004. Aerospace Engineering.

[117] D. Patt, L. Liu, J. Chandrasekar, D. S. Bernstein, and P. P. Friedmann. "Higher-Harmonic-Control Algorithm for Helicopter Vibration Reduction Revisited,". *Journal of Guidance, Control, and Dynamics*, 28(5):918–930, September-October 2005.

[118] D. Patt, L. Liu, and P. P. Friedmann. "Active Flaps for Noise Reduction: A Computational Study,". In *61st Annual Forum of the American Helicopter Society*, Grapevine, TX, June 1-3 2005.

[119] D. Patt, L. Liu, and P. P. Friedmann. "Rotorcraft Vibration Reduction and Noise Prediction Using a Unified Aeroelastic Response Simulation,". *Journal of the American Helicopter Society*, 50(1):95–106, January 2005.

[120] D. Patt, L. Liu, and P. P. Friedmann. "Simultaneous Vibration and Noise Reduction in Rotorcraft Using Aeroelastic Simulation,". *Journal of the American Helicopter Society*, 51(2):127 – 140, 2006.

[121] D. Petot. "Differential Equation Modeling of Dynamic Stall,". *La Recherche Aérospatiale*, 5:59–71, 1989.

[122] B. Popescu and D. H. Hodges. "Asymptotic Treatment of the Trapeze Effect in Finite Element Cross-Sectional Analysis of Composite Beams,". *International Journal of Nonlinear Mechanics*, 34(4):709–721, 1999.

[123] N. V. Queipo, R. T. Haftka, W. Shyy, T. Goel, R. Vaidyanathan, and P. K. Tucker. "Surrogate-Based Analysis and Optimization,". *Progress in Aerospace Sciences*, 41:1–28, 2005.

[124] G. Rahier and Y. Delrieux. "Blade-Vortex Interaction Noise Prediction Using a Rotor Wake Roll-Up Model,". *Journal of Aircraft*, 34(4):522–530, July-August 1997.

[125] R. G. Regis and C. A. Shoemaker. "Improved Strategies for Radial Basis Function Methods for Global Optimization,". *Journal of Global Optimization*, 37:113 – 135, 2007.

[126] L. W. Rehfield, A. R. Atilgan, and D. H. Hodges. "Nonclassical Behavior of Thin-Walled Composite Beams with Closed Cross Sections,". *Journal of the American Helicopter Society*, 35(2):42–50, April 1990.

[127] G. Reichert. "Helicopter Vibration Control – A Survey,". *Vertica*, 5(1):1–20, 1981.

[128] Vanderplaats Research and Inc. Development, *DOT Users Manual*, May 1995.

[129] W. P. Rodden and E. Albano. "A Doublet-Lattice Method for Calculating Lift Distributions on Oscillating Surfaces in Subsonic Flows,". *AIAA Journal*, 7:279 – 285, 1969.

[130] K. L. Rogers, *Airplane Math Modeling Methods for Actively Control Design*. AGARD-CP-228, August 1977.

[131] J. Sacks, W. J. Welch, T. J. Mitchell, and H. P. Wynn. "Design and Analysis of Computer Experiments,". *Statistical Science*, 4(4):409 – 435, 1989.

[132] M. Sasena. *Flexibility and Efficiency Enhancements for Constrained Global Optimization with Kriging Approximations*. PhD Dissertation, University of Michigan, 2002. Mechanical Engineering.

[133] M. J. Sasena, P. Papalambros, and P. Goovaerts. "Exploration of Metamodeling Sampling Criteria for Constrained Global Optimization,". *Engineering Optimization*, 34:263–278, 2002.

[134] L. A. Schmit and H. Miura, *Concepts for Efficient Structural Synthesis*. NASA CR-2552, 1976.

[135] F. H. Schmitz, *Rotor Noise, Aeroacoustics of Flight Vehicles, Vol.1*. Acoustical Society of America and American Institute of Physics, New York, 1995. pp. 65-149.

[136] M. P. Scully. *Computation of Helicopter Rotor Wake Geometry and its Influence on Rotor Harmonic Airloads*. PhD Dissertation, Aeroelastic Research Laboratory, Massachusetts Institute of Technology, 1975.

[137] L. F. Shampine. *Numerical Solution of Ordinary Differential Equations*, Chapman and Hall, New York, 1994.

[138] J. Shaw, N. Albion, E. J. Hanker, and R. S. Teal. "Higher Harmonic Control: Wind Tunnel Demonstration of Fully Effective Vibratory Hub Force Suppression,". *Journal of the American Helicopter Society*, 34(1):14 – 25, January 1989.

[139] L. A. Shultz, B. Panda, F. J. Tarzanin, R. C. Derham, B. K. Oh, and L. Dadone. "Interdisciplinary Analysis for Advanced Rotors - Approach, Capabilities, and Status,". In *American Helicopter Society Aeromechanics Specialists Conference*, 1994. PS 4-1-4-15.

[140] T. W. Simpson, A. J. Booker, D. Ghosh, A. A. Giunta, P. N. Koch, and R. Yang. "Approximation Methods in Multidisciplinary Analysis and Optimization: A Panel Discussion,". *Structural and Multidisciplinary Optimization*, 27(5):302 – 313, July 2004.

[141] T. W. Simpson, T. M. Mauery, J. J. Korte, and F. Mistree. "Kriging Models for Global Approximation in Simulation-based Multidisciplinary Design Optimization,". *AIAA Journal*, 39(12):2233 – 2241, 2001.

[142] T. W. Simpson, D. Peplinski, P. N. Koch, and J. K. Allen. "Metamodels for Computer-based Engineering Design: Survey and Recommendations,". *Engineering with Computers*, 17:129 – 150, 2001.

[143] A. Sóbester, S. J. Leary, and A. J. Keane. "A Parallel Updating Scheme for Approximating and Optimizing High Fidelity Computer Simulations,". *Structural and Multidisciplinary Optimization*, 27:371–383, 2004.

[144] A. Sóbester, S. J. Leary, and A. J. Keane. "On the Design of Optimization Strategies Based on Global Response Surface Approximation Models,". *Journal of Global Optimization*, 33:31 – 59, 2005.

[145] I. M. Sobol. "Sensitivity Analysis for Nonlinear Mathematical Models,". *Mathematical Modeling & Computational Experiment*, 1(4):407–414, 1993.

[146] W. G. O. Sonneborn. "Quo Vadis U.S. Helicopter Community? The 25th Alexander A. Nikolsky Lecture,". *Journal of the American Helicopter Society*, 51(4):291 – 298, Oct. 2006.

[147] W. Splettstoesser, R. Kube, W. Wagner, U. Seelhorst, A. Boutier, F. Micheli, E. Mercker, and K. Pengel. "Key Results From a Higher Harmonic Control Aeroacoustic Rotor Test (HART),". *Journal of the American Helicopter Society*, 42(1):58 – 78, January 1997.

[148] W. Splettstoesser, U. Seelhorst, W. Wagner, A. Boutier, F. Micheli, E. Mercker, and K. Pengel. "Higher Harmonic Control Aeroacoustic Rotor Test (HART) - Test Documentation and Representative Results,". Report IB 129-95/28 and appendices, DLR, December 1995.

[149] N. Stander, W. Roux, M. Giger, M. Redhe, N. Fedorova, and J. Haarhoff. "A Comparison of Metamodeling Techniques for Crashworthiness Optimization,". In *10th AIAA/ISSMO Multidisciplinary Analysis & Optimization Conference*, pages 1–11, Albany, New York, Aug.30 - Sept.1 2004. AIAA Paper 2004-4489.

[150] F. K. Straub. "Active Flap Control for Vibration Reduction and Performance Improvement,". In *Proceedings of the 51st Annual Forum of the American Helicopter Society*, pages 381–392, Fort Worth, TX, May 1995.

[151] F. K. Straub, D. K. Kennedy, D. B. Bomzalski, A. A. Hassan, H. Ngo, V. R. Anand, and T. S. Birchette. "Smart Material Actuated Rotor Technology - SMART,". *Journal of Intelligent Material Systems and Structures*, 15:249 – 260, 2004.

[152] F. K. Straub, D. K. Kennedy, A. D. Stemple, V. R. Anand, and T. S. Birchette. "Development and Whirl Tower Test of the SMART Active Flap Rotor,". *Proceedings of SPIE: Smart Structures and Materials 2004*, 5388:202–212, July 2004.

[153] S. M. Swanson, S. A. Jacklin, A. Blaas, G. Niesl, and R. Kube. "Reduction of Helicopter BVI Noise, Vibration, and Power Consumption through Individual Blade Control,". In *Proceedings of the 51st Annual Forum of the American Helicopter Society*, pages 662–680, Fort Worth, TX, May 1995.

[154] R. Vaidyanathan, T. Goel, W. Shyy, and R. T. Haftka. "Global Sensitivity and Trade-Off Analysis for Multi-Objective Liquid Rocket Injector Design,". In *40th AIAA/ASME/SAE/ASEE Joint Propulsion Conference and Exhibit*, Ft. Lauderdale, FL, July 11-14 2004. AIAA 2004-4007.

[155] G. N. Vanderplaats, *CONMIN - A Fortran Program for Constrained Function Minimization*. NASA TM-X 62282, Aug. 1973.

[156] V. V. Volovoi, D. H. Hodges, C. E. S. Cesnik, and B. Popescu. "Assessment of Beam Modeling Methods for Rotor Blade Applications,". *Mathematical and Computer Modelling*, 33:1099–1112, April 2001.

[157] D. A. Wachspress and T. R. Quackenbush. "BVI Noise Mitigation Via Steady Flap Deflection – An Analysis-Led Test Program,". In *Proceedings of the American Helicopter Society 4th Decennial Specialists Conference on Aeromechanics*, San Francisco, CA, Jan 2004.

[158] J. L. Walsh, *Performance Optimization of Helicopter Rotor Blades*. NASA TM-104054, April 1991.

[159] J. L. Walsh, W. J. LaMarsh II, and H. M. Adelman. "Fully Integrated Aerodynamic/Dynamic Optimization of Helicopter Rotor Blades,". *Mathematical and Computer Modelling*, 18(3/4):53 – 72, 1993.

[160] J. L. Walsh, K. C. Young, J. L. Pritchard, and H. M. Adelman, *Integrated Aerodynamic/Dynamic/Structural Optimization of Helicopter Rotor Blades Using Multilevel Decomposition*. NASA TP-3465, Jan. 1995.

[161] G. G. Wang and S. Shan. "Review of Metamodeling Techniques in Support of Engineering Design Optimization,". *Journal of Mechanical Design*, 129(4):370 – 380, April 2007.

[162] L. Wang, S. Shan, and G. G. Wang. "Mode-Pursuing Sampling Method for Global Optimization on Expensive Black-Box Functions,". *Engineering Optimization*, 36(4):419 – 438, Aug. 2004.

[163] K. Washizu. "Some Considerations on a Naturally Curved and Twisted Slender Beam,". *Journal of Mathematics and Physics*, 43(2):111–116, 1964.

[164] W. H. Weller and M. W. Davis. "Wind Tunnel Tests of Helicopter Blade Designs Optimized for Minimum Vibrations,". *Journal of the American Helicopter Society*, 34(3):40 – 50, 1989.

[165] G. Wempner. *Mechanics of Solids with Application to Thin Bodies*, Sijthoff & Noordoff, 1981.

[166] B. Wilson, D. Cappelleri, T. W. Simpson, and M. Frecker. "Efficient Pareto Frontier Exploration using Surrogate Approximations,". *Optimization and Engineering*, 2:31 – 50, 2001.

[167] K. S. Won and T. Ray. "A Framework for Design Optimization using Surrogates,". *Engineering Optimization*, 37(7):685 – 703, October 2005.

[168] B. A. Wujek and J. E. Renaud. "Improved Trust Region Model Management for Approximate Optimization,". In *Advances in Design Automation*, Atlanta, Georgia, September 13 – 16 1998. Paper No. DETC98/DAC-5616.

[169] D. K. Young and F. J. Tarzanin. "Structural Optimization and Mach Scale Test Validation of a Low Vibration Rotor,". *Journal of the American Helicopter Society*, 38(3):83 – 92, 1993.

[170] W. Yu, D. H. Hodges, V. V. Volovoi, and C. E. S. Cesnik. "On Timoshenko-like Modeling of Initially Curved and Twisted Composite Beams,". *International Journal of Solids and Structures*, 39(19):5101–5121, Sept. 2002.

[171] W. Yu, V. V. Volovoi, D. H. Hodges, and X. Hong. "Validation of the Variational Asymptotic Beam Sectional Analysis,". *AIAA Journal*, 40(10):2105–2112, Oct. 2002.

[172] Y. H. Yu. "Rotor Blade-Vortex Interaction Noise,". *Progress in Aerospace Sciences*, 36(2):97 – 115, February 2000.

[173] Y. H. Yu, T. F. Brooks, and W. Splettstoesser. "Reduction of Helicopter Blade-Vortex Interaction Noise by Active Rotor Control Technology,". *Progress in Aerospace Sciences*, 33(10):647 – 687, September 1997.

[174] K. A. Yuan and P. P. Friedmann, *Aeroelasticity and Structural Optimization of Composite Helicopter Rotor Blades with Swept Tips*. NASA CR 4665, May 1995.

[175] K. A. Yuan and P. P. Friedmann. "Structural Optimization for Vibratory Loads Reduction of Composite Helicopter Rotor Blades with Advanced Geometry Tips,". *Journal of the American Helicopter Society*, 43(3):246–256, July 1998.

[176] L. Zerpa, N. V. Queipo, S. Pintos, and J. Salager. "An Optimization Methodology of Alkaline-Surfactant-Polymer Flooding Process using Field Scale Numerical Simulation and Multiple Surrogates,". *Journal of Petroleum Science and Engineering*, 47:197 – 208, 2005.

[177] J. Zhang. *Active-Passive Hybrid Optimization of Rotor Blades With Trailing Edge Flaps*. PhD Dissertation, The Pennsylvania State University, 2001.

[178] J. Zhang, E. C. Smith, and K. W. Wang. "Active-Passive Hybrid Optimization of Rotor Blades with Trailing Edge Flaps,". *Journal of the American Helicopter Society*, 49(1):54 – 65, January 2004.

[179] Q. Zhao and G. Xu. "A Study on Aerodynamic and Acoustic Characteristics of Advanced Tip-Shape Rotors,". *Journal of the American Helicopter Society*, 52(3):201 – 213, July 2007.

[180] E. Zitzler and L. Thiele. "Multiobjective Evolutionary Algorithms: A Comparative Case Study and the Strength Pareto Approach,". *IEEE Transactions on Evolutionary Computation*, 3(4):257 – 271, 1999.